

INVESTIGATION OF THE PROGENITORS AND OUTBURSTS
OF CLASSICAL AND RECURRENT NOVAE

Farung Surina

Astrophysics Research Institute

A thesis submitted in partial fulfilment of the requirements of
Liverpool John Moores University
for the degree of
Doctor of Philosophy.
March 3, 2014

Declaration

The work presented in this thesis was carried out at the Astrophysics Research Institute, Liverpool John Moores University. Unless otherwise stated, it is the original work of the author.

While registered as a candidate for the degree of Doctor of Philosophy, for which submission is now made, the author has not been registered as a candidate for any other award. This thesis has not been submitted in whole, or in part, for any other degree.

Farung Surina
Astrophysics Research Institute
Liverpool John Moores University
Liverpool Science Park IC2 Building
146 Brownlow Hill
Liverpool
L3 5RF
UK

MARCH 3, 2014

Abstract

Classical novae (CNe) are interacting binary systems whose outbursts are powered by a thermonuclear runaway in accreted material on the surface of a white dwarf (WD). The secondary stars in such systems fill their Roche lobe and material is transferred onto the WD primary star via an accretion disk.

Recurrent novae (RNe) show many similarities to CNe, but have had more than one recorded outburst. They play an important role as one of the suspected progenitor systems of Type Ia supernovae (SNe) which are used as primary distance indicators in cosmology. Thus, it is important to investigate the nature of their central binary systems to determine the relation between the parameters of the central system and outburst type, and finally ascertain the population of novae that might be available to give rise to the progenitors of Type Ia SNe. The investigation looking for characteristics that may distinguish RNe from CNe systems, the selection of initial targets for detailed study, and results of the investigation are presented in this thesis.

The proposal that RNe occupy a region separated from CNe in an outburst amplitude versus speed class diagram was adopted. Since the low amplitude results from the existence of an evolved secondary and/or high mass transfer rate in the quiescent system, RNe candidates should accordingly have low amplitude. The 93 novae with observed V amplitudes given in the literature and 43 novae with photographic amplitudes have been combined and plotted on an outburst amplitude versus rate of decline diagram from which 16 target novae suspected to be RNe candidates were selected for photometric and spectroscopic follow-up.

Quiescent photometric magnitudes and spectra were obtained using RATCam on LT,

FRODOSpec on LT, and RSS on SALT. Spectral type and luminosity class determined from the near-IR colour-magnitude diagrams were compared to those derived from the spectra. Determination of spectral types was accomplished by identifying specific lines and calculating indices from TiO bands, VO bands, and the Na atomic line for giants (finding 4 stars) and sub-giants/giants (3 stars). A spectral library template was used instead of the indices in cases of main-sequence stars (2 stars).

Our investigation also confirmed the positions of AR Cir, V794 Oph and EU Sct where there had been some ambiguity previously. Ultimately, we suggest four prime RNe candidates (2 novae with giant secondaries - V3964 Sgr and EU Sct, and 2 novae with sub-giant secondaries - V794 Oph and V368 Aql) which are currently classified as CNe, to look for more than one outburst in archival plates or large sample sky surveys such as SMEI (see below).

By introducing the high cadence full-sky space-based observational archive of the Solar Mass Ejection Imager (SMEI) which operated on the Coriolis satellite from 2003-2011, we derived light curves of one Mira (O Cet) as a general example and two novae with known outbursts during 2003-2011 (V2467 Cyg and V1187 Sco). The SMEI light curves potentially reveal more details than those given by ground-based observations. The pre-maximum halt was found in V2467 Cyg as well as oscillations in light curves found earlier than those found in previous studies. The precise date of maximum of each nova was provided.

Four bright novae that are potentially RNe candidates (V4074 Sgr, V3964 Sgr, DK Lac and V368 Aql) were searched for second outbursts in the SMEI data, but none were found. Among the nova outbursts detected by SMEI, we found however unprecedented detail in first class data of the Recurrent Nova T Pyx in its 2011 outburst.

We investigated the optical light curve of T Pyx during its 2011 outburst through compiling a database of SMEI and American Association of Variable Star Observers (AAVSO) observations. The SMEI light curve, covering $t=1.5-49$ days post-discovery, was divided into four phases based on the idealised nova optical light curve; the initial rise (1.5-3.3 days), the pre-maximum halt (3.3-13.3 days), the final rise (14.7-27.9

days), and the early decline (27.9 days, until the end of SMEI observations on day 49). The SMEI light curve contains a strongly detected period of 1.44 ± 0.05 days during the pre-maximum halt phase. These oscillations resemble those found in recent TNR models arising from instabilities in the expanding envelope. No spectral variations that mirror the light curve periodicity were found however. The marked dip at $t \sim 22-24$ days just before light curve maximum at $t = 27.9$ days may represent the same (shorter duration) phenomenon seen in other novae observed by SMEI and present in some TNR model light curves.

The spectra of T Pyx from the 2m the Liverpool Telescope and the Small and Moderate Aperture Research Telescope System (SMARTS) 1.5m telescope were obtained from $t = 0.8-80.7$ and $155.1-249.9$ days, covering the major phases of development. The nova was observed very early in its rise where a distinct high velocity ejection phase was evident with derived $V_{ej} \sim 4000 \text{ km s}^{-1}$ initially. A marked drop at $t = 5.7$ days, and then a gradual increase occurred in derived V_{ej} to stabilise at $\sim 1500 \text{ km s}^{-1}$ at the pre-maximum halt. Here we propose two different stages of mass loss, a short-lived phase occurring immediately after outburst and lasting ~ 6 days followed by a more steadily evolving and higher mass loss phase. The overall spectral development follows that typical of a Classical Nova and comparison with the photometric behaviour reveals consistencies with the simple evolving pseudo-photosphere model of the nova outburst. Comparing optical spectra to X-ray and radio light curves, weak [Fe X] 6375 \AA emission was marginally detected before the X-ray rise and was clearly present during the brightest phase of X-ray emission. If the onset of the X-ray phase and the start of the final decline in the optical are related to the cessation of significant mass loss, then this occurred at $t \sim 90-110$ days.

Publications

In the course of completing the work presented in this thesis, the following papers have been published.

Surina, F., Bode, M. F., & Darnley, M. J., 2013, ‘Investigation of the Progenitors of Nova Explosions’, The 11th Asian-Pacific Regional IAU Meeting 2011, NARIT Conference Series, Vol. 1, p161-164

Surina, F., Hounsell, R. A., Bode, M. F., Darnley, M. J., Harman, D. J., Walter, & F. M., 2013 , ‘Spectroscopic and Photometric Development of T Pyxidis (2011) from 0.8 to 250 Days After Discovery’, *Stella Novae: Future and Past Decades*, ASP Conference Series, P. A. Woudt and V. A. R. M. Ribeiro, eds, arXiv-eprint 1303.6592

Darnley, M. J., Bode, M. F. and Harman, D. J., Hounsell, R. A., Munari, U., Ribeiro, V. A. R. M., **Surina, F.**, Williams, R. P., & Williams, S. C., 2014, *Stella Novae: Future and Past Decades*, ASP Conference Series, P. A. Woudt and V. A. R. M. Ribeiro, eds, arXiv-eprint 1303.2711

Surina, F., Hounsell, R. A., Bode, M. F., Darnley, M. J., Harman, D. J., & Walter, F. M., 2014 , ‘The Detailed Photometric and Spectroscopic Study of the Recurrent Nova T Pyxidis (2011) from 0.8 to 250 Days After Discovery’, *Astronomical Journal* (accepted)

Acknowledgements

First and foremost, I would like to thank my supervisors Professor Mike Bode and Dr. Matt Darnley for all their guidance, help and support throughout my PhD. I am so grateful for their patience and encouragement for keeping me going when the end seemed unreachable. Their hard work is very much appreciated.

I would also like to express my gratitude to Professor Fred Walter and Professor Sumner Starrfield for reading manuscripts, additional help and many useful discussions. Many thanks to Dr. Valério A. R. M. Ribeiro, Dr. Rebekah Hounsell and Professor Patrick Woudt for all the wonderful times working together with me. I would like to thank Dr. Dan Harman, Andre Brabin and Anna Hodgkinson for helping me get through many technical problems. I would also like to thank all the members of ARI (past and present) for all their friendly support, friendship and those smiles along the way.

Thanks Stacey, Claire, Emma, Alyssa, and Maia - the fabulous ARI girl gang for being there to chat when frustrated. Many thanks to all my LTS friends especially P'Big, P'Air, P'Jeep, P'Jay and P'Pound for always being there for me and putting up with me when I am crazy here in Liverpool.

Last but not least, I would like to thank my family for all their love and support and also for believing in me even when I did not. This thesis is dedicated to my dad and mom because I could never have come this far without them.

With all my heart,

FARUNG SURINA

MARCH 3, 2014

Contents

Declaration	ii
Abstract	iii
Publications	vi
Acknowledgements	vii
Contents	viii
List of Tables	xiii
List of Figures	xv
1 Introduction	1
1.1 Historical Perspective of Nova Explosions	1
1.2 Outbursts of Classical Novae and Recurrent Novae	2
1.2.1 Classical Novae	2
1.2.2 Recurrent Novae	6
1.3 Frequency and Distribution of Galactic Novae	8
1.4 Light Curves of Novae	9

1.5	Spectra of Novae	11
1.5.1	During Eruption	11
1.5.2	In Quiescence	13
1.6	Progenitors of Type Ia Supernovae	15
1.7	Open Questions	17
1.8	This Work	18
2	Selection of Potential Recurrent Novae among the Classical Novae	20
2.1	Introduction	20
2.2	Relationships between Amplitude, Rate of Decline and Absolute Magnitude	20
2.3	Criteria of Selection	23
2.4	Discussion and Conclusion	28
3	Ground-based Observations of Novae and Data Reduction	31
3.1	The Liverpool Telescope	31
3.1.1	RATCam	34
3.1.2	FRODOSpec	37
3.2	The Southern African Large Telescope	40
3.2.1	The Robert Stobie Spectrograph (RSS)	41
3.3	Relative Flux Calibration with Standard Stars	45
3.4	Discussion and Conclusion	47
4	Observations of Galactic Novae in Quiescence	51

4.1	Introduction	51
4.2	Background to the Analysis	52
4.3	Reddening	53
4.4	Photometric Observations and Results	55
4.5	Spectral Analysis to Determine Luminosity Class and Spectral Type .	59
4.6	Spectroscopic Observations and Results	67
4.6.1	T CrB	67
4.6.2	V2487 Oph	69
4.6.3	CI Aql	71
4.6.4	AR Cir	72
4.6.5	V3964 Sgr	75
4.6.6	V3645 Sgr	76
4.6.7	V794 Oph	78
4.6.8	V368 Aql	79
4.6.9	EU Sct	81
4.6.10	CN Vel, LZ Mus and V888 Cen	82
4.7	Discussion and Conclusion	88
5	Investigation of Novae with the Solar Mass Ejection Imager (SMEI)	91
5.1	Introduction	91
5.2	Acquisition of SMEI Data	95
5.3	Light Curves of Detected Variables	97
5.3.1	Omicron Ceti	97

5.3.2	Detected Novae Outbursts	98
5.4	Searching for Nova Outbursts	103
5.5	SMEI Observations of Nova T Pyxidis	106
5.6	Discussion and Conclusion	110
6	T Pyxidis in its 2011 Outburst	116
6.1	Introduction	116
6.1.1	Central System and Surroundings	116
6.1.2	The Outburst in 2011	119
6.2	Observations	121
6.2.1	Photometric Observations from SMEI	121
6.2.2	Spectroscopic Observations	121
6.3	Results and Discussion	123
6.3.1	SMEI Light Curves	123
6.3.2	Spectra from SMARTS and LT	131
6.3.3	Comparison to the X-ray and Radio Light Curves	157
6.4	Conclusions	159
7	Summary, Conclusions and Future Work	163
7.1	Summary and Conclusions	163
7.1.1	Observations of Galactic Novae in Quiescence	163
7.1.2	Investigation of Novae with the Solar Mass Ejection Imager (SMEI)	165
7.1.3	T Pyxidis in Its 2011 Outburst	166

7.2	Future Work	168
7.2.1	Galactic Novae in Quiescence	168
7.2.2	Investigation of Novae with the Solar Mass Ejection Imager (SMEI)	169
A	Acquisition of SMEI Data	170
A.1	Connecting to the SMEI Computer and Accessing the Database	170
A.2	Adding New Objects to SMEI's Object List	171
A.3	Object Visual Inspection in SMEI's Sky Maps	171
A.4	Fitting a Point Source	173
	Bibliography	175

List of Tables

1.1	Definition of speed class of Classical nova.	6
1.2	Average rate of nova discovery	9
2.1	Typical values of MMRD constants.	21
2.2	Novae from catalogues that are used in target selection.	25
3.1	RATCam photometric observation log.	33
3.2	Spectroscopic observation log	33
3.3	The format of the science-ready data product from the FRODOSpec pipeline.	39
3.4	Final target novae lists for photometric and spectroscopic analysis. . .	50
4.1	Observed optical and NIR apparent magnitudes of target novae at quiescence.	56
4.2	The distances (in kpc) of targets calculated from each extinction map .	58
4.3	Measured $EW(\text{CaT})$ and stellar parameters for target novae.	85
4.4	Line indicators for Luminosity classification.	86
4.5	TiO, VO and Na I indices for target novae.	87
4.6	Proposed spectral and luminosity class of secondaries in target novae.	89

5.1	List of bright novae selected for SMEI investigation.	96
5.2	SMEI observations of T Pyx from Camera 2.	112
6.1	Log of optical spectral observations.	122
6.2	Results from <i>PERIOD04</i>	130
6.3	High ionization lines and some selected lower ionization lines present in the spectra of T Pyx 2011 in its initial rise and pre-maximum halt phases.	142
6.4	Ionization levels at various decline stages according to Bath & Hark- ness (1989; only species with strong optical lines noted).	143

List of Figures

1.1	The equipotential surfaces in a binary system.	2
1.2	Schematic illustration of the initial formation of a ring and its evolution into a disk.	3
1.3	The distribution in Galactic coordinates of classical novae.	8
1.4	The Morphology of a nova light curve.	10
1.5	Spectra showing typical Fe II novae and He/N novae.	14
2.1	Amplitude-rate of decline relationship for CNe.	22
2.2	Target selection from <i>V</i> amplitudes and rate of decline.	29
2.3	Target selection from photographic amplitudes and rate of decline. . .	30
3.1	Founder of the Liverpool Telescope Prof. Mike Bode and the LT itself on La Palma in its fully-opening enclosure.	32
3.2	Image of RATCam on the Liverpool Telescope.	36
3.3	Part of FRODOSpec on an optical bench before shipping to site. . . .	38
3.4	An example of FRODOSpec data product preview.	39
3.5	The Southern African Large Telescope (SALT).	41
3.6	The SALT viewing annulus.	41

3.7	Schematic illustration of spectroscopy modes of RSS.	42
3.8	SALT RSS long-slit data reduction process.	46
3.9	Flux calibration of standard star eg139.	48
3.10	Flux calibration of standard star eg158.	49
4.1	Extinction along the line of sight, A_v , versus the equivalent width of Na I D.	54
4.2	Optical CMD showing 10 targets compared with stars plotted from the <i>Hipparcos</i> data set.	60
4.3	Near-infrared CMD showing 16 targets compared with stars generated by cross-correlating the <i>Hipparcos</i> and 2MASS catalogues.	61
4.4	The relationship between $EW(\text{CaT})$ and $\log g$	62
4.5	The relationship between the gravity-sensitive Na 8190 index and the temperature-sensitive TiO 8465 index.	63
4.6	Dependence of $[\text{TiO}]_1$ on spectral type for giants.	64
4.7	Dependence of $[\text{TiO}]_2$ on spectral type for giants.	65
4.8	Dependence of $[\text{VO}]$ on spectral type for giants.	65
4.9	Dependence of $[\text{Na}]$ on spectral type for giants.	66
4.10	Dependence of $[\text{Na}]$ on $[\text{TiO}]_2$ for giants.	66
4.11	Relative flux-calibrated LT spectrum of T CrB.	68
4.12	Relative flux-calibrated spectrum of V2487 Oph.	70
4.13	Relative flux-calibrated spectrum of CI Aql.	72
4.14	Calibrated MMT spectrum of CI Aql	73
4.15	Relative flux-calibrated SALT spectrum of AR Cir	74

4.16	Relative flux-calibrated SALT spectrum of AR Cir.	75
4.17	Relative flux-calibrated SALT spectrum of V3645 Sgr.	77
4.18	Relative flux-calibrated SALT spectrum of V794 Oph.	78
4.19	Relative flux-calibrated SALT spectrum of V368 Aql.	79
4.20	Calibrated NTT spectrum of V368 Aql	80
4.21	Relative flux-calibrated SALT spectrum of EU Sct.	81
4.22	Calibrated NTT spectrum of EU Sct	82
4.23	Relative flux-calibrated SALT spectrum of CN Vel.	83
4.24	Relative flux-calibrated SALT spectrum of LZ Mus.	84
4.25	Relative flux-calibrated SALT spectrum of V888 Cen.	84
5.1	Coriolis spacecraft with the SMEI on board.	92
5.2	Schematic of SMEI in orbit.	92
5.3	SMEI 60°×3° data frames from each of three cameras.	94
5.4	Composite view of the sky over a full orbit projected from individual SMEI CCD cameras.	94
5.5	SMEI light curve of Mira Omi Cet.	97
5.6	SMEI light curves of nova V2467 Cyg.	99
5.7	SMEI light curve of nova V1187 Sco.	101
5.8	SMEI sky maps for V1187 Sco at peak brightness.	102
5.9	SMEI sky maps for V1187 Sco with the Moon nearby.	103
5.10	SMEI results at the position of nova V4074 Sgr for 2003-2011.	104
5.11	SMEI results at the position of nova V3964 Sgr for 2003-2011.	105

5.12	SMEI results at the position of nova DK Lac for 2003-2011.	105
5.13	SMEI results at the position of nova V368 Aql for 2003-2011.	106
5.14	Secular decline of <i>B</i> magnitude and mass accretion rate	108
5.15	SMEI light curve of Recurrent Nova T Pyx.	109
5.16	SMEI light curve of Recurrent Nova T Pyx.	110
6.1	T Pyx and its shell	118
6.2	The AAVSO optical light curves of T Pyx in its 2011 outburst.	119
6.3	The pre-eruption rise and the initial rise.	120
6.4	The SMEI light curve of T Pyx during its 2011 outburst.	124
6.5	Four idealised phases of the SMEI light curve.	125
6.6	Modelled light curves of a typical nova cycle from Hillman et al. (2013).	127
6.7	The outburst in 2011 from SMEI compared to previous outburst.	128
6.8	Period found by analysing the SMEI light curve from the beginning of SMEI observations to the last observation.	132
6.9	Period found by analysing the SMEI light curve from the beginning of SMEI observations to the end of the pre-maximum halt phase.	133
6.10	Period found by analysing the SMEI light curve from beginning of SMEI observations to visual maximum.	134
6.11	Period found by analysing the SMEI light curve from the end of the pre-maximum halt phase to the last SMEI observation.	135
6.12	Period found by analysing the SMEI light curve from the visual maxi- mum to the last SMEI observation.	136
6.13	SMEI light curve of T Pyx compared to flux and ejection velocities from Balmer and Fe II lines.	137

6.14	P Cygni profile of H α lines from the initial rise to the end of the pre-maximum halt phase	138
6.15	Low-resolution spectra of T Pyx taken from $t=1.7-247$ days.	140
6.16	Detection of high ionization lines (e.g. O III and N III) present during the initial rise.	144
6.17	Evolution of the flux of Fe II lines at 5169, 5018, and 4233Å.	147
6.18	The red spectra during the pre-maximum halt phase.	148
6.19	The blue spectra during the pre-maximum halt phase.	149
6.20	The blue spectra during the final rise phase.	150
6.21	The red spectra during the final rise phase.	151
6.22	The blue spectra during the early decline phase.	152
6.23	The red spectra during the early decline phase.	153
6.24	The blue spectra during the transition phase.	155
6.25	The red spectra during the transition phase.	156
6.26	Comparison between optical, radio and X-ray light curves.	158
A.1	SMEI user interface.	172
A.2	Object point source displayed on SMEI's sky map.	173
A.3	SMEI sky maps for T Pyx at different epochs.	173

Chapter 1

Introduction

1.1 Historical Perspective of Nova Explosions

Nova from *stella nova*, first mentioned around AD 75 by Hipparchus, means *a new star*. This new star of Hipparchus was later considered to be a meteor or a comet, but the term ‘nova’ continues to be used with a different meaning as a star that suddenly increases its light output tremendously and fades away to its former obscurity in a few months or years. Until the 1920s, novae and supernovae were classed together. However some novae in spiral galaxies appeared to be as bright as their host galaxies such as S And in M31 and Z Cen in NGC 5253, and supernovae were subsequently designated as the more luminous stellar explosions (Duerbeck, 2008).

Lundmark (1935), for the first time, classified novae into three groups according to the absolute magnitude and the frequency of the outburst as follows: supernovae with M_{max} at -15 and frequency of 1 per 50 years in the Milky Way, ordinary novae with M_{max} at -7 and frequency of 50 per year, and finally those that are designated as dwarf novae with M_{max} at +3 or +4. Ordinary novae, which might be defined as classical novae (CNe) including the Recurrent Novae (RNe) subtype, and the up-to-date frequency of novae will be explained in Sections 1.2 and 1.3, respectively.

Unlike ordinary novae (CNe and RNe), dwarf novae (DNe) explode due to the increas-

ing mass flow through accretion disks. As a result, their outburst amplitudes of order a few magnitudes, are much smaller than those of CNe and RNe. The relationship between CNe, RNe and DNe has long been established (Warner, 1995). The debate over the relationship of RNe to SNe Ia continues (Bode, 2010) and will be explained in Section 1.7.

1.2 Outbursts of Classical Novae and Recurrent Novae

1.2.1 Classical Novae

Classical novae (CNe) are interacting binary systems whose outbursts are powered by a thermonuclear runaway (TNR) on the surface of a white dwarf (WD). Meanwhile their secondary stars are filling their Roche lobe and transferring material onto the white dwarf primary stars via accretion disks (Starrfield, 2008a) as shown in Figures 1.1 and 1.2.

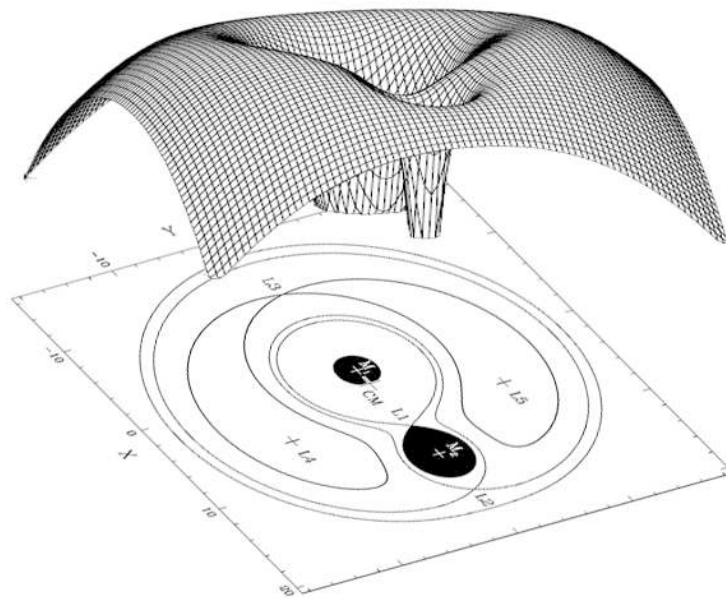


Figure 1.1: The equipotential surfaces in a binary system. The lines represent the effective gravity in the co-rotating frame of a binary system with a mass ratio (M_1/M_2) of 2. The points of zero effective gravity are the Lagrangian points ($L_{1,2,3,4,5}$). The Roche lobes are the equipotential surfaces that only intersect at L_1 . In this Figure, the secondary star has filled its Roche lobe and is transferring material to the primary (Picture modified from Baraffe et al. (1998)).

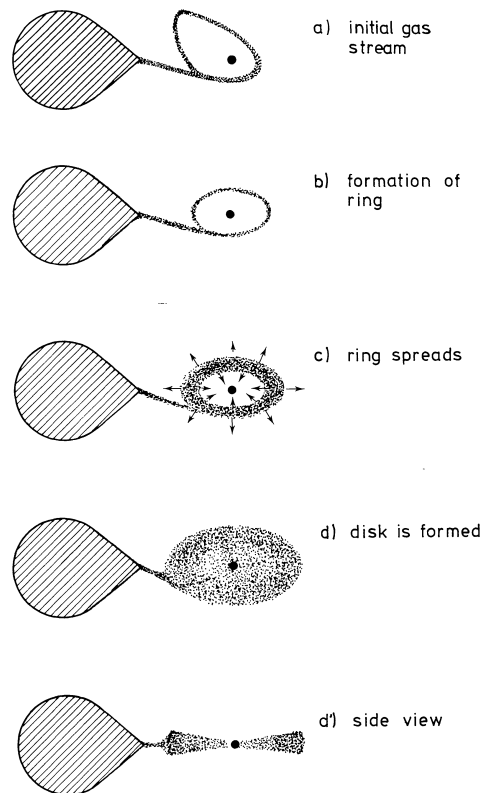


Figure 1.2: Schematic illustration of the initial formation of a ring and its evolution into a disk. Image from Verbunt (1982).

Thermonuclear Runaway

The cause of the nova explosion is the runaway effect of a nuclear chain reaction on the surface of a WD (Hellier, 2001; Starrfield, 2008b). This can be explained step by step as follows:

1. The WD is the remnant core of a star once nuclear burning has ceased. That is, most of the hydrogen in the core has burnt into helium, carbon, and other heavier elements. Thus, fresh hydrogen must be supplied to the WD from a donor secondary star in order to ignite the nuclear reactions again.
2. When material, mainly hydrogen, from the secondary star is transferred to the WD via an accretion disk, the material builds up on the WD surface, and the lowest layers are degenerate.

3. Pressure from degenerate electrons is very high and exceeds the thermal pressure of electrons at the WD surface.
4. As material is accreting, temperature and density are increasing. The main nuclear reactions finally ignite. Helium can be produced in two processes either pp-chain or CNO cycle. The pp-chain (the nuclear energy generation rate per unit volume, $\epsilon_{nuc} \propto T^4$) which is important during the accretion phase becomes efficient at $T \sim 10^6$ K while the CNO cycle ($\epsilon_{nuc} \propto T^{18}$) which is important during TNR and explosion becomes efficient at $T \sim 10^7$ K.
5. Unlike in non-degenerate matter where pressure depends on temperature and matter will expand to cool down when temperature is high to moderate a system, degeneracy pressure is solely dependent on density. As a result, matter does not expand to moderate the burning rate. Thus as the temperature increases, ϵ_{nuc} increases but with no expansion, temperature rises again, hence TNR.
6. When the CNO cycle becomes dominant, in the early stage, energy is transferred by convection due to the temperature gradient between the hot inner layer and the cooler outer layer.
7. Then the runaway effect speeds up as the temperature reaches 10^8 K producing energy at a rapidly increasing rate that heats up the entire envelope and finally stops the convection.
8. Finally, the energy must be released by β -decay particles, the output of both pp-chain reactions and CNO cycle reactions, to help eject material off the WD.

Since their half-lives of ~ 100 s are longer than hydrodynamic expansion time in the outer layer, these β -decay nuclei decay when the temperature in the envelope declines to values that are too low for a proton capture to occur. This yields the isotopic ratios of C, N, O, Ne, and Mg in the ejected material which are different from the predicted values of equilibrium (Starrfield, 2008b).

Initial Conditions for the Outburst

The critical parameter which determines the strength of the outburst is the pressure at the base of the accreted envelope. Starrfield (2008b) provides the initial condition of the outburst

$$P_{crit} \approx \frac{GM_{WD}M_{crit}}{4\pi R_{WD}^4} \quad (1.1)$$

where P_{crit} is the critical pressure at the bottom of accreted layer, M_{crit} is the critical ignition mass of accreted envelope and can be estimated from the mass-radius relation of WDs, and M_{WD} and R_{WD} are mass and radius of the WD. If P_{crit} is assumed to be $\sim 10^{20}$ dyne cm^{-2} , then M_{crit} can range from less than $10^{-5}M_{\odot}$ for WDs near the Chandrasekhar limit (i.e. $M_{WD} \sim 1.4M_{\odot}$) to values exceeding $10^{-2}M_{\odot}$ for $M_{WD} = 0.5M_{\odot}$.

In order to make the TNR occur on a short time scale, the WD has to be massive and luminous and the mass accretion rate (\dot{M}_{acc}) needs to be high (Starrfield, 2008a) implying that the secondary star has to be evolved. First, a massive WD is required because the large amount of mass is necessary for TNR ignition. Second, the more luminous or higher temperature at the surface of the WD initiates a larger nuclear burning rate and energy release in the accreting material. This allows a TNR to occur more easily. Finally, the more evolved secondary star loses mass at the larger rate than the less evolved one. The \dot{M}_{acc} is higher as a result. Moreover, the strength of the outburst is also a function of WD composition and accretion rate.

The one basic problem in obtaining very short recurrence periods is the fact that at very high \dot{M}_{acc} ($\dot{M}_{acc} \gtrsim 10^{-8}M_{\odot} \text{ yr}^{-1}$ for $M_{WD} \lesssim 1M_{\odot}$), ignition has generally been thought to occur under only mildly degenerate conditions and then only a weak flash will be obtained as a consequence. The only way to avoid the fact that the high accretion rates would suppress the strength of the outburst would then be to accrete materials onto a WD with a mass close to the Chandrasekhar limit (Webbink et al., 1987).

Hillman et al. (2013) have recently produced model UV, visible and X-ray light curves for a range of system parameters. They show that the evolutionary timescales of nova

features, from before eruption to the decline stage, depend on the basic nova parameters which are mass of WD, luminosity and accretion rate.

Speed Class

Novae have characteristics in their light curves leading to a classification based on the light curve decay times t_2 and t_3 which represent the time a nova takes to decay by 2 and 3 magnitudes, respectively. This speed class was introduced by McLaughlin (1939) and redefined by Payne-Gaposchkin (1964). Warner (2008) compiled a set of light curves from a catalogue and derived the relations $t_3 = 2.10t_2$ for fast/very fast novae and $t_3 = 1.75t_2$ for moderate fast/slow/very slow novae. Table 1.1 taken from Warner (2008) presents the definition of speed class of CNe which are given by Payne-Gaposchkin (1964) in the first two columns and the calculated t_3 in the last column. More details of novae light curves and the relation of maximum magnitude and rate of decline (MMRD) will be described in Section 1.4 and Chapter 2, respectively.

Table 1.1: Definition of speed class of CNe given by Payne-Gaposchkin (1964).

Class	t_2 (days)	t_3 (days)
very fast	<10	<20
fast	11-25	21-49
moderate fast	26-80	50-140
slow	81-150	141-264
very slow	151-250	265-440

1.2.2 Recurrent Novae

Recurrent novae (RNe) are, by definition, CNe with multiple recorded outbursts and may contain evolved secondaries (Anupama, 2008). There are 10 known Galactic RNe and they group themselves into three distinct subtypes:

1. *RS Oph* type (*T CrB*, *RS Oph*, *V745 Sco* and *V3890 Sgr*) have long orbital periods ($\sim 10^2$ d). Their red giant secondary stars make them similar to symbiotic

systems. The mass transfer rate and outburst ejection velocities are high ($\geq 4,000$ km s⁻¹). Light curves decline rapidly after outbursts (~ 0.3 mag/day). This sub-type of RNe has strong evidence for interaction between ejecta ($\sim 3\text{-}4 \times 10^{-6} M_{\odot}$) and a pre-existing circumstellar wind from the red giant.

2. *U Sco type (U Sco, V394 CrA and V2487 Oph)* have short orbital periods (~ 1 d). The secondaries are main-sequence stars or sub-giants. Outburst ejection velocities are extremely high ($\sim 10,000$ km s⁻¹) with ejected mass $\sim 10^{-7} M_{\odot}$. They decline very rapidly, especially U Sco which is the fastest nova observed. The quiescent spectra are dominated by He lines unlike those in typical novae.
3. *T Pyx type (T Pyx, CI Aql and IM Nor)* have very short orbital periods (\sim hours) similar to typical CNe and show relatively slow light curve decay with oscillations in the transition region of the light curves; ejected mass $\sim 10^{-5} M_{\odot}$. Anupama (2008) and Darnley et al. (2011) grouped CI Aql as a T Pyx type RN due to their similarity in the light curves and outburst spectra which resemble Fe II CNe, but sometimes it is grouped as a U Sco type RN due to its orbital period of 0.6 day.

According to the orbital period, the U Sco and T Pyx type are classified as cataclysmic variables: short period close binary systems consisting of late type main-sequence secondary stars filling their Roche lobes and WD primary stars, similar to CNe. Meanwhile the T CrB type fall into the class of symbiotic variables: long period close binary systems with late type giant secondary stars, because their orbital periods are much longer than typical CNe or cataclysmic variables in general (Starrfield, 2008a).

RNe have been proposed as one of the primary candidates for the progenitors of Type Ia Supernovae through the single degenerate scenario believing that a WD can grow in mass up to the Chandrasekhar limit ($1.4 M_{\odot}$) if accreted mass is larger than ejected mass after eruption during each outburst cycle (see e.g. Kotak, 2008 and Section 1.6 below).

1.3 Frequency and Distribution of Galactic Novae

The frequency of Galactic classical novae over the past century is presented in Table 1.2 showing that the fainter novae tend to be found more frequently than the brighter ones. Many bright novae may be undetected because they fade faster. The total mean detected Galactic novae rate calculated from Table 1.2 is $\sim 3 \text{ yr}^{-1}$.

However, Figure 1.3 showing the distribution of classical novae in Galactic coordinates using data from Downes et al. (2005) implies that fast novae are clustered around the Galactic disk while slow novae are more prevalent in the bulge. Therefore it is also possible to conclude that the data in Table 1.2 has underestimated the number of fast novae due to the difficulty of observation along the Galactic plane (Warner, 2008).

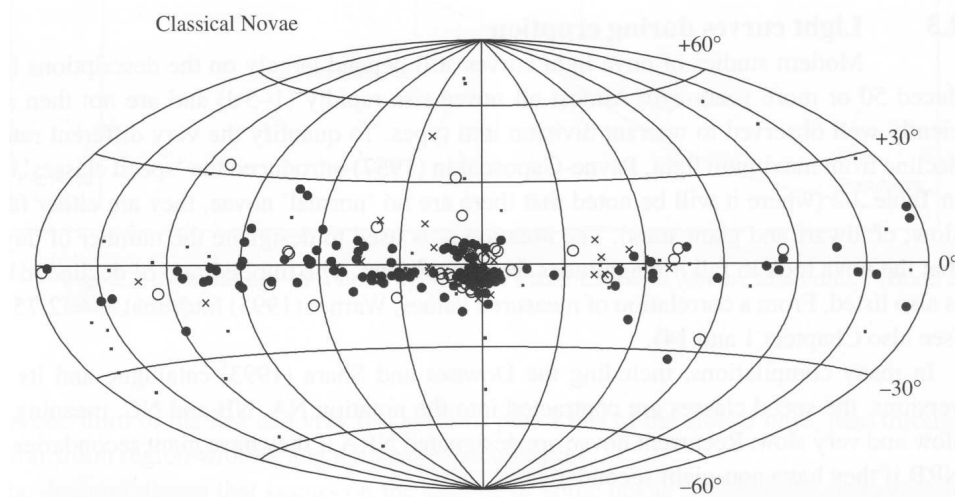


Figure 1.3: The distribution in Galactic coordinates of Classical Novae (from Warner, 2008). Closed circles are 132 fast novae, open circles are 40 slow novae, and crosses are 58 unclassified novae.

When taking the effect from interstellar extinction into account, a total Galactic nova rate of 34 yr^{-1} is proposed by Darnley et al. (2006). However in recent years, $\sim 800 \text{ yr}^{-1}$ are now discovered for M31 (Pietsch, 2010).

Table 1.2: Average rate of nova discovery in Warner (2008)

m_V (max) (mag)	Discovery rate (yr ⁻¹)	m_V (max) (mag)	Discovery rate (yr ⁻¹)
<1	0.04	4-5	0.05
1-2	0.02	5-6	0.14
2-3	0.04	6-7	0.47
3-4	0.03	7-8	0.58

1.4 Light Curves of Novae

The idealized nova optical light curve is shown in Figure 1.4. This comprises nine distinct phases (Warner, 2008).

1. *Pre-nova*: The base line of a nova's brightness at quiescence.
2. *Initial rise*: The nova rises in brightness very rapidly so it is rarely caught in this phase.
3. *Pre-maximum halt*: In many novae, there is a pause at about 2 magnitude below maximum for a few hours for fast novae to a few days for slow novae.
4. *Final rise*: The nova then carries on to its maximum brightness taking a couple of days for fast novae to several weeks for slow novae.
5. *Maximum*: When an outburst occurs, it will stay at the maximum for a few hours for fast novae to a few days for slow novae.
6. *Early decline*: It then begins to decrease in brightness down to approximately 3.5 magnitudes from maximum.
7. *Transition*: Between 3.5 to 6 magnitudes below maximum, the light curve can be smooth, show ~ 1.5 magnitude oscillation with period $\sim 5-15$ days, or a deep drop down for months due to the formation of dust which is evident in infrared observations.

8. *Final decline*: After the novae recover from the transition phase, they continue to be fainter by 6 magnitudes from maximum.
9. *Post nova*: Finally the brightness should meet the base line again.

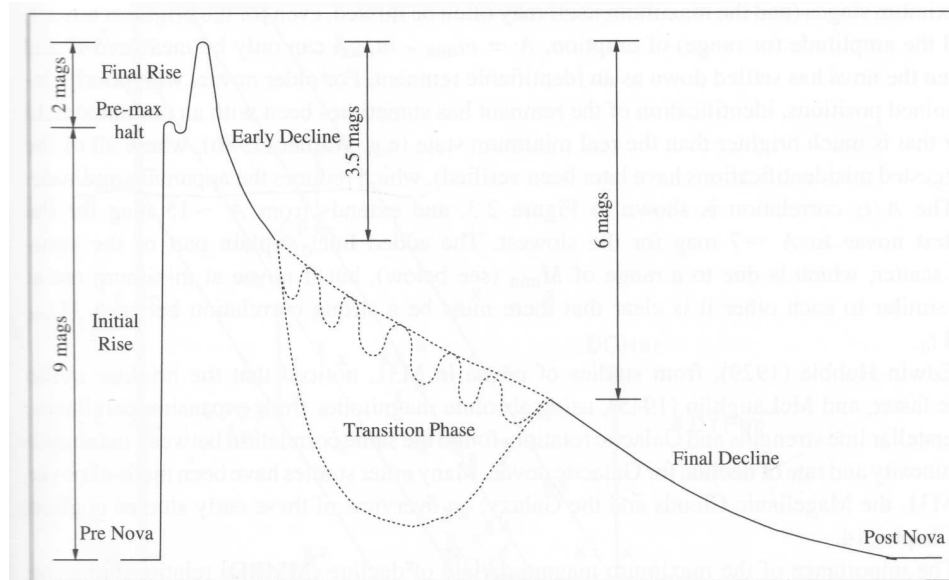


Figure 1.4: The Morphology of a nova light curve (from Darnley, 2005).

In the 1970s, it was revealed that at outburst the sum of optical and infrared energies remains approximately constant at $\sim 1.5 \times 10^4 L_{\odot}$. The bolometric luminosity was also proved to be constant since the drop in visual flux and the rise in ultraviolet were shown to balance in the early decline phase. The changes in brightness at different wavelengths are largely due to the decrease in optical depth of the ejected shell (Gallagher & Code, 1974). This was investigated in more detail by Bath & Harkness (1989) in terms of evolution of the mass loss rate from the surface of the WD and the subsequent effect on the effective radius and temperature of the pseudo-photosphere in the ejected material (see Chapter 6 for more details).

Most novae in immediate pre-eruption and eventual post-eruption stages have similar brightness, except few a novae (i.e. GQ Mus, CP Pup, V1500 Cyg, V2214 Oph, V1874 Cyg, and RN UMi) which are very faint at pre-eruption but significantly brighter at post-eruption (Warner, 2008).

Novae at post-eruption quiescence are powered by accretion luminosity which arises largely in a roughly two-dimensional disk. This implies that their observed magnitude depends extremely on the inclination. Thus the effect of the inclination on M_V is one of the most direct ways to prove the existence of an optically thin disk in such systems (Warner, 1987).

1.5 Spectra of Novae

Many studies reveal that the spectra of novae change dramatically through the outburst until quiescence. These spectral changes are related to different phases of the nova light curve.

1.5.1 During Eruption

Payne-Gaposchkin (1964) proposed that novae during eruption usually have sequences of absorption lines and overlapping sequences of emission lines as follows.

1. *Pre-maximum spectrum:* Few spectra have been obtained during the pre-nova and initial rise phase. Spectra dominated by broad blue-shifted absorption lines, usually resembling stars in the range from B5-F5, have been obtained. Widths of absorption lines are indicative of the expansion velocities which range from 1300 km s^{-1} for fast novae to 100 km s^{-1} for slow novae (Warner, 2008).
2. *Principal spectrum:* This spectrum appears around visual maximum. Therefore, at this phase, absorption lines show more blue-shifted components and contain multiple structure and more enhancement of C, N, or O than in previous phases. At maximum, or immediately after that, absorption lines develop P Cyg profiles which are strongest in H I, Ca II and Fe II. The relation between velocities of absorption lines and speed class given by McLaughlin (1960) is shown in Equation 1.2.

$$\log V_{ej}(\text{km s}^{-1}) = 3.70 - 0.5 \log t_3(d) = 3.75 - 0.5 \log t_2(d) \quad (1.2)$$

A few days after maximum, emission lines of [O I], [N II], and [O III] appear respectively.

3. *Diffuse enhanced spectrum:* This pattern is similar to the principal spectrum but twice as broad and blue-shifted and appears very shortly after maximum. The relation between velocities of absorption lines and speed class in this spectral region given by McLaughlin (1960) is shown in Equation 1.3.

$$\log V_{ej}(kms^{-1}) = 3.81 - 0.41 \log t_3(d) = 3.71 - 0.41 \log t_2(d) \quad (1.3)$$

4. *Orion spectrum:* This name was assigned since it is similar to the spectra arising from the stellar wind of OB stars in the Orion nebula. Absorption lines are usually single, diffuse, and blue-shifted. The velocities become steadily larger until the Orion spectrum disappears. There is not much dramatic change in either optical absorption nor optical emission lines. However the strong nitrogen flare due to the enhancement of N III, and O I flash due to O I 7772 and 8448 Å to rival H α in strength, may occur.

In the ultraviolet, the emission lines do not change much but only increase in equivalent width as the continuum decays. This is a result of reducing the opacity of outer layers to become optically thin. That is the envelope is initially hot and ionized in the inner layers but still neutral or little ionized in the outer layers. The density of the outer layer decreases as it expands and becomes optically thin. As a result, the pseudo-photosphere is effectively moving inward.

5. *The nebular spectrum:* This is a final distinctive stage with an entirely emission spectrum. This stage is similar to a planetary nebula which at first maintains the [O I] and [N II] and then produces the [O III] and [Ne III] lines. Coronal lines can even develop if temperature rises over 10^6 K and such lines also can be seen in the ultraviolet.
6. *The post-nova spectrum:* The ejected shell is resolvable and the individual components of the ejecta can be measured. There are recombination lines of H, He, C, N, O, N III and strong Balmer continuum emission.

Williams (1992) has also grouped the novae on the basis of their strong post-outburst emission lines into 2 classes, the Fe II novae and the He/N novae as shown in Figure 1.5. First, the Fe II novae containing prominent Fe II lines are believed to evolve more slowly, have a lower level of ionization, and show P Cyg absorption profiles. More than half of Fe II novae develop standard forbidden lines. Their narrow Fe II spectrum is suggested to be formed in a wind. Second, the He/N novae contain stronger He and N lines with larger expansion velocities and higher levels of ionization. The spectral evolution is fast and results in coronal lines, very strong neon lines, or no forbidden lines at all. Their broader and more flat-topped lines with little absorption are suggested to be formed in the shell ejected at maximum.

1.5.2 In Quiescence

The spectrum of a nova at quiescence consists of 2 components including the hot component, contributed by the primary star and the disk, and the cool component which is generated from the secondary star. At quiescence, the optical spectra of the longer orbital period RNe are dominated by that of the red giant (Anupama & Mikołajewska, 1999).

Spectra of quiescent novae, with a blue continuum and either, or both, broad Balmer absorption or emission lines, both in pre-and post-eruption, are the consequence of a high \dot{M}_{acc} thick disk similar to those seen in cataclysmic variables. The line strength (e.g. equivalent width) correlates with inclination therefore the continuum would be strong while the absorption and emission lines would be relatively weak if a nova is face on (Warner, 1987). The emission lines of He II 4686 Å, and C III/N III 4650 Å distinguishing quiescent novae from dwarf novae are the results of the hot central source (i.e. the heated primary star) which acts as the source of ionization (Warner, 2008). The ultraviolet and optical spectra of quiescent novae are suggested to be variable due to the fluctuations in \dot{M}_{acc} and the changes in the column density of the optically thick wind envelope (Anupama & Mikołajewska, 1999).

Kenyon & Fernandez-Castro (1987) presented evidence that the red TiO bands at 6180

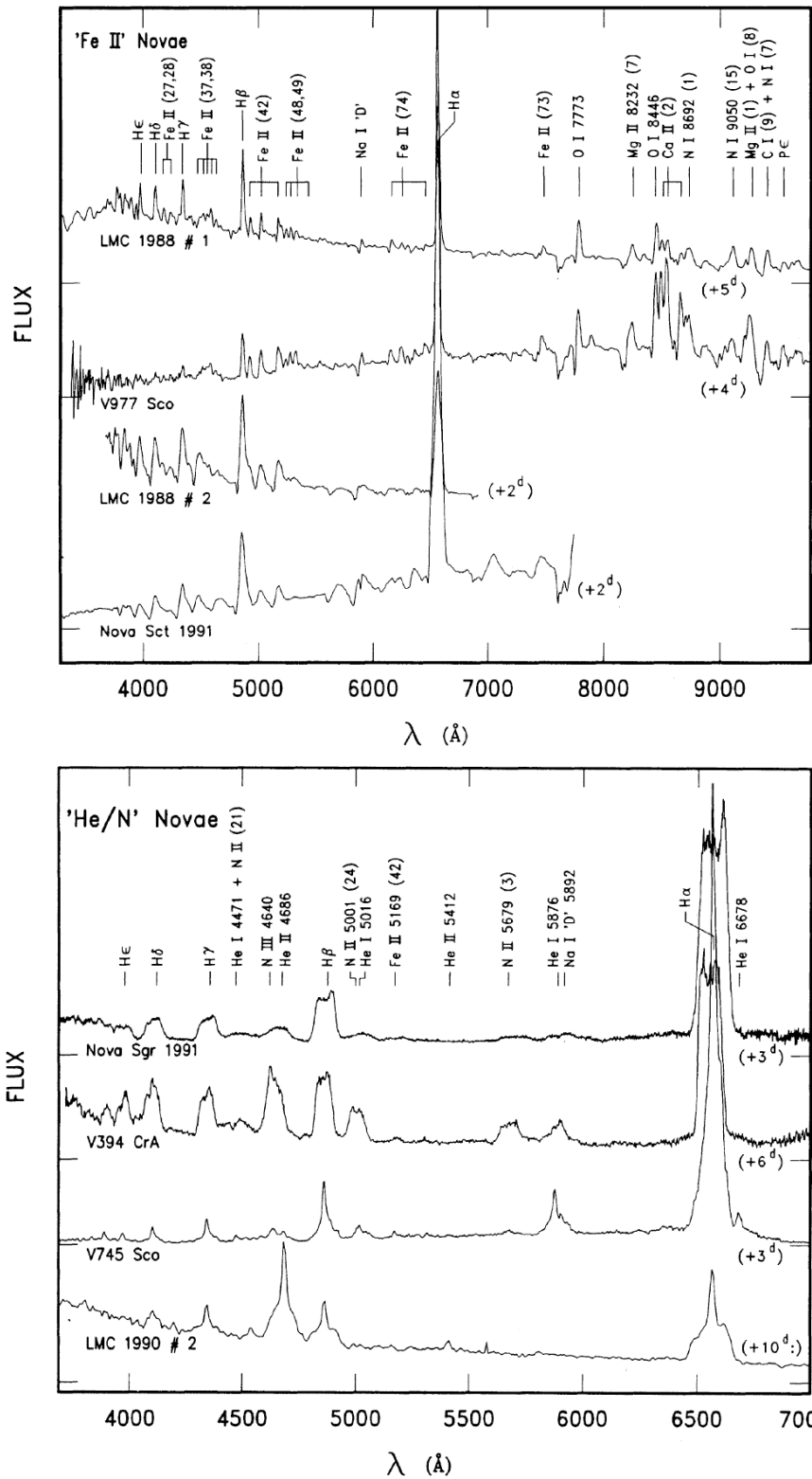


Figure 1.5: Spectra showing typical Fe II novae (top) and He/N novae (bottom). Image from Williams (1992).

\AA and 7100 \AA together with VO 7865 \AA and Na I doublet at 8190 \AA were a good indicator for K-M stars in symbiotic systems. Thus, one may use [TiO], [VO], and [NaI] indices defined by Kenyon & Fernandez-Castro (1987) to identify the spectral type and luminosity class of the giant secondaries. A proposal that the NIR and IR colour-colour diagram can help to indicate the red giant secondary stars was provided by Harrison (1992), Weight et al. (1994), Darnley et al. (2011) and Darnley et al. (2012) (see e.g. Chapter 2. Section 2.2).

1.6 Progenitors of Type Ia Supernovae

RNe play an important role as one of the suspected progenitor systems of Type Ia supernovae (SNe) which are used as primary distance indicators in cosmology (Parthasarathy et al., 2007). It is important therefore to investigate the nature of central binary systems and outbursts of CNe and RNe to determine if they might ultimately be candidates for Type Ia SNe explosions.

Type Ia SNe, one of the most energetic transient events in the Universe, are thought to either result from the single degenerate (SD) channel proposed by Whelan & Iben (1973) or the double degenerate (DD) channel proposed by Iben & Tutukov (1984). The SD scenario suggests that Type Ia SNe result from the runaway thermonuclear burning of Carbon in a WD which has grown up to the Chandrasekhar limit ($\sim 1.4M_{\odot}$) by accreting material from a close binary companion. The primaries in suspected RNe must comprise a CO, not ONe, WD if there is indeed a link between RNe and Type Ia SNe (Kotak, 2008). On the other hand, the DD scenario suggests that Type Ia SNe are a consequence of the merging of two WDs in a binary system due to the emission of gravitational radiation where the orbit shrinks as a result. A donor in the SD system is a non-degenerate main-sequence to giant star while that of DD is another degenerate WD.

Some population syntheses favour the DD scenario (e.g. Yungelson & Livio, 1998) and recent observational studies have identified many DD binaries (e.g. Marsh, 2000).

Yet, none of the observed DD systems has both a potential period short enough (i.e. orbital period ~ 10 hours) to merge in a Hubble time and a total mass that exceeds the Chandrasekhar limit (Napiwotzki et al., 2004). The merging between two CO WDs may also lead to a neutron star instead of a Type Ia SN (Langer et al., 2000; Yoon & Langer, 2003; Han & Podsiadlowski, 2004).

In terms of the SD model, recent theoretical work found that WDs in the SD scenario can reach the Chandrasekhar limit (Han & Podsiadlowski, 2004; Walder et al., 2008; Newsham et al., 2013). As a result, the SD scenario is generally preferred. Different SD models can be distinguished based on the nature of the secondary star: the WD can accrete either from a wind (the “symbiotic channel” - Munari & Renzini, 1992), by Roche lobe overflow (the “RLOF channel” - van den Heuvel et al., 1992), or by mass transfer from a helium star (the “helium star channel” - Nomoto, 1982; Liu et al., 2010). The secondary star in the symbiotic channel is often a red giant, while it is a subgiant or main-sequence star in the RLOF channel.

There is still great debate about the relative importance of each channel however. The lack of the ex-companion star when looking at the centre of a known SN Ia remnant SNR 0509-67.5 appears to suggest the DD progenitor as the only remaining possibility in this case (Schaefer & Pagnotta, 2012).

In addition, the extensive imaging at the location of SN 2011fe/PTF11kly constrains the visible light luminosity of the progenitor to be 10-100 times fainter than the previous limit of SNe Ia progenitors, and then obviously favours either the DD or SD scenarios via the RLOF channel (Li et al., 2011). Luminous red giants and helium stars are now ruled out for being the donor to the exploding WD. RNe systems such as RS Oph and T CrB are now therefore in doubt as to whether they led to the explosion in this case.

On the other hand, a series of high-resolution optical spectra of the SN Ia PTF11kx revealing a complex environment of multiple shells of circumstellar material are best described by a symbiotic nova progenitor, similar to RS Ophiuchi (Dilday et al., 2012).

In addition, Schaefer (2010) proposed that the short-period RNe (T Pyx and IM Nor)

having short orbital period ($\lesssim 0.3$ d) have their accretion driven by the heating from WDs, have long evolutionary cycles, and therefore will *not* become SNe Ia. Meanwhile the long-period RNe (the other 8 RNe) have their accretion driven by the steady expansion of secondary stars, have short evolutionary cycles, and will become SNe Ia.

In summary, although the RLOF channel with subgiant or main-sequence secondaries is currently marginally favoured, there is still no firm conclusion as to the exact progenitors of Type Ia SNe even via this route.

1.7 Open Questions

Although there has been a tremendous increase in our knowledge of the cause and consequences of the nova explosion over the past 50 years, there are still many important questions which remain to be answered. The following are all of those given in Bode (2010).

- Can we use novae to help to understand the evolutionary history of binary stars? The evolutionary track from the binary star to the nova phase itself can be studied from rare novae such as GK Per and V458 Vul where we see the planetary Nebula from a pre-nova phase still surrounds the objects.
- Is there a continuum of inter-outburst timescales from CNe to RNe, or sub-type of RNe at least?
- The durations of the super-Eddington and bolometric plateau phases are not yet determined accurately.
- Does the model of TNR need to be reexamined? There is a significant discrepancy between the ejected mass derived from the models compared to that from the observations.
- What is the cause of variability seen around maximum light in several novae? In addition, a nova after outburst is expected to behave as a supersoft source (SSS) emitting soft X-rays whenever the steady H-burning at the base of WD's envelope heats

up the WD's photosphere T_{eff} from few 10^5 to 10^6 K while the expanding envelope is becoming optically thin to X-rays at the same time. However, the causes of the large variability during the emergence of SSS in RS Oph and other novae is still unknown.

- Does the MMRD relationship need to be refined? The debate between linear and non-linear relations, which states that more slow novae in the sample makes the MMRD more linear (Warner, 2008), can be improved by using an appropriate sub-set of CNe as the sample and by improving the homogeneity and cadence of nova observations both Galactic and extragalactic.

- Do RNe act as progenitors of Type Ia SNe? Although WDs in systems like RS Oph and U Sco seem to gain mass and be very close to the Chandrasekhar limit, several questions remain: For example, what is the type of WD?; can the H in such systems really be hidden at the time of SN eruption? Is there a sufficient population of RNe to explain the Type Ia SNe rate?

- Can we identify potential RNe among the known CNe? Using the fact that RNe should contain more highly evolved secondary stars is a promising, if challenging, line of enquiry.

- How many bright novae are we missing each year? Since bright novae may fade faster, it is possible that we might miss a number of these.

1.8 This Work

The work described in this thesis has the overall aim to address several of the questions above.

In particular, we describe the use of complementary data from different facilities, such as the Liverpool Telescope (LT), Southern African Large Telescope (SALT), and Small and Moderate Aperture Research Telescope System (SMARTS) to perform spectroscopy of selected CNe systems identified from their anomalous outburst amplitudes to investigate the nature of their central systems. In Chapter 2, the criteria and method

of target selection are explained in order to look for characteristics that may distinguish RNe and CNe systems. In Chapter 3, details of observations and data reduction are presented and in Chapter 4, we describe the detailed investigation of the 16 old Galactic novae in quiescence which are suspected RNe based on their low outburst amplitudes and accessibility for observations. Positions of targets on colour-magnitude diagrams and characteristics of the spectra are investigated to ascertain the spectral type of the secondary stars and also to compare to those of the known Galactic RNe. We then determine whether or not these show characteristics that merit further investigation as potential RNe.

Chapter 5 introduces the Solar Mass Ejection Imager (SMEI) database which has the potential to be searched for outbursts of bright novae that have otherwise gone unrecorded. It also allows the investigation of whether known CNe may have had additional otherwise unrecorded outbursts and hence show characteristics of RNe. Light curves derived for some bright objects are presented.

In Chapter 6, an investigation of the physics of the outburst and spectroscopic evolution of the Recurrent Nova T Pyx in its 2011 outburst is described. The unprecedented detail of SMEI photometric observations is compared to the spectra of T Pyx obtained by the LT and SMARTS telescopes. The investigations of how the spectra evolve together with brightness are presented in order to determine the origin of light curve variability in the early stage of the nova outburst and comparison is made to TNR models.

A summary, conclusions, and future work are presented in Chapter 7.

Chapter 2

Selection of Potential Recurrent Novae among the Classical Novae

2.1 Introduction

As noted in Chapter 1, of the approximately 400 known Galactic novae, only 10 of them have more than one recorded eruption and are thus so called RNe. At least eight of these RNe are known to harbour evolved secondary stars rather than the main sequence secondaries which are found to be typical for CNe (Darnley et al., 2012). On the basis of the evolved secondaries, the novae must be brighter at quiescence than CNe and then have a lower outburst amplitude as a result. Therefore the relationship between outburst amplitude, rate of decline and absolute magnitude is investigated and applied in this Chapter to distinguish the possible RNe among CNe.

2.2 Relationships between Amplitude, Rate of Decline and Absolute Magnitude

Since brighter novae were found to fade faster, the relation of maximum magnitude and rate of decline (MMRD) is often cited as a possible extragalactic distance indicator.

MMRD relationships were suggested to be more linear if the sample includes more slow novae (Warner, 2008). The linear MMRD relationship is usually expressed as follows

$$M_{max} = a_n \log t_n(d) + b_n \quad (2.1)$$

where M_{max} is the absolute magnitude in the V , B , or photographic band at maximum and n is 2 or 3. Table 2.1 shows typical values of a_n and b_n adopted from Warner (2008).

Table 2.1: Typical values of MMRD constants adopted from Warner (2008).

M	n	a_n	b_n
pg	3	2.4	-11.3
B	3	1.80 (± 0.20)	-10.67 (± 0.30)
V	2	2.41 (± 0.23)	-10.70 (± 0.30)
V	2	2.52 (± 0.32)	-11.32 (± 0.44)
V	3	2.54 (± 0.35)	-11.99 (± 0.56)

The emitting region of a nova during eruption is roughly spherically symmetric, while in post-eruption quiescence it is powered by accretion luminosity which depends on the disk inclination. Warner (1987) proposed

$$A' = M_V(max) - M'_V(min) \quad (2.2)$$

where A' is the observed amplitude with unknown inclination and $M'_V(min)$ is the absolute magnitude at minimum with unknown inclination. This can be assumed to be an average $M_V(min)$ over all speed class, $\overline{M}_V(min)$ ($=3.8$, adopted from Warner, 1986). $M_V(max)$ is the absolute magnitude at maximum which is independent of inclination because of the assumption of spherical symmetry at eruption. We note that A' is independent of distance and reddening. However $A' \neq \Delta M_V(i)$ which is the amplitude with known inclination.

Since the A' values are uncorrected for inclination of the disks, the effects of inclination

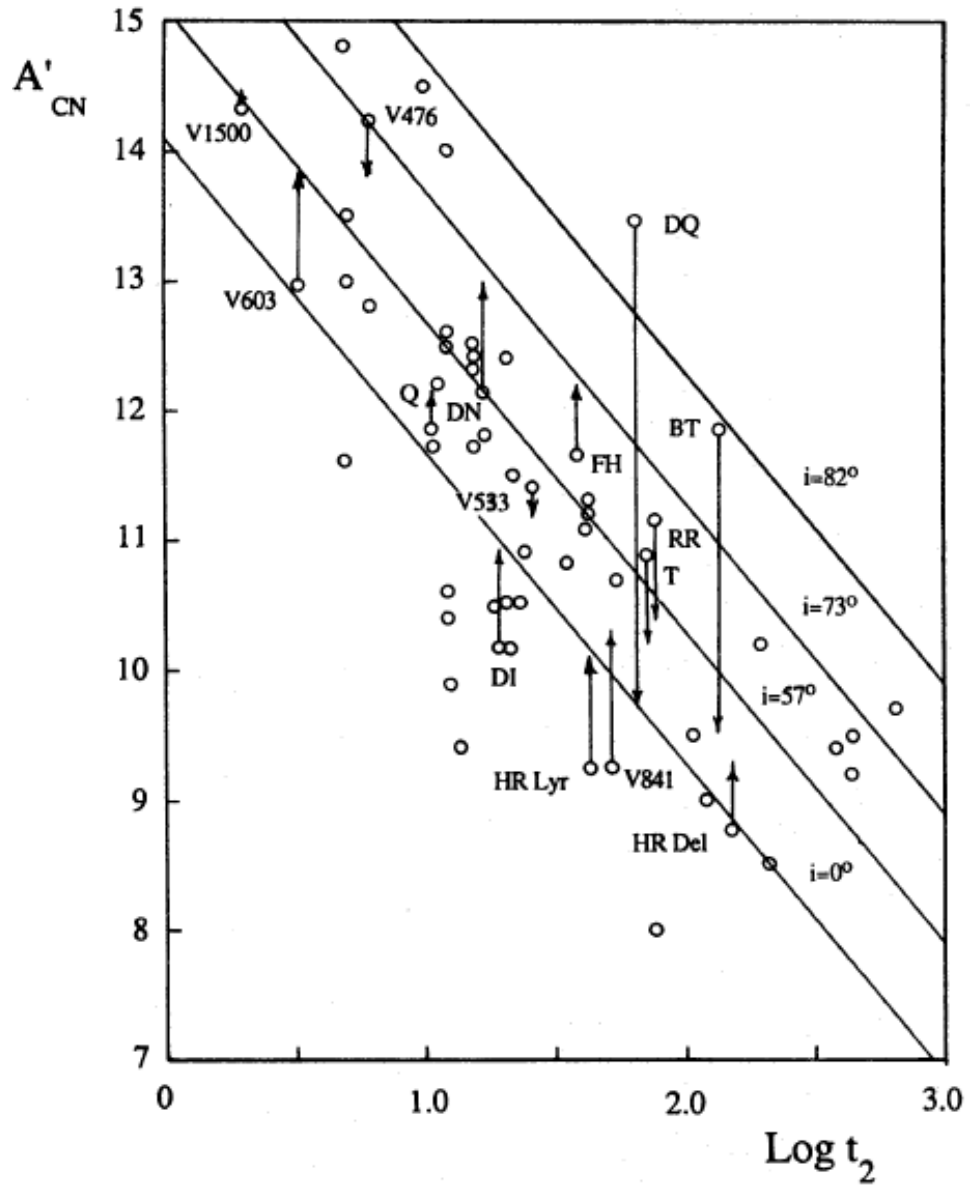


Figure 2.1: Amplitude-rate of decline relationship for CNe from Warner (1987). The amplitude A' values are uncorrected for inclination of the disks; the effects of inclination are shown by the diagonal lines where inclinations 0° , 56.7° , 73.7° , 82.4° correspond to $\Delta M_V = -1, 0, 1,$ and 2 respectively - see text for more details.

are shown by the diagonal lines in Figure 2.1 which shows data for a large sample of novae from Warner (1987). This variation in absolute magnitude of an accretion disk can be expressed as a function of inclination as given by Paczynski & Schwarzenberg-Czerny (1980) as follows

$$\Delta M_V(i) = -2.5 \log \left[\cos i + \frac{3}{2} \cos^2 i \right] \quad (2.3)$$

where $\Delta M_V = -1, 0, 1, 2, 3$ and 4 correspond to inclinations $0^\circ, 56^\circ.7, 73^\circ.7, 82^\circ.4, 86^\circ.7,$ and $88^\circ.6$ respectively.

Thus, knowing A', t_n and inclination i , one may be able to trace the true value of $\Delta M_V(i)$ as shown in Figure 2.1. For example, DQ Her has a known inclination of 89° which corresponds to $\Delta M_V \sim 4$ by using Equation 2.3. Then the position corrected for the inclination effect should be ~ 4 magnitudes vertically down from its observed position. We now describe the use of this diagram to look for the potential RNe among the CNe population.

2.3 Criteria of Selection

The proposal that RNe occupy a region separated from CNe in an amplitude- t_3 diagram initially suggested by Duerbeck (1988b), was adopted. The low amplitude results from the existence of an evolved secondary and/or high mass transfer rate in the quiescent system.

Among many catalogues providing A' and t_3 , a catalogue given by Strope et al. (2010) provides details of many well-observed nova light curves in V magnitude. Meanwhile a catalogue produced by Duerbeck (1988a) provides another sample with photographic magnitudes. Therefore 93 novae with V amplitudes from Strope et al. (2010) and 43 novae with photographic amplitudes from Duerbeck (1988a) were combined and plotted on an A' versus t_3 diagram as shown in Figures 2.2 and 2.3, respectively, from which the initial targets that are suspected to be RNe candidates were selected. All

data plotted for target selection are listed in Table 2.2.

Figure 2.2 shows that all Galactic RNe occupy the bottom area of the plot representing the low V amplitude region among the CNe. A solid diagonal line represents a typical CNe trend line calculated by using the MMRD relation from Equation 2.1 where $[\overline{M}_V]_{min} = 3.8$ is an average $[M_V]_{min}$ over all speed class adopted from Warner (1986), and coefficients a and b for V magnitude are adopted as 2.54 and -11.99 from Table 2.1. Since the A' values are uncorrected for inclination of the disks, the effects of inclination are shown by the diagonal lines calculated from Equation 2.3 where $\Delta M_V = -1, 0, 1, 2, 3$ and 4 correspond to inclinations $0^\circ, 56^\circ.7, 73^\circ.7, 82^\circ.4, 86^\circ.7,$ and $88^\circ.6$ respectively.

Figure 2.3 also shows the same relations with respect to photographic amplitudes. The typical CNe trend line was plotted from the same equation (2.1) but with coefficients $a=2.4$ and $b=11.3$ from Table 2.1 for photographic magnitude.

Sixteen targets, including known RNe, were initially selected according to their deviation (the amplitude difference) from the typical CNe line from both catalogues. Among them, according to the visibility constraint of the observation, ten were assigned to be observed photometrically at LT and therefore we obtained photometric magnitude. We note here that other novae with positions at the bottom of the amplitude- t_3 diagram would also be candidates, but are not on our target list because of telescope scheduling constraints.

Having selected targets for follow-up photometric and spectroscopic observations, we now describe the detail of instruments and processes of data reduction in the next Chapter.

Table 2.2: Novae from catalogues that are used in target selection.

No. ^a	Nova	Recurrent	Year	Filter	m_{max}	$m_{quiescent}$	t_3	A'	$Logt_3$	Deviation	Selected
1	RS Oph	✓	2006	V	4.8	11	14	6.2	1.15	-6.68	
2	T CrB	✓	1946	V	2.5	9.8	6	7.3	0.78	-6.51	✓ LT
3	V4074 Sgr		1965	pg	8.6	12.3	120	3.7	2.07	-6.41	
4	V4643 Sgr		2001	V	7.7	>16	6	8.3	0.78	-5.51	
5	V3890 Sgr	✓	1990	V	8.1	15.5	14	7.4	1.15	-5.48	
6	V2487 Oph	✓	1998	V	9.5	17.7	8	8.2	0.9	-5.3	✓ LT, SALT
7	U Sco	✓	1999	V	7.5	17.6	3	10.1	0.48	-4.48	
8	V2313 Oph		1994	V	7.5	>20	17	12.5	1.23	-4.46	
9	CI Aql	✓	2000	V	9	16.7	32	7.7	1.51	-4.27	✓ LT, SALT
10	LS And		1971	pg	11.7	20.5	8	8.8	0.903	-4.13	
11	AR Cir		1906	pg	10.3	15	451	4.7	2.65	-4.03	✓ SALT
12	BC Cas		1929	pg	10.7	17.4	75	6.7	1.87	-3.89	
13	V3964 Sgr		1975	pg	9.4	17	32	7.6	1.5	-3.88	✓ LT, SALT
14	V351 Pup		1991	V	6.4	19.6	26	13.2	1.41	-3.8	
15	HZ Pup		1963	pg	7.7	17	70	9.3	1.84	-3.8	
16	V4160 Sgr		1991	V	7	>19	3	12	0.48	-3.78	
17	V3645 Sgr		1970	pg	12.6	18	300	5.4	2.47	-3.75	✓ LT, SALT
18	V445 Pup		2000	V	8.6	14.6	240	6	2.38	-3.74	✓ LT
19	V2214 Oph		1988	V	8.5	20.5	89	12	1.95	-3.63	
20	V4743 Sgr		2002	V	5	16.8	12	11.8	1.08	-3.55	
21	V4740 Sgr		2001	V	6.7	>18	33	11.3	1.52	-3.43	
22	V794 Oph		1939	pg	11.7	18	220	6.3	2.34	-3.17	✓ LT, SALT
23	V1330 Cyg		1970	pg	9	18.1	18	9.1	1.25	-2.98	✓ HET ^b
				V	9.9	17.5	217	7.6	2.34	-2.26	
24	FH Ser		1970	V	4.5	16.8	62	12.3	1.79	-2.94	
25	V382 Vel		1999	V	2.8	16.6	13	13.8	1.11	-2.86	
26	QU Vul		1984	V	5.3	17.9	36	12.6	1.56	-2.74	
				V	7.1	18	47	10.9	1.67	-0.64	
27	V4739 Sgr		2001	V	7.2	>18	3	10.8	0.48	-2.58	
28	FS Sct		1952	pg	10.1	18	86	7.9	1.93	-2.55	✓ LT ^c
29	BT Mon		1939	V	8.1	15.7	182	7.6	2.26	-2.45	✓ LT, Yunnan ^b
30	V1819Cyg		1986	V	9.3	17	181	7.7	2.26	-2.36	
31	OS And		1986	V	6.5	17.5	23	11	1.36	-2.23	
32	V4742 Sgr		2002	V	7.9	>18	23	10.1	1.36	-2.23	
33	T Pyx	✓	1966	V	6.4	15.5	62	9.1	1.79	-2.14	
				pg	6.5	15.3	88	8.8	1.94	-1.63	
34	DK Lac		1950	V	5.9	13.8	202	7.9	2.31	-2.03	
				pg	5.9	15.5	32	9.6	1.5	-1.88	
35	V2275 Cyg		2001	V	6.9	18.4	8	11.5	0.9	-2	
36	V5116Sgr		2005	V	7.6	>16	26	8.4	1.41	-1.95	
37	V574 Pup		2004	V	7	17.2	27	10.2	1.43	-1.81	
38	V368 Aql		1936	pg	5	15.4	17	10.4	1.23	-1.74	✓ LT, SALT
39	V450 Cyg		1942	pg	7.8	16.3	108	8.5	2.03	-1.71	

continued on next page

Table 2.2 – continued

No. ^a	Nova	Recurrent	Year	Filter	m_{max}	$m_{quiescent}$	t_3	A'	$Logt_3$	Deviation	Selected
40	EU Sct		1949	pg	8.4	18	42	9.6	1.62	-1.6	✓ SALT
41	V1016 Sgr		1899	pg	8.5	17	140	8.5	2.14	-1.44	
42	V732 Sgr		1936	V	6.4	~16	75	9.6	1.88	-1.43	
43	HR Lyr		1919	pg	6.5	15.8	74	9.3	1.86	-1.37	
44	V2264 Oph		1991	V	10	>21	22	11	1.34	-1.33	
45	CN Vel		1905	pg	10.2	17	800	6.8	2.9	-1.33	✓ SALT
46	T CrB	✓	1866	pg	2	11.3	6	9.3	0.832	-1.31	
47	HR Del		1967	V	3.6	12.1	231	8.5	2.36	-1.29	
48	LZ Mus		1998	V	8.5	>18	12	9.5	1.08	-1.25	✓ SALT
49	V373 Set		1975	V	6.1	>18.3	79	11.9	1.9	-1.16	
50	V1370 Aql		1982	V	7.7	18	28	10.3	1.45	-1.04	
51	V2295 Oph		1993	V	9.3	>21	16	11.7	1.2	-1.03	
52	V992 Sco		1992	V	7.7	17.2	120	9.5	2.08	-1.01	
53	LV Vul		1968	V	4.5	15.3	38	10.8	1.58	-0.98	
54	V465 Cyg		1948	pg	8	17	140	9	2.14	-0.94	
55	V723 Cas		1995	V	7.1	15.7	299	8.6	2.48	-0.9	
56	V2467 Cyg		2007	V	7.4	~19	20	11.6	1.3	-0.89	
57	V603 Aql		1918	V	-0.5	11.7	12	12.2	1.08	-0.85	
58	LW Ser		1978	V	8.3	19.4	52	11.1	1.72	-0.81	
59	V4021 Sgr		1977	V	8.9	18	215	9.1	2.33	-0.77	
60	V2274 Cyg		2001	V	11.5	>20	33	8.5	1.52	-0.63	
61	V842 Cen		1986	V	4.9	15.8	48	10.9	1.68	-0.62	
62	V1493 Aql		1999	V	10.1	~21	50	10.9	1.7	-0.57	
63	KT Mon		1942	pg	10.3	21	40	10.7	1.6	-0.55	
64	T Aur		1891	V	4.5	14.9	84	10.4	1.92	-0.5	
				pg	4.2	15.2	100	11	2	0.7	
65	V1229 Aql		1970	V	6.6	18.1	32	11.5	1.51	-0.47	
66	NQ Vul		1976	V	6.2	17.2	50	11	1.7	-0.47	
67	V838 Her		1991	V	5.3	19.1	4	13.8	0.6	-0.46	
68	V705 Cas		1993	V	5.7	16.4	67	10.7	1.83	-0.45	
69	LU Vul		1968	pg	9.5	21	21	11.5	1.32	-0.42	
70	V446 Her		1960	V	4.8	16.1	42	11.3	1.62	-0.37	
				pg	3	18	16	15	1.2	2.78	
71	CP Lac		1936	V	2	15	9	13	0.95	-0.37	
72	V827 Her		1987	V	7.5	18.1	53	10.6	1.72	-0.33	
73	V4633 Sgr		1998	V	7.4	18.7	44	11.3	1.64	-0.32	
74	V4745 Sgr		2003	V	7.3	>17	190	9.7	2.28	-0.3	
75	V2491 Cyg		2008	V	7.5	~20	16	12.5	1.2	-0.23	
76	V528 Aql		1945	pg	7	18.1	37	11.1	1.56	-0.23	
				V	6.9	18.5	38	11.6	1.58	-0.18	
77	GK Per		1901	V	0.2	13	13	12.8	1.11	-0.16	
78	V1187 Sco		2004	V	9.8	18	17	8.2	1.23	-0.16	
79	V356 Aql		1936	pg	7.7	17.7	115	10	2.06	-0.154	
				V	7	18.3	140	11.3	2.15	0.96	

continued on next page

Table 2.2 – continued

No. ^a	Nova	Recurrent	Year	Filter	m_{max}	$m_{quiescent}$	t_3	A'	$Logt_3$	Deviation	Selected
80	V606 Aql		1899	pg	6.7	17.3	65	10.6	1.81	-0.14	
81	DD Cir		1999	V	7.6	20.2	16	12.6	1.2	-0.13	
82	PW Vul		1984	V	6.4	16.9	116	10.5	2.06	-0.05	
83	V849 Oph		1919	pg	7.3	17	175	9.7	2.24	-0.016	
				V	7.6	18.8	270	11.2	2.43	1.59	
84	RR Pic		1925	V	1	12.2	122	11.2	2.09	0.03	
85	V4444 Sgr		1999	V	7.6	>21	9	13.4	0.95	0.03	
86	V500 Aql		1943	pg	6.5	17.8	42	11.3	1.62	0.09	
87	DN Gem		1912	V	3.6	15.6	35	12	1.54	0.13	
				pg	3.5	15.8	37	12.3	1.56	0.96	
88	V443 Set		1989	V	8.5	>20	60	11.5	1.78	0.23	
89	V1494 Aql		1999	V	4.1	17.1	16	13	1.2	0.27	
90	V868 Cen		1991	V	8.7	19.9	82	11.2	1.91	0.27	
91	QZ Aur		1964	pg	6	18	26	12	1.41	0.29	
92	V533 Her		1963	V	3	15	43	12	1.63	0.36	
				pg	3	15	44	12	1.64	0.84	
98	V5114Sgr		2004	V	8.1	>21	21	12.9	1.32	0.47	
99	GI Mon		1918	pg	5.6	18	23	12.4	1.36	0.56	
100	BY Cir		1995	V	7.4	17.9	124	10.5	2.09	0.71	
101	V4169 Sgr		1992	V	7.9	>17	36	9.1	1.56	0.76	
102	V5115Sgr		2005	V	7.9	>18	13	10.1	1.11	0.84	
103	V1974 Cyg		1992	V	4.3	16.9	43	12.6	1.63	0.96	
104	OY Ara		1910	pg	6	17.5	80	11.5	1.9	0.96	
105	V1668 Cyg		1978	V	6.2	19.7	26	13.5	1.41	1	
				pg	6.7	20	23	13.3	1.36	1.46	
106	V400 Per		1974	pg	7.8	20	43	12.2	1.63	1.02	
107	IM Nor	✓	2002	V	8.5	18.3	80	9.8	1.9	1.03	
108	V604 Aql		1905	pg	8.2	21	25	12.8	1.39	1.05	
109	V1186 Sco		2004	V	9.7	>18	62	8.3	1.79	1.06	
110	HS Sge		1977	V	7.2	20.7	21	13.5	1.32	1.07	
				pg	7	20.5	20	13.5	1.3	1.52	
111	V888 Cen		1995	V	8	15.2	90	7.2	1.95	1.16	✓ SALT
112	DO Aql		1925	V	8.5	18	900	9.5	2.95	1.21	
113	V1425 Aql		1995	V	8	~20	79	12	1.9	1.23	
114	V1188 Sco		2005	V	8.9	>19	23	10.1	1.36	1.3	
115	XX Tau		1927	pg	5.9	18.5	42	12.6	1.62	1.39	
116	V693 CrA		1981	V	7	>21	18	14	1.26	1.4	
117	V1419 Aql		1993	V	7.6	~21	32	13.4	1.51	1.43	
118	V476 Cyg		1920	V	1.9	16.2	16	14.3	1.2	1.57	
119	V1039 Cen		2001	V	9.3	~21	174	11.7	2.24	1.6	
120	V1500 Cyg		1975	V	1.9	17.9	4	16	0.6	1.74	
121	HS Pup		1963	pg	8	20.5	65	12.5	1.81	1.75	
122	EL Aql		1927	pg	6.4	20	25	13.6	1.39	1.85	
123	DQ Her		1934	V	1.6	14.3	100	12.7	2	1.99	

continued on next page

Table 2.2 – continued

No. ^a	Nova	Recurrent	Year	Filter	m_{max}	$m_{quiescent}$	t_3	A'	$Logt_3$	Deviation	Selected
124	V2540 Oph		2002	V	8.1	>21	115	12.9	2.06	2.34	
125	V2362 Cyg		2006	V	8.1	>21	246	12.9	2.39	3.18	
126	DY Pup		1902	pg	7	20	160	13	2.2	3.18	
127	RW UMi		1956	pg	6	21	140	15	2.14	5.05	
128	CP Pup		1942	V	0.7	>19.5	8	18.3	0.9	5.3	

^a Numbers are arranged by deviation from the CNe trend line.

^b Novae were observed but have not been yet reduce the data. These novae are excluded in the list of twelve target novae.

^c FS Sct was observed photometrically but not successfully obtained a good spectrum due to the underestimated exposure time.

It is therefore excluded in the list of twelve target novae.

2.4 Discussion and Conclusion

The proposal that RNe occupy a region separated from CNe in an outburst amplitude versus speed class diagram was adopted. The low amplitude results from the existence of an evolved secondary and/or high mass transfer rate in the quiescent system. The 93 novae with observed V amplitudes given in the literature and 43 novae with photographic amplitudes have been combined and plotted on an outburst amplitude versus rate of decline diagram as shown in Figures 2.2 and 2.3, from which sixteen target novae suspected to be RNe candidates were selected for the photometric and spectroscopic observations described in Chapters 3 and 4.

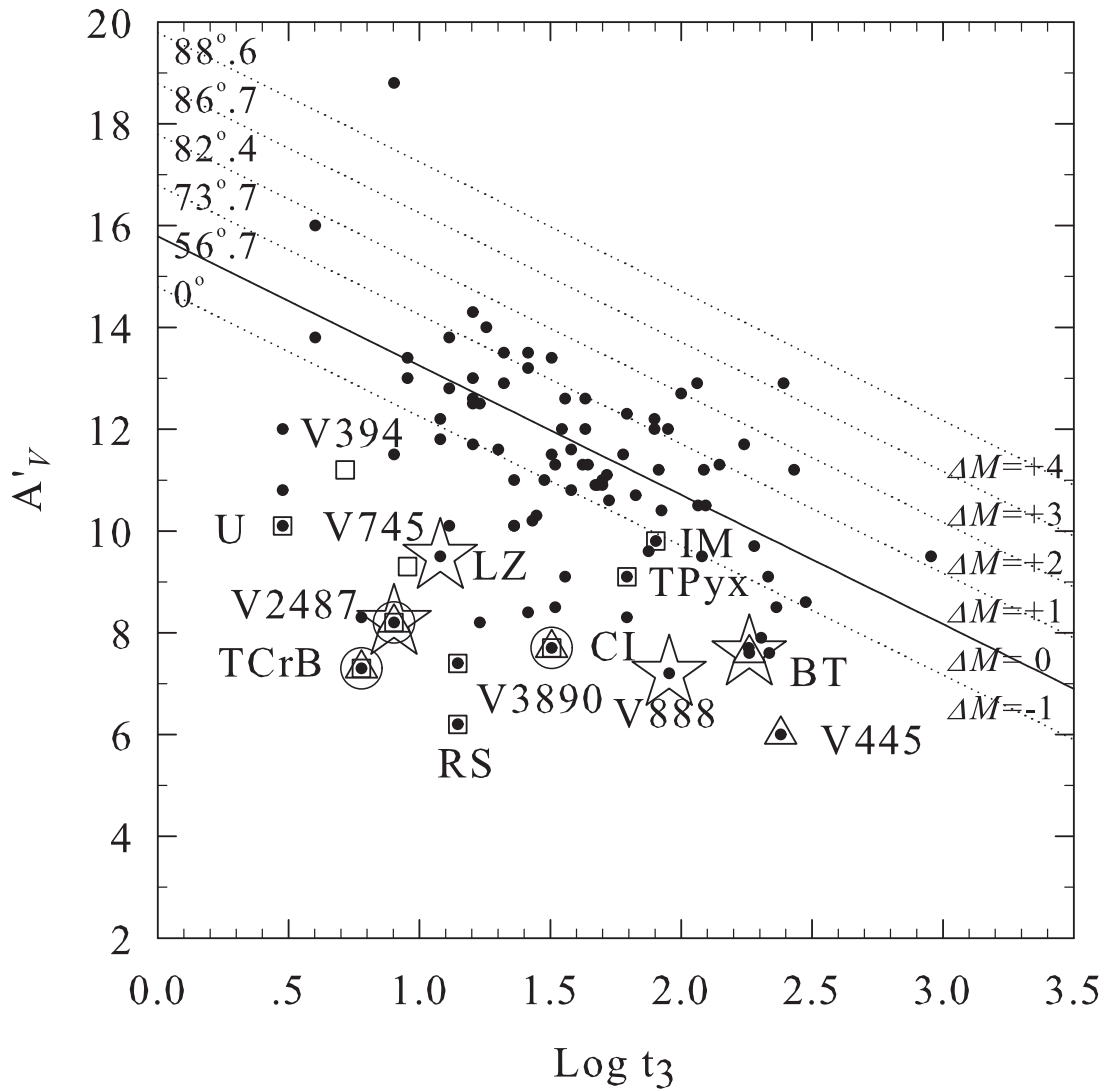


Figure 2.2: Target selection from V amplitudes and rate of decline. Recurrent novae (squares) are plotted together with 93 novae (closed circles) from Strope et al. (2010). Target novae have been observed spectroscopically by SALT (stars) and LT (open circles) and some also have been observed photometrically by LT (triangles).

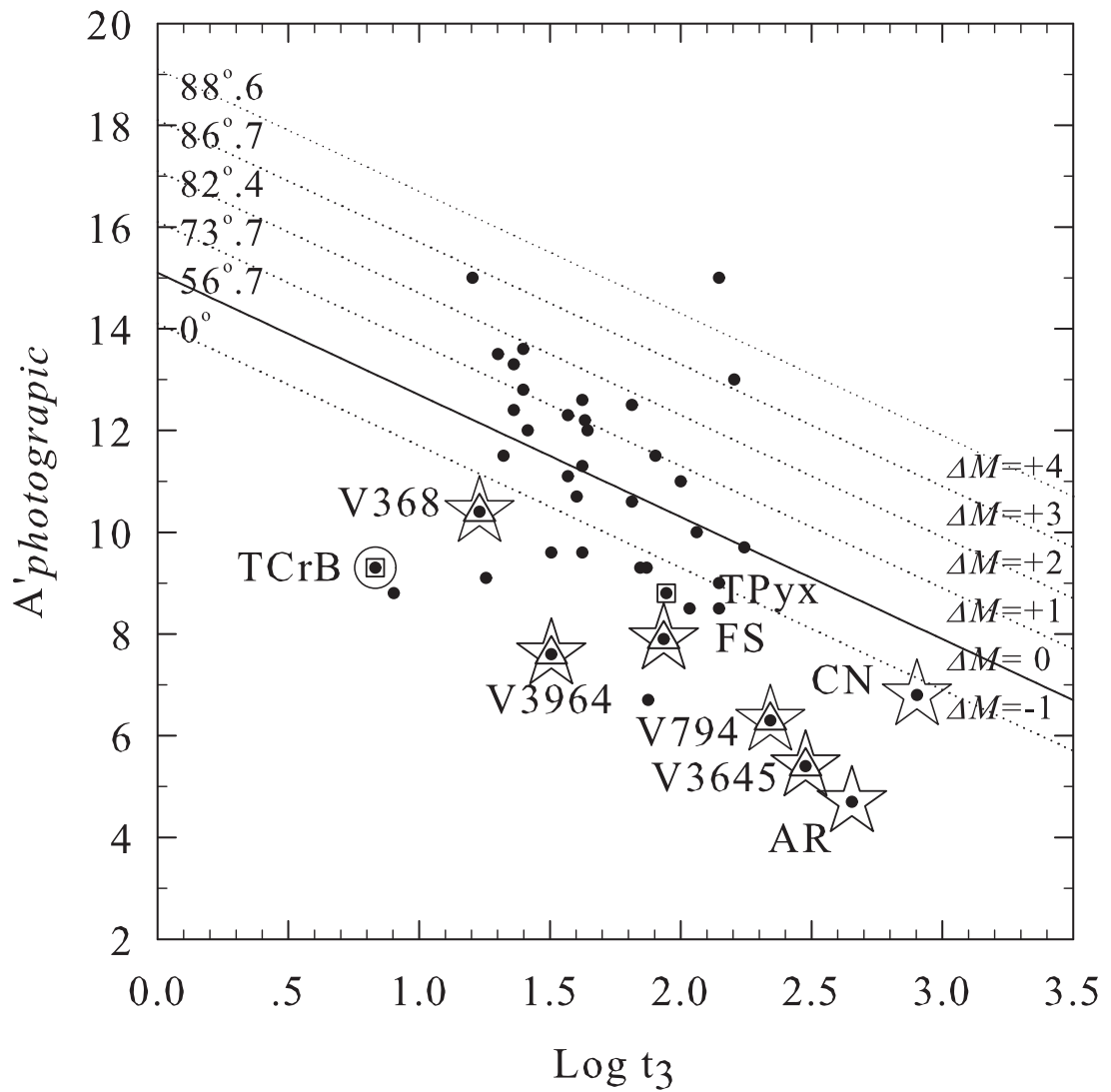


Figure 2.3: Target selection from pg amplitudes and rate of decline. Recurrent novae (squares) are plotted together with 43 novae (closed circles) from Duerbeck (1988a). Target novae have been observed spectroscopically by SALT (stars) and LT (open circles) and some also have been observed photometrically by LT (triangles).

Chapter 3

Ground-based Observations of Novae and Data Reduction

This Chapter provides details of photometric and spectroscopic data acquisition and reduction for the selected targets in Chapter 2, primarily observed by the LT and SALT. The photometric and spectroscopic data taken by LT were obtained and reduction performed by myself. The spectroscopic observations taken by SALT were carried out by Dr. Valério A. R. M. Ribeiro (University of Cape Town) and then were passed onto me for reduction and analysis. The selection criteria in Chapter 2 and the preliminary photometric results for selected novae in Section 3.1 have been published in Surina et al. (2013a).

3.1 The Liverpool Telescope

The Liverpool Telescope, a 2 metre unmanned fully robotic telescope located at the Observatorio del Roque de Los Muchachos on the Canary Island of La Palma, Spain, is owned and operated by the Astrophysics Research Institute of Liverpool John Moores University with financial support from the UK Science and Technology Facilities Council (STFC; see Figure 3.1).



Figure 3.1: Founder of the Liverpool Telescope Prof. Mike Bode and the LT itself on La Palma in its fully-opening enclosure.

There are several instruments mounted at the LT: *RATCam*, an optical camera; *RISE*, a fast-readout camera designed for the precision measurement of transiting exoplanet timing; *RINGO3*, a fast-readout imaging optical polarimeter with simultaneous polarised imaging in three wavebands; *FRODOSpec*, a dual-beam integral-field input spectrograph; *SkyCam*, comprising three cameras providing simultaneous wide field observations with normal LT data-taking; *IO:O*, a camera providing a wider field of view than that of *RATCam* with improved image quality, and *IO:I*, a new near-IR camera (see Steele et al., 2004 for a review).

The LT has been used to obtain observations at multiple wavelengths for Galactic novae in outburst and approaching quiescence. Spectroscopic observations with FRO-

Table 3.1: RATCam photometric observation log

No.	Nova Name	$m_{quiescent}$ (mag)	Filter	Date of observation	Exposure times (s)					
					u'	B	V	r'	i'	z'
1	T CrB	9.8	V	14-04-2011	2×5	2×5	2×5	2×5	2×5	2×5
2	V2487 Oph	17.7	V	02-04-2011	2×400	2×30	2×30	2×25	2×50	2×100
3	CI Aql	16.7	V	03-05-2011	2×50	2×5	2×10	2×10	2×15	2×30
4	V3964 Sgr	17	pg	01-04-2011	2×200	2×15	2×15	2×10	2×20	2×50
5	V3645 Sgr	18	pg	05-04-2011	2×500	2×40	2×40	2×40	2×200	2×300
6	V445 Pup	14.6	V	31-03-2011	2×500	2×50	2×50	2×25	2×50	2×100
7	V794 Oph	18	pg	07-05-2011	2×2500	2×50	2×350	2×50	2×100	2×250
8	FS Sct	18	pg	08-05-2011	2×500	2×40	2×40	2×40	2×100	2×250
9	BT Mon	15.7	V	30-03-2011	2×50	2×5	2×5	2×5	2×5	2×10
10	V368 Aql	15.4	pg	04-04-2011	2×40	2×5	2×5	2×5	2×5	2×10

Table 3.2: Spectroscopic observation log

No.	Nova Name	$m_{quiescent}$ (mag)	Filter	Spectroscopy observation	Exposure times (s) ^d		Note
					Blue	Red	
1	T CrB	9.8	V	24-06-2012 (LT)	3×100	3×500	RN
2	V2487 Oph	17.7	V	17-08-2012 (SALT)	2×450.8	2×188.0	RN
3	CI Aql	16.7	V	06-05-2012 (SALT)	2×82.0	2×90.2	RN
4	AR Cir	20.2	V	01-05-2012 (SALT)	1×180.2	3×60.2	
5	V3964 Sgr	17	pg	11-06-2012 (SALT)	2×221.4	2×92.4	
6	V3645 Sgr	18	pg	27-08-2012 (SALT)	2×274.2	2×114.2	suspect RN ¹
7	V794 Oph	18	pg	10-05-2012 (SALT)	3×160.2	(3×66.2) ^b	suspect RN ²
8	V368 Aql	15.4	pg	06-05-2012 (SALT)	2×150.2	2×65.2	eclipsing ⁵
9	EU Sct	18	pg	30-05-2012 (SALT)	2×204.2	2×84.2	suspect RN ¹
10	CN Vel	17	pg	06-05-2012 (SALT)	3×89.7	1×120.0	
11	LZ Mus	>18	V	01-05-2012 (SALT)	3×160.4	3×66.2	
12	V888 Cen	15.2	V	01-05-2012 (SALT)	3×42.7, 2×90.2 ^c		

^dBlue SALT observations were obtained with filter PC05400, grating angle 13.25° and spectrograph angle 26.51°.

Red SALT observations were obtained with filter PC04500, grating angle 19.25° and spectrograph angle 38.50°.

^b Red observations were obtained with no red arc, therefore only blue spectra were analysed for V794 Oph.

^c Red combined spectrum was very faint and indistinguishable from the background, therefore only blue spectra are presented for V888 Cen.

DOSpec have been used in conjunction with kinematic modelling of the ejecta of novae, e.g. nova V2491 Cyg (Ribeiro et al., 2011) and nova KT Eri (Ribeiro, 2011). Observations with LT were part of the international campaign on the 2010 outburst of short the period RN U Sco (Schaefer et al., 2010b). Moreover, the use of LT SkyCams provided complementary data for the light curve of KT Eri to those obtained with the Solar Mass Ejecta Imager (SMEI; Hounsell et al., 2010 - see Chapter 5). There is also another extensive extragalactic programme for LT. This includes the observations of an extremely luminous nova in M31 (Shafter et al., 2009). In addition, with complementary use of the Hubble Space Telescope (HST), LT observations revealed a nova progenitor system in M31 for the first time (Bode et al., 2009). LT also conducted

a complementary programme to Spitzer observations of novae in M31 (Shafter et al., 2011a). The compilation of light curves from LT and spectroscopic data from HET on novae in M31 is given in Shafter et al. (2011b).

In the work presented here, all photometry reported was obtained with RATCam on LT while spectroscopic observations were obtained with FRODOSpec on LT and the Robert Stobie Spectrograph on SALT (see Table 3.1 for a photometric observation log and Table 3.2 for its spectroscopic counterpart).

3.1.1 RATCam

RATCam is an optical 2048×2048 pixel CCD camera with a 4.6'×4.6' field of view and eight filters (Sloan u' , g' , r' , i' , z' , Bessell B , V and $H\alpha$). The pixel size is 13.5 microns with approximately 0.135arcsec/pixel. The data can be binned by either 1×1 (gain 2.34 electron/count), 2×2 (gain 2.13 electron/count), 3×3, 4×4. The readout noise is <5 electrons with readout times of ~10 s (for 1×1 binning), ~5 s (for 2×2). The peak quantum efficiency is 93.8% at ~500 nm.

To investigate the preliminary evolutionary status of the secondary stars in the target novae via the colour-magnitude diagram (CMD), the photometric RATCam observations in u' , B , V , r' , i' , z' bands were carried out during 2011 Mar - May via LT proposal JL11A02. We used the Exposure Calculator¹ to estimate the exposure time required in order to get a signal-to-noise ratio of 100 with 2×2 binning.

Image Pre-processing

The data from RATCam had already been pre-processed by the pipeline² before they are passed to users, the processing stages of which include:

¹ Exposure Calculator for RATCam is available online at <http://telescope.livjm.ac.uk/Info/TelInst/calc/>

² Details of the pipeline are available online at <http://telescope.livjm.ac.uk/Info/TelInst/Inst/RATCam/>

1. **Bias Subtraction.** Bias subtraction is based purely on analysis of the underscan region. Linear regression is used to determine a fit to the bias counts as a function of pixel row number and values deducted across the image according to this smooth function. RATCam does have a small ramp in the bias down each column and therefore the first order fit is required.
2. **Overscan Trimming.** The overscan regions are trimmed off, leaving a 2048x2048 pixel image.
3. **Dark Subtraction.** This is not currently performed through the pipeline since the dark current appears not to be significant when the camera is at normal operating temperature.
4. **Flat Fielding.** A library of the current calibration frames is maintained as part of the data archive and updated daily so that images are always reduced using the latest available flat-field image. The appropriate master flat field is therefore selected from the library to match the filter and binning configuration of the current exposure.
5. **Bad Pixel Mask.** No bad pixel mask is applied via the pipeline.
6. **Vignetting.** In the extreme corners of the worst affected bands (i' and g') the flux is reduced by up to 15% compared to the unobstructed beam. In the other filters, obscuration is about 5% in the very corner of the observed field, falling to negligible values between 10 - 20 arcsec from the field edge. The vignetting generally flat fields out very well and is rarely obvious in the reduced data although sometimes can leave distortions within 3 - 5 arcsec from the field corner.

Photometric Data Reduction

Following the pre-processing stage, the data reduction steps below were carried out using custom automated scripts from within the NOAO IRAF³ environment.

³ IRAF is distributed by the National Optical Astronomy Observatories, which are operated by the Association of Universities for Research in Astronomy, Inc., under cooperative agreement with the

1. **Image Alignment.** Before the first step involving geometrically aligning the image stack which aids the detection of objects, the images were examined interactively by using `imexamine`. The FWHM and average sigma value of bright point sources were obtained as a result. Using IRAF's `starfind` task with HWHM of the PSF calculated from the previously obtained FWHM/2, a list of stellar objects automatically detected in the image was created. Then the same three reference stars were identified in each frame via `tvmark`. These reference stars were used by the alignment software to calculate the initial transformation. The alignment was carried out by using three packages: `xyxymatch` to produce matched pixel coordinate lists; `geomap` to compute geometric transformations between images using matched coordinate lists, and `geotran` to apply the geometric transforms to the images. The images can then be combined via `imcombine`.
2. **Aperture Photometry.** Following the alignment and the image combination, the task `setairmass`⁴ was implemented as a good habit prior to starting new photometry. Then the aperture photometry was carried out using IRAF/DIGIPHOT/

National Science Foundation.

⁴ A task in the IRAF/ASTUTIL Package - Computing effective airmass and middle UT for an exposure



Figure 3.2: Image of RATCam on the Liverpool Telescope.

APPHOT Package⁵ analysis. By examining the reference frames established from the previous step, parameters required for this analysis including *sigma* (standard deviation of the background sky in counts), *datamin* (minimum good data value in counts), *datamax* (maximum good data value in counts), and FWHM were obtained. Image keyword parameters (e.g. exposure, airmass, filter, observation time, gain, etc.) had to be updated according to the reference headers. Then the tool `qphot` measuring instant magnitudes for a list of stars was performed. The interactive PSF modelling interface requires input parameters including:

- Centring box width = (2 x FWHM)
- Inner radius of sky annulus = (4 or 5 x FWHM)
- Width of sky annulus = (2.5 x FWHM)
- List of Photometry apertures = (FWHM)

Finally, the output of selected fields from `apphot` could be dumped by using `txdump` task.

3.1.2 FRODOSpec

The Fibre-fed RObotic Dual-beam Optical Spectrograph (FRODOSpec) is a multi-purpose integral-field bench-mounted optical spectrograph with a dual beam design so that the beam splits before the entrance to the individually optimized collimators (see Barnsley et al., 2012 for the details).

Two resolution options are available on each arm. With low resolution selected on each arm, the entire spectrum covers 3900-5700Å in the blue arm ($R \sim 2200$ with 0.8 Å/pixel) and 5800-9400Å in the red arm ($R \sim 2600$ with 1.6 Å/pixel). The low resolution mode is implemented using conventional transmission gratings.

The higher resolution option for each arm is provided using a Volume Phase Holographic (VPH) grating bonded to a prism in order to throw the beam to the same angle

⁵ Aperture Photometry Package See <http://iraf.net/irafdocs/apuser.pdf>

as that obtained using the diffraction grating at low resolution. The spectral range is 3900-5100Å in the blue ($R \sim 5500$ with $0.35 \text{ \AA}/\text{pixel}$) and 5800-8000Å in the red arm ($R \sim 5300$ with $0.8 \text{ \AA}/\text{pixel}$).

Optical spectra of target novae were obtained using FRODOSpec for the brighter objects from Table 3.2 in low resolution mode via LT proposals JL11A02 and JL11B04b.



Figure 3.3: Part of FRODOSpec on an optical bench before shipping to site.

Spectroscopic Data Reduction

The data from FRODOSpec is already pre-processed and reduced by the fully automated pipeline given in Barnsley et al. (2012) before they are passed to users. The pipeline specifically consists of **i)** finding and tracing the positions of the fibres at points along the dispersion axis, **ii)** unweighted aperture extractions, **iii)** wavelength calibration, **iv)** fibre throughput correction, **v)** spectral rebinning to a linear wavelength calibration, **vi)** identification and subtraction of sky-only fibres (only possible if they are available in the field) and **vii)** reformatting of data to the desired output format. The science-ready data product, an eight part multi-extension FITS file with each extension containing a snapshot of the data taken at key stages of the reduction process, is shown in Table 3.3. A composite image of the L1_IMAGE, SPEC_NONSS and

COLCUBE_NONSS extensions is made available through the LT archive website⁶. An example is shown in Figure 3.4.

Table 3.3: The format of the science-ready data product from the FRODOSpec pipeline. The science-ready data product includes; Image, Row Stacked Spectra (RSS) frames used to display each extracted spectrum as a single row of height one pixel, and Datacubes that reimage the focal plane at each wavelength. Wavelength is calibrated in units of Å. The Table is adapted from Barnsley et al. (2012).

Extension Index	Extension Name	Format	Wavelength Calibrated?	Throughput Corrected?	Sky Subtracted?
0	L1_IMAGE	Image			
1	RSS_NONSS	RSS	✓	✓	
2	CUBE_NONSS	Datacube	✓	✓	
3	RSS_SS	RSS	✓	✓	✓
4	CUBE_SS	Datacube	✓	✓	✓
5	SPEC_NONSS	Spectrum	✓	✓	
6	SPEC_SS	Spectrum	✓	✓	✓
7	COLCUBE_NONSS	Image		✓	

Data Product Preview

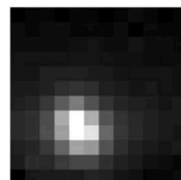
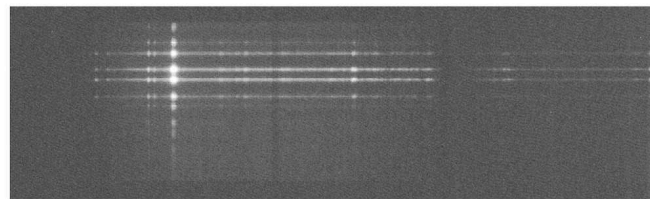
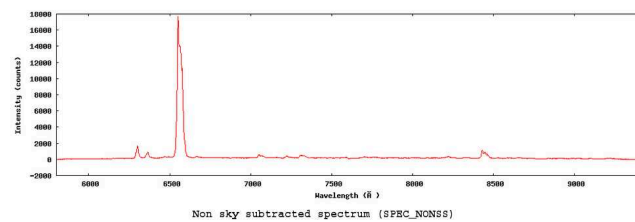


Figure 3.4: An example of FRODOSpec data product preview, presenting SPEC_NONSS (top), L1_IMAGE (middle), and COLCUBE_NONSS (bottom).

⁶ <http://lt-archive.astro.livjm.ac.uk/>

In this study, the spectra in extension [6] were used. If sky subtraction was not successful, the corresponding extensions ([3], [4] and [6]) will be blank. Therefore the sky subtraction was performed manually to spectra in extension [5] using IRAF task `dofibers` in this case.

Failure of sky subtraction of the pipeline can be because either the target may be located toward the edges of the Integral field unit (IFU) or the target may be extended as FRODOSpec's IFU has a small field of view, so the pipeline cannot identify the sky-only fibres (Barnsley et al., 2012). Thus, by using `dofibers` manually, we can identify the sky fibre and then subtract it off all the spectra in extension [5]. According to Barnsley et al. (2012), it is concluded that the sky subtraction products from the pipeline are of a scientific standard from the `dofibers` routine.

Spectra were finally median combined the via `imcombine` IRAF routine and ready to be used in further analysis.

3.2 The Southern African Large Telescope

SALT (see Buckley et al., 2006, for a review) is one of five 10-m class segmented mirror telescopes (the others being GranTeCan in La Palma, 2 Keck Telescopes in Hawaii, and HET in Texas) and the only one situated in the southern hemisphere. SALT is closely based on the innovative HET design. The telescope is situated at the South African Astronomical Observatory (SAAO) field station near the small town of Sutherland ~380 km from Cape Town at an altitude of 1798m above mean sea level.

The primary mirror consists of a $9.8 \text{ m} \times 11.1 \text{ m}$ hexagonal array of 91 identical $1.2 \text{ m} \times 1.0 \text{ m}$ hexagonal mirror segments (see Figure 3.5) with spherical surfaces, tilted at 37° to the zenith. SALT has a fixed elevation angle (53°) and can rotate only about its azimuth axis to acquire objects. This gives the telescope an annulus-shaped observing area in the sky as shown in Figure 3.6. In this study, observations were obtained, following a successful proposal, in service mode.

3.2.1 The Robert Stobie Spectrograph (RSS)

The Robert Stobie Spectrograph (RSS)⁷ is the Prime Focus Imaging Spectrograph with wavelength coverage from 3200-9000Å. RSS provides the highest possible efficiency spectroscopy using Volume Phase Holographic (VPH) gratings providing resolutions of $R \sim 800-6000$ with a 0.9 arcsec slit width (with seeing FWHM 0.9 arcsec).

⁷ Detail specification can be found at <http://www.salt.ac.za/telescope/instrumentation/rss/>

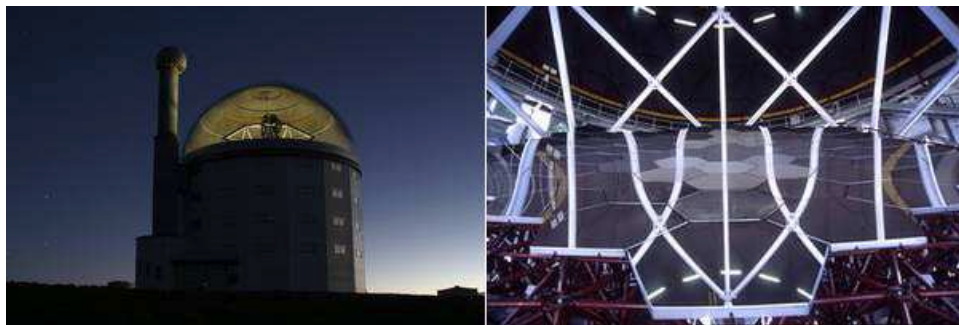


Figure 3.5: The Southern African Large Telescope (SALT) situated at the SAAO field station (top) with a hexagonal primary mirror array 11 metres across (bottom).

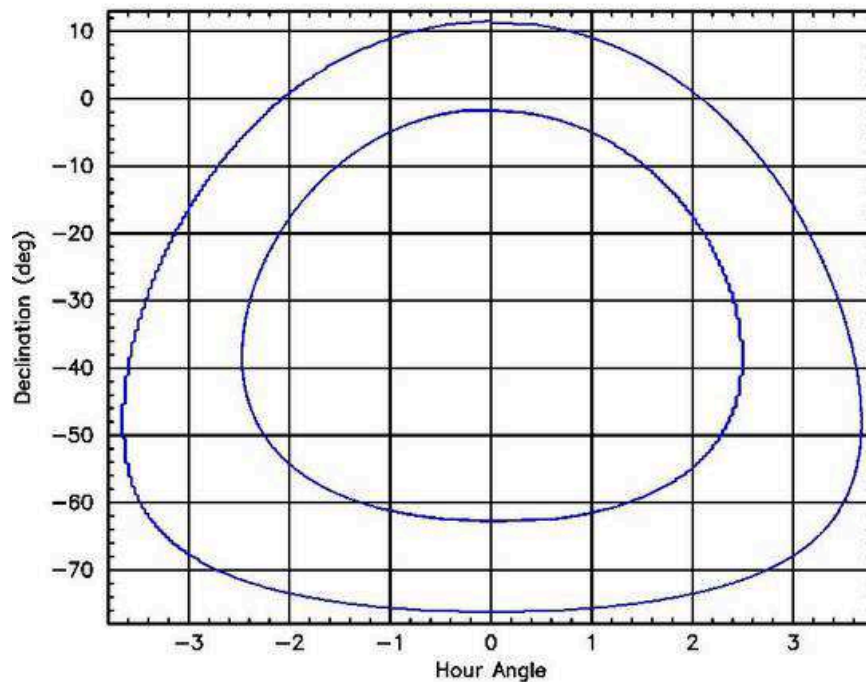


Figure 3.6: The SALT viewing annulus.

In this study, the RSS was used in low resolution mode with the pg0900 VPH grating with the long slit set at 1.5 arcsec was used. This gave us the required sensitivity and spectral resolution for our target. In order to cover both the blue (accretion disk dominated component) and red (cool stellar component, covering the diagnostic bands to $\sim 8500\text{\AA}$) wavelength ranges, two spectrograph angles per object (26.5° and 38.5° respectively, which also gives decent spectral overlap) were specified. The determination of exposure time for each object was done by collaborators by using the RSS exposure time calculator with a combination of a canonical accretion disk spectrum and a cool (3500 K) black body, assumed to give equal contributions to the flux. With the observed optical magnitude we then determined the total exposure time to give a S/N per resolution element of 20 at the central wavelength of the resulting spectrum for each grating setting.

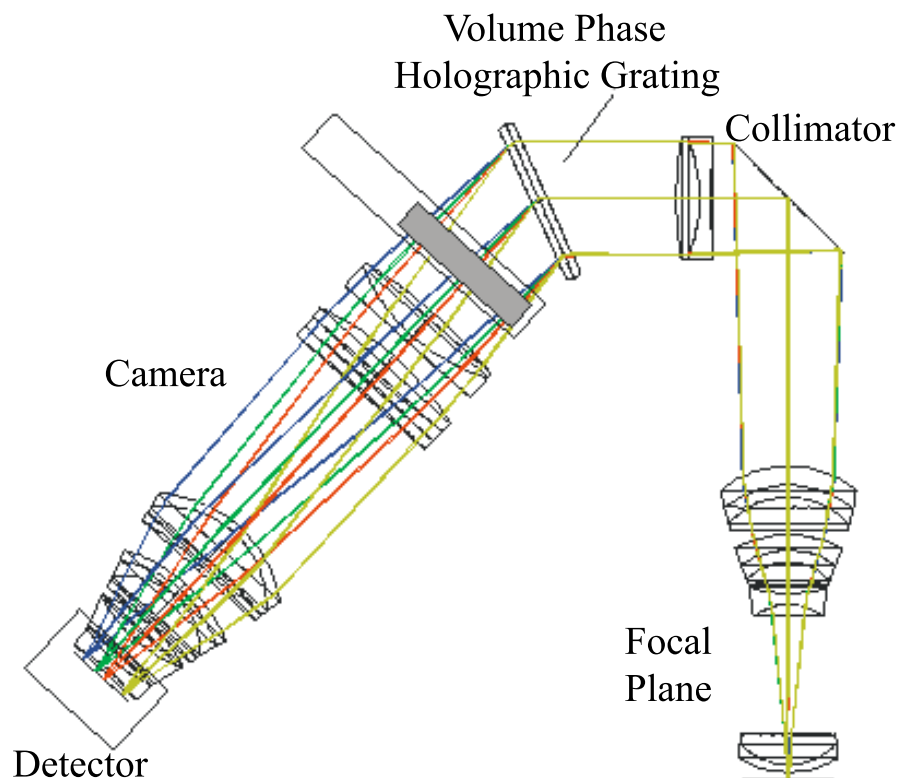


Figure 3.7: Schematic illustration of spectroscopy modes of RSS.

Spectroscopic Data Reduction

The IRAF/Longslit Package was used to reduce data from the SALT RSS long-slit. The following are the steps⁸ used to reduce data provided from the SALT pipeline (the “product” data) into the extracted spectra. Each set of reductions requires science images, flat fields, and an arc lamp image (only red files are shown as an example as detailed below).

1. **Flat fielding.** All flat field frames in each grating angle were combined to make the illumination frame. Then the illumination was examined and a normalised flat frame created (after being divided by the mean) which would be finally applied to the object frames. Figure 3.8a shows the combined red flat field frame. Steps of commands and parameters are then:

```
<flatcombine red_flat*.fits output=red_Flat.fits combine=
median reject=none scale=mean rdnoise=2.51 gain=1.51
<mkillumflat red_Flat.fits red_Flat_illum.fits xboxmin=3
yboxmin=3 xboxmax=5 yboxmax=5
<imstat red_Flat_illum.fits
<imarith red_Flat_illum.fits/20742 red_Flat_norm.fits
<imarith @red_object.lst/red_Flat_norm.fits cc_//
@red_object.lst
```

2. **Arc files.** Here we identify, fit coordinates, and transform the lines in the blue and red arcs. After that the transformation is applied to the object frame. Note that the Argon lamp (not the NeAr lamp) is used in the case of blue spectra. Figure 3.8b shows an arc spectrum and line identification, Figure 3.8c shows an object spectrum before transformation, and Figure 3.8d shows an object spectrum after transformation. Again, steps of commands and parameters are:

```
<identify red_arc.fits coordlist=linelists$NeAr.txt function=
```

⁸ Detail reduction is available at http://www.dartmouth.edu/~kevinhainline/salt_redux.html

```

chebyshev order=5 fwidth=6 cradius=6
<reidentify reference=red_arc.fits images=red_arc.fits
interactive=no newaps=yes override=no refit=yes nlost=20
coordlist=linelists$NeAr.txt verbose=yes
<fitcoords images=red_arc interactive=yes combine=no functio=
legendre xorder=5 yorder=3
<transform input=red_arc output=red_transform_arc fitnames=
red_arc interptype=linear flux=yes blank=INDEF x1=INDEF
x2=INDEF dx=INDEF y1=INDEF y2=INDEF dy=INDEF
<transform input=cc_//@red_object.lst output=red_transform_//
@red_object.lst fitnames=red_arc interptype=linear flux=yes
blank=INDEF x1=INDEF x2=INDEF dx=INDEF y1=INDEF y2=INDEF
dy=INDEF

```

3. **Removing cosmic rays.** Here we make use of the alternative cosmic ray remover algorithm, L.A.Cosmic⁹, which appears to address one individual file at a time. Figure 3.8e shows an object spectrum after removing cosmic rays, using the following steps:

```

<lacos_spec input=red_transform_red_object001.fits output=
cos_red_object001.fits outmask=cos_red_mask001.fits gain=
1.51 readn=2.51 niter=10
<hedit cos_//@red_object.lst BPM "cosmic_mask.fits"

```

4. **Background Subtraction.** To remove the sky lines and make the background level to be approximately zero, the IRAF task background is used. A range of specified columns collapse into a 2D image where the object spectrum has the peak in the very centre and the background to the left and right. Fitting interactively a few times will fit the non-linear background. Figure 3.8f shows a object spectrum after background subtraction, using the following steps:

⁹ L.A.Cosmic is an algorithm for robust cosmic ray identification. It detects cosmic rays of arbitrary shapes and sizes, and distinguishes between undersampled point sources and cosmic rays. The method is explained in van Dokkum (2001) see <http://www.astro.yale.edu/dokkum/lacosmic/>

```
<background input=cos_//@red_object.lst output=bg_//
@red_object.lst axis=2 interactive=yes naverage=1 function=
cheby order=2 low_rej=2 high_rej=1.5 niterate=5 grow=0
```

5. **Combining images and extracting the traces.** Object frames are combined and then created the variance frame is created afterwards. Note that “im1/2” refers to being divided by the number of images. Figure 3.8g shows a combined object spectrum. Finally the `apall` task is used to extract 1D spectra from 2D spectra:

```
<imcombine bg_//@red_object.lst red_obj_med.fits sigma=red_obj
_med_sig.fits combine=median scale=mean masktype=goodvalue
<imcalc red_obj_med_sig.fits red_obj_med_sig_sqr.fits "im1**2"
<imcalc red_obj_med_sig_sqr.fits red_obj_med_sig_var.fits "im1/2"
<imdel red_obj_med_sig_sqr.fits
<apall input=red_obj_med.fits output=red_obj_med_ms.fits
line=910 nsum=10
```

There are some artefacts in spectra obtained by SALT due to the gaps in instrumental response between 4450-4550Å and 7750-7850Å. Extension of the artefact area also arises near the edges of each gap after each process of reduction, so they need to be deleted manually. For some cases, the deleting of the artefact extends to the scientific region (i.e. K I 7665Å and 7699Å which is very strong and wide in dwarf stars but much weaker in giants - see Chapter 4 for details).

3.3 Relative Flux Calibration with Standard Stars

All nova observations from LT and SALT were supplemented by obtaining standard stars along with the observations of the novae themselves. Two WDs listed in the spectroscopic standard stars library¹⁰ in the `onedspec` package; eg139 ($\alpha=20^h34^m21^s.883$,

¹⁰a library of standard star can be found in `/iraf/iraf/noao/lib/onedstds/spec50cal/`

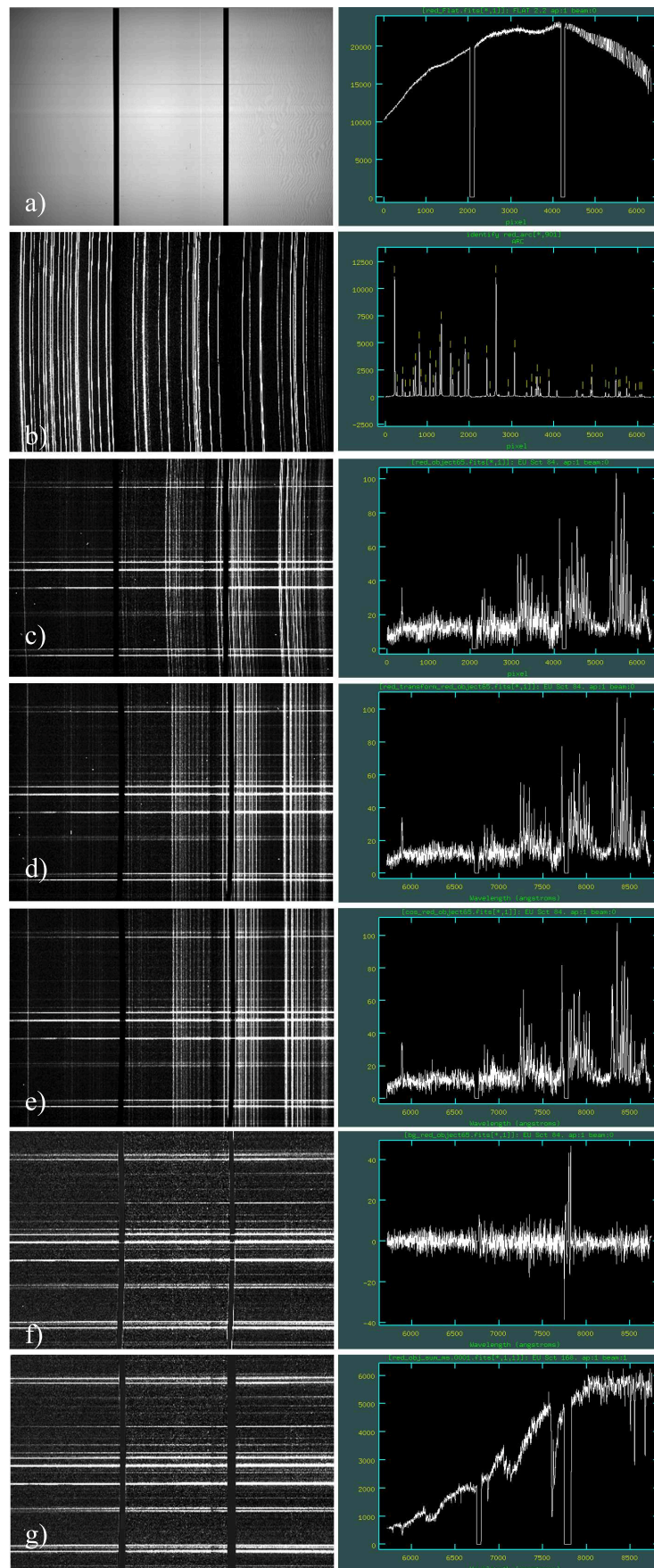


Figure 3.8: SALT RSS long-slit data reduction showing data images (left) and spectra (right) at each steps of the process.

$\delta=+25^{\circ}03'49''.74$) and eg158 ($\alpha=23^h19^m58^s.398$, $\delta=-05^{\circ}09'56''.16$) with quiescent magnitude of $V=11.56$ and 11.50 , respectively, were observed at similar airmass to the targets.

The IRAF `onedspec` package was used to create the sensitivity function of a standard star and apply that to the object spectrum to get a relative flux calibrated spectrum. Once the `onedspec` package is loaded, some parameters require correcting for each spectrum prior to the calibration. For example, an exposure time can be implemented via `hedit`, airmass can be corrected by using `setairmass` in the `astutil` task, and radial velocity corrections can be done in `rvcorrect`.

For the standard star spectrum (see Figures 3.9 and 3.10), the `standard` task is first performed in order to identify standard stars and call its flux from the library. Then the sensitivity function is created by using `sensfunc`. The output of this interactive task is something that is used by the `calibrate` task which applies extinction and flux calibrations to our target novae spectra. These processes are presented below.

```
onedspec> standard STDstar.fits STDstar.flux
onedspec> sensfunc STDstar.flux STDstar.sens ignoreap+
onedspec>calibrate obj.fits obj-cal obs=lapalma sens=STDstar.sens
ignoreap+
```

3.4 Discussion and Conclusion

The proposal that RNe occupy a region separated from CNe in an A' vs t_3 diagram given in Chapter 2, allowed us to select sixteen RNe candidates for detailed observations. Photometric magnitudes in u , B , V , r , i and z were obtained for 10 novae at quiescence using RATCam on LT (see Table 3.1). Spectra for twelve of them were obtained using FRODOSpec on LT and RSS on SALT (see Table 3.2). Of these, only nine spectra could be successfully fully reduced and ready for further analysis (see Table 3.4). Spectra for the other three objects (CN Vel, LZ Mus and V888 Cen) were

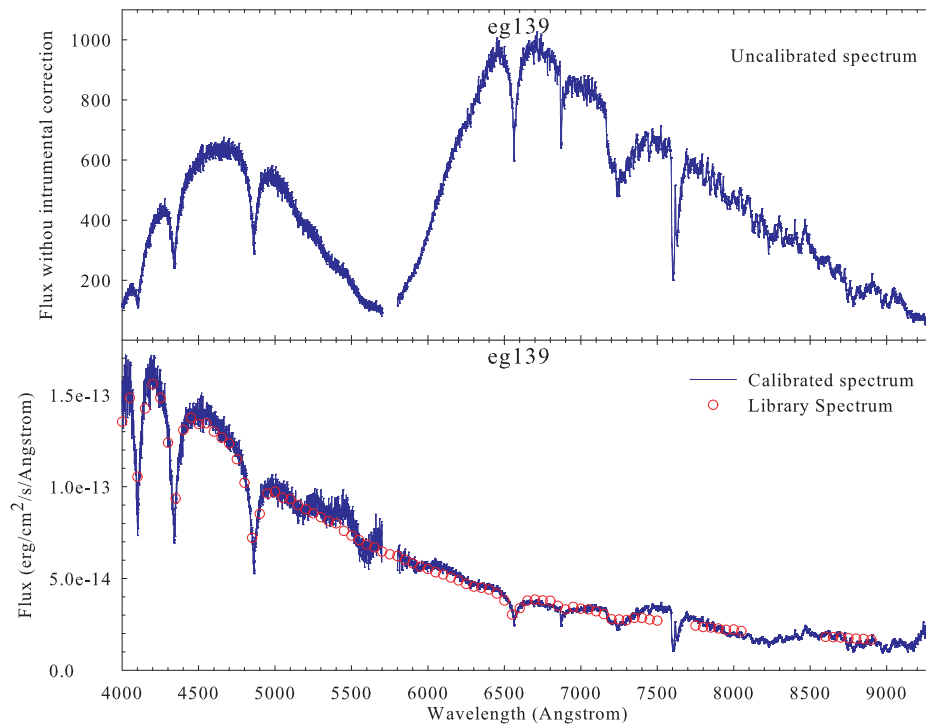


Figure 3.9: Flux calibration of standard star eg139 showing spectrum before (top) and after the calibration (bottom).

not fully reduced at the moment due to the unclearly matched arc line identifications which causes a shift in wavelength (for CN Vel and V888 Cen) and an underestimate of the exposure times making the spectra indistinguishable from the background (for LZ Mus).

This chapter provided an introduction of facilities that were used and gave details of photometric and spectroscopic data reduction from pre-processing to flux calibration with standard stars. In the next Chapter, results of the photometry, and especially the spectroscopy, will be discussed.

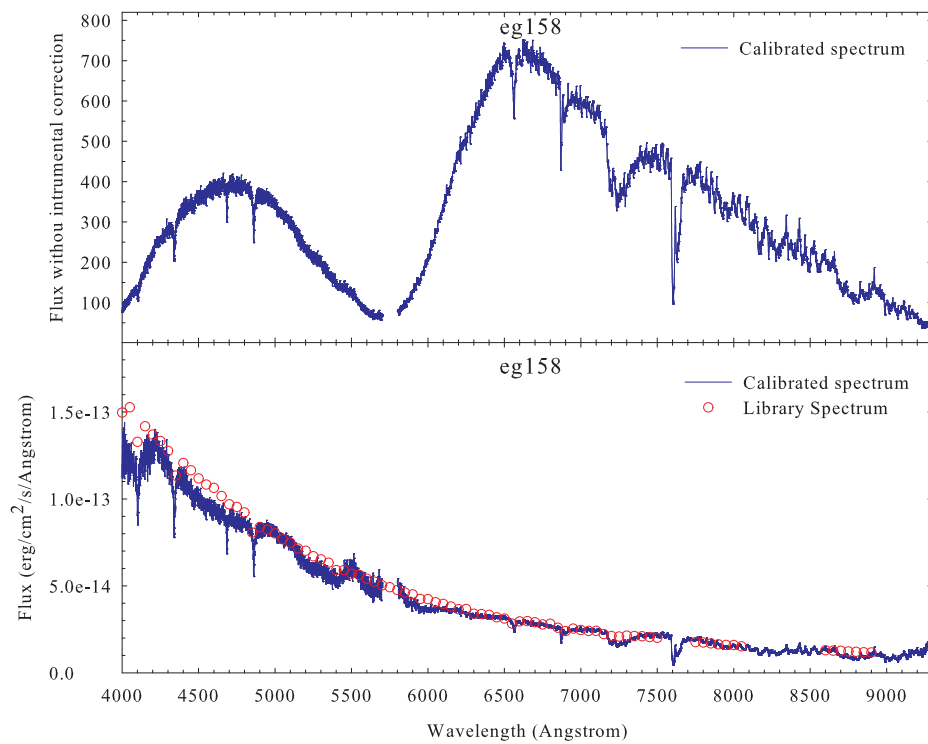


Figure 3.10: Flux calibration of standard star eg158 showing spectrum before (top) and after the calibration (bottom).

Table 3.4: Final target novae lists for photometric and spectroscopic analysis.

No.	Name	Observation		Spectroscopic Data Reduced?	Successful Spectra?
		Photometry	Spectroscopy		
1	T CrB (RN)	✓ LT	✓ LT	✓	✓ (No.1)
2	V2487 Oph (RN)	✓ LT	✓ SALT	✓	✓ (No.2)
3	CI Aql (RN)	✓ LT	✓ SALT	✓	✓ (No.3)
4	AR Cir		✓ SALT	✓	✓ (No.4)
5	V3964 Sgr	✓ LT	✓ SALT	✓	✓ (No.5)
6	V3645 Sgr	✓ LT	✓ SALT	✓	✓ (No.6)
7	V445 Pup	✓ LT		-	-
8	V794 Oph	✓ LT	✓ SALT	no red observation	✓ (No.7)
9	V1330 Cyg		✓ HET	future work	-
10	FS Sct	✓ LT	✓ LT	cannot see spectrum	-
11	BT Mon	✓ LT	✓ Yunnan	future work	-
12	V368 Aql	✓ LT	✓ SALT	✓	✓ (No.8)
13	EU Sct		✓ SALT	✓	✓ (No.9)
14	CN Vel		✓ SALT	✓	λ shift
15	LZ Mus		✓ SALT	✓	too faint
16	V888 Cen		✓ SALT	✓	λ shift

Chapter 4

Observations of Galactic Novae in Quiescence

In the previous Chapter, the photometric magnitudes of ten novae and the flux calibrated spectra of twelve novae were derived at quiescence. In this Chapter, the magnitudes are plotted on colour-magnitude diagrams (CMDs) and the spectra are analysed for specific features. The evolutionary status of the secondary stars derived via the CMDs and the spectral lines are compared. Parts of the results in this Chapter have been published in Surina et al. (2013a).

4.1 Introduction

Currently, there are only 10 known Galactic RNe among the approximately 400 Galactic CNe. They group themselves into three distinct subtypes: T CrB/RS Oph type (with red giant secondary stars), U Sco type (with evolved main sequence or sub-giant stars) and the T Pyx type which have similar secondaries to those in most CNe (i.e. main sequence stars; see Chapter 1 for details).

Knowledge of the true population of RNe obviously has a bearing on their potential relationship to SN Ia. At least eight of these Galactic RNe are known to harbour

evolved secondary stars rather than the main sequence secondaries which are found to be typical for CNe (Darnley et al., 2012).

At quiescence, the optical spectra of particular RNe are suggested to be dominated by that of the red giant (Anupama & Mikołajewska, 1999). Spectral features indicating giants secondaries are used to investigate the quiescent spectra of novae that are suspected RNe in this Chapter by using the following approach.

4.2 Background to the Analysis

The optical emission from all quiescent nova systems is a composition of the emission from three components: the WD, the accretion disk, and the secondary where the contribution from WD in the optical region is expected to be negligible (Darnley et al., 2012). While the contribution of the accretion disk depends on several factors including the accretion rate, disk size, system inclination, and observed wavelength, the contribution from the secondary star is much more straightforward and simply depends on the type of star (i.e. mass, age, and metallicity) and again of course the observed wavelength (Darnley et al., 2012).

In this study, we adopted the simplified classification of the evolutionary status of the secondaries proposed in Darnley et al. (2012); i.e. whether a main-sequence star (MS-Nova), a sub-giant star (SG-Nova), and a red giant branch star (RG-Nova). All the known U Sco type RNe would then be placed into the SG-Nova group, all the known RS Oph/T CrB type RNe into the RG-Nova group, and the T Pyx type RNe and Classical Novae will populate the MS-Nova group; This classification, by virtue of the geometry of these systems, would effectively be the same as nova classification by orbital period since systems with orbital periods longer than 8 hr should contain evolved secondaries (Warner, 1995). The MS-Novae would have orbital periods of order hours, the SG-Novae of order a day, and the RG-Novae of order a year (Darnley et al., 2012). Thus one can distinguish the RG-Novae and SG-Novae from the MS-Novae population based on solely their quiescent optical and near-IR (NIR) properties.

Therefore our aim is to determine the spectral and luminosity type of the secondaries in our target systems by comparing the results derived from the nova positions on the optical and NIR CMDs to the results derived from the detailed spectral analysis where specific indicator lines are expected.

4.3 Reddening

Prior to the spectroscopic analysis, each nova is required to be given a reliable interstellar extinction. Known extinction found in previous work in the literature was adopted where possible. Where this was not available, the A_V of each object is estimated by comparing values taken from two different methods.

In the first method, the A_V is derived from 4 different extinction maps¹ along the line of sight including those of Neckel et al. (1980), Schlegel et al. (1998), Dobashi et al. (2005), and Rowles & Froebrich (2009).

Neckel et al. (1980) provided reddening maps giving $E(B - V)$ versus heliocentric distance (r) and Galactic position (l, b) at low galactic latitudes ($-7^\circ.6 < b < 7^\circ.6$ and $r \lesssim 5$ kpc) by computing from more than 11000 O to F stars with known A_V and r . Schlegel et al. (1998) constructed a map of the Galactic dust temperature based upon its far-infrared emission and normalized this dust map to the $E(B - V)$ per unit flux density of $100 \mu\text{m}$ emission by using the colours of background elliptical galaxies. Their A_V represents the value to the edge of our Galaxy, thus it should be the largest reddening compared to the other three sources. Dobashi et al. (2005) derived a large-scale extinction map covering the region in the Galactic latitude range $|b| \leq 40^\circ$ by applying a star counting technique to the optical database of the Digitized Sky Survey. Rowles & Froebrich (2009) generated an all-sky extinction map by studying the column density distribution of all nearby Galactic giant molecular clouds using the nearest 100 neighbour stars. The A_V given by Rowles & Froebrich (2009) turns out to be systematically larger by 20% compared to Dobashi et al. (2005) and 40% smaller compared

¹ Available online at <http://astro.kent.ac.uk/extinction/>

to Schlegel et al. (1998). This is most likely because of the star counting technique used in the former and the systematic uncertainty in dust temperature and emissivity presented in the latter.

Thus, in case of novae with unknown extinction, the A_V/kpc derived from Neckel et al. (1980) was then compared to the total A_V in that direction given by Schlegel et al. (1998), Dobashi et al. (2005), and Rowles & Froebrich (2009). The most reliable A_V was finally adopted in the analysis for each object.

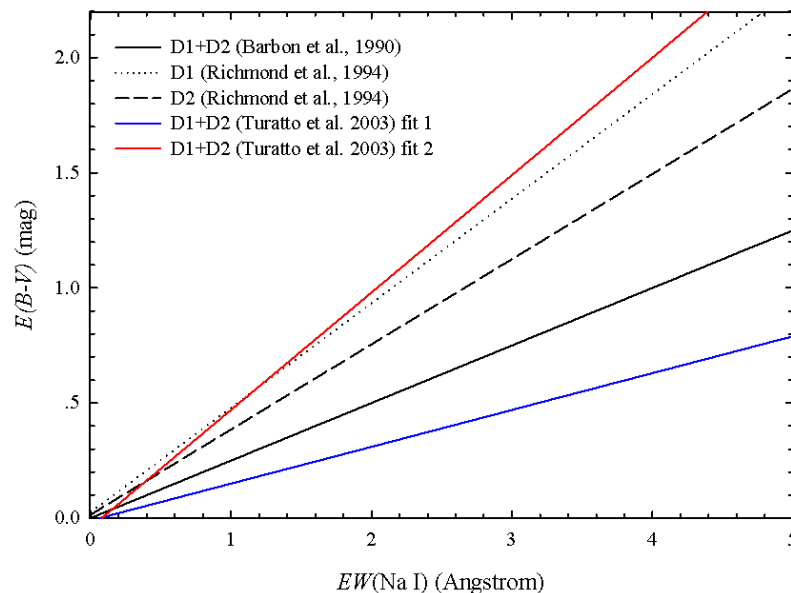


Figure 4.1: Extinction along the line of sight (A_V) versus the equivalent width of Na I D of ($EW(\text{Na I})$) various correlations proposed by Barbon et al. (1990), Richmond et al. (1994), and Turatto et al. (2003).

In the second method, the A_V is derived from the equivalent width (hereafter EW) of the absorption doublet of Na I D, at 5890\AA (D1) and 5896\AA (D2), which is a well-known tracer of gas and dust and its strength is generally expected to indicate the amount of dust along the line of sight (Poznanski et al., 2012). Several empirical correlations between EW and colour excess $E(B - V)$ are proposed e.g. Barbon et al. (1990); Richmond et al. (1994); Turatto et al. (2003). Richmond et al. (1994) have used 57 high-resolution stellar spectra compiled from literature and shown that the EW does indeed correlate with $E(B - V)$. Meanwhile Barbon et al. (1990) and Turatto

et al. (2003) used 6 and ~ 30 spectra, respectively, low- to medium-resolution spectra of SNe Ia to derive the relations which have been used widely in the literature over the last two decades. Figure 4.1 shows that different published relations are not totally consistent with one another. This can be either due to the different dust-to-gas ratios in different galaxy types or the uncertainty in EW measurement contaminated from the atmospheric sodium which is difficult to remove, therefore Poznanski et al. (2012) suggested that the low-resolution Na I D absorption measurement may not be a good extinction indicator.

In this study, we however adopted the most recent relations using $EW(D1+D2)$ given by Turatto et al. (2003) for both fit 1 and fit 2 since some of our spectra do not resolve the D1 and D2 doublet. Their larger sample also provided larger range coverage in $EW(D1+D2)$ than that given by Barbon et al. (1990). The results for derived $E(B - V)$ and A_V were calculated by using the following relations and presented in Table 4.2.

Barbon et al. (1990):

$$E(B - V) \sim 0.25 \times EW(D1 + D2) \quad (4.1)$$

Turatto et al. (2003) fit 1 and fit 2:

$$E(B - V) = -0.01 + 0.16 \times EW(D1 + D2) \quad (4.2)$$

$$E(B - V) = -0.01 + 0.16 \times EW(D1 + D2) \quad (4.3)$$

Note here that the preferred A_V for each nova is given in Table 4.2, as indicated by ‘*’.

4.4 Photometric Observations and Results

Quiescent B, V, u', r', i', z' magnitudes were obtained for 10 target novae using the RAT-CAM CCD camera at the LT (see Chapter 3) during 2011 May. Observed apparent magnitudes are presented in Table 4.1.

Table 4.1: Observed optical and NIR apparent magnitudes of target novae at quiescence. The optical magnitudes were obtained by LT for ten novae. The *JHK* magnitudes were taken from 2MASS for these ten LT novae and other novae and other novae observed spectroscopically from SALT.

No.	Star	u'	B	V	r'	i'	z'	J	H	K
1	T CrB	saturated	12.66±0.02	10.97±0.02	10.30±0.02	9.13±0.02	9.36±0.02	5.99±0.02	5.15±0.04	4.81±0.02
2	V2487 Oph	18.30±0.07	19.9±0.3	19.1±0.2	18.8±0.1	18.17±0.06	17.44±0.06	15.36±0.08	14.88±0.10	14.41±0.09
3	CI Aql	17.42±0.07	17.34±0.05	16.17±0.02	15.73±0.01	15.18±0.02	14.82±0.01	13.67±0.04	13.33±0.08	12.69
4	AR CIR	-	-	-	-	-	-	11.81±0.02	11.10±0.02	10.98±0.02
5	V3964 Sgr	19.74±0.2	19.13±0.05	18.09±0.03	17.54±0.02	17.00±0.02	16.81±0.02	10.86±0.03	10.02±0.03	9.74±0.03
6	V3645 Sgr	18.77±0.1	18.37±0.05	16.75±0.02	16.20±0.02	15.53±0.02	15.07±0.01	15.45±0.06	14.89±0.08	13.17
7	V445 Pup	20.38±0.08	19.8±0.2	19.1±0.1	19.0±0.1	18.83±0.04	18.94±0.01	12.27±0.02	11.94±0.02	11.52±0.03
8	V794 Oph	20.24±0.08	19.76±0.07	17.64±0.02	16.95±0.02	16.02±0.02	15.61±0.03	14.15±0.02	13.38±0.02	13.21±0.03
9	V1330 Cyg	-	-	-	-	-	-	15.81±0.06	15.23±0.09	15.14±0.16
10	FS Sct	20.63±0.2	19.25±0.05	17.60±0.03	16.96±0.02	16.18±0.02	15.85±0.01	14.65±0.04	13.93±0.04	13.71±0.05
11	BT Mon	14.80±0.02	16.00±0.02	15.58±0.02	15.46±0.02	15.24±0.02	15.21±0.02	14.40±0.04	13.96±0.05	13.72±0.05
12	V368 Aql	16.22±0.04	16.59±0.03	15.97±0.02	15.72±0.02	15.59±0.02	15.49±0.02	14.53±0.05	14.15±0.06	14.03±0.07
13	EU Sct	-	-	-	-	-	-	12.26±0.05	11.18±0.04	10.80±0.04
14	CN Vel	-	-	-	-	-	-	15.66±0.07	15.12±0.09	15.15±0.20
15	LZ Mus	-	-	-	-	-	-	14.46±0.04	13.75±0.04	13.51±0.06
16	V888 Cen	-	-	-	-	-	-	15.6±0.2	14.92±0.41	14.79±0.27

In order to obtain the absolute magnitudes and colours, the correction from reddening was applied by the method described in Section 4.3. This enabled us to calculate the ranges of absolute magnitudes and distance using the following MMRD relationship (i.e. Equation 2.1) with the information from Tables 2.1 and 2.2.

$$M_V(max) = 2.54 \log t_3 - 11.99 \quad (4.4)$$

The distances and absolute magnitudes shown in Table 4.2 are calculated from the following relations

$$\log d = \frac{V - M_V(max) + 5 - A_V}{5} \quad (4.5)$$

where V is the apparent magnitude presented in Table 4.1, $M_V(max)$ is maximum absolute magnitude calculated from the MMRD relation from Equation 4.4, and A_V is the extinction from the literature or extinction maps mentioned above.

The parameters including absolute magnitudes, A_V , and distances are presented in Table 4.2. Resulting calculated absolute magnitudes were plotted in CMDs. Figure 4.2 shows an optical CMD of 10 novae observed by LT compared to Hipparcos data taken from Perryman & ESA (1997).

Figure 4.2 is the standard CMD with the most commonly used filters. However B and V are strongly affected by the accretion disk, unless the secondaries are particularly bright or the systems are very close to edge-on. According to Darnley et al. (2012), typical RG-Novae are interdispersed among SG-Novae while MS-Novae do appear separately on the blue side of the main-sequence track. Figure 4.2 implies there are 4 RG-Novae (T CrB, V3645 Sgr, V749 Oph and FS Sct), 2 MS-Novae (V445 Pup and V368 Aql), and 4 RG/SG-Novae (V2487 Oph, CI Aql, V445 Pup and V3964 Sgr).

Table 4.2: The distances (in kpc) of targets calculated from each extinction map

Parameters	TCrB	V2487 Oph	CI Aql	AR Cir B	V3964 Sgr	V3645 Sgr
$M_{Vmax-MMRD}$	-10.01	-9.64	-8.18	-5.593	-8.17	-5.70
$EW(D1+D2)$ (Å)	2.91	2.3	2.13	5.4	3.39	3.41
A_V R&F09	0.01±0.2	1.7±0.2	5.8±0.2	5.8±0.2	1.6±0.2*	1.3±0.2*
A_V Dob05	-	0.46±0.01	1.45±0.01	1.64±0.01	0.91±0.01	0.64±0.01
A_V Sch98	0.20±0.09	2.31±0.09	11.55±0.09	15.81±0.09	2.03±0.09	1.84±0.09
A_V Nec80	-	-	~3.4	~2.5	-	-
A_V from $EW(Na I)_1$	1.43	1.12	1.02	2.64	1.64	1.67
A_V from $EW(Na I)_2$	4.46	3.50	3.25	8.40	5.24	3.63
A_V known ^a	0.3±0.3*(1)	1.6±0.6*(1)	2.6±0.9*(1)	~3.5*(4)	-	1.209(2)
d_{known} (kpc)	0.9±0.2(1)	12.0 ⁺¹³ _{-0.2} (1)	5.0 ⁺⁵ _{-2.5} (1)	4.5±0.5(4)	-	-
M_V^b	0.9±0.8	2.19 ^{-0.8} _{-0.4}	0.1±0.6	-	0.5±0.2	-
$M_B - M_V^b$	1.6±0.1	0.3±0.2	0.3±0.3	-	0.5±0.1	-
Parameters	V794 Oph	V368 Aql	EU Set	CN Vel	LZ Mus	V888 Cen
$M_{Vmax-MMRD}$	-6.04	-8.86	-7.87	-4.62	-9.25	-7.03
$EW(D1+D2)$ (Å)	-	0.64	4.7	0.59	3.07	1.9
A_V R&F09	2.802±0.2	1.1±0.2	2.0±0.2	0.3±0.2*	1.5±0.2*	1.6±0.2*
A_V Dob05	1.549±0.01	0.38±0.01	1.11±0.01	0.24±0.01	0.71±0.01	0.37±0.01
A_V Sch98	3.336±0.09*	2.10±0.09	3.34±0.09	0.74±0.09	3.44±0.09	5.37±0.09
A_V Nec80	-	-	-	-	-	-
A_V from $EW(Na I)_1$	-	0.28	2.29	0.25	1.49	0.90
A_V from $EW(Na I)_2$	-	0.90	7.32	0.81	4.74	2.88
A_V known ^a	-	2.387*(2)	2.6±0.6*(2)	-	-	-
d_{known} (kpc)	-	-	5.1±1.7 (5)	-	-	-
M_V^b	-0.10±0.09	2.1±0.1	-	-	-	-
$M_B - M_V^b$	1.1±0.1	-0.12±0.06	-	-	-	-

Notes: ^a A_V known were derived from $A_V = 3.1 \times E(B - V)$ and $A_B = A_V \times 1.31$ for the Galactic novae.

^b M_V and $M_B - M_V$ calculated from the selected (*) A_V are plotted in Figures 4.2 and 4.3.

* Selected A_V for the calculated absolute magnitude which is therefore plotted in the CMDs and used to deredden spectra.

References: (1) Schaefer (2010), (2) Weight et al. (1994), (3) Goranskij et al. (2010), (4) Duerbeck & Grebel (1993), (5) Duerbeck (1981).

We also made use of archival data from the Two Micron All Sky Survey (2MASS, Cutri et al. (2003))² to search for a potential infrared component of the 16 target novae. Such plots are expected to focus strongly on the secondaries which are expected to dominate the emission. The plot in Darnley et al. (2012) shows there is a clear separation between the RG-Novae and the MS-Novae, and possibly a small distinct region belonging to the SG-Novae.

Comparing the positions of our novae on the NIR CMD to those presented in Darnley et al. (2012), Figure 4.3 indicates that there are 10 RG-Novae (T CrB, V749 Oph, FS Sct, V2487 Oph, EU Sct, V3964 Sgr, AR Cir, V1330 Cyg, LZ Mus and V445 Pup), 3 MS-Novae (V445 Pup, V368 Aql and V3645 Sgr), and 3 SG-Novae (CI Aql, CN Vel and V888 Cen).

The commonalities and discrepancies between results of spectral type determined from Figures 4.2 and 4.3 are discussed in Section 4.6 below.

4.5 Spectral Analysis to Determine Luminosity Class and Spectral Type

The dereddened spectra were first subjected to the analysis to distinguish the luminosity class of main-sequence (V class), sub-giants (IV class) and giants (III class). This analysis includes the measurement of $EW(\text{CaT})$ ³ that yields $\log g$ (Jones et al., 1984; Mallik, 1997) as shown in Figure 4.4, the measurement diagram of Na I 8190 index versus TiO 8465 index (Slesnick et al., 2008) as shown in Figure 4.5, and the identification of indicators from specific lines.

Specific spectral lines that are usually used to indicate either the spectral class or luminosity class including Mgb, MgH, Na I, Ca I, CaH, VO and K I (see Table 4.4 for detail) are also identified in each system.

² Available online at <http://irsa.ipac.caltech.edu/>

³ $EW(\text{CaT})$ is the sum of EW of Ca II at 8498Å 8542Å 8662Å (Jones et al., 1984; Mallik, 1997)

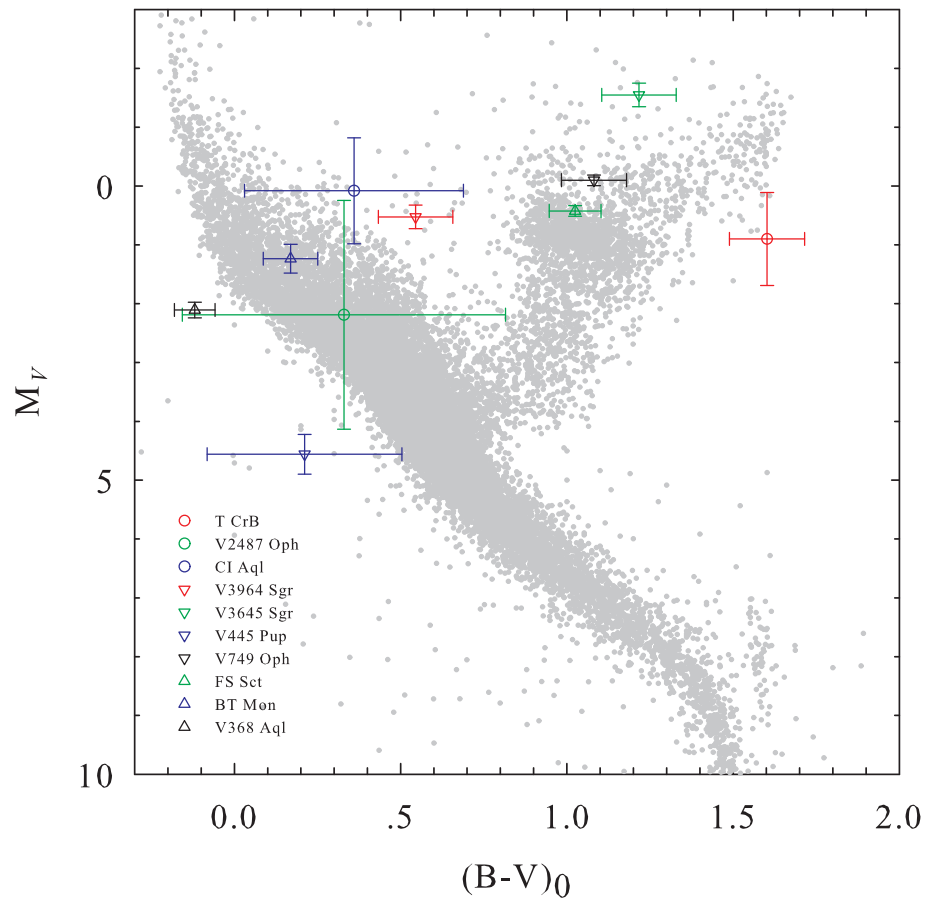


Figure 4.2: Optical CMD showing 10 targets compared with stars plotted from the *Hipparcos* data set. The positions of the novae shown in Table 4.2 using the selected extinction for each object are plotted.

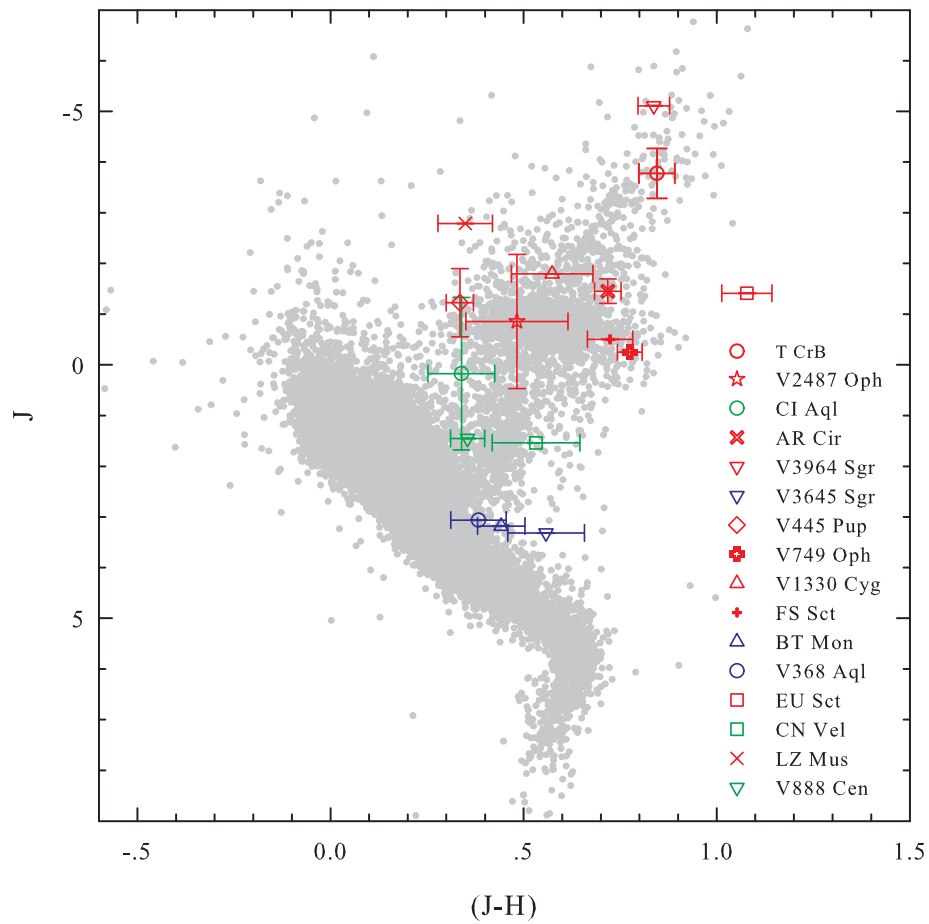


Figure 4.3: Near-infrared CMD showing 16 targets compared with stars generated by cross-correlating the *Hipparcos* and 2MASS catalogues. The positions of the novae shown in Table 4.2 using the selected extinction for each object are plotted.

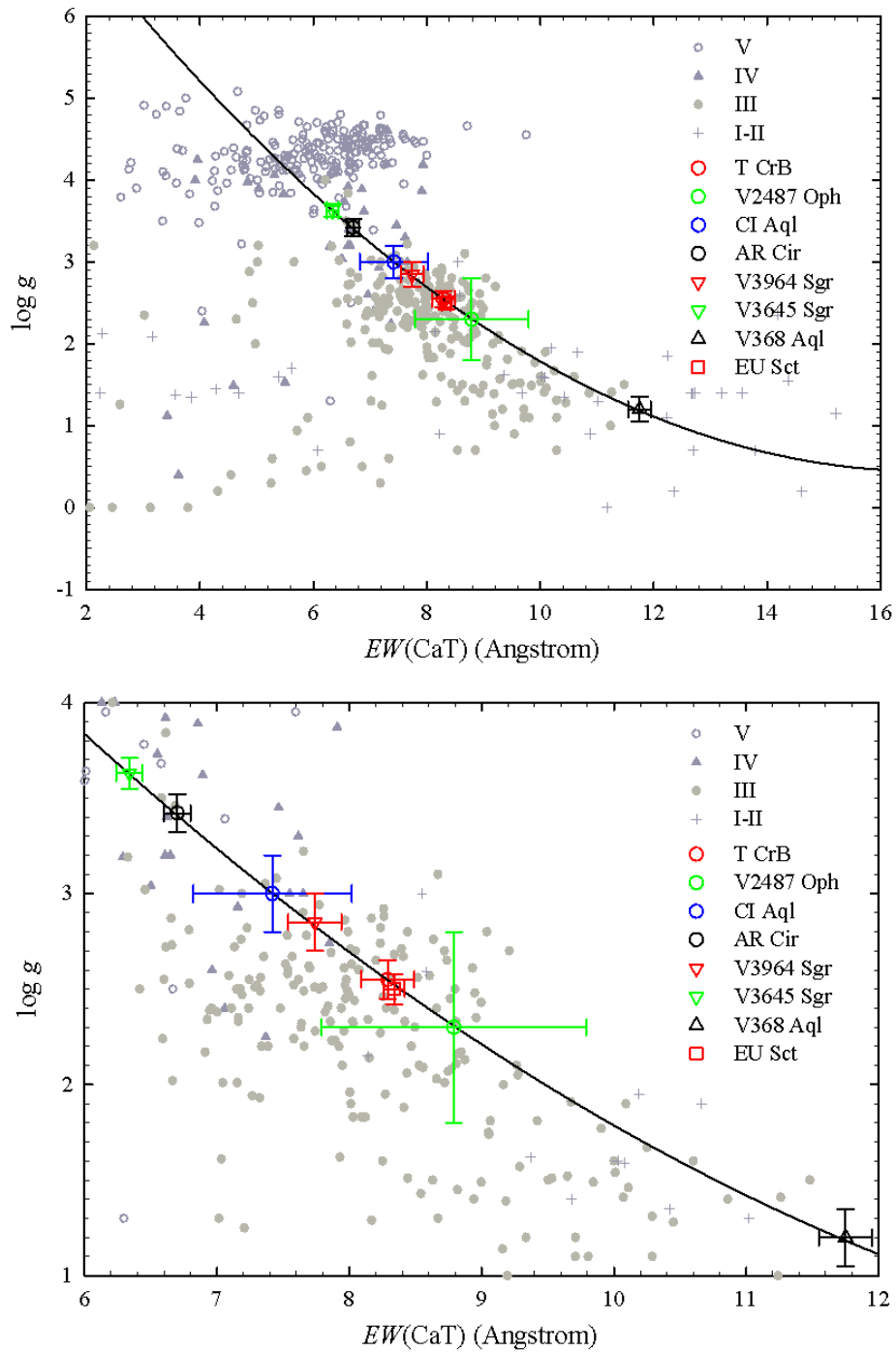


Figure 4.4: The relationship between $EW(\text{CaT})$ and $\log g$ of objects in Class V (open circles), IV (closed triangles), III (closed circles), I-II (plus signs). Data from Jones et al. (1984) and Mallik (1997). The bottom panel is the zoomed-in version of the top panel. Relative positions of our target stars are noted.

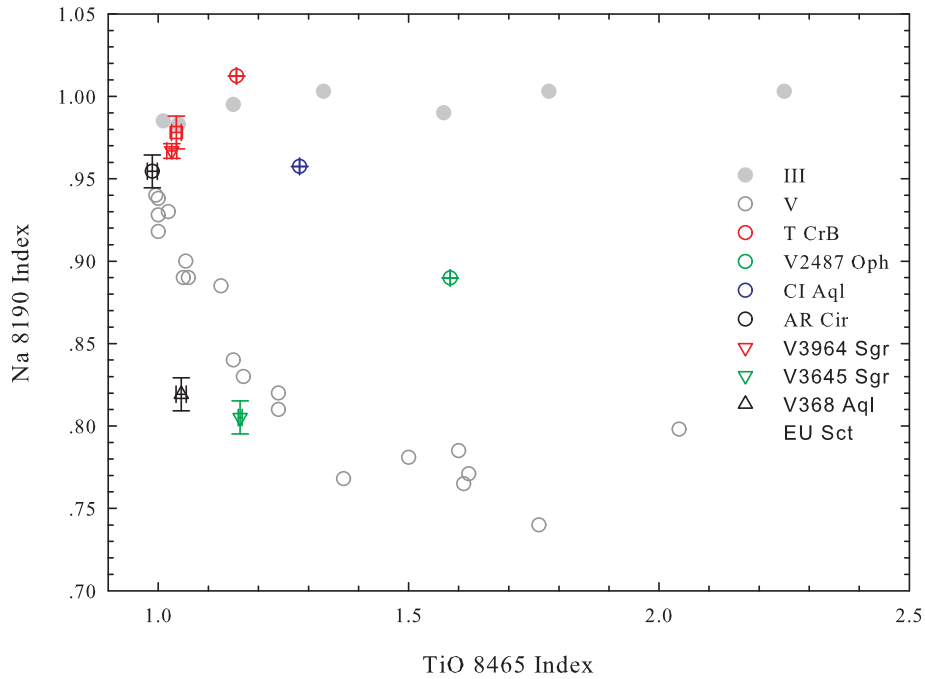


Figure 4.5: The relationship between the gravity-sensitive Na 8190 index and the temperature-sensitive TiO 8465 index of object class V (open circles) and III (closed circles) given by Slesnick et al. (2008). Relative positions of our target stars are noted.

Once the luminosity class is determined, our determination of spectral types for giant secondaries in these novae relies on the measurement of an absorption index, defined as the depth of a feature at a wavelength λ relative to an interpolated continuum point (O’Connell, 1973). Thus, index

$$[I]_{\lambda} = -2.5 \log \left(\frac{F_{\lambda}}{[I_{\lambda_1} + (F_{\lambda_2} - F_{\lambda_1}) \times (\lambda - \lambda_1) / (\lambda_2 - \lambda_1)]} \right) \quad (4.6)$$

where λ_1 and λ_2 are continuum wavelengths, and F_{λ} is the flux in a bandpass centered at λ .

O’Connell (1973) noted that TiO bands at 6180Å and 7100Å are sensitive to temperature, and Sharpless (1956) showed that a VO band at 7865Å appears in giants cooler than ~M5, and suggested that the Na I infrared doublet at 8181Å and 8195Å potentially is a good luminosity discriminant among M stars. Using these correlations,

we therefore adopted four indices proposed by Kenyon & Fernandez-Castro (1987) to measure the molecular and atomic absorptions:

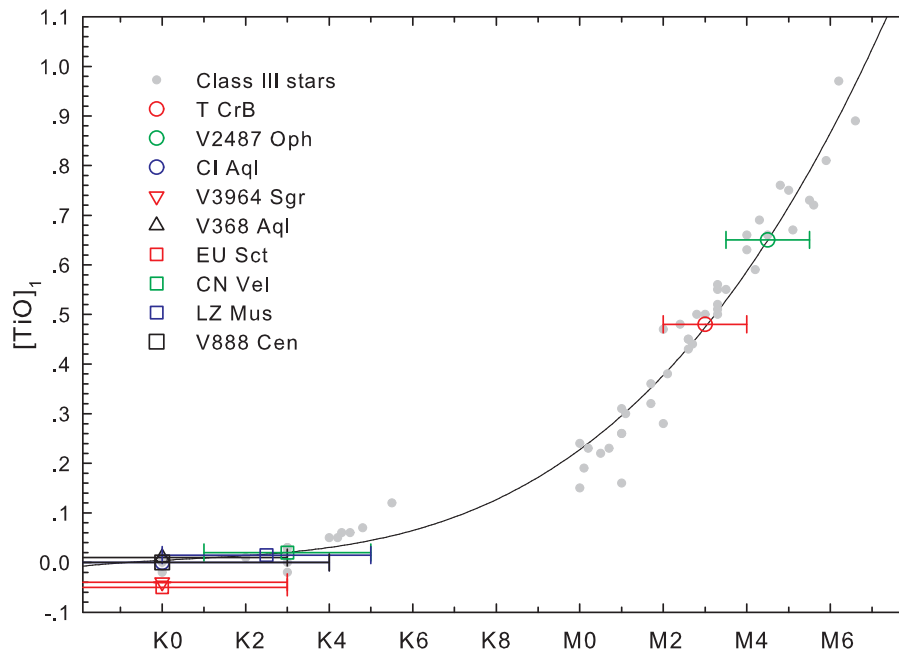


Figure 4.6: Dependence of $[TiO]_1$ on spectral type for giants (closed grey circles) given by Slesnick et al. (2008). Relative positions of our target stars are noted.

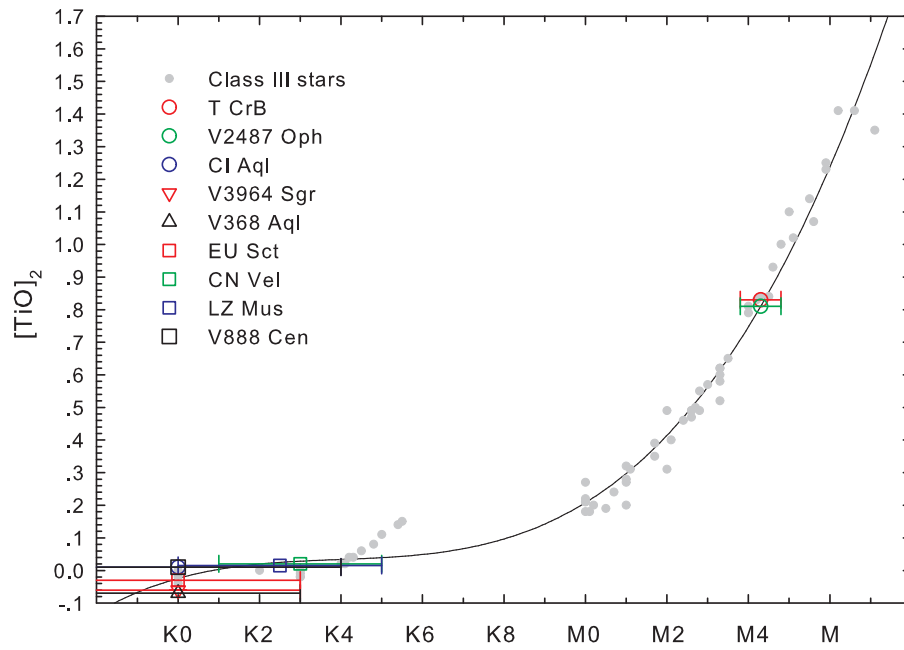
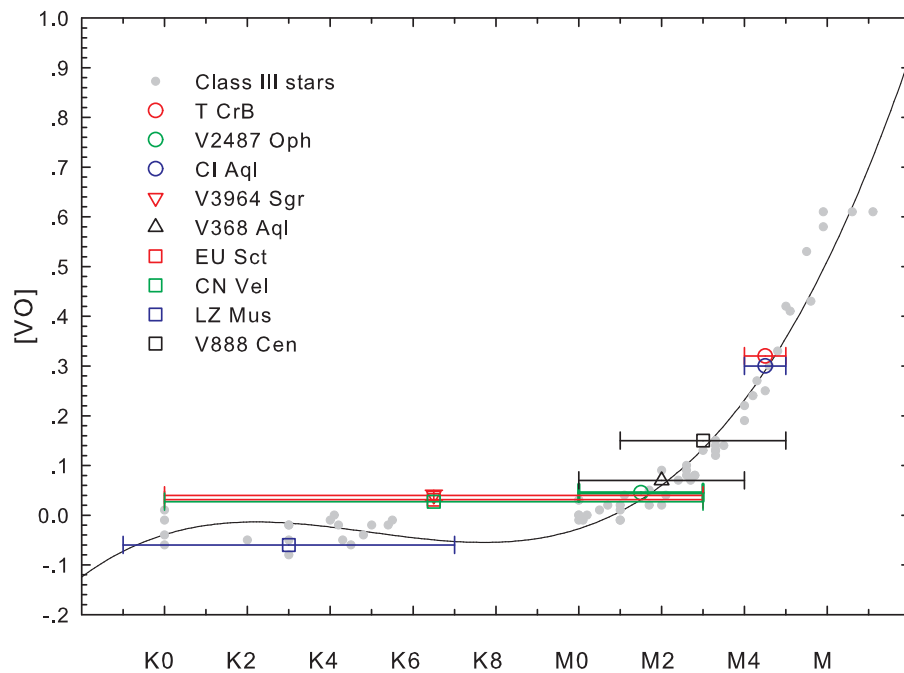
$$[TiO]_1 = -2.5 \log \left(\frac{F_{6180}}{[F_{6125} + (F_{6370} - F_{6125}) \times (6180 - 6125) / (6370 - 6125)]} \right) \quad (4.7)$$

$$[TiO]_2 = -2.5 \log \left(\frac{F_{7100}}{[F_{7025} + (F_{7400} - F_{7025}) \times (7100 - 7025) / (7400 - 7025)]} \right) \quad (4.8)$$

$$[VO] = -2.5 \log \left(\frac{F_{7865}}{[F_{7400} + (F_{8050} - F_{7400}) \times (8050 - 7865) / (8050 - 7400)]} \right) \quad (4.9)$$

$$[Na] = -2.5 \log \left(\frac{F_{8190}}{[F_{8050} + (F_{8400} - F_{8050}) \times (8400 - 8190) / (8400 - 8050)]} \right) \quad (4.10)$$

The dependence of the four indices $[TiO]_1$, $[TiO]_2$, $[VO]$ and $[Na]$, on spectral types is presented in Figures 4.6, 4.7, 4.8 and 4.9, respectively. The $[Na]$ distinguishing hot giants ($<M3$) from cooler giants, can also provide an independent check on spectral types derived from the $[TiO]$ indices as shown in Figure 4.10.

Figure 4.7: As Figure 4.6 but for the $[\text{TiO}]_2$.Figure 4.8: As Figure 4.6 but for the $[\text{VO}]$.

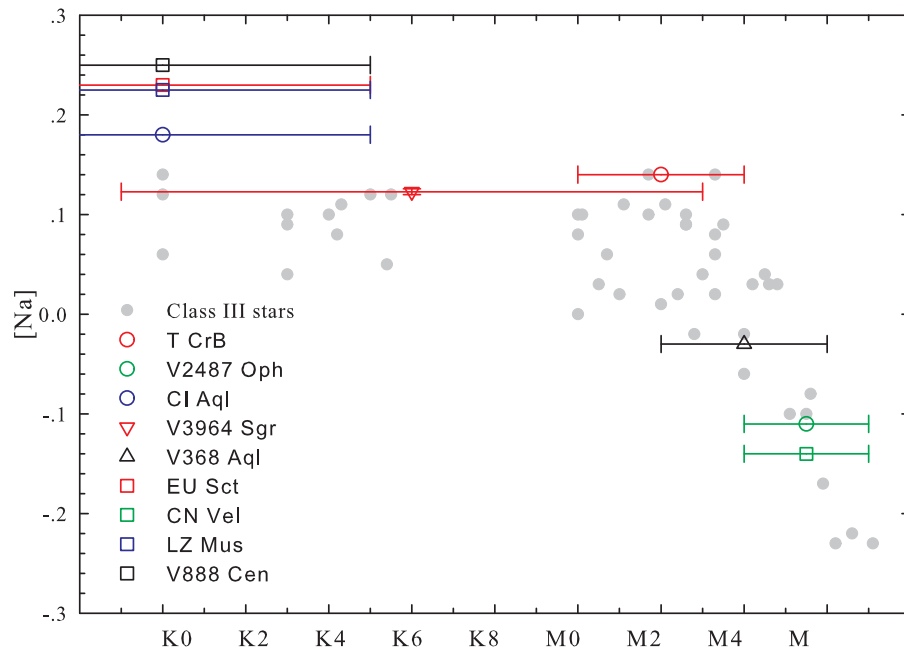


Figure 4.9: As Figure 4.6 but for the [Na].

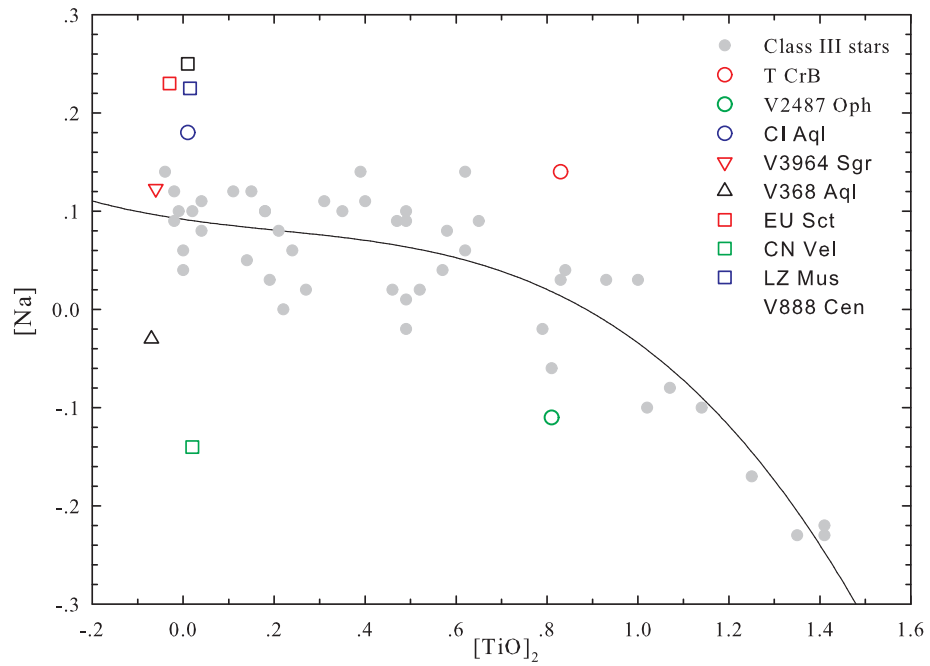


Figure 4.10: Dependence of [Na] on $[TiO]_2$ for giants (closed grey circles) given by Slesnick et al. (2008). Relative positions of our target stars are noted.

On the other hand, for luminosity class V stars, the determination of spectral type was done by comparing our spectra to a spectral library⁴.

4.6 Spectroscopic Observations and Results

The spectroscopic observations and results for each individual nova are described below with the overall summary towards the end of this Section. All figures of individual objects for classification presented in this Chapter are non-dereddened otherwise the spectral features used would be more difficult to see clearly. However, for the analysis, all spectra were dereddened using approximate value of $E(B - V)$ as given in the text.

4.6.1 T CrB

T CrB ($\alpha=15^h59^m30^s.161$, $\delta=+25^\circ55'12''.59$), a RN with previous recorded outbursts in 1866 and 1946, is designated to harbour an M3 III secondary star (Anupama, 2008). When we compared our spectrum to the those taken in 1984 by Kenyon & Garcia (1986) and during 1990-1998 by Anupama & Mikołajewska (1999), we found that the overall feature of strong absorption TiO bands remains similar but our spectrum shows much less in emission line fluxes of both Hydrogen Balmer series and He I and absorption in CH G-band at 4285-4315Å than that taken by Kenyon & Garcia (1986) but similar to one of those taken (on 1995 Apr 13.8) by Anupama & Mikołajewska (1999). With P_{orb} of 227.67 days, Anupama & Mikołajewska (1999) suggested that the considerable variations of optical emission line fluxes are due to the significant brightening of the optical continuum which is the result of the activity on the WD.

Figure 4.11 shows that our spectrum has no CaH 6385Å to confirm that there is no dwarf in the system. The insets show the presence of CN and G-band and weak K I lines. The K I 7665Å, 7699Å lines and Na I D lines (which are strong in dwarfs) are also weak and therefore suggest a giant secondary star. The visibility of the strong TiO

⁴ Available at <https://www.cfa.harvard.edu/~pberlind/atlas/atframes.html>

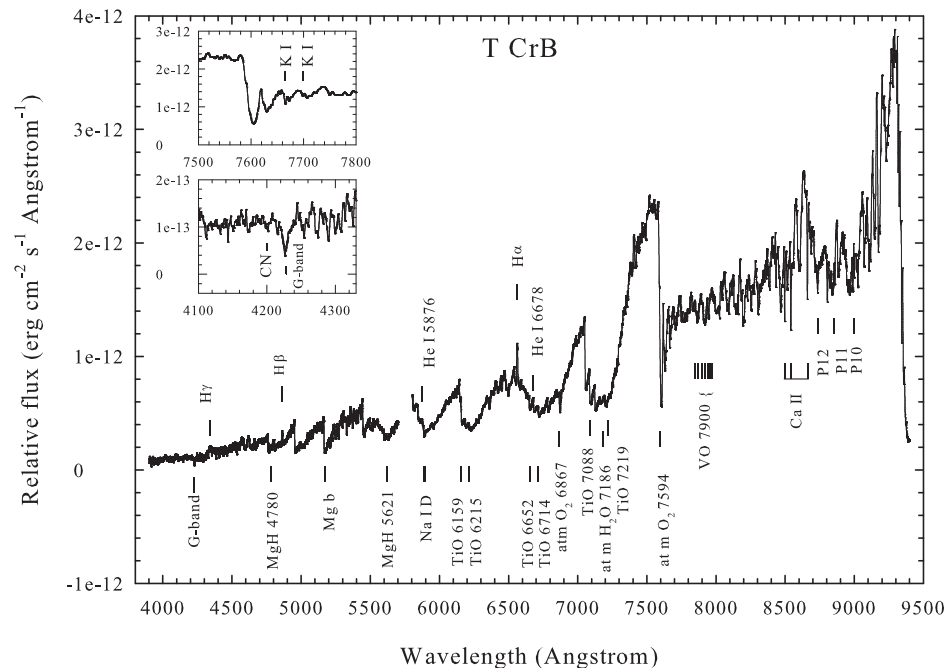


Figure 4.11: Relative flux-calibrated and non-dereddened LT spectrum of T CrB.

band at 6159Å (seen in all spectra by K5), 6652Å and 6714Å (visible from M0) and 7219Å (seen by M1) indicates a spectral type later than M0. Figures 4.4 and 4.5 both confirm again a class III star.

The $E(B - V) = 0.1 \pm 0.1$ ($A_V = 0.3 \pm 0.3$) given in Schaefer (2010) is adopted to deredden the spectrum. As a result, the derived $[\text{TiO}]_1 = 0.48$ and $[\text{TiO}]_2 = 0.83$ are in good agreement with those found by Anupama & Mikołajewska (1999) ($[\text{TiO}]_1 = 0.49-0.59$, $[\text{TiO}]_2 = 0.64-0.81$), but the $[\text{VO}] = 0.32$ and $[\text{Na}] = 0.15$ are greater than those of Anupama & Mikołajewska (1999) ($[\text{VO}] = 0.16$, $[\text{Na}] = -0.03$). As a result, our spectrum indicate a spectral type of M4III from all four indices while Anupama & Mikołajewska (1999) propose a broader range of M3-M4III. In this case, the more confidence of spectral type range should be placed on that derived from $[\text{TiO}]$ and $[\text{Na}]$ rather than $[\text{VO}]$ since TiO bands are strong but VO at 7865Å is weak here. We note that errors in index measurement are very small so they are not presented here. Meanwhile the ranges of indices presented from the literature were derived from the measurements at several different epochs.

Our classification from [TiO] and [Na] is in the range of M3.5-M3.8III which is in good agreement with the position of T CrB in both optical and NIR CMDs as shown in Figure 4.2 and 4.3, respectively where the nova is at the top of RGB.

4.6.2 V2487 Oph

V2487 Oph ($\alpha=17^h31^m59^s.8$, $\delta=-19^\circ13'56''.0$), having two previous recorded outbursts in 1900 and 1998, is identified as a U Sco type nova from the analysis of the light curve of the 1998 outburst by Hachisu et al. (2002). $P_{orb} \sim 1$ day indicates the presence of an evolved secondary (Anupama, 2013) which should be \sim K2 sub-giant for a typical U Sco type RN (Kahabka et al., 1999; Schaefer, 2010). While the U Sco type RNe are suggested to exhibit dominant He II lines at quiescence (Hanes, 1985), we note here that our spectrum shows prominent emission lines of CIII/NIII 4645Å and He II 4686Å that rival the Balmer emission lines, as shown in Figure 4.12. The insets also show a presence of CN and G-band and weak K I lines indicating a late-type evolved secondary star.

However, by looking at the system in NIR colours, Darnley et al. (2012) found that the system is consistent with one containing a secondary that is climbing the RGB and concluded that V2487 Oph is an RG-Nova with a less luminous/evolved secondary than that of RS Oph or T CrB.

Our spectrum shows neither CaH 6385Å nor Ca I 6103Å, 6122Å, 6162Å, and very weak Na I D at 8183Å and 8194Å lines and K I 7665Å and 7699Å (see the inset of Figure 4.12). Thus the secondary cannot be a dwarf but a more evolved star. Figure 4.4 indicates a giant while Figure 4.5 places the secondary among the sub-giants. Nevertheless, the spectral lines themselves place more constraint to the giants since the VO 7865 (which appears in only giants cooler than \sim M5) is present, although marginally. Moreover, TiO and VO bands are visible. The secondary star however should not be later type than M7III due to the absence in VO 6478Å and 6532Å.

The $E(B-V) = 0.5 \pm 0.2$ ($A_V = 1.6 \pm 0.6$) given in Schaefer (2010) is adopted to deredden

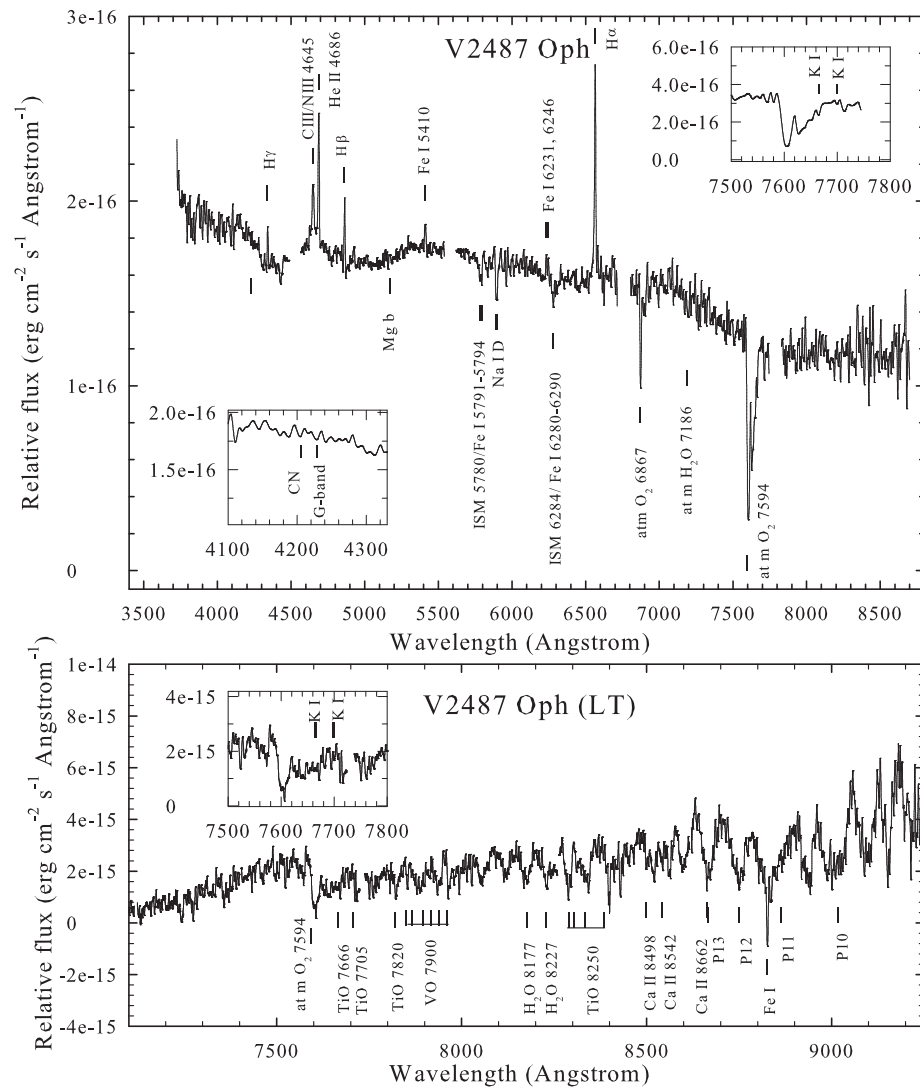


Figure 4.12: Relative flux-calibrated spectrum of V2487 Oph without dereddening correction. The nova spectra were obtained from SALT (top, binned every 5Å) and LT (bottom).

the spectrum. We note that, for all objects cooler than \sim M4, the classification from [VO] is not reliable since the absorption is negligible and the [Na] index which is a good luminosity discriminant among M stars should be used instead (Kenyon & Fernandez-Castro, 1987). As a result, the derived [TiO]₁, [TiO]₂ and [Na] indices agree to indicate an M4-M4.8III (or possibly IV) star.

4.6.3 CI Aql

CI Aql ($\alpha=18^h52^m03^s.57$, $\delta=-01^\circ28'39''.4$) is occasionally grouped among T Pyx type RNe (MS-Nova) due to the similarity in the light curves and outburst spectra which resemble Fe II CNe (Darnley et al., 2011). However it is grouped as a U Sco type RN (SG-Nova) due to its orbital period of 0.6 day and position on a NIR CMD and the short recurrence time of the outburst also indicated the system is a member of the U Sco type RNe (Darnley et al., 2012).

Similar to the V2487 Oph case, the $EW(\text{CaT})$ in Figure 4.4 indicates the secondary star as a giant while the Na I versus TiO 8465 indices in Figure 4.5 indicate somewhat a sub-giant. However, in the case of CI Aql, the position in the indices diagram is much closer to that of giants than main-sequence stars.

Our spectrum shows no CaH 6385Å nor Na I 8183Å and 8195Å (i.e. the MS-Nova is ruled out). However, the weak Ca I 6162Å line (which is enhanced in M dwarfs) is still seen and molecular TiO bands are visible. These may possibly tend towards indicating a sub-giant.

The $E(B - V) = 0.8 \pm 0.3$ ($A_V = 2.6 \pm 0.9$) given in Schaefer (2010) is adopted to deredden the spectrum. As a result, the derived $[\text{TiO}]_1$, $[\text{TiO}]_2$ and $[\text{Na}]$ indices agree to indicate a G6-K4IV star. This is in good agreement with CMD in Figure 4.3 where CI Aql places itself in the sub-giant region. We note however that Sahman et al. (2013) estimate $M_2 = 2.3 \pm 0.2 M_\odot$ and $R_2 = 2.07 \pm 0.06 R_\odot$ implying a slightly evolved A type star, while our spectrum shape cannot be from an A-type star, neither can its position on the CMDs.

We also compared our spectrum to that observed using the Multiple Mirror Telescope (MMT) at Mount Hopkins, Arizona, in 1992 as shown in Figures 4.12 and 4.14. The two spectra are similar in overall features, but with much clearer emission lines of CIII/NIII 4645Å and He II 4686Å in the SALT spectrum.

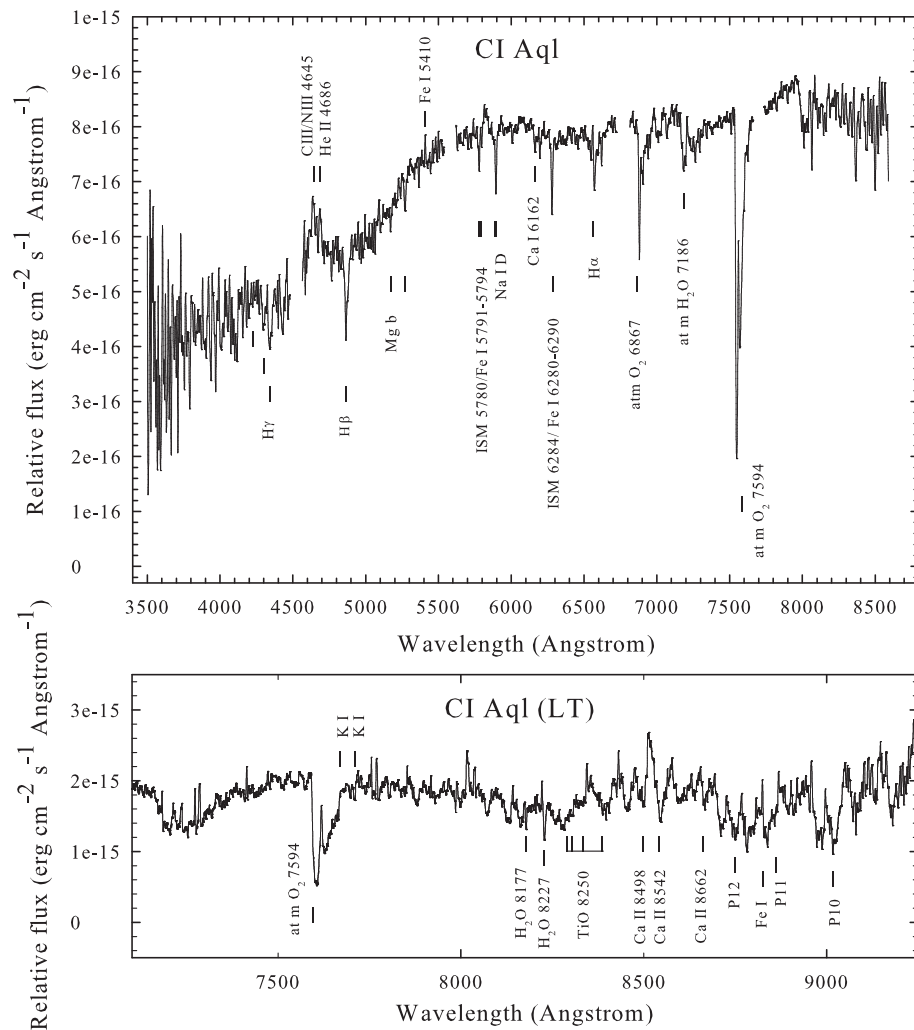


Figure 4.13: As Figure 4.12 but for CI Aql.

4.6.4 AR Cir

AR Cir ($\alpha=14^h48^m09^s.53$, $\delta=-60^\circ00'27''.5$, coordinate designated in published nova catalogues) is an optical pair with a separation of 3.1 arcsec comprising a 14-mag K3V star (AR Cir A) and the 18-mag ex-nova (AR Cir B) with a very red continuum (Duerbeck & Grebel, 1993). The light curve classifies the nova as a very slow nova and probably a symbiotic star (Bianchini et al., 1991). It is suggested to possibly be a Recurrent Nova by Harrison (1992) due to the low outburst amplitude and the IR colours which are those of an unreddened M0III star which later proved to be dominated effectively by component A. The spectrum of AR Cir B given by (Duerbeck & Grebel,

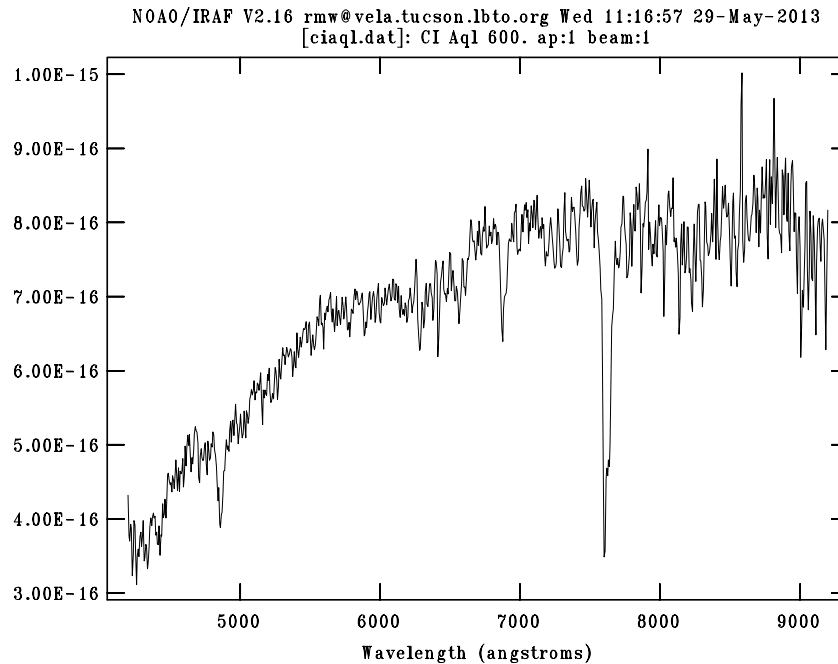


Figure 4.14: Calibrated MMT spectrum of CI Aql obtained by the 4.5 m MMT on 1992 Sep 3.

1993) showing the medium-strength H and He II emission lines which are often found in the CNe allowed them to conclude that the nova is indeed a Classical Nova.

Our spectrum (Figure 4.15) resembles that of component A, which is not the nova, given in Duerbeck & Grebel (1993) with the presence of late-type indicators including CN 4200Å and G-band at around 4285-4315Å (Griffin & Redman, 1960) which are shown in the inset. Broad Mg b and strong Na I 5890Å, 5896Å, 8183Å, 8195Å, and Ca I 6162Å indicate a dwarf star. However, the CaH 6385Å which is a dwarf indicator is undetected or very weak. The VO 6478Å, 6532Å, and 7865Å are absent, therefore it is a MS not cooler than ~M5. Figures 4.4 and 4.5 also confirm again the class V star designation.

Since it turns out that our slit was not placed correctly in order to observe AR Cir B, but AR Cir A instead (even though the input coordinate is AR Cir B), we do not compare the resulting spectral classification to that plotted on the CMDs. For AR Cir B, we adopted the colour $B - V = 1.25 \sim 0.2$, $V = 18.31 \pm 0.03$, $A_V \sim 3.5$ and $d \sim 4-5$ kpc given in Duerbeck & Grebel (1993) to plot the CMDs yielding the position of an

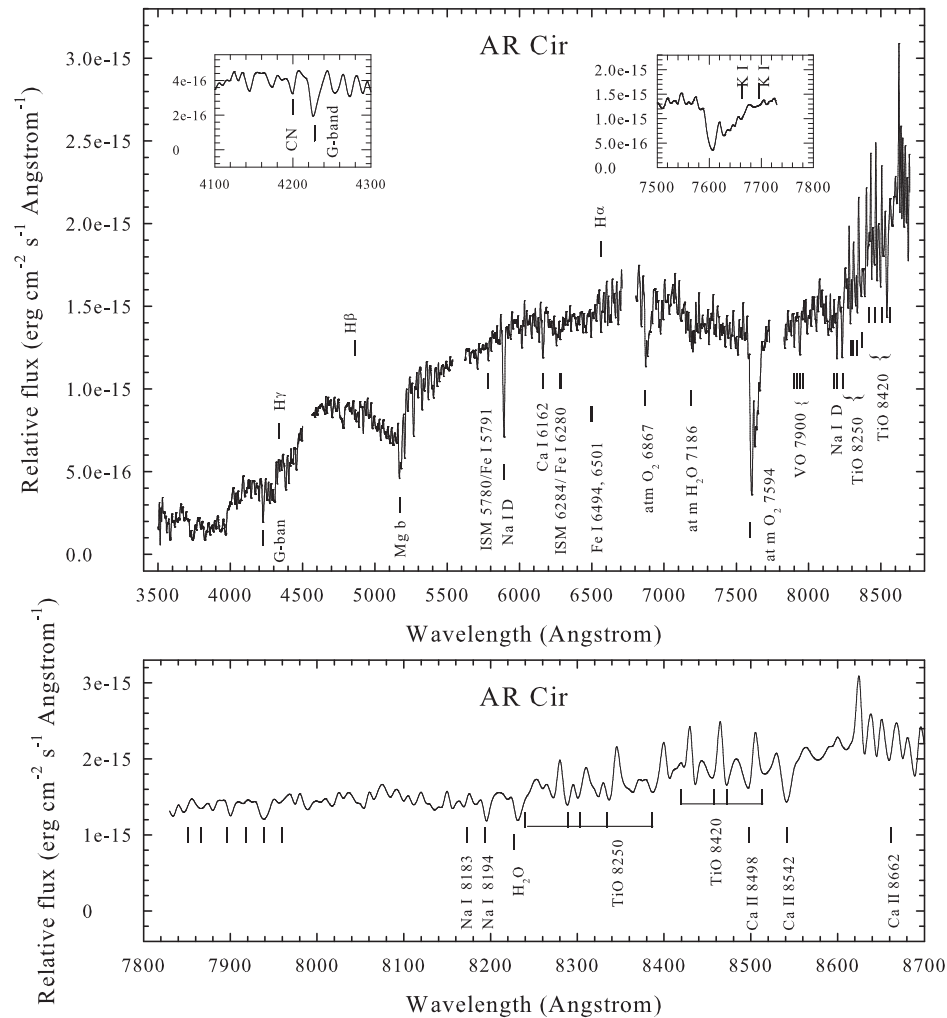


Figure 4.15: Relative flux-calibrated SALT spectrum of AR Cir without dereddening correction. The spectrum was binned every 5Å. Bottom panel is the zoomed-in version of the top panel. Small panels show line indicators e.g. CN, G-band and K I lines.

RGB star. Meanwhile we adopted $A_V \sim 0.7$ and $d \sim 250$ pc for AR Cir A (Duerbeck & Grebel, 1993) to deredden the spectrum resulting in the classification of this object as a K0-K3V star.

By investigation of the 2MASS data set, we now refine the true coordinates of AR Cir A as $\alpha = 14^h 48^m 09^s.53$, $\delta = -60^\circ 00' 27''.5$) and AR Cir B as $\alpha = 14^h 48^m 08^s.97$, $\delta = -60^\circ 00' 23''.3$.

4.6.5 V3964 Sgr

V3964 Sgr ($\alpha=17^h49^m42^s.34$, $\delta=-17^\circ23'35''.6$) was found on an objective prism plate by Huth (1976) with $m_{pg}\leq 9.4$ in June 1975. The only published spectrum of the nova was taken by Lundstrom & Stenholm (1977) and shows the diffuse enhanced type which is a characteristic for a nova about two magnitude below peak (see Chapter 1). Therefore Lundstrom & Stenholm (1977) suggested that the maximum magnitude of the nova should be around $m_{pg}\sim 7$.

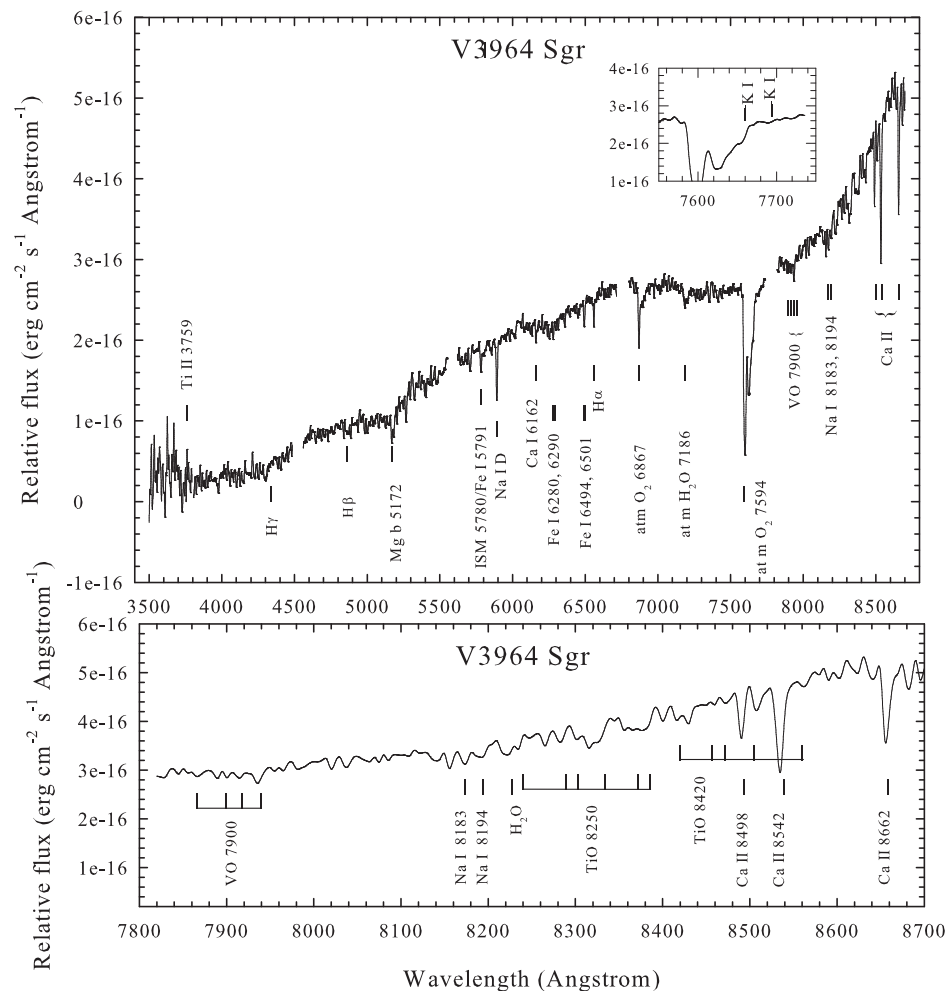


Figure 4.16: As Figure 4.15 but for V3964 Sgr.

Our spectrum (Figure 4.16) still shows the emission line of Ti II as that found by Lundstrom & Stenholm (1977). The absence of both K I absorption lines in the inset and the CaH 6385Å indicate an evolved secondary star. Weak Na I 8183Å, 8195Å

and the absence of VO 7865Å can indicate a sub-giant or a giant hotter than M4). The $EW(\text{CaT})$ (Figure 4.4) and Na I versus TiO indices diagram (Figure 4.5) that it resembles a giant.

The $A_V = 1.6 \pm 0.2$ derived from extinction map of Rowles & Froebrich (2009) is used to deredden the spectrum because a similar value is found from the $EW(\text{Na I})$ method also (see Table 4.2). As a result, the derived $[\text{TiO}]_1$, $[\text{TiO}]_2$ and $[\text{Na}]$ indices agree to indicate a G9-M3III star, also agreeing well with a position at the top of the RGB in the CMDs (Figures 4.2 and 4.3).

4.6.6 V3645 Sgr

V3645 Sgr ($\alpha=18^h35^m49^s.31$, $\delta=-18^\circ41'44''.3$) was discovered in July 1970, roughly 6 months after the outburst which was suspected to be during the winter months of 1969/1970, in an objective prism plate (Mobberley, 2009) with the brightness reaching 12.6 magnitude and fading very slowly ($t_3=300$ days) to 18.0 magnitude at quiescence (Downes et al., 2001).

The system was previously suggested to be a potential Recurrent Nova candidate due to the low amplitude and with NIR colour by Weight et al. (1994). Quiescent light curve and period studies are not yet obtained. The system was noted as a uncertain ID object and Hoard et al. (2002) proposed new coordinates. We confirmed the position proposed by Hoard et al. (2002) is correct.

Weight et al. (1994) adopted $A_V \sim 1.2$ (or $E(B - V) \sim 0.4$ for a distance $\lesssim 2$ kpc) derived from Neckel et al. (1980) but were not totally convinced and suggested the reddening to this nova has been underestimated. Therefore we adopted an $A_V = 1.3 \pm 0.2$ derived from the extinction map of Rowles & Froebrich (2009) to deredden the spectrum because a similar value is found from the $EW(\text{Na I})$ method.

Our spectrum (Figure 4.17) shows the dwarf indicator line CaH 6385Å. This is in good agreement with the classification from $EW(\text{CaT})$ (Figure 4.4), the NaI-TiO indices diagram (Figure 4.5) indicating a class V (or possibly IV) star. The K I absorption

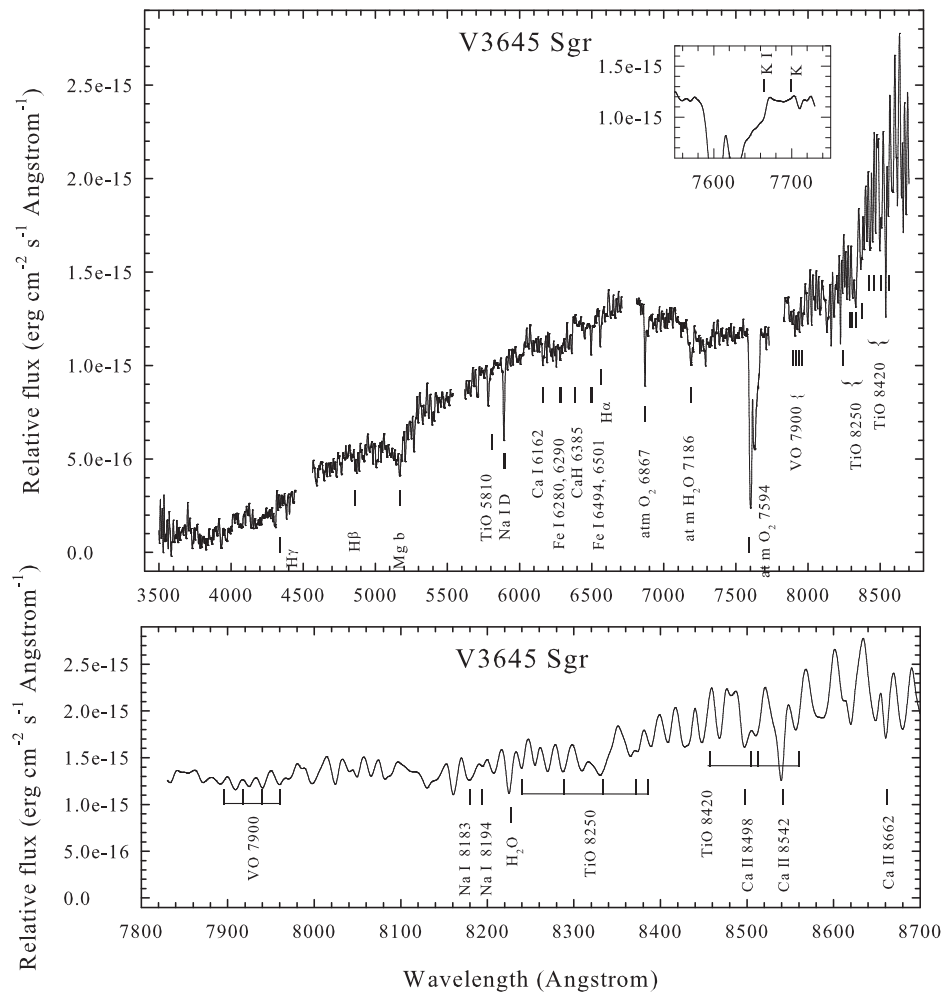


Figure 4.17: As Figure 4.15 but for V3645 Sgr.

however is weak, therefore a class IV secondary cannot be ruled out and is still consistent with the position on the NIR CMD (Figure 4.3). When compared with the library template, we estimate the spectral range to be K1-M1V/IV.

4.6.7 V794 Oph

V794 Oph ($\alpha=17^h38^m49^s.25$, $\delta=-22^\circ50'48''.9$) was suggested as one of the RNe candidates due to its low outburst amplitude by Duerbeck (1988b). Its current identification is also suspected to be incorrect since Woudt & Warner (2003) found no variation in this $V = 17.2$ magnitude star.

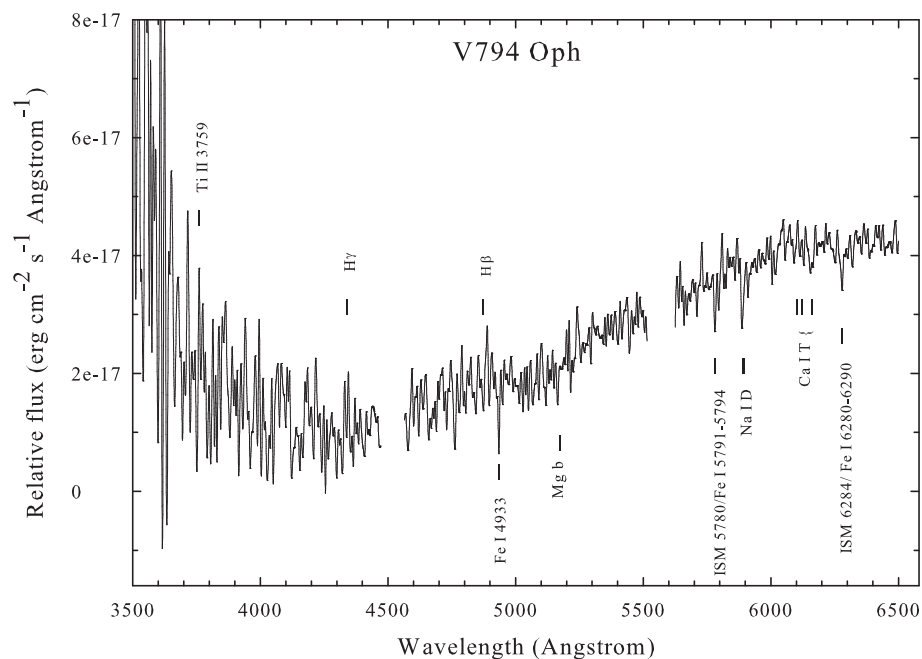


Figure 4.18: Relative flux-calibrated SALT spectrum of V794 Oph in blue region without dereddening correction. The spectrum was binned every 5\AA .

Only our spectrum in the blue is presented here since the SALT observations in the red region were done with the wrong arc files, so the red spectra was dereddened by using the prominent skylines in stead of arc lines. By adopting $A_V = 3.34 \pm 0.09$ given in an extinction map of Schlegel et al. (1998) which is the maximum extinction at the edge of the Galaxy, $EW(\text{CaT})$ was measured in our dereddened spectrum and we can

at least estimate the evolutionary status of the secondary as a giant star (see Figure 4.4) which is consistent with positions on CMDs.

4.6.8 V368 Aql

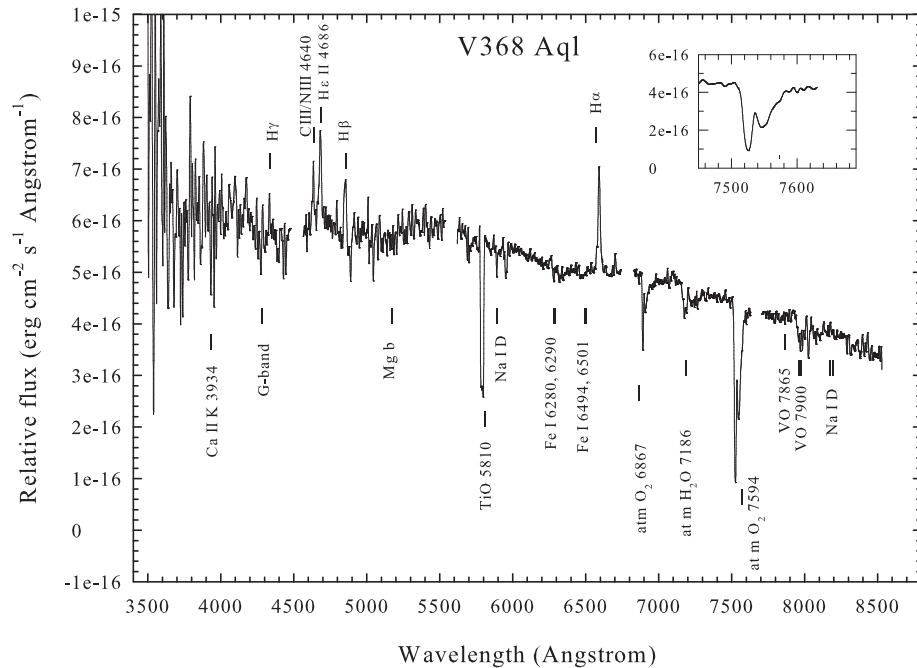


Figure 4.19: Relative flux-calibrated SALT spectrum of V368 Aql without dereddening correction. The spectrum was binned every 5 Å. The inset panel shows the region of the K I lines.

V368 Aql ($\alpha=19^h26^m34^s.46$, $\delta=+07^\circ36'13''.8$) is an eclipsing nova with $P_{orb}=16.57$ hours (Marin & Shafter, 2009). The previous spectrum of the nova was published by Ringwald et al. (1996) but was not of sufficient S/N to tell whether a G-type secondary is present as predicted by Diaz & Bruch (1994) who estimated this from the photometric period study.

We compared our spectrum obtained by SALT in 2010 (Figure 4.19) to those observed by Ringwald et al. (1996) in 1996 and the spectrum observed by Sumner Starrfield using the 3.5m New Technology Telescope (NTT) in 1995 (Figure 4.20). We found that spectra of V368 Aql are all very noisy in the blue with a flat continuum, obvious Ca II K (3934 Å) emission, and He II 4686 Å being stronger than H β and compatible

with $H\alpha$. Our spectrum shows obvious G-band and CIII/NIII 4640-50Å which are not clearly seen in the other two spectra. The behaviour of a flat continuum and strong He II and CIII/NIII emission is reminiscent of that of a dwarf nova (Ringwald et al., 1996).

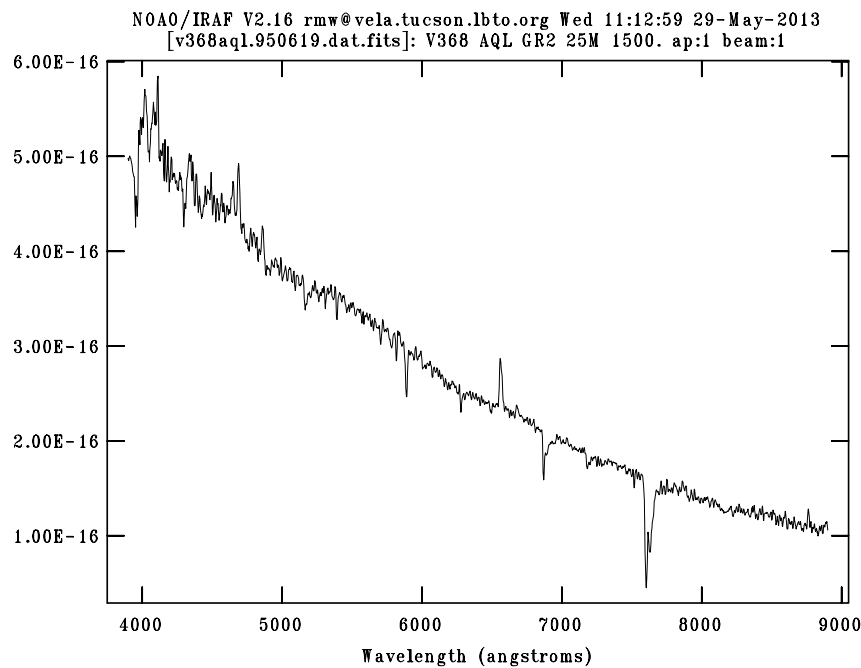


Figure 4.20: Calibrated NTT spectrum of V368 Aql obtained by a 3.5 m NTT with EMMI on 1995 June 19.

Our spectrum shows neither Ca I 6103Å, 6122Å, 6162Å, CaH 6385Å, K I 7865Å, 7699Å (see the inset) nor Na I 8183Å and 8195Å. A dwarf secondary can thus be ruled out. While the Na I 5890Å, 5896Å, weak VO 7865Å, and few lines in the VO 7900Å band are present, it can indicate a sub-giant. This classification of a sub-giant agrees with that seen from the NIR CMD (Figure 4.3) that V368 Aql has just left the main-sequence. However the $EW(\text{CaT})$ places it among giants.

The $A_V \sim 2.39$ ($E(B-V) = 0.77$) given by Weight et al. (1994) was adopted to deredden the spectrum. The $[\text{TiO}]_1$ and $[\text{TiO}]_2$ classified the secondary as a G7-K3IV while the $[\text{VO}]$ and $[\text{Na}]$ indicate M2-M4IV. Although the spectrum show Na I 890Å, 5896Å (which are visible in G-M stars), it also show few lines of VO 7900Å band (which is observed in star later than M7). Moreover, considering the placement of V368 Aql in

Figure 4.10, this implies that our measurement deviates from the proper values and is therefore unreliable. Thus our classification will rely on the G7-K3IV derived from $[\text{TiO}]_1$ and $[\text{TiO}]_2$. This classification as a sub-giant is in line with $P_{orb}=16.57$ hours.

4.6.9 EU Sct

EU Sct ($\alpha=18^h56^m13^s.12$, $\delta=-04^\circ12'32''.3$) was suspected as a potential RN due to its position on the colour-colour diagram by Weight et al. (1994) and due to the derived small ‘optical-IR range’ $R \equiv K - V = 2.6$ which is consistent with a RG secondary star (Harrison, 1992).

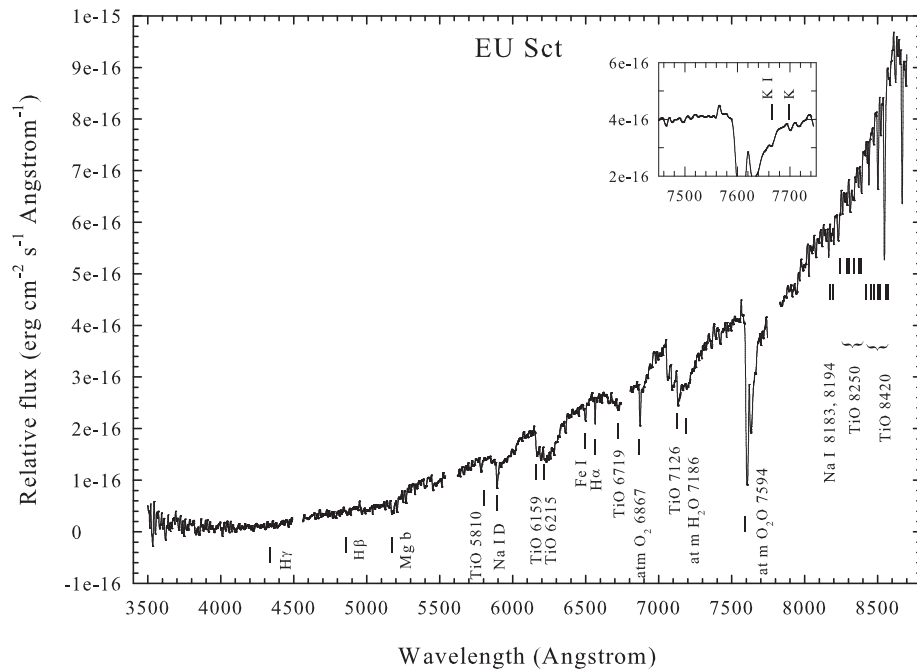


Figure 4.21: As Figure 4.19 but for EU Sct.

Woudt & Warner (2003) suspected an uncertain ID of the system since their observations found no rapid variation in the candidate star (EU Sct) but there is a 19.1 magnitude companion star (EU Sct-comp) at 4 arcsec to the South of candidate star. However, we have inspected the spectra of both positions and confirmed that the current position of EU Sct is correct.

We compared our spectrum obtained by SALT in 2010 (Figure 4.21) to the spectrum observed by Sumner Starrfield using the 3.5m New Technology Telescope (NTT) in 1995 June 18 (Figure 4.22). We found that the two spectra of V368 Aql are very similar in details showing clearly late-type evolve secondary.

An $E(B - V) = 0.84$ used in Weight et al. (1994) and a distance of 5.1 ± 1.7 kpc from Duerbeck (1981) are adopted. Our spectrum shows clearly the late-type secondary with molecular TiO bands. A weak K I absorption also can be seen in the onset. As in the case of V368 Aql, Figure 4.10 indicates an unreliable measurement of [Na]. Therefore the spectral type is determined from $[\text{TiO}]_1$, $[\text{TiO}]_2$ and [Na] which agree on a range of G7-K0III, which is consistent with its position on the NIR CMD.

4.6.10 CN Vel, LZ Mus and V888 Cen

Figures 4.23, 4.24 and 4.25 show spectra for these 3 novae. Only red spectra were obtained properly for CN Vel and V888 Cen. Ultimately, spectra of CN Vel and V888

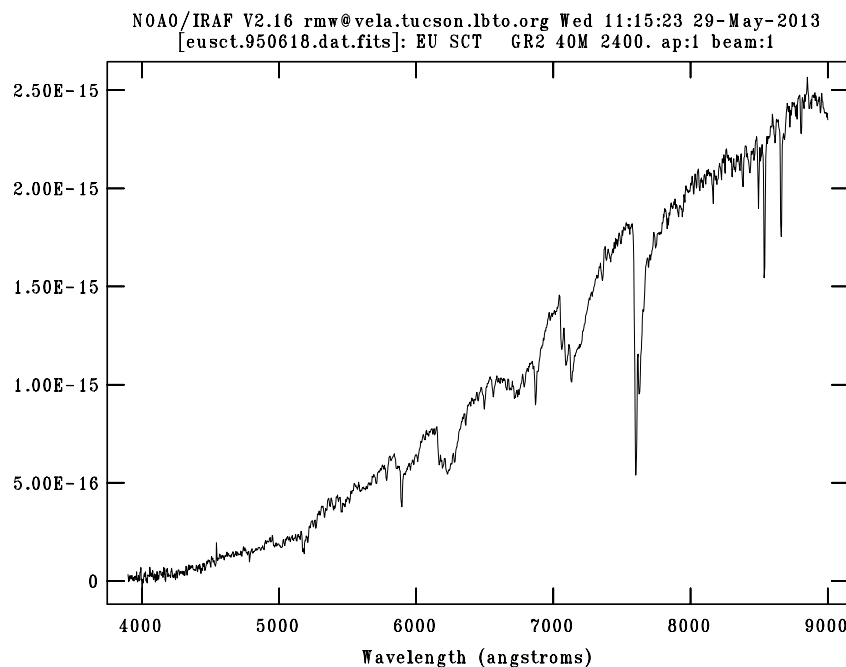


Figure 4.22: Calibrated NTT spectrum of EU Sct obtained by the 3.5 m NTT with EMMI on 1995 June 18.

Cen encounter a shift in wavelength due to the unclearly matched arc line identification process (as mentioned in Chapter 3). In the case of LZ Mus, the exposure times were underestimated making the spectra indistinguishable from the background and too faint to see line features. There was no spectral measurement made for these three novae therefore. Line identification was then done by eye. We may see the main common feature of VO 7900 bands (which is observed in stars later than M7) in these three novae, especially in V888 Cen.

Since Na I 5890Å, 5896Å lines are known to be seen in all G-M stars and greatly enhanced in dwarfs (Turnshek, 1985), a strong absorption line of Na I D in V888 Cen implies that the nova harbours a late-type main-sequence secondary star while CN Vel and LZ Mus might have more evolved late-type secondaries.

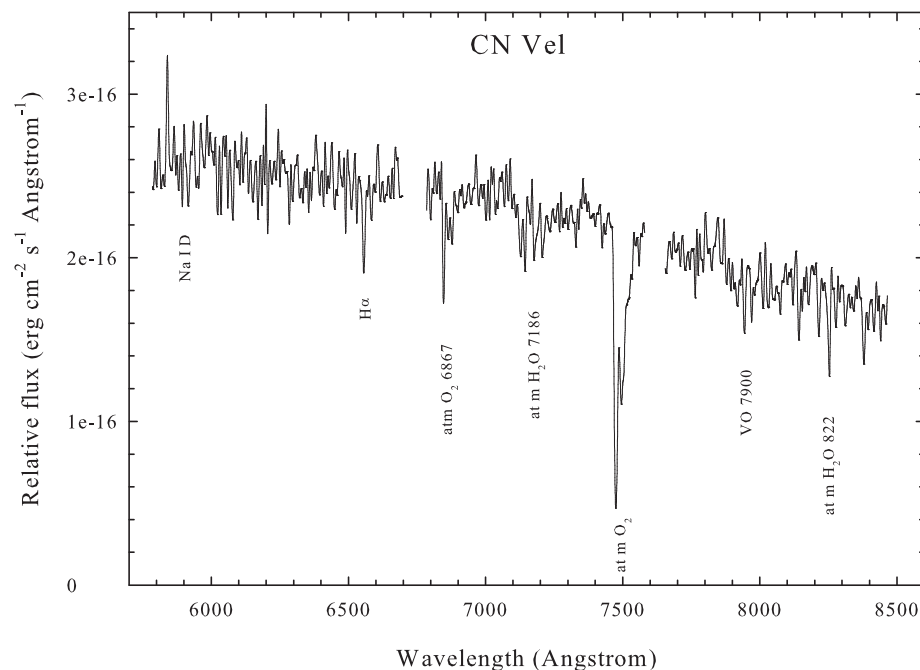


Figure 4.23: Relative flux-calibrated SALT spectrum of CN Vel in red region without dereddening correction. The spectrum was binned every 5Å.

The resulting summary of the $EW(\text{CaT})$ measurement indicating $\log g$ of all targets is presented in Table 4.3 while Figure 4.4 shows the plot of targets with comparison to stars of classes III and V. Table 4.4 summarises specific line indicators found in each target nova. Table 4.5 shows the results of derived indices including $[\text{TiO}]_1$, $[\text{TiO}]_2$,

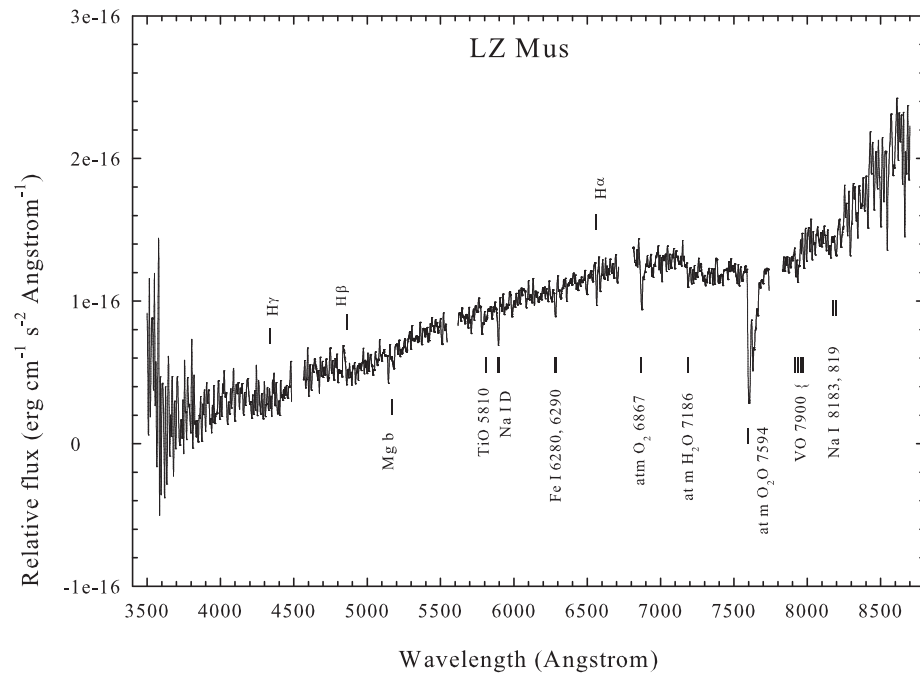


Figure 4.24: As Figure 4.23 but for LZ Mus.

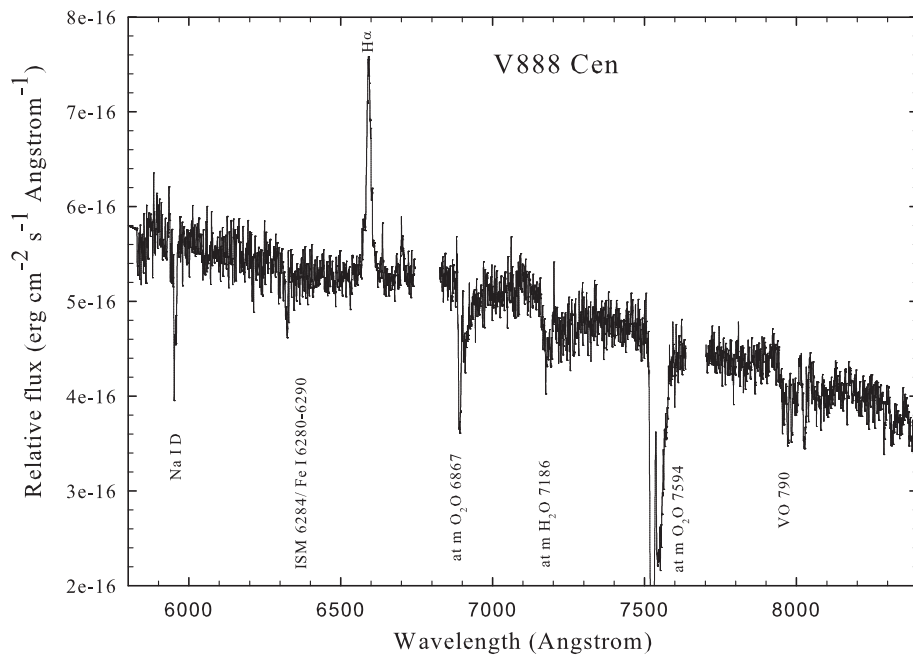


Figure 4.25: As Figure 4.23 but for V888 Cen in red region.

[VO] and [Na] measured from the dereddened spectra of the novae. Finally Table 4.6 compares the results of the evolutionary status of the secondaries between the two methods; from CMDs and from the spectra.

Table 4.3: Measured $EW(\text{CaT})$ and stellar parameters for target novae.

No.	System	$EW(\text{Ca II}) (\text{\AA})$	$EW(\text{Ca II}) (\text{\AA})$	$EW(\text{Ca II}) (\text{\AA})$	$EW(\text{CaT}) (\text{\AA})$	$\log g^a$	Corresponding Luminosity Class
		8498 \AA	8542 \AA	8662 \AA			
1	T CrB	2.2 \pm 0.1	3.0 \pm 0.1	3.0 \pm 0.2	8.3 \pm 0.2	2 \pm 1	III
2	V2487 Oph	2.6 \pm 0.5	2.5 \pm 0.4	4 \pm 1	9 \pm 1	2 \pm 1	III
3	CI Aql	1.7 \pm 0.1	5.4 \pm 0.6	0.3 \pm 0.6	7.4 \pm 0.6	3.3 \pm 0.4	III/IV
4	AR Cir	1.04 \pm 0.05	3.37 \pm 0.08	0.97 \pm 0.04	10.7 \pm 0.1	3.4 \pm 0.1	V/IV (AR Cir A)
5	V3964 Sgr	1.21 \pm 0.05	3.6 \pm 0.3	2.96 \pm 0.04	7.7 \pm 0.2	2.6 \pm 0.6	III
6	V3645 Sgr	0.82 \pm 0.04	3.13 \pm 0.02	2.4 \pm 0.1	6.3 \pm 0.1	3.63 \pm 0.08	V
7	V794 Oph	-	-	-	-	-	(no red observation)
8	V368 Aql	2.9 \pm 0.2	8.43 \pm 0.04	0.45 \pm 0.04	11.8 \pm .2	1.2 \pm 0.2	III
9	EU Sct	1.68 \pm 0.05	3.83 \pm 0.03	2.83 \pm 0.01	8.34 \pm .08	2.50 \pm .08	III

Table 4.4: Line indicators for Luminosity classification.

No.	Systems	Mg b (Å)	MgH (Å)	Na I (Å)	Ca I (Å)	CaH (Å)	VO (Å)	K I (Å)	VO (Å)	Na I (Å)
1	T CrB	✓	5167, 5173, 5184	5890, 5896	6103, 6122, 6162	6385	✓	7665, 7699	7865	8183, 8195
2	V2487 Oph	weak	very weak	weak	×	×	×	very weak	✓	weak
3	CI Aql	very weak	-	✓	×	×	×	×	✓	×
4	AR Cir	✓very broad	×	✓	very weak	×	very weak	very weak	×	×
5	V3964 Sgr	✓	-	✓	✓	×	×	-	×	weak
6	V3645 Sgr	✓ broad	-	✓	✓	weak	×	weak	weak	very weak
7	V794 Oph	✓	×	✓	✓	-	-	-	-	-
8	V368 Aql	weak	-	✓	×	×	×	×	weak	×
9	EU Sct	✓	×	✓	×	×	×	✓	×	✓

Note:

Mg b 5167, 5173, 5184 : Good criterion of the luminosity class for $B - V = 0.7-1.3$ (Deeming, 1960).

MgH 5621 : Broad feature marginally visible in late K to early M dwarfs (Turnshek, 1985).

Na I 5890, 5896 : Visible in all G-M stars; greatly enhanced in dwarfs (Turnshek, 1985).

Ca I 6103, 6122, 6162 : Enhanced in M dwarf (Turnshek, 1985; Peat, 1964).

CaH 6385 : M dwarf indicator (Turnshek, 1985).

VO 6478, 6532 : Marginally visible in M7III and later types (Turnshek, 1985).

K I 7665, 7699 : Very strong and wide in dwarfs, much weaker in giants (Turnshek, 1985).

VO 7865 (in VO 7900) : Appears in only giants cooler than $\sim M5$ (Turnshek, 1985).

Na I 8183, 8195 : Strong in dwarfs (Turnshek, 1985).

The line strength is designated as 'clearly detected' (✓), 'weak', 'very weak', 'absent' (×), or the spectra are unavailable (-).

Table 4.5: TiO, VO and Na I indices for target novae.

No.	System	[TiO] _I	Type	[TiO] ₂	Type	[VO]	Type	[Na]	Type
1	T CrB	0.48	M2-M4III	0.83	M3.8-M4.8III	0.32	M4-M5III	0.14	M0-M4III
2	V2487 Oph	0.65	M3.5-M5.5III(IV)	0.81	M3.8-M4.8III(IV)	0.04	M0-M3III(IV)*	-0.11	M4-M7III(IV)
3	CI Aql	0.00	G6-K4IV	0.01	G6-K4IV	0.30	M4-M5III(IV)	0.18	G4-K5III(IV)
4	AR Cir ^a	-	-	-	-	-	-	-	V-IV (AR Cir A)
5	V3964 Sgr	-0.04	G7-K3III	-0.06	G7-K3III	0.04	K0-M3III*	0.123	G9-M3III
6	V3645 Sgr ^d	-	K4-K8V	-	-	-	-	-	-
7	V794 Oph ^b	-	-	-	-	-	-	-	-
8	V368 Aql	0.01	G7-K3IV	-0.07	G7-K3IV	.07	M0-M4IV*	-0.03	M2-M6IV
9	EU Sct	-0.05	G7-K3III	-0.03	G7-K3III	.03	K0-M3III	0.23	G4-K5III

^a $EW(CaT)$ classifies the secondaries of these novae as main-sequence stars which these indices are not applied to. Classification by using the spectral template is applied instead.

^b V794 Sgr has only blue observations in the range from 3500-6500Å.

* The classification from the VO band is reliable when objects are giants cooler than ~M5 since the absorption is negligible for stars earlier than M4 (Kenyon & Fernandez-Castro, 1987).

4.7 Discussion and Conclusion

Sixteen novae were selected initially for photometric and spectroscopic follow-up from the list in Chapter 2. Among them, ten were observed with LT and photometric magnitudes obtained. All sixteen novae were plotted in a NIR CMD to determine the spectral type of the secondaries.

Determinations of reddening were adopted from the literature for seven novae with known extinction. Extinction for another five novae was estimated from extinction maps and equivalent widths of Na I D lines.

The dereddened spectra were used to determine luminosity class by using relations including the $EW(\text{CaT})$ versus $\log g$, the Na I 8190 index versus TiO 8465 index, and the identification of specific line indicators.

Determination of spectral types was accomplished by identifying specific lines and calculating indices from TiO bands, VO bands, and the Na atomic line for giants (4 stars) and sub-giants/giants (3 stars). The spectral library template was used instead of the indices in cases of main-sequence stars (2 stars). The summary of findings on the evolutionary status of secondaries in nine novae with observed spectra is shown in Table 4.6.

Spectral type identifications from both optical and NIR CMDs are consistent with one another for 7 systems; 3 RG-Novae (T CrB, V749 Oph, FS Sct), 3 RG/SG-Novae (V3964 Sgr, V2487 Oph, CI Aql), and 1 MS-Nova (V368 Aql).

Comparison of results from NIR CMD (based on the definition of secondaries in nova systems given by Darnley et al., 2013) to those from spectroscopy again shows 7 systems are in good agreement (4 RG-Novae: T CrB, V2487 Oph, V3964 Sgr and EU Sct; and 3 SG-Novae: CI Aql, V794 Oph and V368 Aql). Only 2 systems (AR Cir and V3645 Sgr) disagree.

Table 4.6: Proposed spectral and luminosity class of secondaries in target novae.

No ^a .	Nova Name	Recurrent	System Type ^a	Secondary Spectral Class ^b
1	T CrB	✓	RG-Nova(1,2)	M3-M4III(4), M4III
2	V2487 Oph	✓	RG-Nova(1,2),SG-Nova(1,5)	M4-M4.8III(IV)
3	CI Aql	✓	SG-Nova(1,2)	K-MIV(4), G6-K4IV
4	AR Cir		RG/SG-Nova(1)	K3V (6), K0-K3V
5	V3964 Sgr		RG-Nova(1)	G9-M3III
6	V3645 Sgr		RG-Nova(1)	K1-M1V/IV
7	V445 Pup		MS-Nova(1)	-
8	V794 Oph		RG-Nova(1)	III
9	V1330 Cyg		RG-Nova(1)	-
10	FS Sct		RG-Nova(1)	-
11	BTMon		SG-Nova(1)	-
12	V368 Aql		SG-Nova(1)	G7-K3IV
13	EU Sct		RG-Nova(1)	G7-K3III
14	CN Vel		SG-Nova(1)	-
15	LZ Mus		RG-Nova(1)	-
16	V888 Cen		SG/MS-Nova(1)	-

Notes:

^a Spectral class of the secondary stars designated by using NIR CMD in this study, unless otherwise stated.^b An average of spectral classes ranges derived from Table 4.5.

References: (1) This paper, (2) Darnley et al. (2012), (3) Schaefer (2010), (4) Anupama (2008), (5) Hachisu et al. (2002)

In the case of AR Cir, we cannot do the comparison since the our slit was not placed correctly in order to observe AR Cir B (the nova) but AR Cir A (a field star). We however designated AR Cir B as an RGB star from the CMDs, and AR Cir A as a K0-K3V star from the spectra. In the case of V3645 Sgr, the optical NIR CMD and spectrum designating it as a RG/SG-Nova by the CMDs, but showing spectra of class V stars is a discrepancy that we still need to investigate.

Our investigation also confirmed the positions of AR Cir, V794 Oph and EU Sct where there had been some ambiguity previously. Ultimately, we suggest here four prime candidates (2 RG-Novae - V3964 Sgr and EU Sct, and 2 SG-Novae - V794 Oph and V368 Aql) which are currently classified as CNe, to look for more than one outburst in archival plates or large sample sky surveys such as SMEI. This will be explored further in the next Chapter.

Chapter 5

Investigation of Novae with the Solar Mass Ejection Imager (SMEI)

The ground-based observations and results presented in Chapters 2 and 3 show spectroscopically that novae with low outburst amplitude potentially harbour evolved secondaries which might then help identify them as potential RNe. In this Chapter, we introduce a novel space-based observational archive that might detect the unrecorded outbursts of bright novae which are suggested to be missed due to their fast fading (see Chapter 1). Among many other variable and transient sources, the archive also contains light curves of novae during outbursts, including important data used for an investigation of the Recurrent Nova T Pyx, described in Chapter 6.

5.1 Introduction

The Solar Mass Ejection Imager (SMEI), a full-sky white-light CCD-based camera system for observing the inner heliosphere from Earth orbit, is on board the U.S. Air Force *Coriolis* Mission spacecraft which was launched into an 840 km Sun-synchronous terminator orbit on 2003 Jan 6 (Jackson et al., 2004). The operation ceased on 2011 Sep 28, although the spacecraft and instruments were still functioning well. Figure 5.1 shows the Coriolis spacecraft with the SMEI instrument on board prior to Vanden-

berg Air Force Base launch. Three CCD cameras are seen on the lower portion of the spacecraft.



Figure 5.1: Coriolis spacecraft (4.69 m height \times 1.34 m diameter) with the SMEI three CCD cameras (circled in red) on board. Image from Jackson et al. (2004).

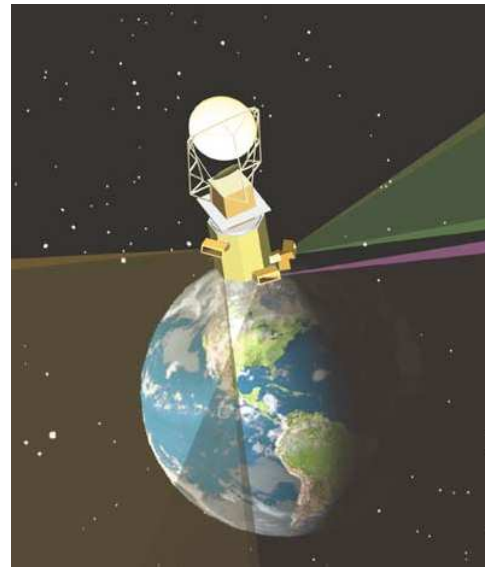


Figure 5.2: Schematic of SMEI in orbit. SMEI scans an area over a $\sim 180^\circ$ range of the sky from three cameras looking outward from the Earth. Image from Jackson et al. (2004).

SMEI consists of three CCD cameras each with a roughly $60^\circ \times 3^\circ$ field of view. It continuously took 4-second exposures, swept nearly over all the sky every 102 minutes, with $\sim 1^\circ$ spatial resolution, and therefore provided about 1500 frames from each camera per Earth orbit (Hick et al., 2005). SMEI thus scans an area over a $\sim 180^\circ$ range of the sky from the three baffled cameras looking outward from the Earth as shown in Figure 5.2.

SMEI was operated as a high precision differential photometer (Buffington et al., 2006) and can reliably detect brightness changes in point sources down to $m_{SMEI} \sim 8$ with the instrument's peak quantum efficiency at ~ 700 nm (corresponding roughly to an R

photometric band) and FWHM ~ 300 nm (Hounsell et al., 2010).

Approximately 5600 point sources brighter than $m_{SMEI} < 6$ were removed individually from the composite skymaps in order not to compromise the photometric specification for SMEI. These sources were removed by fitting the ‘standard’ point spread function (PSF) which was created from the observation of several bright isolated stars over a year (Hick et al., 2005). That is, a sidereal map was being subtracted removing the stars below 6^{th} magnitude, so anything we pick up in the maps are just the variation of that object, e.g. when it peaks.

Therefore with its high-cadence-all-sky observations, SMEI can investigate bright nova explosions ($m_{SMEI} < 8$) whose outbursts occurred within the time period of operation (i.e. during 2003-2011) and produce extremely detailed light curves. These caught, for example, the pre-maximum halts during the outbursts of several novae, as presented in Hounsell et al. (2010).

The SMEI real-time data pipeline produces calibrated sky maps in which brightness contributions from zodiacal dust and unresolved sidereal background have been subtracted. Figure 5.3 shows SMEI data frames from Cameras 1, 2 and 3 from top to bottom. While Camera 1 is always the farthest in angular distance from the Sun, Camera 3 is almost facing the Sun at the same time. Camera 1 and 2 operate at their designed temperature of -30°C , while Camera 3 operates at temperatures between -10°C and 3°C . The images from the cameras showing the point sources are intentionally defocused and extended into a fish-like shape spreading the light over 200 CCD pixels in order to prevent the pixels from saturating.

SMEI was originally designed to map large-scale variation of electron densities in the heliosphere by observing Thomson-scattered sunlight from the solar-wind (Jackson et al., 2004). In order to isolate the Thomson-scattered sunlight, other sources including the white-light contributions from the zodiacal dust cloud, the sidereal background, and the individual point sources (i.e. bright stars and planets) are subtracted (see Hick et al., 2007, for details). The contribution of these signals as a function of elongation from the Sun is shown in Figure 5.4.

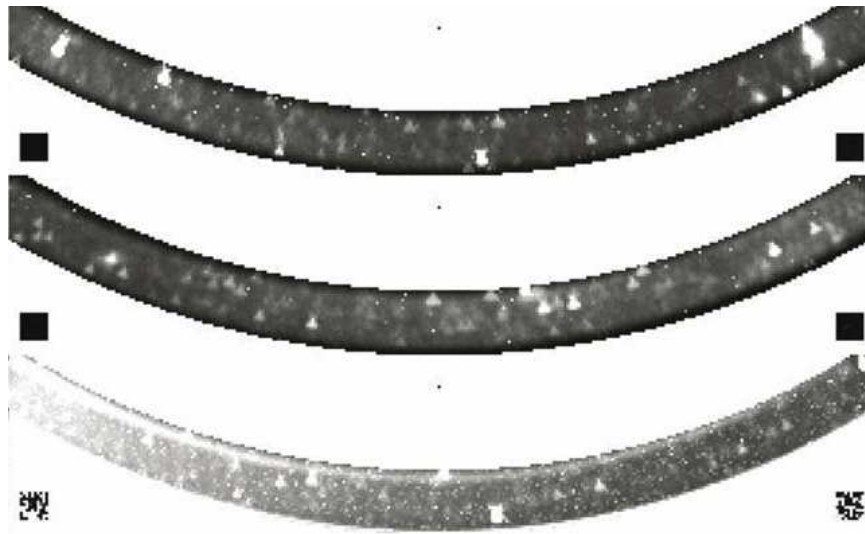


Figure 5.3: SMEI $60^\circ \times 3^\circ$ data frames from each of three cameras; Camera 1, 2 and 3 from top to bottom, the one viewing farthest to the one viewing nearest the Sun. Image from Jackson et al. (2004).

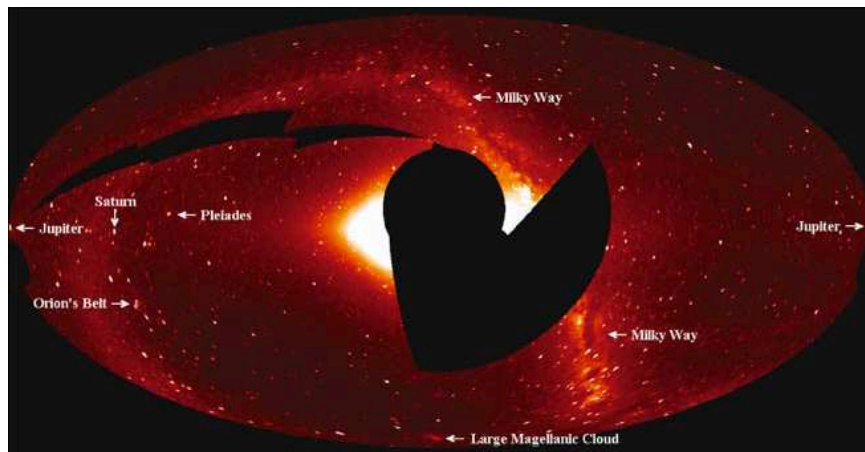


Figure 5.4: Composite view of the sky over a full orbit projected from individual SMEI CCD cameras. The Sun is at the centre with the ecliptic plane along the horizontal axis. Bright features are labelled, and blank areas are excluded due to either being inaccessible to the cameras during the orbit or the contamination of high particle flux from the Sun. Image from Hick et al. (2005).

5.2 Acquisition of SMEI Data

A week in November 2011 was spent working with Rebekah Hounsell alongside the SMEI team at UCSD in order to gain familiarity with the data and their reduction. Here we give a short overview of the data reduction process remotely controlled from LJMU. Detail description and subsequences of each step are given in the Appendix.

1. **Connecting to the SMEI Computer and Accessing the Database.** In order to access the SMEI database running on the UCSD computer from abroad, the remote control software was installed. In this study we used two software packages, working together called ‘PuTTY’ and ‘TightVNC’ to run on the Windows machine properly. Then we connect them to the server at UCSD.
2. **Adding New Objects to SMEI’s Object List.** Before fitting the point sources in SMEI maps, the objects must be included in SMEI’s object list which requires information including name, magnitude, RA and DEC.
3. **Object Visual Inspection in SMEI’s Sky Maps.** Objects and their surrounding region on SMEI’s sky map were inspected visually prior to the point source fitting for bad orbits (i.e. orbits that are contaminated by artefacts from the pipeline reduction process) which were then identified and excluded.
4. **Fitting a Point Source.** The photometry of a single point source was obtained by fitting the standard PSF mentioned above using a least-squares procedure implemented in IDL (see Hounsell, 2012, for more details). In this study, all investigated objects were fitted by using the same set of parameters, e.g. automatic adjusting for PSF centroid, automatic calculating of the size of the PSF radius which depends on the object’s brightness, removal of background, removal of zodiacal light, cleaning edge when an object moves from one camera to another.

Table 5.1: List of bright novae selected for SMEI investigation, and adapted from Table 2.2. Novae which have recorded outburst during 2003-2011 were investigated during the outburst. Otherwise, novae with no recorded outburst during that time were searched for an unrecorded outburst that might have occurred. The horizontal line separates bright novae with recent outbursts during 2003-2011 (in the upper part) from the novae with no outburst recorded from other sources during 2003-2011.

No.	Priority ^a	Name	Year	2003-2011?	m_{peak}	Filter	Spectrum	comment
1	36	V5116 Sgr	2005	1	7.6	V		Not visible ^{1,2}
2	37	V574 Pup	2004	1	7.0	V		Not visible ^{1,2}
3	56	V2467 Cyg	2007	1	7.4	V		Visible ^{1,2} , $t_2=9\pm 3$ days
4	74	V4745 Sgr	2003	1	7.3	V		Not visible ²
5	75	V2491 Cyg	2008	1	7.5	V		Barely visible ^{1,2}
6	78	V1187 Sco	2004	1	9.8	V		Visible ^{1,2} , $t_2=9.5\pm 0.5$ days
7	102	V5115 Sgr	2005	1	7.9	V		Not visible
8	109	V1186 Sco	2004	1	9.7	V		Not visible ^{1,2}
9	114	V1188 Sco	2005	1	8.9	V		Not visible ^{1,2}
10	3	V4074 Sgr	1965	0	8.6	pg		Not visible
11	4	V4643 Sgr	2001	0	7.7	V		Not visible
12	8	V2313 Oph	1994	0	7.5	V		
13	13	V3964 Sgr	1975	0	9.4	pg	LT, SALT	Not visible
14	16	V4160 Sgr	1991	0	7.0	V		Not visible
15	18	V445 Pup	2000	0	8.6	V		
16	20	V4743 Sgr	2002	0	5.0	V		
17	21	V4740 Sgr	2001	0	6.7	V		
18	23	V1330 Cyg	1970	0	9.0	V		
19	24	FH Ser	1970	0	4.5	V		
20	26	QU Vul	1984	0	5.3	V		
21	27	V4739 Sgr	2001	0	7.2	V		Not visible
22	29	BT Mon	1939	0	8.1	V		
23	31	OS And	1986	0	6.5	V		
24	32	V4742 Sgr	2002	0	7.9	V		Not visible
25	34	DK Lac	1950	0	5.9	V	LT	Not visible
26	35	V2275 Cyg	2001	0	6.9	V		
27	38	V368 Aql	1936	0	5.0	pg	LT, SALT	Not visible
28	39	V450 Cyg	1942	0	7.8	pg		
29	40	EU Sct	1949	0	8.4	pg	SALT	
30	41	V1016 Sgr	1899	0	8.5	pg		
31	42	V732 Sgr	1936	0	6.4	V		
32	47	HR Del	1967	0	3.6	V		
33	50	V1370 Aql	1982	0	7.7	V		
34	53	LV Vul	1968	0	4.5	V		
35	55	V723 Cas	1995	0	7.1	V		
36	57	V603 Aql	1918	0	-0.5	V		
37	64	T Aur	1891	0	4.5	V		
38	65	V1229 Aql	1970	0	6.6	V		
39	66	NQ Vul	1976	0	6.2	V		
40	67	V838 Her	1991	0	5.3	V		
41	68	V705 Cas	1993	0	5.7	V		
42	70	V446 Her	1960	0	4.8	V		
43	71	CP Lac	1936	0	2.0	V		
44	72	V827 Her	1987	0	7.5	V		
45	73	V4633 Sgr	1998	0	7.4	V		
46	76	V528 Aql	1945	0	6.9	V		
47	77	GK Per	1901	0	0.2	V		
48	79	V356 Aql	1936	0	7.0	V		
49	82	PW Vul	1984	0	6.4	V		
50	83	V849 Oph	1919	0	7.6	V		
51	85	V4444 Sgr	1999	0	7.6	V		
52	87	DN Gem	1912	0	3.6	V		
53	89	V1494 Aql	1999	0	4.1	V		
54	92	V533 Her	1963	0	3.0	V		
55	101	V4169 Sgr	1992	0	7.9	V		

Notes: ^a Priority set from Table 2.2 according to the low amplitude criteria.

References: (1) This study, (2) Hounsell (2012).

5.3 Light Curves of Detected Variables

5.3.1 Omicron Ceti

As an illustration of the light curves that can be derived from SMEI data we undertook a short investigation of an example variable.

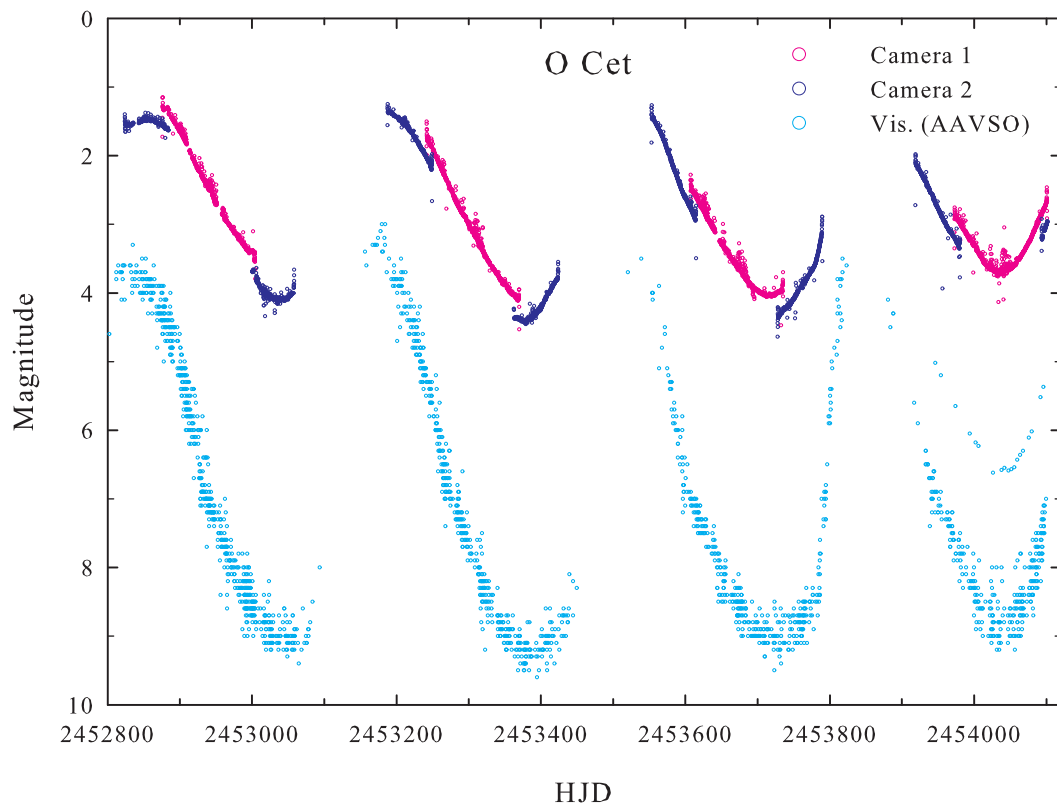


Figure 5.5: SMEI light curve of Mira Omi Ceti from Camera 1 (pink) and 2 (blue) and visible light observation from AAVSO (light blue).

Omicron Ceti ($\alpha=02^h19^m20^s.792$, $\delta=-02^\circ58'39''.50$), discovered on 1596 Aug 13 by D. Fabricius, is a prototype of Mira stars with period of 332 days (Mattei et al., 2002). Miras are the brightest and most famous long-period pulsating variables. They are cool and evolved stars associated with the asymptotic giant branch (AGB) and undergo radial pulsations which lead to cycles of visual light variations (Ireland et al., 2008). Although the pulsation models of Miras already exist, the precise mechanism responsible for the pulsation has not been yet identified (Fabas et al., 2011). Miras normally

change visual brightness by up to 8 magnitudes over their roughly yearly cycle (Reid & Goldston, 2002). Figure 5.5 shows SMEI observations present far higher cadence and potentially reveal more light curve details than those given by AAVSO.

The discrepancies in photometry from Camera 1 and 2 seen in the light curves of O Ceti will be discussed in Section 5.3.2 (Nova V1187 Sco) below.

5.3.2 Detected Novae Outbursts

Searching for the outbursts of novae that occurred during 2003-2011 in the SMEI data was first undertaken by Hounsell (2012) and resulted in classification into two groups; the “first class data” and the “second class data”. The first class data are unprecedented in their detail compared to previous observations. The second class data are light curves that are much fainter than those in the first class data. Since many of the novae have peak brightness at around 8th magnitude, detection of the subsequent light curve is hence unreliable. In this study, reanalysis of data from all three cameras independently of those done by Hounsell, 2012 was carried out for each target nova. Table 5.1 summarises the main findings.

Bright novae ($\lesssim 8^{\text{th}}$ magnitude) from Table 2.2 in Chapter 2 were selected and a new list of targets was created as presented in Table 5.1. Bright novae with recent outbursts during 2003-2011 were added to the list (in the upper part) and therefore were investigated during the outburst. Otherwise, novae with no outburst recorded from other sources during 2003-2011 were arranged by the amplitude criteria (see Chapter 2) and therefore were searched for an unrecorded outburst that might have occurred.

Except in the case of T Pyx which will be presented at the end of this Chapter, all light curves presented in this Chapter are second class data. The light curves derived, although more noisy than those of the first class data above, have however provided precise dates for the peak, further evidence for the existence of the premaximum halt, outburst magnitude, and in some cases decay time.

Nova V2467 Cyg

Nova V2467 Cyg ($\alpha=20^h28^m12^s.52$, $\delta=+41^\circ48'36''.5$) was discovered by A. Tago at 7.4 magnitude on 2007 Mar 15.787 UT (HJD 2454175.2843) and reached maximum at 6.8 ± 0.4 magnitude on 2007 Mar. 16.768 UT (2454176.2653) by using an unfiltered CCD (Nakano et al., 2007). It was suggested as an Fe II nova (Munari et al., 2007). The photometric light curve analysis derives parameters including $V_{max}=7.67$, $B_{max}=9.38$, $t_2=9$ days (from V) and 12 days (from B), $E(B-V)=1.38$ distance= 2.5 ± 0.3 kpc, and $M_{WD}=0.97\pm0.01$ (Shugarov et al., 2010). Around the time of the discovery, an extremely strong OI line at 8446\AA was present in spectra, proposed as a result of overabundance of oxygen (Tomov et al., 2007).

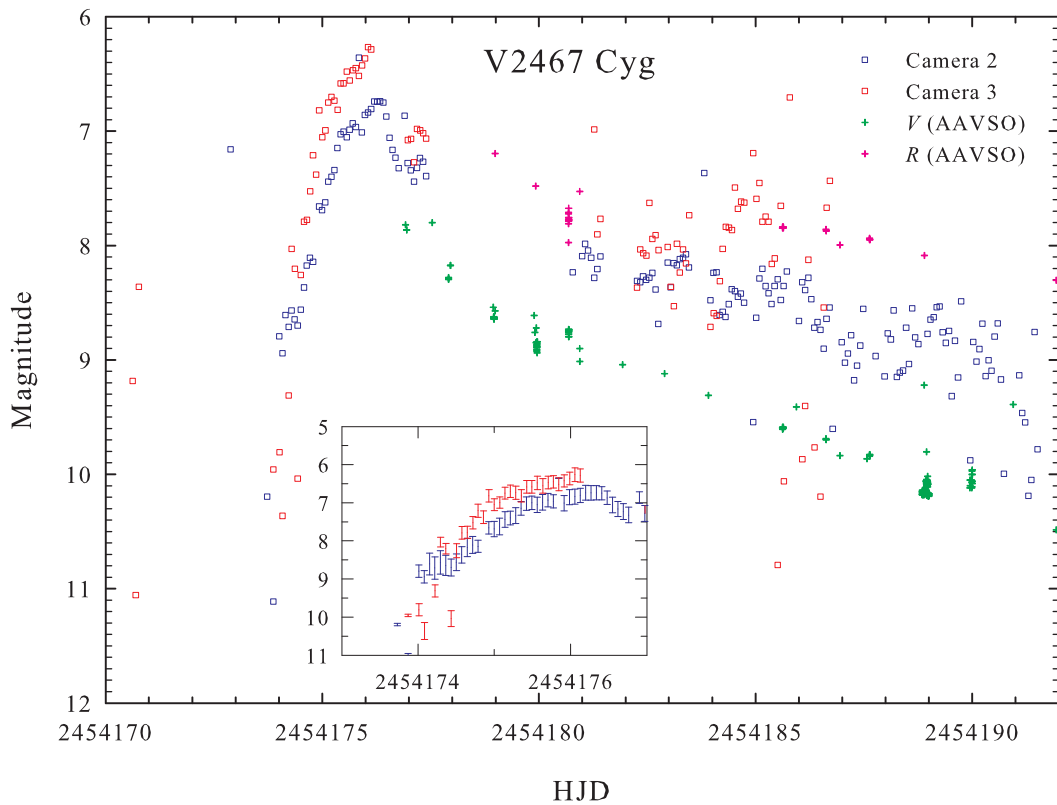


Figure 5.6: SMEI light curves of nova V2467 Cyg from Camera 2 (blue) and 3 (red).

During the transition phase, the V light curve shows some periodic brightness oscillations starting in April with a period of ~ 20 -30 days and an amplitude of 0.7 mag during the decline (Nakano et al., 2007). The periodic oscillations during the transi-

tion phase are typical and proposed to be related to an accretion disk process. V2467 Cyg also showed an early appearance of forbidden lines during the transition stage (Poggiani, 2009).

One year after the outburst, Ness et al. (2008) reported that V2467 Cygni was a soft X-ray source. Two distinct periods of 3.8 h and 35 min were found by Swierczynski et al. (2010) who propose the nova is possibly an intermediate polar.

Previously only the light curve viewed from Camera 3 was investigated by Hounsell (2012). In this study, data from Cameras 2 and 3 of the SMEI archive provided the light curves for nova V2467 Cyg presented in Figure 5.6. No detection was found in Camera 1. The SMEI data both from Cameras 2 and 3 show the initial rise at $m_{SMEI}=11.1\pm 0.2$ on HJD 2454173.8687 (~ 1.4 days prior to the discovery date) which must have risen from $V_{quiescent}\sim 19$ mag (Strope et al., 2010) to peak at $m_{SMEI}=6.7\pm 0.2$ on HJD 2454176.3382 (similar to that reported by Nakano et al. (2007)). Within this rise the pre-maximum halt was detected from HJD 2454174.0-2454174.5 at $m_{SMEI}=8.7\pm 0.1$ for 0.5 days by Camera 2. This pre-maximum halt was not detected before in Hounsell (2012). This short duration of halt might be reasonable for a very fast nova like V2467 Cyg (see Hounsell et al., 2010). In fact we find the approximate $t_2=9\pm 3$ days. The SMEI light curve from Camera 2 also presents oscillations starting around HJD 2454182 which is about a week earlier than that reported in Nakano et al. (2007).

We note that light curves from Cameras 2 and 3 are offset in magnitude because the sky subtraction in Camera 2 is better than that in Camera 3. This artifact is also found and explained in detail in the case of V1187 Sco (see Figure 5.8 for example).

Nova V1187 Sco

Nova V1187 Sco ($\alpha=17^h29^m18^s.81$, $\delta=-31^\circ46'01''.5$) was discovered by A. Takao at 9.9 magnitude on 2004 Aug 2.071 UT (HJD 2453219.5749) with an unfiltered CCD, and reached maximum 7.4 magnitude on 2004 Aug 3.583 UT (HJD 2453221.0868) (Yamaoka, 2004). It harbours an ONeMg WD which did not form dust before entering

its nebular phase, and with $E(B - V) = 1.56 \pm 0.08$, a distance of 4.9 ± 0.5 kpc is derived (Lynch et al., 2006).

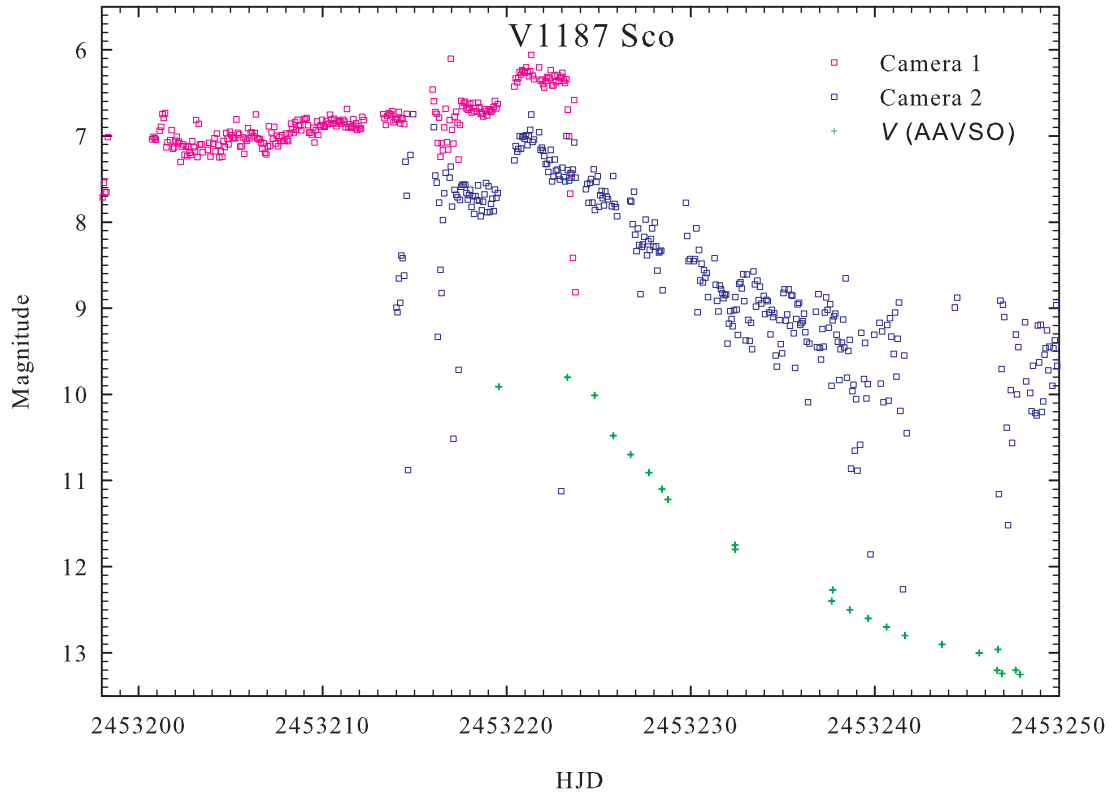


Figure 5.7: SMEI light curve of nova V1187 Sco from Camera 1 (pink) Camera 2 (blue) and 3 (red).

Previously only the light curve viewed from Camera 2 was investigated by Hounsell (2012). Again in this study, data from Cameras 1 and 2 of the SMEI archive provided light curves for nova V1187 Sco, as presented in Figure 5.7. No detection was found in Camera 3. Although the data do not show the rise from quiescence ($V_{quiescent} \sim 18$ mag Strope et al., 2010), they catch the peak at $m_{SMEI} = 6.9 \pm 0.2$ on HJD 2453221.2688. The approximate $t_2 = 9.5 \pm 0.5$ days again classifies the system as a fast nova.

We note there is an offset in magnitude between the two cameras and a high background level in Camera 1 prior to the outburst. The discrepancy can be explained by Figure 5.8 where the background subtraction in Camera 2 is cleaner than that in Camera 1. As a result, the derived magnitudes from Camera 2 are more reliable. The high

background level in both Camera 1 and 2 presented in light curves prior to the outburst is due to the nearby Moon that contributes more brightness to the object, as shown in Figure 5.9.

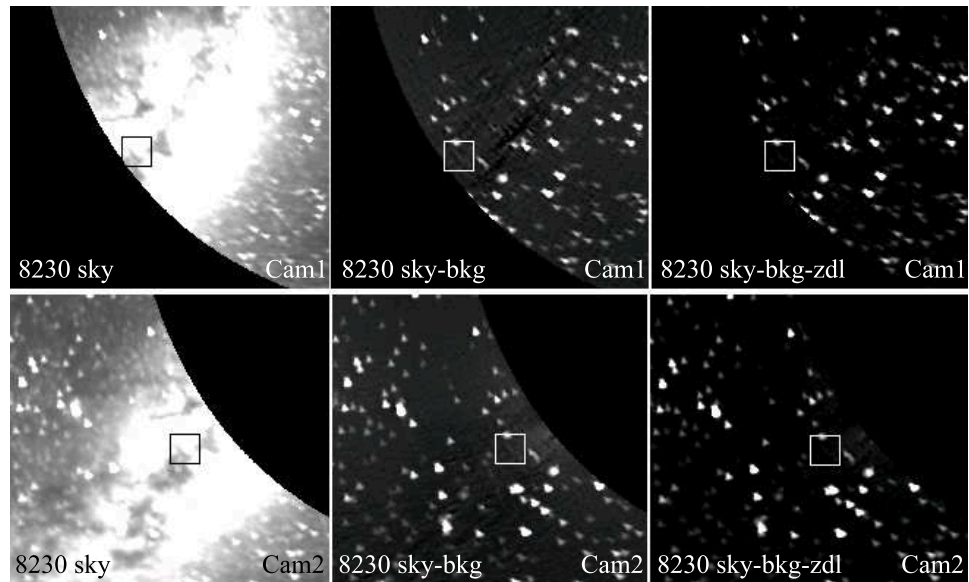


Figure 5.8: SMEI sky maps for V1187 Sco at peak brightness (i.e. all images are taken at the same orbit 8230) where images are non-subtraction (left), with background subtraction (middle) and with background and zodiacal light subtraction (right). Top and bottom panels are data from Camera 1 and 2, respectively. Middle panels show that Camera 2 has better background subtraction than Camera 1 and a more reliable derived magnitude as a result.

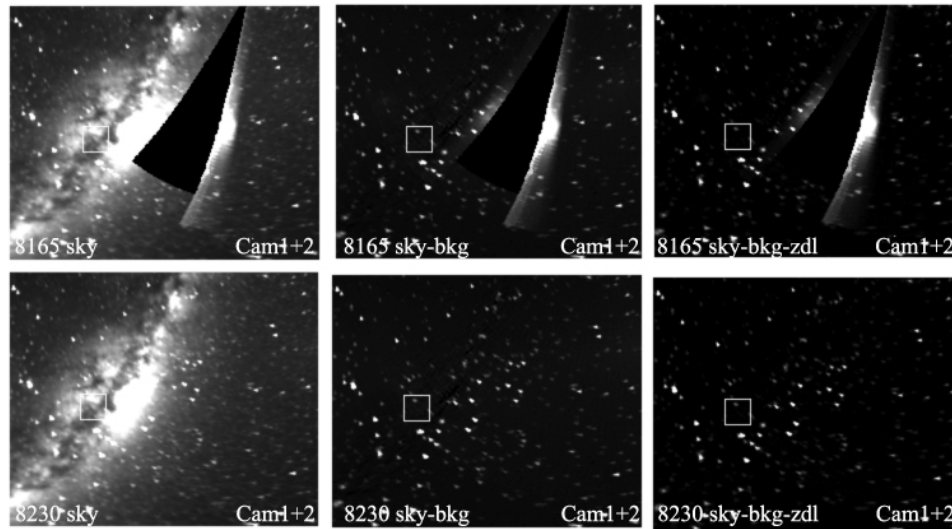


Figure 5.9: SMEI sky maps for V1187 Sco with the Moon nearby (orbit 8165, top panels) compared with those taken at peak when the Moon is far away (orbit 8230, bottom panels). Images presented are non-subtraction (left), with background subtraction (middle) and with background and zodiacal light subtraction (right) images.

5.4 Searching for Nova Outbursts

This section presents four examples of novae (e.g. V4074 Sgr, V3964 Sgr, DK Lac and V368 Aql) which do not have any otherwise recorded outbursts during 2003-2011 and are marked as ‘*Not visible*’ in Table 5.1. They were selected based on two main reasons. First, the low outburst amplitude criterion (see Chapter 2) in the case of V4074 Sgr, V4643 Sgr, V3964 Sgr and V4160 Sgr, and carried out the investigation following the list in Table 5.1. The second factor is the availability of observed optical spectra taken by the LT (see Chapter 4) in the case of DK Lac and V368 Aql. This is to look for the second outbursts of CNe that suggested they are RNe candidates due to their colour on a CMD (see Chapter 4). We note that the work presented in Chapter 4 was begun prior to that presented in this Chapter, this is why the investigation order listed in Table 5.1 sometimes jumped to the faint novae instead of the brighter novae or the novae with lower outburst amplitudes. These bright novae with higher priority on the list should however be investigated further in the future (see Chapter 7).

The resultant failure of our search for missing outbursts is illustrated in Figure 5.10-5.13 where variations are those of the background light. This shows a wave shape in

each figure. This variation in background is the seasonal variation in the SMEI sky maps (Buffington et al., 2007). Note that it is also possible however that outbursts could have occurred in the gaps in the data.

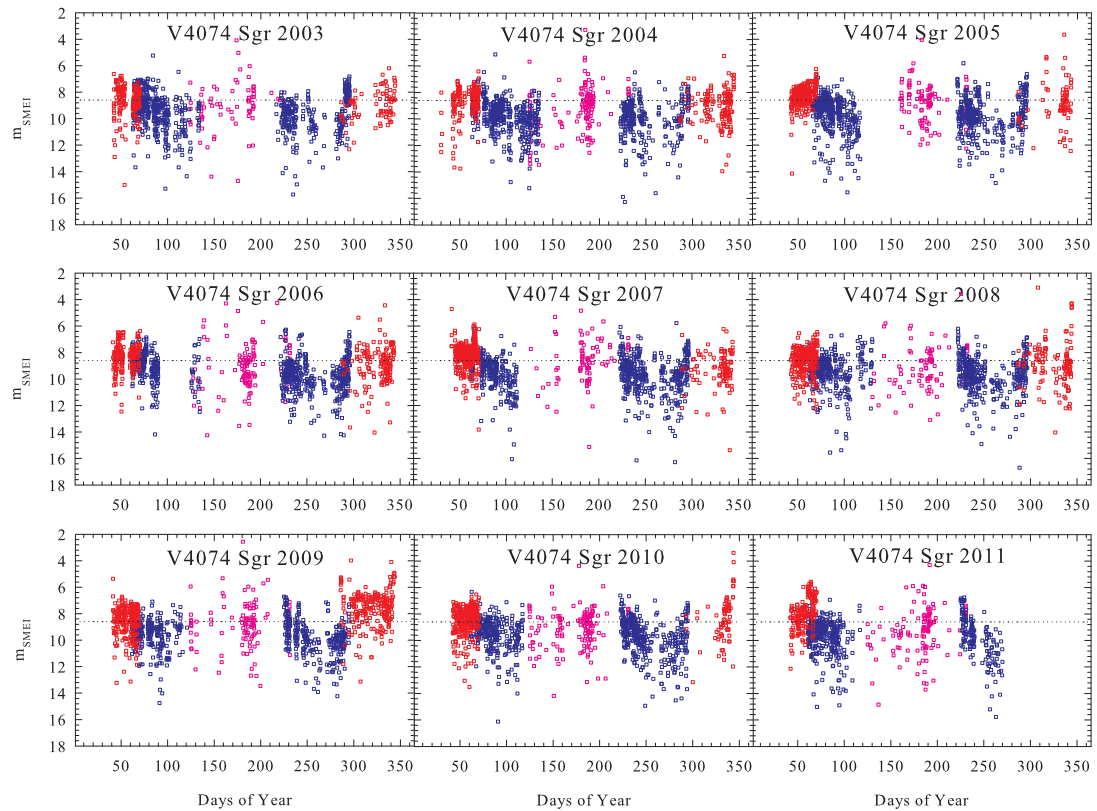


Figure 5.10: SMEI results at the position of nova V4074 Sgr from 2003 (top left) to 2011 (bottom right) observed by Camera 1 (pink) Camera 2 (blue) and 3 (red). Dotted lines indicate the previous recorded outburst magnitude.

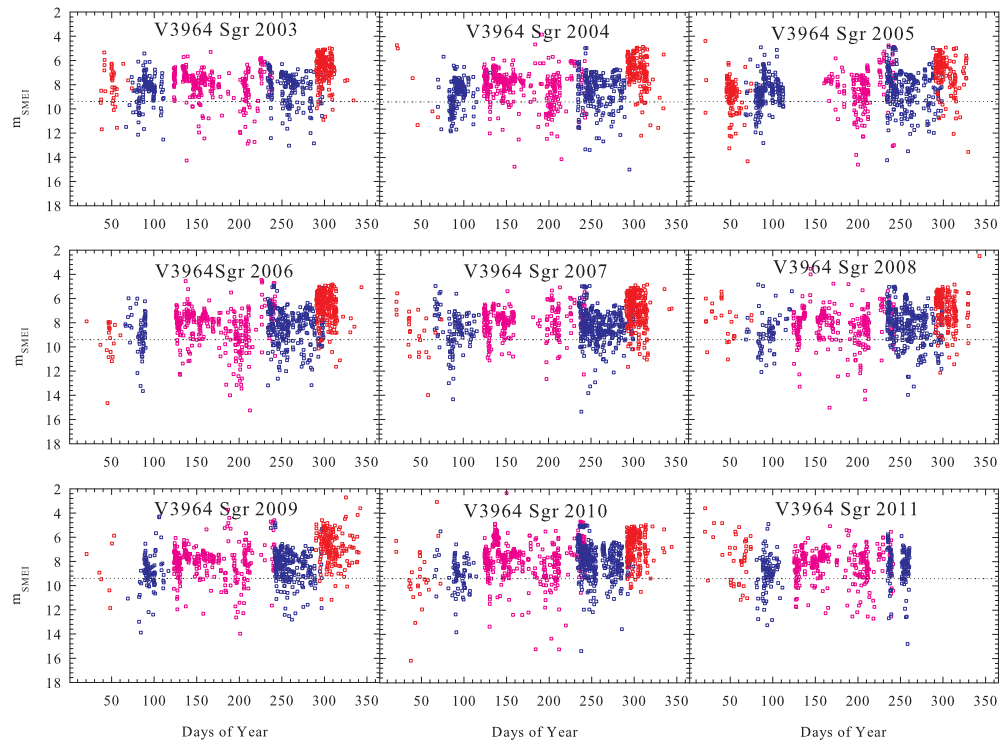


Figure 5.11: As Figure 5.10 but for nova V3964 Sgr.

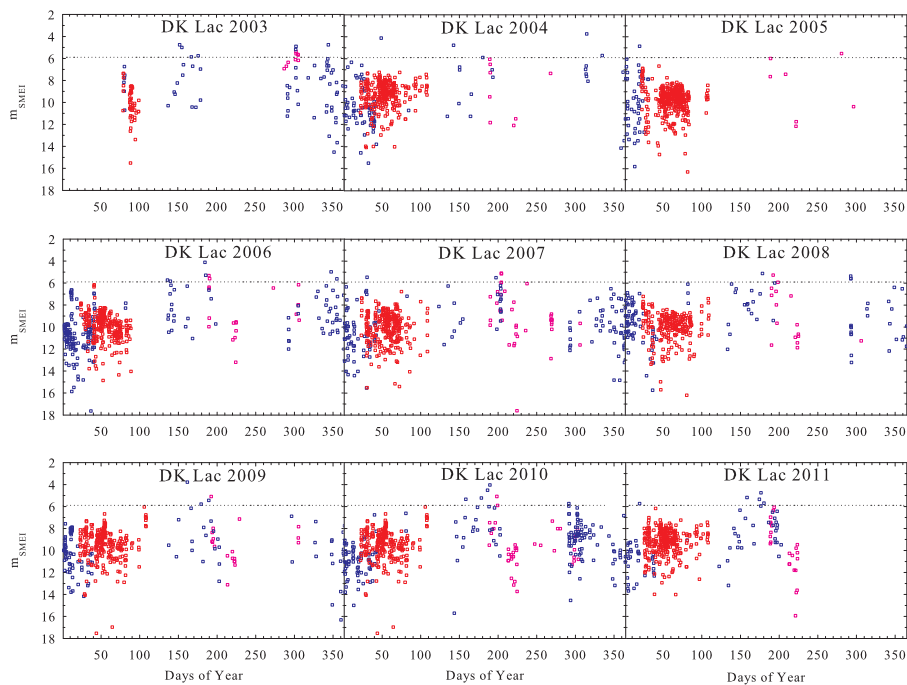


Figure 5.12: As Figure 5.10 but for nova DK Lac.

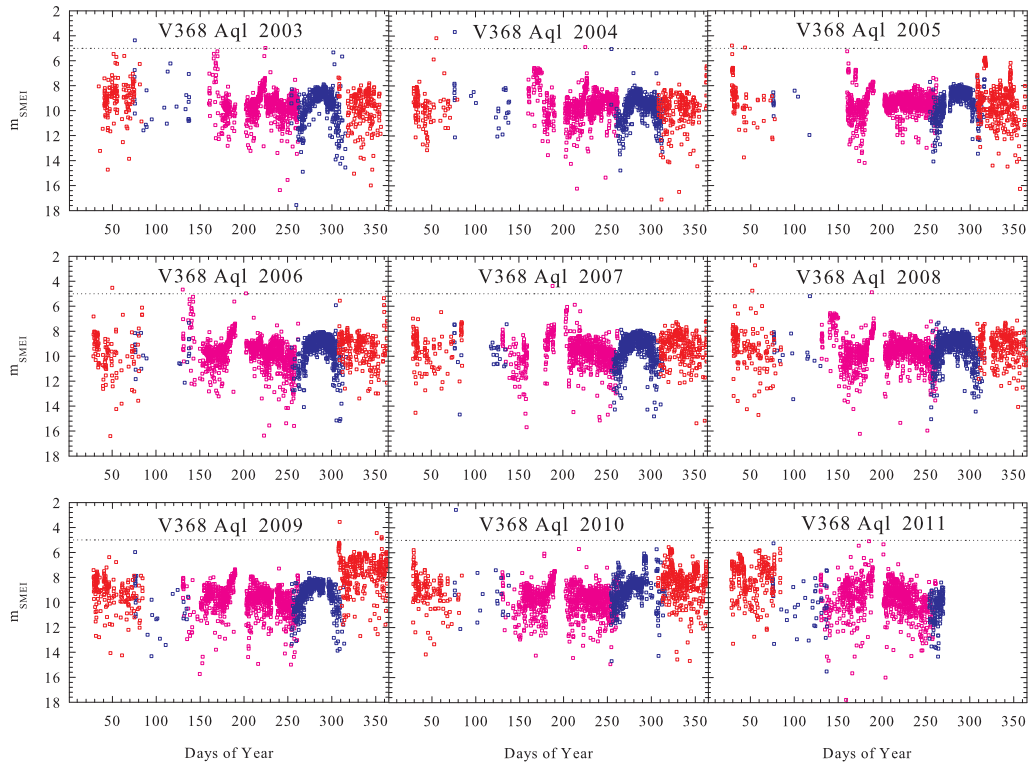


Figure 5.13: As Figure 5.10 but for nova V368 Aql.

When considering Figures 5.10, 5.11, 5.12 and 5.13 overall, two features were noticed in general. First, the background sky levels have a wave shape over the year through which might be fitted and subtracted and yield therefore better result. Second, there were some detections which are brighter than the line indicating the previous recorded outburst magnitude. More intensive investigation should be carried out in the future work.

5.5 SMEI Observations of Nova *T Pyxidis*

T Pyx ($\alpha=9^h4^m41^s.50$, $\delta=-32^\circ22'47''.5$) has the shortest known orbital period (~ 0.076 or $1^h.824$) of any Recurrent Nova (see Anupama, 2008, for a review) and the only RN that is below the cataclysmic variable (CV) period gap (Schaefer et al., 1992; Patterson et al., 1998; Uthas et al., 2010).

According to standard evolutionary models, a CV below the period gap should be faint and have a low accretion rate (\dot{M}_{acc}) driven by gravitational radiation (Warner, 2002, 2008). T Pyx's pre-outburst mass transfer rate turned out to be $\gtrsim 10^{-8} M_{\odot} \text{yr}^{-1}$ (Patterson et al., 1998; Selvelli et al., 2010) which is higher than that expected ($\sim 10^{-10} M_{\odot} \text{yr}^{-1}$) in CVs with this period (Hellier, 2001). This unusually high \dot{M}_{acc} is understandable if the system is a wind-driven supersoft X-ray source (SSS) which can accelerate the binary evolution (Knigge et al., 2000). Although the SSS has not been seen yet in quiescence, T Pyx is a weak hard source detected in an XMM-Newton spectrum (Selvelli et al., 2010). A recent model reveals that nuclear burning WDs do not need to be bright in soft X-rays during the phase of mass accretion to reach the Chandrasekhar mass (Di Stefano, 2010; Newsham et al., 2013). Thus the absence of a SSS therefore may not invalidate Knigge et al.'s (2001) postulate.

T Pyx has had previous observed outbursts in 1890, 1902, 1920, 1944, 1966/1967, and now 2011, with an extensive shell of ejected gas associated with these. The photometric and spectroscopic characteristics of the first outbursts were briefly presented in Payne-Gaposchkin (1964) while the 1966 event was discussed post-outburst by Catchpole (1969) and Landolt (1970). All the outbursts have exhibited brightness fluctuations near the optical peak and the subsequent declines have been slow. The ejection velocity observed previously was $\sim 2000 \text{ km s}^{-1}$ in 1967 (Catchpole, 1969; Williams, 1982) with $t_3=63$ days (Schaefer, 2010). The distance has been revised most recently by Shore et al. (2011) to be ≥ 4.5 kpc, with a strict lower limit of 3.5 kpc which was the previously accepted value. Taking $M_{bol}=-7.0$ given by Schaefer (2010) gives $L_{bol} \sim 2 \times 10^{38} \text{ erg s}^{-1}$ at maximum light ($\sim L_{edd}$ for a $1 M_{\odot}$ WD).

T Pyx is unique for having an outburst light curve plateau in the decline stage which is different from the five other RNe (IM Nor, CI Aql, V2487 Oph, U Sco, and RS Oph) with observed (so-called 'true') plateaus in their light curves. While the latter true plateaus are believed to be the result of the combination of the irradiation of the disk (by the supersoft emission from nuclear burning near the WD after the wind associated with the ejecta has stopped) and the steady light decline from the shell which leads to a flattening of the light curve until the nuclear burning turns off, the plateau in T Pyx

is thought to arise from a different mechanism including the emission lines increasing in brightness (Hachisu et al., 2000). Unlike true plateaus that have the flat portion starting during an apparently final decline, T Pyx's plateau starts immediately after a sharp drop (~ 2.0 mag in 20 days after peak) and starts again in the final decline (~ 105 days after peak). This feature, of a plateau starting after a sharp drop, is also present in RS Oph; however, the presence of a Super Soft Source (SSS) and the lack of colour changes during the plateau phase in RS Oph indicates a true plateau (Hachisu et al., 2008). On the other hand, the shape of T Pyx's plateau in *B* and *V* band light curves is significantly different (Schaefer, 2010).

Another unique feature of T Pyx is the secular decline from 1890 to the present across many eruptions. It is the only RN that shows a decreasing trend in quiescent *B* magnitude which has declined from 13.8 before the eruption in 1890 to 14.38, 14.74, 14.88, and 14.72 for the next four inter-eruption periods and finally faded to 15.5 from the 1980's until 2004 (Schaefer, 2005) and then to 15.7 from 2009 to 2011 (Schaefer et al., 2013) as shown in Figure 5.14. By looking at this drop of a total of 1.9 magnitudes corresponding to a factor of 5.75 in flux, and using $\dot{M}_{acc} \propto F^\beta$ where $\beta=2.0$ given by Schaefer (2005), Schaefer et al. (2010a) commented that the \dot{M}_{acc} has dropped by a total factor of 33 since 1890. This convinced them to predict the next eruption to be 10^3 to 10^6 years from that time, which was of course shown to be a gross overestimate of the timescale to outburst.

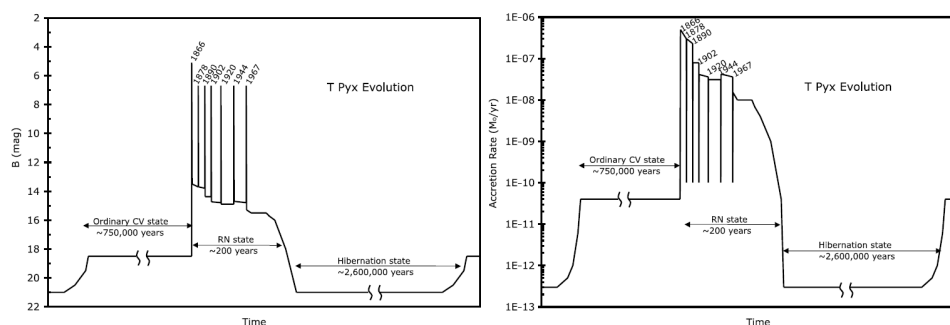


Figure 5.14: Secular decline of *B* magnitude and mass accretion rate of T Pyx. The schematic plot of quiescent *B* magnitude of previous eruptions (left) implies the mass accretion rate (right) has dropped to within 3% of its earlier value (from Schaefer et al., 2010a).

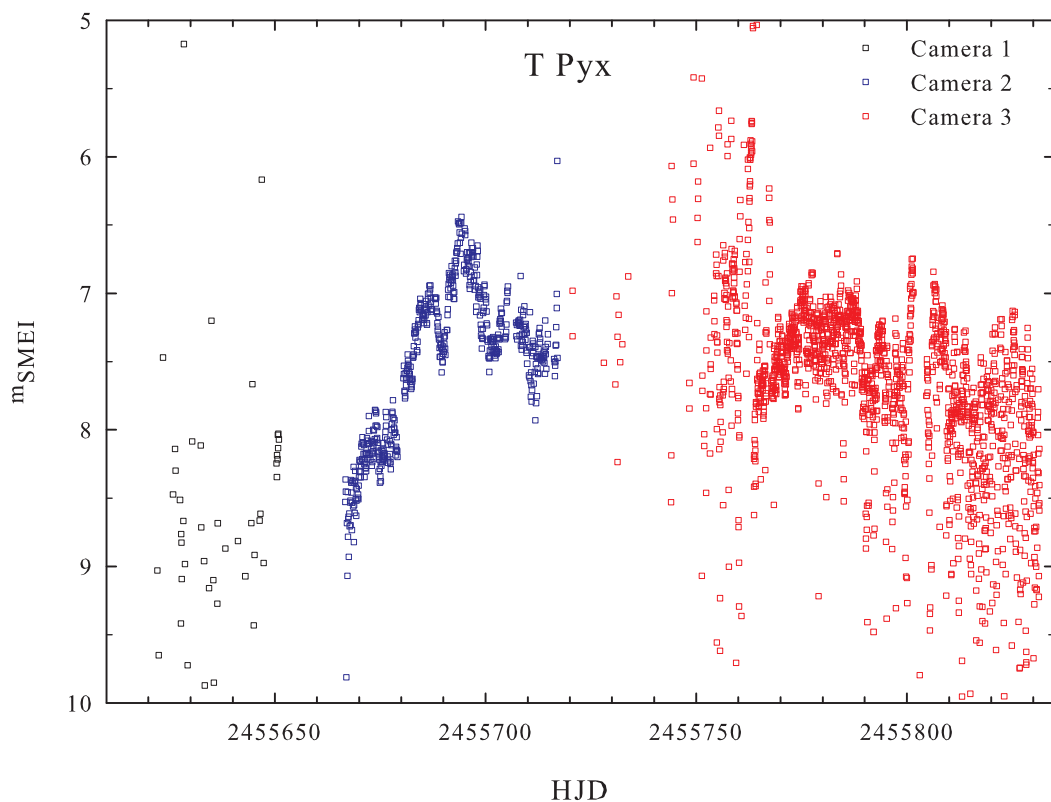


Figure 5.15: SMEI light curve of Recurrent Nova T Pyx. The outburst of T Pyx in 2011 was discovered by AAVSO observer M. Linnolt at a visual magnitude of 13.0 on JD 2455665.7931 (see Chapter 6 for more details). Data from Camera 2 (blue) is much less scattered compared to those from Camera 1 (black) and Camera 3 (red). As a result, only data from Camera 2 are used in Chapter 6.

The latest outburst of T Pyx in 2011 is detected in the SMEI data. The preliminary analysis was given in Hounsell (2012), showing the light curve from Camera 2. In this study, all three cameras were investigated, again independently of work done by Hounsell (2012). It is found that, similar to the case of V1187 Sco, data from Camera 2 are more reliable than those from Cameras 1 and 3 as seen in Figure 5.15. As a result, only data from Camera 2 (Table 5.2) as shown in Figure 5.16 are used in the detailed investigation of T Pyx in its 2011 outburst, described in Chapter 6.

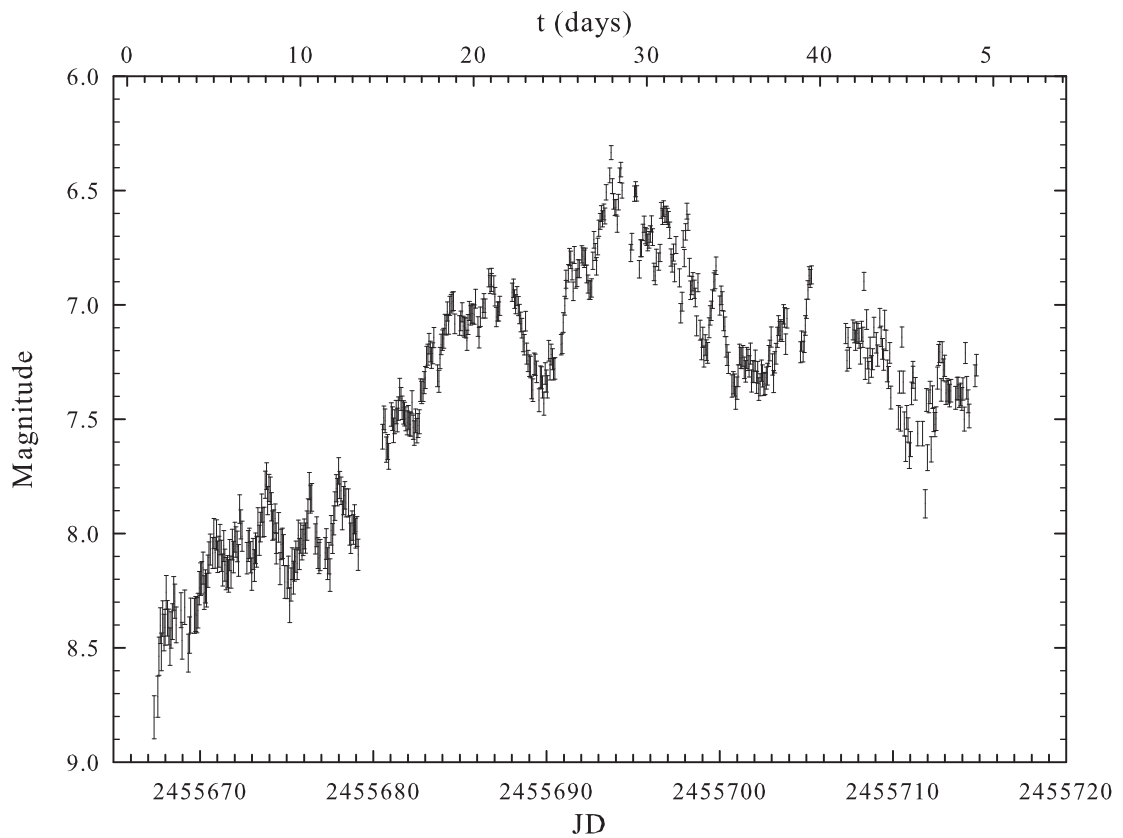


Figure 5.16: SMEI light curve of Recurrent Nova T Pyx in its 2011 outburst as viewed by Camera 2.

5.6 Discussion and Conclusion

In this Chapter, we have introduced the high cadence full-sky space-based observational archive of SMEI. Selected targets were added into the SMEI's object list, each

was inspected in SMEI's sky maps by eye to identify bad orbits. Background light and sidereal zodiacal light were then subtracted from sky maps, and finally the magnitudes of the the targets were obtained by fitting the standard PSF.

Using data from the SMEI archive, we derived light curves of one Mira (O Cet) and two novae with known outbursts during 2003-2011 (V2467 Cyg and V1187 Sco). The SMEI light curves potentially reveal more details than those given by ground-based observations. The pre-maximum halt was found in V2467 Cyg as well as oscillations in light curves found earlier than those found in previous studies. The precise date of maximum of each nova was provided.

Four bright novae that are potentially RNe candidates, as suggested in Chapters 2 and 3, were searched for second outbursts, but none were found. It should be noted that further investigation of bright novae with high priority in Table 5.1 should be carried out. Hounsell (2012) proposed that over 50 novae may be found within the SMEI data archive since the estimated number of novae brighter than 8th magnitude occurring each year is ~ 6 (Shafter, 2002).

Among the nova outbursts detected by SMEI, the unprecedented detail in first class data of the Recurrent Nova T Pyx in its 2011 outburst reveals important results which will be used for detailed investigations, as described in Chapter 6.

Table 5.2: SMEI observations of T Pyx from Camera 2.

JD	t	m_{SMEI}	JD	t	m_{SMEI}	JD	t	m_{SMEI}
2455667.3422	1.55	8.80 ± 0.09	2455672.2802	6.49	7.89 ± 0.06	2455676.8656	11.07	8.11 ± 0.07
2455667.5538	1.76	8.71 ± 0.09	2455672.3508	6.56	7.96 ± 0.06	2455676.9361	11.14	8.10 ± 0.07
2455667.6244	1.83	8.54 ± 0.08	2455672.4213	6.63	8.01 ± 0.07	2455677.2183	11.43	8.09 ± 0.07
2455667.6949	1.90	8.40 ± 0.08	2455672.7035	6.91	8.11 ± 0.07	2455677.2888	11.50	8.05 ± 0.07
2455667.7654	1.97	8.52 ± 0.08	2455672.7741	6.98	8.06 ± 0.07	2455677.3594	11.57	8.13 ± 0.07
2455667.8402	2.05	8.37 ± 0.08	2455672.8446	7.05	8.04 ± 0.07	2455677.4299	11.64	8.11 ± 0.07
2455667.9066	2.11	8.43 ± 0.08	2455672.9151	7.12	8.10 ± 0.07	2455677.5004	11.71	8.18 ± 0.07
2455667.9771	2.18	8.41 ± 0.08	2455672.9857	7.19	8.18 ± 0.07	2455677.5710	11.78	7.99 ± 0.06
2455668.0476	2.25	8.26 ± 0.07	2455673.0563	7.26	8.09 ± 0.07	2455677.6415	11.85	8.02 ± 0.07
2455668.1182	2.33	8.37 ± 0.08	2455673.1267	7.33	8.14 ± 0.07	2455677.7121	11.92	7.94 ± 0.06
2455668.1887	2.40	8.41 ± 0.08	2455673.1973	7.40	8.07 ± 0.07	2455677.7826	11.99	7.88 ± 0.06
2455668.2593	2.47	8.50 ± 0.08	2455673.2679	7.47	8.08 ± 0.07	2455677.8532	12.06	7.80 ± 0.06
2455668.3298	2.54	8.42 ± 0.08	2455673.3384	7.55	7.95 ± 0.06	2455677.9237	12.13	7.82 ± 0.06
2455668.4003	2.61	8.39 ± 0.08	2455673.4089	7.62	8.03 ± 0.07	2455677.9942	12.20	7.73 ± 0.06
2455668.4709	2.68	8.26 ± 0.07	2455673.4795	7.69	7.97 ± 0.06	2455678.0648	12.27	7.79 ± 0.06
2455668.5414	2.75	8.30 ± 0.07	2455673.5500	7.76	7.89 ± 0.06	2455678.1354	12.34	7.81 ± 0.06
2455668.6120	2.82	8.40 ± 0.08	2455673.6205	7.83	7.95 ± 0.06	2455678.2059	12.41	7.92 ± 0.06
2455668.6826	2.89	8.34 ± 0.08	2455673.6911	7.90	7.95 ± 0.06	2455678.2764	12.48	7.86 ± 0.06
2455668.7531	2.96	8.47 ± 0.08	2455673.7617	7.97	7.79 ± 0.06	2455678.3470	12.55	7.83 ± 0.06
2455669.0237	3.03	8.32 ± 0.08	2455673.8322	8.04	7.75 ± 0.06	2455678.4175	12.62	7.87 ± 0.06
2455669.0942	3.10	8.52 ± 0.08	2455673.9027	8.11	7.86 ± 0.06	2455678.4880	12.69	7.87 ± 0.06
2455669.1647	3.17	8.44 ± 0.08	2455673.9733	8.18	7.80 ± 0.06	2455678.5586	12.76	7.99 ± 0.06
2455669.2352	3.24	8.36 ± 0.08	2455674.0439	8.25	7.81 ± 0.06	2455678.6292	12.83	7.99 ± 0.06
2455669.3057	3.31	8.36 ± 0.08	2455674.1144	8.32	7.88 ± 0.06	2455678.6997	12.90	8.02 ± 0.07
2455669.3762	3.38	8.36 ± 0.08	2455674.1849	8.39	7.88 ± 0.06	2455678.7702	12.97	7.97 ± 0.06
2455669.4467	3.45	8.35 ± 0.08	2455674.2555	8.46	7.97 ± 0.06	2455678.8408	13.04	7.98 ± 0.06
2455669.5172	3.52	8.36 ± 0.08	2455674.3260	8.53	7.96 ± 0.06	2455678.9113	13.11	7.94 ± 0.06
2455669.5877	3.59	8.34 ± 0.08	2455674.3966	8.60	7.93 ± 0.06	2455678.9818	13.18	8.00 ± 0.07
2455669.6582	3.66	8.24 ± 0.07	2455674.4671	8.67	8.02 ± 0.07	2455679.0524	13.25	7.99 ± 0.07
2455669.7287	3.73	8.20 ± 0.07	2455674.5377	8.74	8.07 ± 0.07	2455679.1230	13.32	8.09 ± 0.07
2455669.7992	3.80	8.19 ± 0.07	2455674.6082	8.81	7.97 ± 0.06	2455680.1936	13.39	7.58 ± 0.05
2455669.8697	3.87	8.15 ± 0.07	2455674.6787	8.88	8.15 ± 0.07	2455680.2642	13.46	7.49 ± 0.05
2455669.9402	3.94	8.26 ± 0.07	2455674.7493	8.95	8.05 ± 0.07	2455680.3348	13.53	7.51 ± 0.05
2455669.0107	4.01	8.23 ± 0.07	2455674.8198	9.02	8.04 ± 0.07	2455680.4054	13.60	7.63 ± 0.06
2455669.0812	4.08	8.25 ± 0.07	2455674.8904	9.09	8.07 ± 0.07	2455680.4760	13.67	7.62 ± 0.06
2455669.1517	4.15	8.17 ± 0.07	2455674.9609	9.16	8.21 ± 0.07	2455680.5466	13.74	7.66 ± 0.06
2455669.2222	4.22	8.11 ± 0.07	2455675.0315	9.23	8.21 ± 0.07	2455680.6172	13.81	7.66 ± 0.06
2455669.2927	4.29	8.07 ± 0.07	2455675.1020	9.30	8.17 ± 0.07	2455680.6878	13.88	7.53 ± 0.05
2455669.3632	4.36	8.09 ± 0.07	2455675.1725	9.37	8.31 ± 0.08	2455680.7584	13.95	7.50 ± 0.05
2455669.4337	4.43	8.00 ± 0.07	2455675.2431	9.44	8.22 ± 0.07	2455680.8290	14.02	7.55 ± 0.05
2455669.5042	4.50	8.08 ± 0.07	2455675.3136	9.51	8.22 ± 0.07	2455680.8996	14.09	7.51 ± 0.05
2455669.5747	4.57	8.08 ± 0.07	2455675.3842	9.58	8.13 ± 0.07	2455680.9702	14.16	7.47 ± 0.05
2455669.6452	4.64	8.01 ± 0.07	2455675.4547	9.65	8.19 ± 0.07	2455681.0408	14.23	7.50 ± 0.05
2455669.7157	4.71	8.10 ± 0.07	2455675.5252	9.72	8.14 ± 0.07	2455681.1114	14.30	7.45 ± 0.05
2455669.7862	4.78	8.08 ± 0.07	2455675.5958	9.79	8.10 ± 0.07	2455681.1820	14.37	7.55 ± 0.05
2455669.8567	4.85	8.03 ± 0.07	2455675.6663	9.86	8.13 ± 0.07	2455681.2526	14.44	7.41 ± 0.05
2455669.9272	4.92	8.10 ± 0.07	2455675.7369	9.93	8.01 ± 0.07	2455681.3232	14.51	7.45 ± 0.05
2455669.9977	4.99	8.16 ± 0.07	2455675.8074	10.00	8.09 ± 0.07	2455681.3938	14.58	7.47 ± 0.05
2455670.0682	5.06	8.06 ± 0.07	2455675.8780	10.07	8.02 ± 0.07	2455681.4644	14.65	7.48 ± 0.05
2455670.1387	5.13	8.14 ± 0.07	2455675.9485	10.14	8.05 ± 0.07	2455681.5350	14.72	7.50 ± 0.05
2455670.2092	5.20	8.18 ± 0.07	2455676.0190	10.21	8.03 ± 0.07	2455681.6056	14.79	7.52 ± 0.05
2455670.2797	5.27	8.17 ± 0.07	2455676.0896	10.28	8.00 ± 0.07	2455681.6762	14.86	7.49 ± 0.05
2455670.3502	5.34	8.19 ± 0.07	2455676.1601	10.35	8.02 ± 0.07	2455681.7468	14.93	7.52 ± 0.05
2455670.4207	5.41	8.10 ± 0.07	2455676.2307	10.42	7.97 ± 0.06	2455681.8174	15.00	7.52 ± 0.05
2455670.4912	5.48	8.17 ± 0.07	2455676.3012	10.49	7.91 ± 0.06	2455681.8880	15.07	7.43 ± 0.05
2455670.5617	5.55	8.05 ± 0.07	2455676.3718	10.56	7.79 ± 0.06	2455681.9586	15.14	7.54 ± 0.05
2455670.6322	5.62	8.10 ± 0.07	2455676.4423	10.63	8.02 ± 0.07	2455682.0292	15.21	7.56 ± 0.05
2455670.7027	5.69	8.10 ± 0.07	2455676.5129	10.70	7.85 ± 0.06	2455682.1000	15.28	7.51 ± 0.05
2455670.7732	5.76	8.02 ± 0.07	2455676.5834	10.77	7.84 ± 0.06	2455682.1706	15.35	7.51 ± 0.05
2455670.8437	5.83	8.04 ± 0.07	2455676.6540	10.84	8.02 ± 0.07	2455682.2412	15.42	7.55 ± 0.05
2455670.9142	5.90	8.06 ± 0.07	2455676.7245	10.91	8.02 ± 0.07	2455682.3118	15.49	7.55 ± 0.05
2455670.9847	5.97	8.06 ± 0.07	2455676.7950	10.98	7.99 ± 0.07	2455682.3824	15.56	7.53 ± 0.05
2455671.0552	6.04	8.12 ± 0.07			8.09 ± 0.07	2455682.4530	15.63	7.51 ± 0.05

continued on next page

Table 5.2 – continued

JD	t	m_{SMEI}	JD	t	m_{SMEI}	JD	t	m_{SMEI}
2455682.7206	16.93	7.37 ± 0.05	2455688.2229	22.43	7.00 ± 0.04	2455692.8786	27.09	6.83 ± 0.04
2455682.7912	17.00	7.38 ± 0.05	2455688.2934	22.50	6.96 ± 0.04	2455692.9492	27.16	6.75 ± 0.04
2455682.8617	17.07	7.37 ± 0.05	2455688.3640	22.57	7.01 ± 0.04	2455693.0197	27.23	6.67 ± 0.04
2455682.9322	17.14	7.34 ± 0.05	2455688.4345	22.64	7.04 ± 0.04	2455693.0902	27.30	6.64 ± 0.04
2455683.0028	17.21	7.32 ± 0.05	2455688.5051	22.71	7.08 ± 0.04	2455693.1608	27.37	6.60 ± 0.03
2455683.0733	17.28	7.23 ± 0.05	2455688.5756	22.78	7.10 ± 0.04	2455693.2313	27.44	6.62 ± 0.03
2455683.1439	17.35	7.22 ± 0.05	2455688.6461	22.85	7.16 ± 0.04	2455693.3018	27.51	6.59 ± 0.03
2455683.2144	17.42	7.17 ± 0.04	2455688.7167	22.92	7.17 ± 0.04	2455693.3724	27.58	6.61 ± 0.03
2455683.2850	17.49	7.21 ± 0.05	2455688.7872	22.99	7.07 ± 0.04	2455693.4429	27.65	6.51 ± 0.03
2455683.3555	17.56	7.23 ± 0.05	2455688.8578	23.06	7.21 ± 0.05	2455693.5134	27.72	6.43 ± 0.03
2455683.4260	17.63	7.21 ± 0.05	2455688.9283	23.14	7.25 ± 0.05	2455693.5839	27.79	6.33 ± 0.03
2455683.4966	17.70	7.14 ± 0.04	2455688.9988	23.21	7.27 ± 0.05	2455693.6544	27.86	6.48 ± 0.03
2455683.5671	17.77	7.31 ± 0.05	2455689.0694	23.28	7.27 ± 0.05	2455693.7249	27.93	6.55 ± 0.03
2455683.6376	17.84	7.33 ± 0.05	2455689.1399	23.35	7.36 ± 0.05	2455693.7954	28.00	6.58 ± 0.03
2455683.7081	17.91	7.23 ± 0.05	2455689.2105	23.42	7.37 ± 0.05	2455693.8659	28.07	6.57 ± 0.03
2455683.7786	17.98	7.17 ± 0.04	2455689.2810	23.49	7.26 ± 0.05	2455693.9364	28.14	6.65 ± 0.03
2455683.8491	18.05	7.15 ± 0.04	2455689.3516	23.56	7.26 ± 0.05	2455694.0069	28.21	6.57 ± 0.03
2455683.9196	18.12	7.15 ± 0.04	2455689.4221	23.63	7.29 ± 0.05	2455694.0774	28.28	6.65 ± 0.04
2455683.9901	18.19	7.09 ± 0.04	2455689.4927	23.70	7.42 ± 0.05	2455694.1479	28.35	6.55 ± 0.03
2455684.0606	18.26	7.09 ± 0.04	2455689.5632	23.77	7.42 ± 0.05	2455694.2184	28.42	6.43 ± 0.03
2455684.1311	18.33	7.09 ± 0.04	2455689.6337	23.84	7.32 ± 0.05	2455694.2889	28.49	6.41 ± 0.03
2455684.2016	18.40	7.03 ± 0.04	2455689.7043	23.91	7.32 ± 0.05	2455694.3594	28.56	6.50 ± 0.03
2455684.2721	18.47	7.09 ± 0.04	2455689.7748	23.98	7.36 ± 0.05	2455694.4299	28.63	6.77 ± 0.04
2455684.3426	18.54	7.01 ± 0.04	2455689.8453	24.05	7.43 ± 0.05	2455694.5004	28.70	6.51 ± 0.03
2455684.4131	18.61	7.00 ± 0.04	2455689.9159	24.12	7.30 ± 0.05	2455694.5709	28.77	6.49 ± 0.03
2455684.4836	18.68	6.99 ± 0.04	2455689.9864	24.19	7.33 ± 0.05	2455694.6414	28.84	6.51 ± 0.03
2455684.5541	18.75	6.98 ± 0.04	2455690.0569	24.26	7.36 ± 0.05	2455694.7119	28.91	6.84 ± 0.04
2455684.6246	18.82	7.08 ± 0.04	2455690.1275	24.33	7.20 ± 0.05	2455694.7824	28.98	6.75 ± 0.04
2455684.6951	18.89	7.09 ± 0.04	2455690.1980	24.40	7.28 ± 0.05	2455694.8529	29.05	6.75 ± 0.04
2455684.7656	18.96	7.07 ± 0.04	2455690.2686	24.47	7.22 ± 0.05	2455694.9234	29.12	6.68 ± 0.04
2455684.8361	19.03	7.03 ± 0.04	2455690.3391	24.54	7.24 ± 0.05	2455694.9939	29.19	6.65 ± 0.04
2455684.9066	19.10	7.09 ± 0.04	2455690.4097	24.61	7.28 ± 0.05	2455695.0644	29.26	6.70 ± 0.04
2455684.9771	19.17	7.10 ± 0.04	2455690.4802	24.68	7.28 ± 0.05	2455695.1349	29.33	6.70 ± 0.04
2455685.0476	19.24	7.10 ± 0.04	2455690.5508	24.75	7.17 ± 0.04	2455695.2054	29.40	6.73 ± 0.04
2455685.1181	19.31	7.16 ± 0.04	2455690.6213	24.82	7.17 ± 0.04	2455695.2759	29.47	6.72 ± 0.04
2455685.1886	19.38	7.09 ± 0.04	2455690.6919	24.89	7.08 ± 0.04	2455695.3464	29.54	6.69 ± 0.04
2455685.2591	19.45	7.03 ± 0.04	2455690.7624	24.96	7.00 ± 0.04	2455695.4169	29.61	6.65 ± 0.04
2455685.3296	19.52	7.03 ± 0.04	2455690.8329	25.03	6.89 ± 0.04	2455695.4874	29.68	6.70 ± 0.04
2455685.4001	19.59	7.04 ± 0.04	2455690.9035	25.10	6.93 ± 0.04	2455695.5579	29.75	6.86 ± 0.04
2455685.4706	19.66	7.04 ± 0.04	2455690.9740	25.17	6.86 ± 0.04	2455695.6284	29.82	6.87 ± 0.04
2455685.5411	19.73	7.04 ± 0.04	2455691.0446	25.24	6.79 ± 0.04	2455695.6989	29.89	6.79 ± 0.04
2455685.6116	19.80	7.05 ± 0.04	2455691.1151	25.31	6.89 ± 0.04	2455695.7694	29.96	6.81 ± 0.04
2455685.6821	19.87	7.04 ± 0.04	2455691.1857	25.38	6.85 ± 0.04	2455695.8399	30.03	6.77 ± 0.04
2455685.7526	19.94	7.04 ± 0.04	2455691.2562	25.45	6.86 ± 0.04	2455695.9104	30.10	6.87 ± 0.04
2455685.8231	20.01	7.04 ± 0.04	2455691.3267	25.52	6.79 ± 0.04	2455695.9809	30.17	6.79 ± 0.04
2455685.8936	20.08	6.97 ± 0.04	2455691.3972	25.59	6.80 ± 0.04	2455696.0514	30.24	6.81 ± 0.04
2455685.9641	20.15	7.10 ± 0.04	2455691.4678	25.66	6.85 ± 0.04	2455696.1219	30.31	6.77 ± 0.04
2455686.0346	20.22	7.14 ± 0.04	2455691.5383	25.73	6.94 ± 0.04	2455696.1924	30.38	6.59 ± 0.03
2455686.1051	20.29	7.05 ± 0.04	2455691.6089	25.80	6.78 ± 0.04	2455696.2629	30.45	6.61 ± 0.03
2455686.1756	20.36	7.02 ± 0.04	2455691.6794	25.87	6.89 ± 0.04	2455696.3334	30.52	6.58 ± 0.03
2455686.2461	20.43	6.99 ± 0.04	2455691.7500	25.94	6.88 ± 0.04	2455696.4039	30.59	6.61 ± 0.03
2455686.3166	20.50	7.02 ± 0.04	2455691.8205	26.01	6.84 ± 0.04	2455696.4744	30.66	6.60 ± 0.03
2455686.3871	20.57	6.88 ± 0.04	2455691.8910	26.08	6.84 ± 0.04	2455696.5449	30.73	6.61 ± 0.03
2455686.4576	20.64	6.91 ± 0.04	2455691.9616	26.15	6.78 ± 0.04	2455696.6154	30.80	6.63 ± 0.04
2455686.5281	20.71	6.90 ± 0.04	2455692.0321	26.22	6.79 ± 0.04	2455696.6859	30.87	6.67 ± 0.04
2455686.5986	20.78	6.88 ± 0.04	2455692.1026	26.29	6.80 ± 0.04	2455696.7564	30.94	6.79 ± 0.04
2455686.6691	20.85	6.88 ± 0.04	2455692.1732	26.36	6.80 ± 0.04	2455696.8269	31.01	6.79 ± 0.04
2455686.7396	20.92	6.91 ± 0.04	2455692.2438	26.43	6.79 ± 0.04	2455696.8974	31.08	6.82 ± 0.04
2455686.8101	20.99	6.97 ± 0.04	2455692.3143	26.50	6.87 ± 0.04	2455696.9679	31.15	6.77 ± 0.04
2455686.8806	21.06	7.05 ± 0.04	2455692.3848	26.57	6.91 ± 0.04	2455697.0384	31.22	6.86 ± 0.04
2455686.9511	21.13	7.03 ± 0.04	2455692.4554	26.64	6.94 ± 0.04	2455697.1089	31.29	6.74 ± 0.04
2455687.0216	21.20	7.03 ± 0.04	2455692.5260	26.71	6.94 ± 0.04	2455697.1794	31.36	6.88 ± 0.04
2455687.0921	21.27	7.01 ± 0.04	2455692.5965	26.78	6.93 ± 0.04	2455697.2499	31.43	7.04 ± 0.04
2455687.1626	21.34	6.95 ± 0.04	2455692.6670	26.85	6.81 ± 0.04	2455697.3204	31.50	6.99 ± 0.04
2455687.2331	21.41	6.93 ± 0.04	2455692.7376	26.92	6.72 ± 0.04	2455697.3909	31.57	6.71 ± 0.04
2455687.3036	21.48	6.98 ± 0.04	2455692.8081	26.99	6.77 ± 0.04	2455697.4614	31.64	6.80 ± 0.04

continued on next page

Table 5.2 – continued

JD	t	m_{SMEI}	JD	t	m_{SMEI}	JD	t	m_{SMEI}
2455698.0281	32.24	6.68 ± 0.04	2455702.5427	36.75	7.35 ± 0.05	2455709.5966	43.80	7.16 ± 0.04
2455698.0987	32.31	6.59 ± 0.03	2455702.6132	36.82	7.34 ± 0.05	2455709.6672	43.87	7.29 ± 0.05
2455698.1692	32.38	6.64 ± 0.04	2455702.6837	36.89	7.32 ± 0.05	2455709.7377	43.94	7.32 ± 0.05
2455698.2397	32.45	6.84 ± 0.04	2455702.7543	36.96	7.30 ± 0.05	2455709.8083	44.02	7.21 ± 0.05
2455698.3103	32.52	6.94 ± 0.04	2455702.8248	37.03	7.22 ± 0.05	2455709.8788	44.09	7.41 ± 0.05
2455698.3808	32.59	6.92 ± 0.04	2455702.8954	37.10	7.20 ± 0.05	2455710.3020	44.51	7.49 ± 0.05
2455698.4513	32.66	6.90 ± 0.04	2455702.9624	37.17	7.14 ± 0.04	2455710.3726	44.58	7.34 ± 0.05
2455698.5219	32.73	6.93 ± 0.04	2455703.0365	37.24	7.26 ± 0.05	2455710.4431	44.65	7.50 ± 0.05
2455698.5924	32.80	6.97 ± 0.04	2455703.1070	37.31	7.34 ± 0.05	2455710.5137	44.72	7.14 ± 0.04
2455698.6630	32.87	7.09 ± 0.04	2455703.1775	37.38	7.25 ± 0.05	2455710.5842	44.79	7.34 ± 0.05
2455698.7335	32.94	6.90 ± 0.04	2455703.2481	37.46	7.21 ± 0.05	2455710.6547	44.86	7.52 ± 0.05
2455698.8746	33.08	7.11 ± 0.04	2455703.3186	37.53	7.14 ± 0.04	2455710.7253	44.93	7.63 ± 0.06
2455698.9451	33.15	7.20 ± 0.05	2455703.3892	37.60	7.09 ± 0.04	2455710.7958	45.00	7.49 ± 0.05
2455699.0157	33.22	7.14 ± 0.04	2455703.4597	37.67	7.12 ± 0.04	2455710.8663	45.07	7.55 ± 0.05
2455699.0862	33.29	7.23 ± 0.05	2455703.5302	37.74	7.11 ± 0.04	2455710.9369	45.14	7.66 ± 0.06
2455699.1567	33.36	7.18 ± 0.04	2455703.6008	37.81	7.12 ± 0.04	2455711.0074	45.21	7.61 ± 0.05
2455699.2273	33.43	7.20 ± 0.05	2455703.6713	37.88	7.04 ± 0.04	2455711.0780	45.28	7.39 ± 0.05
2455699.2978	33.50	7.21 ± 0.05	2455703.7418	37.95	7.06 ± 0.04	2455711.1485	45.36	7.32 ± 0.05
2455699.3684	33.58	7.10 ± 0.04	2455703.8124	38.02	7.17 ± 0.04	2455711.1485	45.36	7.30 ± 0.05
2455699.4389	33.65	7.05 ± 0.04	2455703.8829	38.09	7.06 ± 0.04	2455711.2896	45.50	7.37 ± 0.05
2455699.5095	33.72	7.03 ± 0.04	2455704.6589	38.87	7.21 ± 0.05	2455711.4307	45.64	7.56 ± 0.05
2455699.5800	33.79	6.98 ± 0.04	2455704.7294	38.94	7.16 ± 0.04	2455711.7128	45.92	7.56 ± 0.05
2455699.6505	33.86	6.90 ± 0.04	2455704.7999	39.01	7.20 ± 0.05	2455711.8539	46.06	7.87 ± 0.06
2455699.7211	33.93	6.89 ± 0.04	2455704.8705	39.08	7.16 ± 0.04	2455711.9244	46.13	7.42 ± 0.05
2455699.7916	34.00	6.83 ± 0.04	2455704.9410	39.15	7.09 ± 0.04	2455711.9950	46.20	7.67 ± 0.06
2455700.0032	34.21	7.00 ± 0.04	2455705.0116	39.22	7.02 ± 0.04	2455712.0655	46.27	7.42 ± 0.05
2455700.0738	34.28	6.96 ± 0.04	2455705.0821	39.29	6.94 ± 0.04	2455712.1360	46.34	7.38 ± 0.05
2455700.1443	34.35	6.98 ± 0.04	2455705.1527	39.36	6.87 ± 0.04	2455712.2066	46.41	7.63 ± 0.06
2455700.2149	34.42	7.07 ± 0.04	2455705.2232	39.43	6.88 ± 0.04	2455712.2771	46.48	7.40 ± 0.05
2455700.2854	34.49	7.10 ± 0.04	2455705.2937	39.50	6.87 ± 0.04	2455712.3477	46.55	7.50 ± 0.05
2455700.3559	34.56	7.18 ± 0.05	2455707.2688	41.48	7.13 ± 0.04	2455712.4185	46.63	7.52 ± 0.05
2455700.4265	34.63	7.22 ± 0.05	2455707.3394	41.55	7.24 ± 0.05	2455712.4887	46.70	7.50 ± 0.05
2455700.4970	34.70	7.25 ± 0.05	2455707.4099	41.62	7.14 ± 0.04	2455712.5593	46.77	7.32 ± 0.05
2455700.7086	34.92	7.36 ± 0.05	2455707.4805	41.69	7.23 ± 0.05	2455712.6298	46.84	7.22 ± 0.05
2455700.7792	34.99	7.34 ± 0.05	2455707.6921	41.90	7.11 ± 0.04	2455712.7004	46.91	7.21 ± 0.05
2455700.8497	35.06	7.35 ± 0.05	2455707.7626	41.97	7.12 ± 0.04	2455712.7709	46.98	7.37 ± 0.05
2455700.9203	35.13	7.41 ± 0.05	2455707.8331	42.04	7.16 ± 0.04	2455712.8414	47.05	7.21 ± 0.05
2455700.9908	35.20	7.36 ± 0.05	2455707.9037	42.11	7.12 ± 0.04	2455712.9120	47.12	7.28 ± 0.05
2455701.0613	35.27	7.31 ± 0.05	2455707.9743	42.18	7.13 ± 0.04	2455712.9825	47.19	7.27 ± 0.05
2455701.1319	35.34	7.22 ± 0.05	2455708.0448	42.25	7.15 ± 0.04	2455713.0530	47.26	7.39 ± 0.05
2455701.2024	35.41	7.23 ± 0.05	2455708.1153	42.32	7.21 ± 0.05	2455713.1236	47.33	7.37 ± 0.05
2455701.2730	35.48	7.23 ± 0.05	2455708.1859	42.39	7.12 ± 0.04	2455713.1941	47.40	7.38 ± 0.05
2455701.3435	35.55	7.22 ± 0.05	2455708.2564	42.46	7.14 ± 0.04	2455713.2647	47.47	7.40 ± 0.05
2455701.4140	35.62	7.28 ± 0.05	2455708.3269	42.53	6.90 ± 0.04	2455713.3352	47.54	7.38 ± 0.05
2455701.4846	35.69	7.29 ± 0.05	2455708.3975	42.60	7.28 ± 0.05	2455713.6174	47.82	7.41 ± 0.05
2455701.5551	35.76	7.23 ± 0.05	2455708.4680	42.67	7.06 ± 0.04	2455713.6879	47.89	7.37 ± 0.05
2455701.6257	35.83	7.24 ± 0.05	2455708.5386	42.75	7.24 ± 0.05	2455713.7584	47.97	7.37 ± 0.05
2455701.6962	35.90	7.27 ± 0.05	2455708.6091	42.82	7.30 ± 0.05	2455713.8290	48.04	7.40 ± 0.05
2455701.7668	35.97	7.21 ± 0.05	2455708.6796	42.89	7.19 ± 0.05	2455713.8995	48.11	7.39 ± 0.05
2455701.8373	36.04	7.33 ± 0.05	2455708.7502	42.96	7.27 ± 0.05	2455713.9700	48.18	7.41 ± 0.05
2455701.9078	36.11	7.29 ± 0.05	2455708.8207	43.03	7.24 ± 0.05	2455714.0406	48.25	7.37 ± 0.05
2455701.9783	36.19	7.29 ± 0.05	2455708.8913	43.10	7.10 ± 0.04	2455714.1111	48.32	7.50 ± 0.05
2455702.0489	36.26	7.24 ± 0.05	2455709.0323	43.24	7.17 ± 0.04	2455714.1817	48.39	7.21 ± 0.05
2455702.1195	36.33	7.34 ± 0.05	2455709.1029	43.31	7.22 ± 0.05	2455714.2522	48.46	7.36 ± 0.05
2455702.1900	36.40	7.30 ± 0.05	2455709.2440	43.45	7.06 ± 0.04	2455714.3227	48.53	7.42 ± 0.05
2455702.2605	36.47	7.37 ± 0.05	2455709.3145	43.52	7.14 ± 0.04	2455714.3933	48.60	7.49 ± 0.05
2455702.3311	36.54	7.35 ± 0.05	2455709.3850	43.59	7.19 ± 0.05	2455714.4640	48.95	7.31 ± 0.05
2455702.4016	36.61	7.29 ± 0.05	2455709.4556	43.66	7.24 ± 0.05	2455714.8165	49.02	7.26 ± 0.05
2455702.4721	36.68	7.31 ± 0.05	2455709.5261	43.73	7.07 ± 0.04			

Chapter 6

T Pyxidis in its 2011 Outburst

6.1 Introduction

In this Chapter, we first describe our extensive photometric and spectroscopic datasets. We then use the results of these to explore the various phases of development of the nova both in comparison to those found in other novae and also with models of the outburst. Periodicities in the SMEI light curve are also investigated. Comparison with extensive observations at X-ray and radio wavelengths is detailed. The summary of this Chapter has been published in Surina et al. (2013b) while the full paper will be published in Surina et al. (2014).

6.1.1 Central System and Surroundings

In a classical nova, the mass of the WD (M_{WD}) is typically around $1M_{\odot}$ (Uthas et al., 2010). For a RN, in order for the thermonuclear runaway (TNR) to occur on a short time scale, the WD has to be more massive (i.e. $M_{WD} \gtrsim 1M_{\odot}$) and luminous with high \dot{M}_{acc} (Starrfield, 2008a) implying that the secondary star has to be evolved. As a result of the unusually high \dot{M}_{acc} , T Pyx is more luminous than CNe at quiescence in which the Roche lobe filling main-sequence donor star is transferring mass onto a high-mass WD. Unfortunately, M_{WD} is not accurately known for this system.

Based on optical spectroscopy obtained at the Very Large Telescope and the Magellan Telescope, Uthas et al. (2010) estimated a mass ratio $q=0.2\pm0.03$. Thus with the mass of the secondary star $M_2=0.14\pm0.03M_\odot$ derived from the main-sequence mass-radius relation of a 5-Gyr isochrone given by Baraffe et al. (1998) then the mass of the primary WD is $M_{WD}=0.7\pm0.2M_\odot$. This estimate of M_{WD} is lower than that expected from previous theoretical studies which range from 1.30-1.37 M_\odot (Kato, 1990), 1.25-1.30 M_\odot (Schaefer et al., 2010a), and 1.25-1.4 M_\odot (Selvelli et al., 2010). Therefore Uthas et al. (2010) turned the problem around by mentioning that if $M_{WD}>1M_\odot$ then $M_2>0.2M_\odot$ for their estimated $q=0.2$ mass ratio.

The results of Uthas et al. (2010) were derived without putting any spectroscopic constraints to the mass of the secondary star since T Pyx has a bright accretion disk that outshines the spectral signature from the donor in the optical. They however used the period-density relation for a Roche lobe filling secondary star given by Eggleton (1983) to set some constraints. They adopted 0-20% inflation to the donor star while Patterson et al. (2005) and Knigge (2006) suggested the donor stars in ordinary CVs below the period gap are inflated by approximately 10% due to mass loss relative to ordinary main-sequence stars of the same mass.

The orbital period at quiescence, $P=0^d.076$, is well established (Patterson et al., 1998; Schaefer et al., 1992; Uthas et al., 2010) with an increasing period $\dot{P} = 6 \times 10^{-10}$ (Patterson et al., 1998). The light curve had a highly significant modulation in the 1966 eruption with a period of 0.0990 ± 0.0001 days found by Schaefer (1990). Other transient periodicities at 0.109 ± 0.001 days and 1.240 ± 0.001 days were found by Patterson et al. (1998) in quiescence. Patterson et al. (1998) suggested that the 1.24-day period might arise from precession in the accretion disk as it is roughly in the range of that in CVs while there is no explanation for the 0.1098-day period.

The orbital inclination, i , is thought to be low from the spectral profiles and low radial velocity amplitude (Uthas et al., 2010). It has been estimated to be $\sim 6^\circ$ (Shahbaz et al., 1997), $10^\circ-20^\circ$ (Patterson et al., 1998), $20^\circ-30^\circ$ (Selvelli et al., 2010), $i=10^\circ\pm 2^\circ$ (Uthas et al., 2010) and recently $i=15^\circ$ (Chesneau et al., 2011). Such a fairly low inclination is suggested to be the cause of the long dip, which lasts for half of the orbit

in the flat top light curve, due to the heating effect on the companion star (Patterson et al., 1998).

T Pyx is the only RN that presents a persistent nova shell as shown in Figure 6.1. This has a radius of $\sim 5''$, discovered by Duerbeck & Seitter (1979). A fainter outer halo around the shell discovered by Shara et al. (1997) extends to a radius of $\sim 10''$. The shell has been found to be slowly expanding with thousands of discrete knots (Duerbeck & Seitter, 1979; Williams, 1982; Shara et al., 1997) and is suggested to be a result of the shocks from the new eruption ejecta that interact with the ejecta from the previous eruption (Contini & Prialnik, 1997).

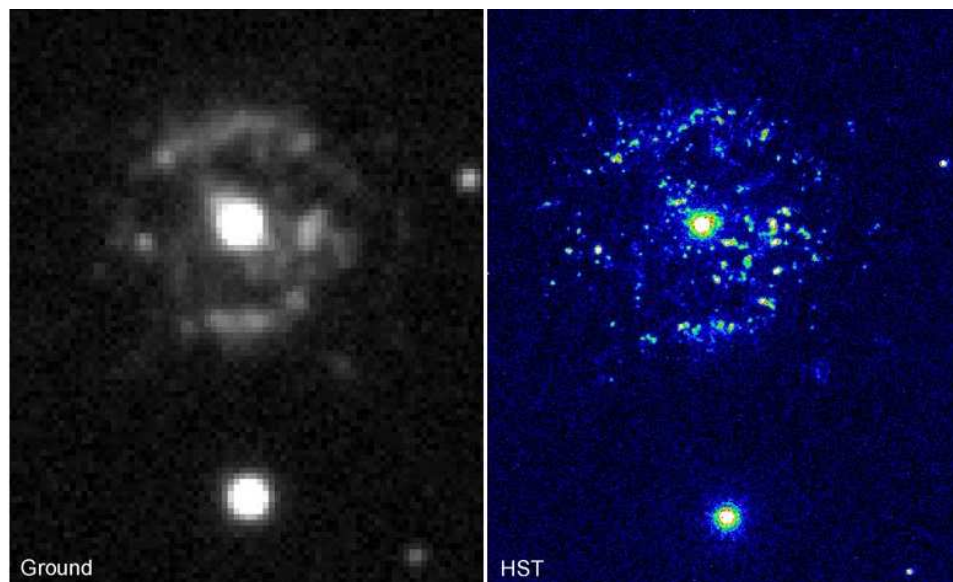


Figure 6.1: T Pyx and its shell (on 18 September 1997) as seen from the ground by the ESO 5.58m NTT (left) and from space by *HST* WFPC2 (right). Image Credit: M. M. Shara, R. E. Williams, and D. R. Zurek (STScI); R. Gilmozzi (ESO); D. Prialnik (Tel Aviv University); and NASA. The excellent angular resolution of *HST* allow us to see that shell consists of thousands knots which are extremely slowly expanding.

Using *HST* images over 13 years, Schaefer et al. (2010a) inferred that a nova shell was first ejected in the year 1866 ± 5 at a velocity of $500\text{--}715 \text{ km s}^{-1}$ with shell total ejected mass $\sim 10^{-4.5} M_{\odot}$. This very low velocity and too high ejected shell mass for a typical RN allowed them to conclude that the first eruption in 1866 must have been a normal classical nova eruption with a very long time of prior quiescence. T Pyx is proposed to have originally formed with a high mass WD (Schaefer et al., 2010a)

and the 1866 eruption has triggered the high- \dot{M}_{acc} -wind-driven phase suggested by Knigge et al. (2000). However this phase was not completely self-sustained (Uthas et al., 2010) resulting in the decreasing nuclear burning rate and brightness as seen in the 1890 eruption and later.

6.1.2 The Outburst in 2011

The outburst of T Pyx in 2011 was discovered by AAVSO observer M. Linnolt at a visual magnitude of 13.0 on 2011 Apr 14.29 UT (JD 2455665.7931, hereafter $t=0$ day) and published in Schaefer et al. (2013). Figure 6.2 presents the AAVSO optical light curves of T Pyx in its 2011 outburst from before the eruption to 2012 Mar 31 (JD 2456018, $t=353$ days).

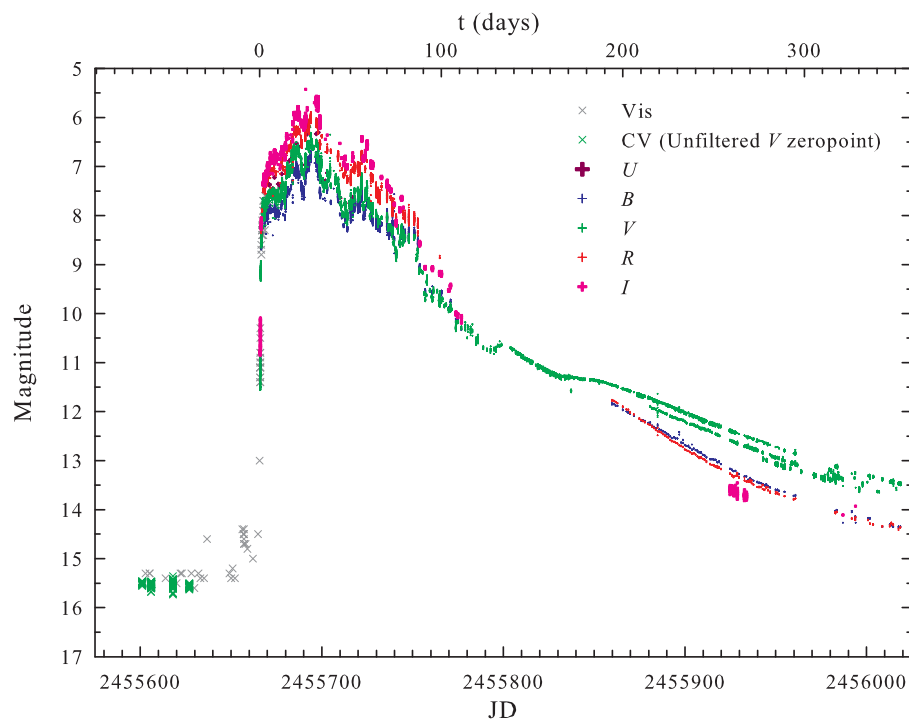


Figure 6.2: The AAVSO optical light curves of T Pyx in its 2011 outburst.

Schaefer et al. (2013) reported that from 2008 to 2011 Mar 31 (JD 2455652, $t=-13.8$ days) T Pyx's brightness was steady at $V=15.5$ with the usual periodic variation of <0.2 mag and it was never brighter than $V=15.0$. On 2011 Apr 5.51 UT, it was observed

with variations from $V=14.4$ - 14.7 and continued to fade slowly until 2011 Apr 10.54 UT (JD 2455662.0417, $t=-3.7$ days). There was a short brightness increase, a so called “pre-eruption rise” (peak around $V=14.4$ mag) as shown in Figure 6.3, occurring about 13 days prior to the initial rise (Schaefer et al., 2013). After the sharp initial rise on day $t=0$, a small fading occurred roughly 2 days after that (Schaefer et al., 2013).

Patterson et al. (2013) studied the post-outburst light curve in 2011 and found that an orbital period signal appeared by $t=170$ days ($V=11.2$) with a period increase of $0.0054(7)\%$ implied to be the result of mass ejection from the WD. They derived an ejected mass of at least $3\times 10^{-5}M_{\odot}$, similar to that in CNe.

Spectroscopic observations of the 2011 outburst are discussed in Shore et al. (2011, 2013) and in Imamura & Tanabe (2012). Shore et al. (2011) report high resolution observations at 7 epochs from $t=1.6$ - 46.6 days and Shore et al. (2013) describe observations at a further 4 epochs much later in the outburst ($t=179$, 180, 349 and 360 days). Imamura & Tanabe (2012) meanwhile report 11 epochs of low resolution spectroscopy at early times ($t=2.7$ - 30.8 days). Comparison with results of our more extensive and intensive spectroscopic coverage is given below, together with high cadence photometry.

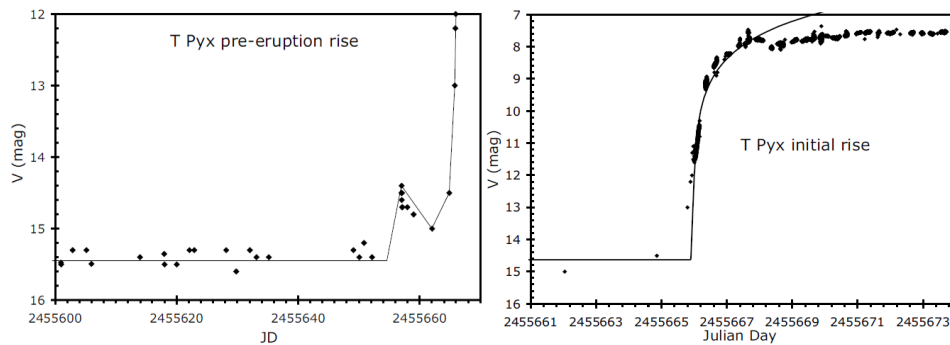


Figure 6.3: The pre-eruption rise (left) is believed not to be a part of the TNR. The initial rise (right) shows the TNR has started with a small break at about 2 days later which indicates that the photosphere may have receded (from Schaefer et al., 2013).

6.2 Observations

6.2.1 Photometric Observations from SMEI

Photometric observations of T Pyx were obtained with the Solar Mass Ejection Imager (SMEI, see Chapter 5). In this case, the white light observations of T Pyx by SMEI were made from 2011 Apr 15.84 UT (JD 2455667.3422, $t=1.5$ days) to 2011 Jun 2.32 UT (JD 2455714.8165, $t=49.0$ days) - see Figure 6.4.

6.2.2 Spectroscopic Observations

Spectroscopic observations were secured with the 1.5m telescope of the Small and Moderate Aperture Research Telescope System (SMARTS) and the 2m Liverpool Telescope (LT). A log of the observations is given in Table 6.1.

Small and Moderate Aperture Research Telescope System (SMARTS)

The 1.5m telescope of the SMARTS II Consortium located at CTIO Chile is equipped with a long-slit R-C spectrograph. An ultraviolet transmitting grating is used at the $f/7.5$ focus with a plate scale 18.1 arcseconds/mm and a 1200×800 CCD. We obtained 99 low-to-moderate-resolution ($300 < R < 3400$) optical spectra of T Pyx. These spectra include 49 moderate-resolution spectra in the blue region ($3655\text{-}5424\text{\AA}$ and $3870\text{-}4544\text{\AA}$), 37 moderate-resolution spectra in the red region ($5630\text{-}6950\text{\AA}$), and 13 low-resolution spectra in a wide wavelength region ($3250\text{-}9520\text{\AA}$). Fifty six spectra of particular interest here were obtained from 2011 Apr 14 (JD 2455666.55056, $t=0.757$ days, given hereafter 0.8 days), which was the earliest epoch T Pyx was observed spectroscopically, to 2011 Jul 3 (JD 2455746.49198, $t=80$ days). Another 43 spectra were obtained from 2011 Sep 15 (JD 2455820.92030, $t=155.127$) to 2011 Dec 19 (JD 2455915.72555, $t=249.9$ days). All data were obtained pre-reduced through the SMARTS atlas - see Walter et al. (2012)¹.

¹ Available online at <http://www.astro.sunysb.edu/fwalter/SMARTS/NovaAtlas/tpyx/tpyx.html>

Table 6.1: Log of optical spectral observations. The time in the third column is counted from the discovery on 2011 Apr 14.29 UT (JD 2455665.7931, $t=0$ days).

Observation dates	JD	t (d)	λ range (Å)*	Telescope	Observation dates	JD	t (d)	λ range (Å)*	Telescope
2011-04-14	2455666.55056	0.8	5630-6950	SMARTS	2011-06-23	2455736.45998	70.7	3870-4544	SMARTS
2011-04-15	2455667.49308	1.7	3250-9520	SMARTS	2011-06-25	2455738.44247	72.6	3250-9520	SMARTS
2011-04-16	2455668.44853	2.7	3655-5424	SMARTS	2011-06-26	2455739.45381	73.7	3870-4544	SMARTS
2011-04-17	2455669.43890	3.6	5630-6950	SMARTS	2011-06-28	2455741.40939	75.6	3870-4544	SMARTS
2011-04-18	2455670.51676	4.7	3870-4544	SMARTS	2011-06-30	2455743.44596	77.7	3655-5424	SMARTS
2011-04-19	2455671.47293	5.7	5630-6950	SMARTS	2011-07-01	2455744.47839	78.7	3250-9520	SMARTS
2011-04-22	2455674.38198	8.6	3900-5700, 5800-9400	LT	2011-07-02	2455745.46245	79.7	3870-4544	SMARTS
2011-04-22*	2455674.61188	8.8	5630-6950	SMARTS	2011-07-03	2455746.49198	80.7	5630-6950	SMARTS
2011-04-23	2455675.38192	9.6	3900-5700, 5800-9400	LT	2011-09-15	2455820.92030	155.1	3655-5424	SMARTS
2011-04-23	2455675.46047	9.7	3655-5424	SMARTS	2011-09-19	2455824.89457	159.1	3655-5424	SMARTS
2011-04-24	2455676.38186	10.6	3900-5700, 5800-9400	LT	2011-09-21	2455826.89632	161.1	5630-6950	SMARTS
2011-04-24	2455676.50600	10.7	5630-6950	SMARTS	2011-09-21a	2455826.92193	161.1	4060-4735	SMARTS
2011-04-25	2455677.38180	11.6	3900-5700, 5800-9400	LT	2011-09-23	2455828.91213	163.1	3250-9520	SMARTS
2011-04-25	2455677.44188	11.6	3655-5424	SMARTS	2011-09-25	2455830.87711	165.1	3655-5424	SMARTS
2011-04-27	2455679.45705	13.7	3655-5424	SMARTS	2011-09-27	2455832.89575	167.1	5630-6950	SMARTS
2011-04-28	2455680.55124	14.8	5630-6950	SMARTS	2011-09-29	2455834.86413	169.1	3870-4544	SMARTS
2011-04-29	2455681.38713	15.6	5630-6950	SMARTS	2011-10-03	2455838.86920	173.1	3870-4544	SMARTS
2011-05-01	2455683.51565	17.7	3250-9520	SMARTS	2011-10-03a	2455838.89211	173.1	5630-6950	SMARTS
2011-05-02	2455684.46054	18.7	3655-5424	SMARTS	2011-10-05	2455840.83755	175.0	3870-4544	SMARTS
2011-05-03	2455685.29780	19.5	3870-4544	SMARTS	2011-10-05a	2455840.87123	175.1	5630-6950	SMARTS
2011-05-04	2455686.44255	20.6	3870-4544	SMARTS	2011-10-07	2455842.85832	177.1	3250-9520	SMARTS
2011-05-05	2455687.45694	21.7	3655-5424	SMARTS	2011-10-09	2455844.85722	179.1	5630-6950	SMARTS
2011-05-07	2455689.46274	23.7	3655-5424	SMARTS	2011-10-15	2455850.84231	185.0	5630-6950	SMARTS
2011-05-08	2455690.45846	24.7	6230-7550	SMARTS	2011-10-16	2455851.86406	186.1	3250-9520	SMARTS
2011-05-09	2455691.47495	25.7	3655-5424	SMARTS	2011-10-17	2455852.86060	187.1	5630-6950	SMARTS
2011-05-10	2455692.45741	26.7	5630-6950	SMARTS	2011-10-19	2455854.83327	189.0	3655-5424	SMARTS
2011-05-11	2455693.46645	27.7	3655-5424	SMARTS	2011-10-23	2455858.83362	193.0	5630-6950	SMARTS
2011-05-13	2455695.45393	29.7	3655-5424	SMARTS	2011-10-29	2455864.78561	199.0	3655-5424	SMARTS
2011-05-14	2455696.55773	30.8	3870-4544	SMARTS	2011-11-01	2455867.83583	202.0	3250-9520	SMARTS
2011-05-15	2455697.45702	31.7	3250-9520	SMARTS	2011-11-03	2455869.82510	204.0	5630-6950	SMARTS
2011-05-16	2455698.43956	32.6	5630-6950	SMARTS	2011-11-05	2455871.82328	206.0	3655-5424	SMARTS
2011-05-17	2455699.46366	33.7	5985-9480	SMARTS	2011-11-15	2455881.78178	216.0	3870-4544	SMARTS
2011-05-18	2455700.40413	34.6	3655-5424	SMARTS	2011-11-15a	2455881.80037	216.0	5630-6950	SMARTS
2011-05-20	2455702.45740	36.7	5630-6950	SMARTS	2011-11-16	2455882.77670	217.0	3250-9520	SMARTS
2011-05-24	2455706.43767	40.6	3655-5424	SMARTS	2011-11-19	2455885.78113	220.0	3655-5424	SMARTS
2011-05-25	2455707.45922	41.7	3655-5424	SMARTS	2011-11-21	2455887.74116	221.9	3870-4544	SMARTS
2011-05-26	2455708.54164	42.7	3870-4544	SMARTS	2011-11-21a	2455887.84304	222.0	5630-6950	SMARTS
2011-05-29	2455711.37204	45.6	3655-5424	SMARTS	2011-11-23	2455889.74104	223.9	3250-9520	SMARTS
2011-05-30	2455712.45091	46.7	5630-6950	SMARTS	2011-11-25	2455891.80641	226.0	5630-6950	SMARTS
2011-05-31	2455713.45613	47.7	5630-6950	SMARTS	2011-11-29	2455895.69458	229.9	3655-5424	SMARTS
2011-06-01	2455714.43748	48.6	3250-9520	SMARTS	2011-12-08	2455904.67796	238.9	3655-5424	SMARTS
2011-06-02	2455715.50471	49.7	5630-6950	SMARTS	2011-12-09	2455905.69137	239.9	3870-4544	SMARTS
2011-06-03	2455715.51736	49.7	3655-5424	SMARTS	2011-12-12	2455908.67536	242.9	3655-5424	SMARTS
2011-06-08	2455721.51827	55.7	3655-5424	SMARTS	2011-12-13	2455909.81406	244.0	5630-6950	SMARTS
2011-06-09	2455722.45866	56.7	3870-4544	SMARTS	2011-12-14	2455910.66410	244.9	3870-4544	SMARTS
2011-06-10	2455723.47018	57.7	3250-9520	SMARTS	2011-12-14a	2455910.77023	245.0	5630-6950	SMARTS
2011-06-11	2455724.45218	58.7	3655-5424	SMARTS	2011-12-15	2455911.76083	246.0	3655-5424	SMARTS
2011-06-12	2455725.44831	59.7	5630-8860	SMARTS	2011-12-16	2455912.74787	247.0	3250-9520	SMARTS
2011-06-14	2455727.47669	61.7	5630-6950	SMARTS	2011-12-17	2455913.74309	247.9	5630-6950	SMARTS
2011-06-16	2455729.46994	63.7	5630-6950	SMARTS	2011-12-18	2455914.73296	248.9	3870-4544	SMARTS
2011-06-22	2455735.45566	69.7	3655-5424	SMARTS	2011-12-19	2455915.72555	249.9	5630-6950	SMARTS

* Spectra with λ range 3250-9520Å are taken with low resolution.

Liverpool Telescope (LT)

T Pyx's spectra on the nights of 2011 Apr 22-25 were secured using the FRODOSpec spectrograph (see Chapter 3) on LT over 3900-5700Å in the blue (R~2200) and 5800-9400Å in the red arm (R~2600), with exposures of 60 s. Data reduction was performed through a pipeline that initially performs bias, dark frame, and flat field subtraction. A spectroscopic standard star HD289002 ($\alpha=06^h45^m13^s.371$, $\delta=+02^\circ08'14''.70$) was observed at a similar airmass and used to remove instrumental and atmospheric response. We used the *onedspec* package in IRAF² to analyse all LT spectra.

6.3 Results and Discussion

6.3.1 SMEI Light Curves

The SMEI light curve was compiled from 533 observations (see Chapter 5) and provides unprecedented detail with high cadence data that are compared to AAVSO light curves as shown in Figures 6.4 and 6.5.

Phases of the 2011 Outburst from the SMEI Light Curve

We divide the SMEI light curve into 4 parts based on the idealised nova optical light curve given in Warner (2008) - see Figure 6.5:

1. *The initial rise (2011 Apr 15-16, $t=1.5-3.3$ days):* The first reliable detection of the nova outburst by SMEI occurred at the end of the rapid rise seen in AAVSO data, at $m_{SMEI}=8.80\pm0.09$ on 2011 Apr 15.84 UT (JD 2455667.3422, $t=1.5$ days). After that time SMEI observed T Pyx approximately every 102 minutes. The light curve rose to $m_{SMEI}=8.26$ on JD 2455668.0476 ($t=2.2$ days)

² IRAF is distributed by the National Optical Astronomy Observatories, which are operated by the Association of Universities for Research in Astronomy, Inc., under cooperative agreement with the National Science Foundation.

and began quasi-periodic variations (Hounsell et al., 2011) as shown in the top left panel of Figure 6.5. This phase ended at $t \sim 3.3$ days when the light curve began to flatten.

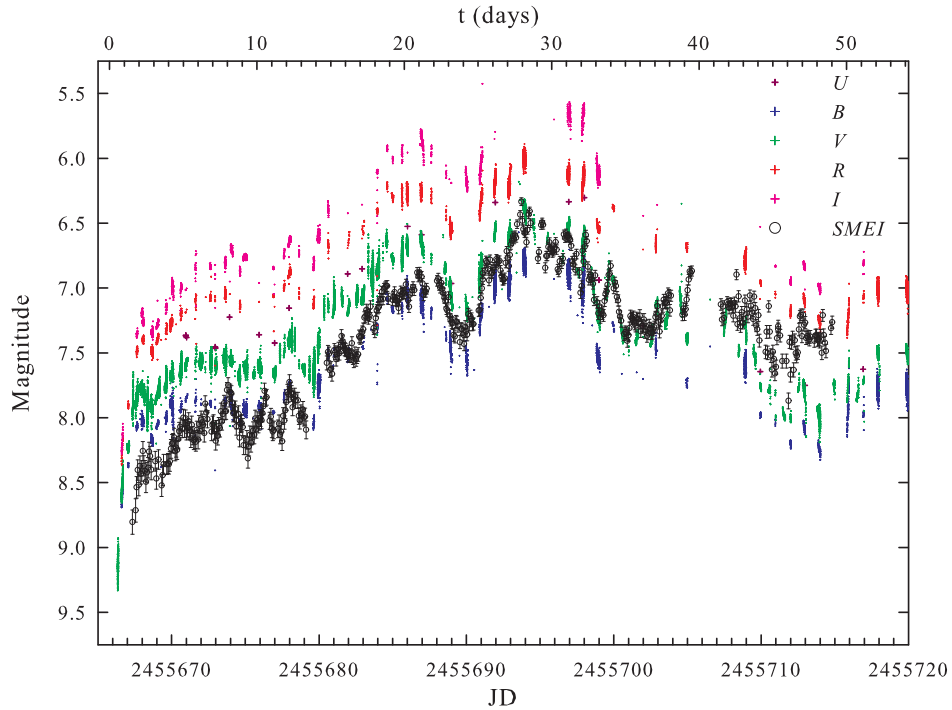


Figure 6.4: The SMEI light curve of T Pyx during its 2011 outburst (open black circles with error bars) compared to *UBVRI* light curves observed by AAVSO (plus signs).

2. *Pre-maximum halt* (2011 Apr 16-27, $t=3.3-13.3$ days): Following the initial rise, the SMEI light curve rose very slowly (noted as “almost plateau”, by Hounsell et al. (2011)) with clear quasi-periodic variations as shown in Figure 6.5 (b). The peak-to-peak times of the variations vary between 1.1-2.8 days. The magnitudes ranged between 7.7-8.5 mags. The first peak and dip of this variation was also noticed by Schaefer et al. (2013). However the AAVSO light curve does not clearly show the quasi-periodic variations detectable in the SMEI light curve. This phase may coincide with the pre-maximum halt defined as a pause at about 2 magnitudes below maximum for a few days for slow novae (Warner, 2008; Hounsell et al., 2010). There was then a gap in the SMEI data (due to instrumental problems) lasting 1.4 days ($t=13.3-14.7$ days).

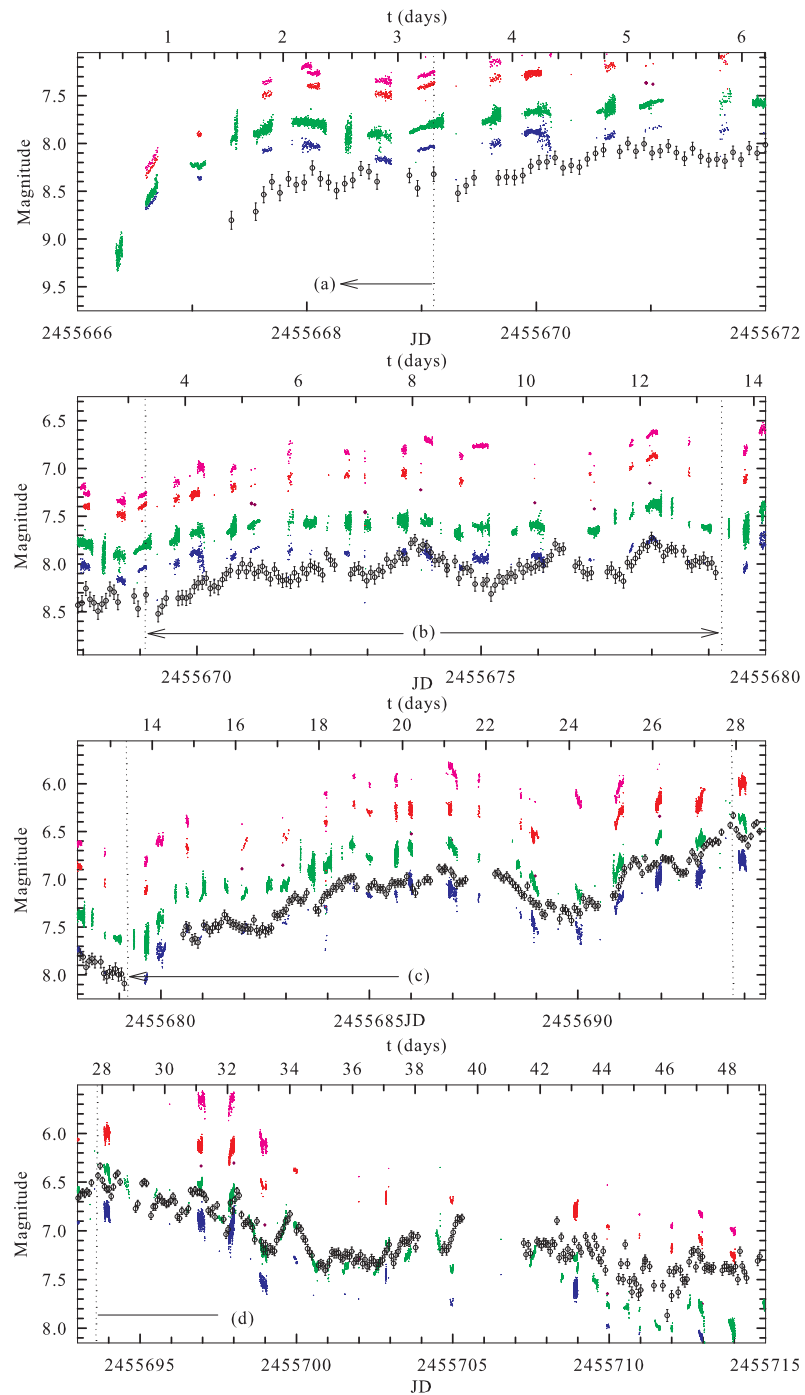


Figure 6.5: Four idealised phases of the SMEI light curves including the initial rise (a), the pre-maximum halt (b), the final rise (c), and the early decline (d). Vertical dotted lines separate each phase of the light curve.

3. *Final rise (2011 Apr 28 - May 11, $t=14.7-27.9$ days):* After the pre-maximum halt phase, the light curve was seen to rise more steeply to $m_{SMEI}=6.88\pm 0.04$ at $t=20.9$ days. Meanwhile the apparent quasi-periodic variations still persisted with approximately half the amplitude of those seen in the previous phase.

The light curve then suddenly dropped at $t=22.1$ days to $m_{SMEI}\sim 7.4$ for about two days. This event appeared as a major dip in the light curve before it reached maximum light. After this dip, the light curve rose again to $m_{SMEI}=6.79\pm 0.04$ at $t=25.5$ days and stayed there for roughly two days before it reached visual maximum at $m_{SMEI}=6.33\pm 0.03$ on 2011 May 12.22 UT (JD 2455693.7251, $t=27.9$ days) as seen in the bottom left panel of Figure 6.5.

4. *Early decline (2011 May 11 – [~Oct 3] , $t=27.9$ days – [~90 days]):* After optical maximum, the nova declined with variations (amplitude ranges roughly between 0.1-0.3 mags) to $m_{SMEI}\sim 7.2-7.4$ from 2011 May 19.42-20.76 UT (JD 2455700.9203-2455702.2605, $t=35.1-36.5$ days). The light curve experienced a dip again at around $t\sim 36$ days and followed this with a broad hump lasting from $t\sim 44-47$ days as seen in Figure 6.5 (d). The last reliable detection of T Pyx by SMEI was at $m_{SMEI}=7.26\pm 0.05$ on 2011 Jun 2.37 UT (JD 2455714.8165, $t=49.02$ days).

Further light curve observations provided by the AAVSO in Figure 6.2 show that the early decline phase ends at around $t\sim 90$ days with the brightness having declined by approximately 2.5-3.5 magnitudes from maximum. The final decline (~ 6 magnitudes from maximum) began around $t\sim 260$ days.

We may compare the early stages of the outburst captured by SMEI to the light curves presented by Hillman et al. (2013) from TNR modelling with a range of parameters as shown in Figure 6.6. There is certainly some resemblance to some of these model light curves in terms of the pre-maximum halt and subsequent smaller reversal just before optical peak. The former is attributed to a temporary drop in energy flux as convection in the expanding, thinning envelope ceases to be efficient near the surface of the envelope. The later dip resembles the shorter time scale feature noticed in e.g.

RS Oph and KT Eri by Hounsell et al. (2010) just before maximum light.

When directly comparing the SMEI to the AAVSO light curves, we see that the nova seems to be bluer and similar to the magnitude in the B filter at the pre-maximum halt phase, then exhibits the same brightness in the B and V filters at visual maximum where it is expected to behave like an early type star, usually in the range from B5-F5 (Warner, 2008). After visual maximum, it tends to be redder, approaching the magnitude in the R filter as shown in Figure 6.4.

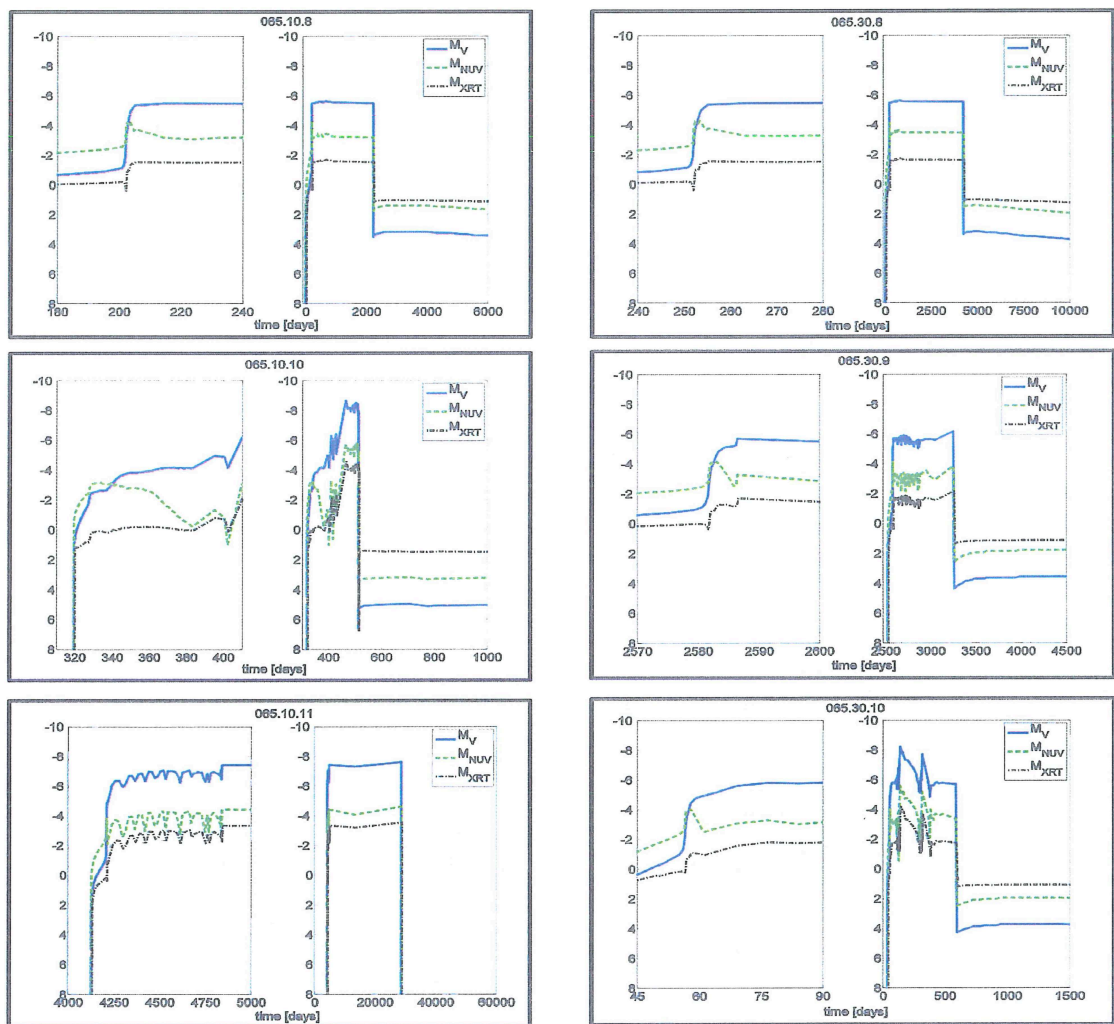


Figure 6.6: Modelled light curves of a typical nova cycle from Hillman et al. (2013). Each light curve is given in its entirety (right panel) and a close-up of its pre-nova rise (left panel). These show the evolution of nova luminosity given in M_V (solid blue), M_{NUV} (green dash), and M_{XRT} (black dash-dot) of the three nova phases proposed by Hillman et al. (2013) – pre-nova rise, mass loss phase, and post-nova decline phase.

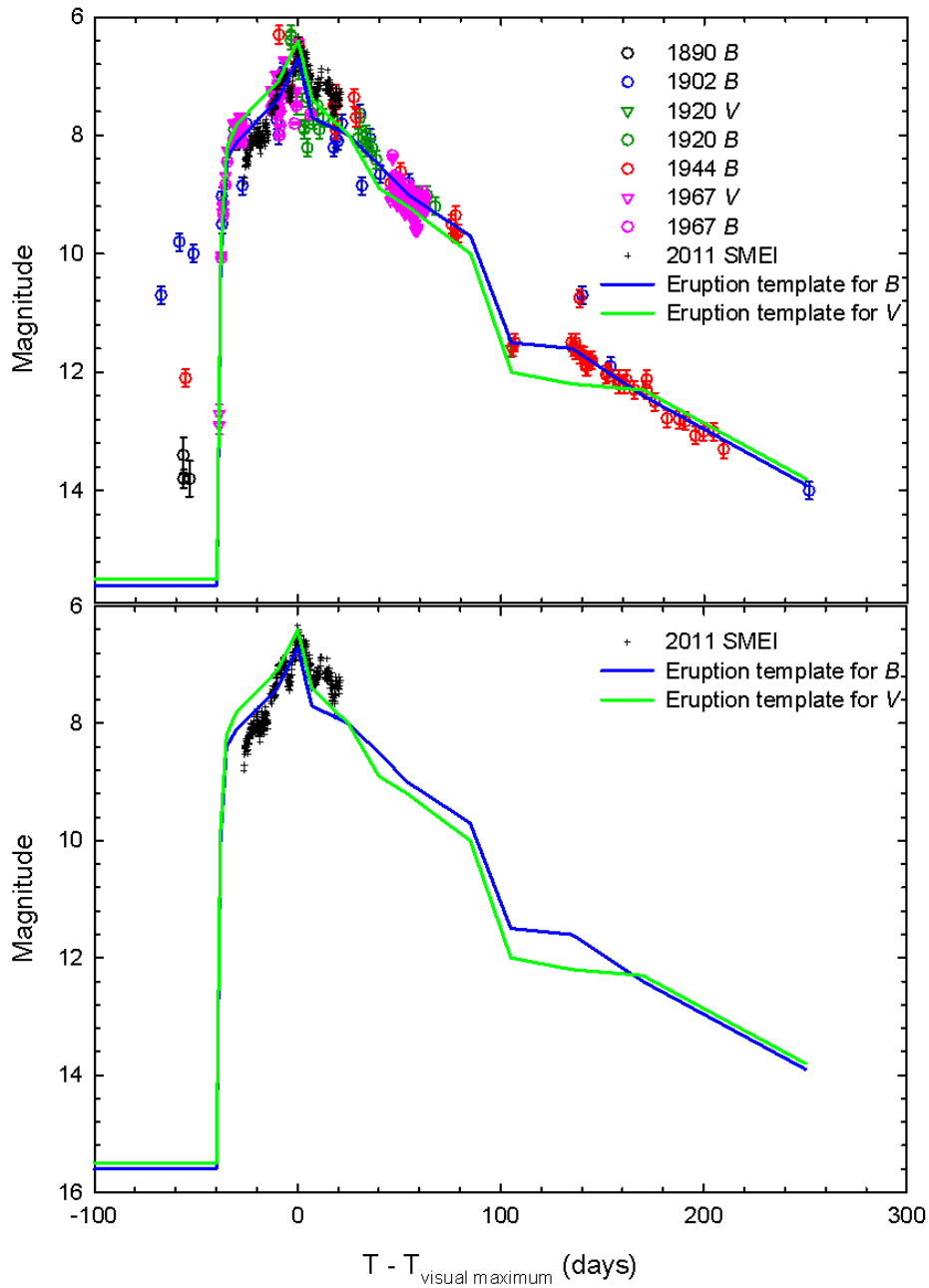


Figure 6.7: The outburst in 2011 from SMEI (plus signs) compared to previous outburst observations (upper panel) and to previous outburst templates (lower panel). In upper panel, the *B* (circles) and *V* (triangles) observations are highlighted in different colours to represent each year of outburst (1890:open black, 1902:open blue, 1920:open green, 1944:open red, 1967:open pink). Data for the previous outbursts are taken from Schaefer (2010).

When comparing the SMEI data to the previous five outbursts in *B* and *V* and their resulting eruption templates provided in Schaefer (2010), we find that the shape and the

magnitude of the visual peak in 2011 are compatible with previous outbursts. However the pre-maximum halt phase in 2011 seems to be fainter while during the decline after the visual maximum the nova is brighter in 2011 than shown in the templates (Figure 6.7). All the maxima, including the 2011 maximum, have exhibited brightness fluctuations near the optical peak and the declines have been slow. This is consistent with observations noted in Catchpole (1969) and Williams (1982) for the 1966 outburst.

Investigation of Periodicities

The SMEI light curve was searched for any periodic modulations. The analysis was undertaken using all the available SMEI data but we separated it into 5 cases which are (a) from the first observation to the last observation, (b) from the first observation to the end of pre-maximum halt, (c) from the first observation to visual maximum, (d) from the end of pre-maximum halt to the last observation, and (e) from visual maximum to the last observation. The analysis used the *PERIOD04*³ PC code from Lenz & Breger (2004, 2005). *PERIOD04* is especially useful for analysis of astronomical time series containing gaps. The program extracts the individual frequencies from the multi-periodic content and provides the frequencies, semi-amplitude, and phase of the harmonic signals of the light curve by using a combination of least-squares fitting and the discrete Fourier transform algorithm. The uncertainty of the estimated periods was also derived from Monte Carlo simulations by the *PERIOD04* code.

The resulting periodograms for all 5 cases are displayed in Figures 6.8, 6.9, 6.10, 6.11, and 6.12. The top panels show how closely the calculations agree with the observations, and the most prominent peaks are presented in Table 6.2. The second panels are derived from the fitted curves and these curves are constructed from an incremental sinusoidal curves fitting process. The third panels are derived directly from the data.

The prominent period of 1.8 days is apparent after the pre-maximum halt. However, by far the most strongly detected period, $P=1.44\pm 0.05$ days, with the highest signal ratio $\sim 10^6$ as shown in Figure 6.9, is found up to this time. This period is close to the weak

³ Available online at <http://www.univie.ac.at/tops/Period04/>

signal of 1.24 days found by Patterson et al. (1998) who suggested it might originate from precession in an accretion disc.

Table 6.2: Results from *PERIOD04*

Cases	Parts of light curve	t (days)	Most prominent period (days)
(a)	first observation - last observation	1.5-49.0	$1.8\pm 0.1, 3.6\pm 0.5$
(b)	first observation - end of pre-maximum halt	1.5-13.4	1.44 ± 0.05
(c)	first observation - visual maximum	1.5-27.9	$3.5\pm 0.08, 1.34\pm 0.03$
(d)	end of pre-maximum halt - last observation	13.4-49.0	1.7 ± 0.1
(e)	visual maximum - last observation	27.9-49.0	$0.77\pm 0.02, 1.84\pm 0.05$

Precession is a phenomenon seen in astrophysical jets and is usually attributed to motion of the collimating mechanism such as a circumstellar torus or disk (Crocker et al., 2002). The angular speed of a torus or disk, with radius r , undergoing forced precession as a result of the influence of a companion star can be estimated using the equation given by Crocker et al. (2002) following Merritt & Petterson (1980)

$$\Omega = -\frac{3}{4} \sqrt{\frac{G}{m_h}} \frac{m_h m_c}{m_h + m_c} \frac{r^{\frac{3}{2}}}{a^3} \cos \alpha$$

where m_h is the mass of the hot component which is in this case m_{WD} , m_c is the mass of the cool component, a is their separation, r is a radius of a disk, and α is the angle between the equatorial plane of the disk and the orbital plane of the stars. This relation assumes that the disk is centred on the hot component; the companion star causing the forced precession is the cool companion. We then take the average value of $m_{WD}=1.3M_{\odot}$ (Kato, 1990; Schaefer et al., 2010a; Selvelli et al., 2010), $q=0.2$ (Uthas et al., 2010) and therefore $m_c=0.26M_{\odot}$, and the inclination $i\sim 15^{\circ}$ which is an average value from Patterson et al. (1998); Uthas et al. (2010); Chesneau et al. (2011), and calculate possible disk radius.

To obtain a precession period of 1.44 days assuming the average value of Ω with α ranges from 0° - 90° requires a disk radius of around 0.2 AU ($\sim 10^{12}$ cm) which is much bigger than the semi-major axis a calculated from Kepler's third law (~ 0.004 AU or 6.1×10^{10} cm) of the binary and the distance of L_1 from the primary star R_{L_1} (0.0026

AU). Hence, the forced precession mechanism does not appear to be responsible in this case. Indeed, it is doubtful whether the disk would re-form so soon after the outburst, and at this early time, the central system is expected to lie well within the pseudo-photosphere (see below) and therefore not be directly observed.

Some of the TNR models by Hillman et al. (2013) however produced marked oscillations prior to or during extensive mass loss, caused by the restructuring and rebalancing of the envelope as it expands (see Figure 6.6). However, we found no significant changes in $H\alpha$ line shape with the 1.44 day period when we compared the four red spectra ($t=5.7, 8.6, 9.6, 11.6$ days) taken during the optical pre-maximum halt. Similarly, we found no significant differences in the overall ionization during a cycle from consideration of the appearance of lines across the full spectral range. These two aspects are also found to be the same in the blue spectra, where the $H\gamma$ line was of course investigated rather than $H\alpha$.

6.3.2 Spectra from SMARTS and LT

The spectra of T Pyx are also used here to try to understand what causes the gross changes in the light curve - e.g. changes in mass loss rate from the WD surface as the TNR proceeds - and to derive other parameters of the outburst. In order to compare the spectra to the light curve at the exactly the same date, we interpolate the m_{SMEI} of the date (at the start time of the observations) for which the spectra are available as shown in the top panel of Figure 6.13.

The light curve was compared to the flux and ejection velocities measured from $H\alpha$, $H\beta$, and $H\gamma$ lines as shown in this figure. The variation in flux of the Balmer lines is similar to that found in the light curves before visual maximum. For example, the variation in $H\alpha$ flux around on 2011 May 17 ($t=33.7$ days) is obviously responsible for the sharp and high-amplitude peak light curve at this time.

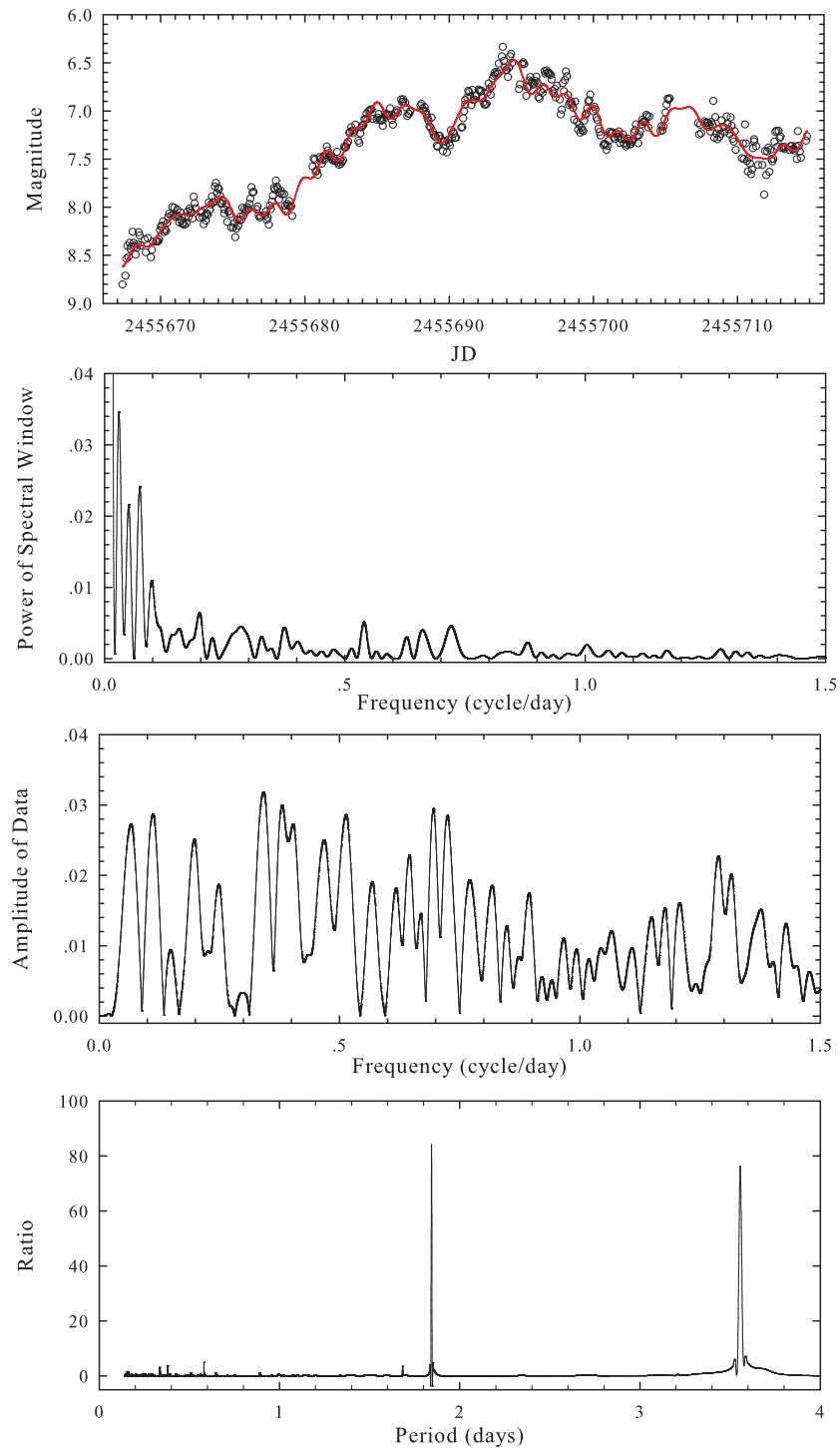


Figure 6.8: Period found by analysing the SMEI light curve from the beginning of SMEI observations to the last observation. The observation points were fitted (top) and yielded the spectral window (below), the observational data (middle), and the ratio of the spectral window to the amplitude which gives us the possible periods (bottom).

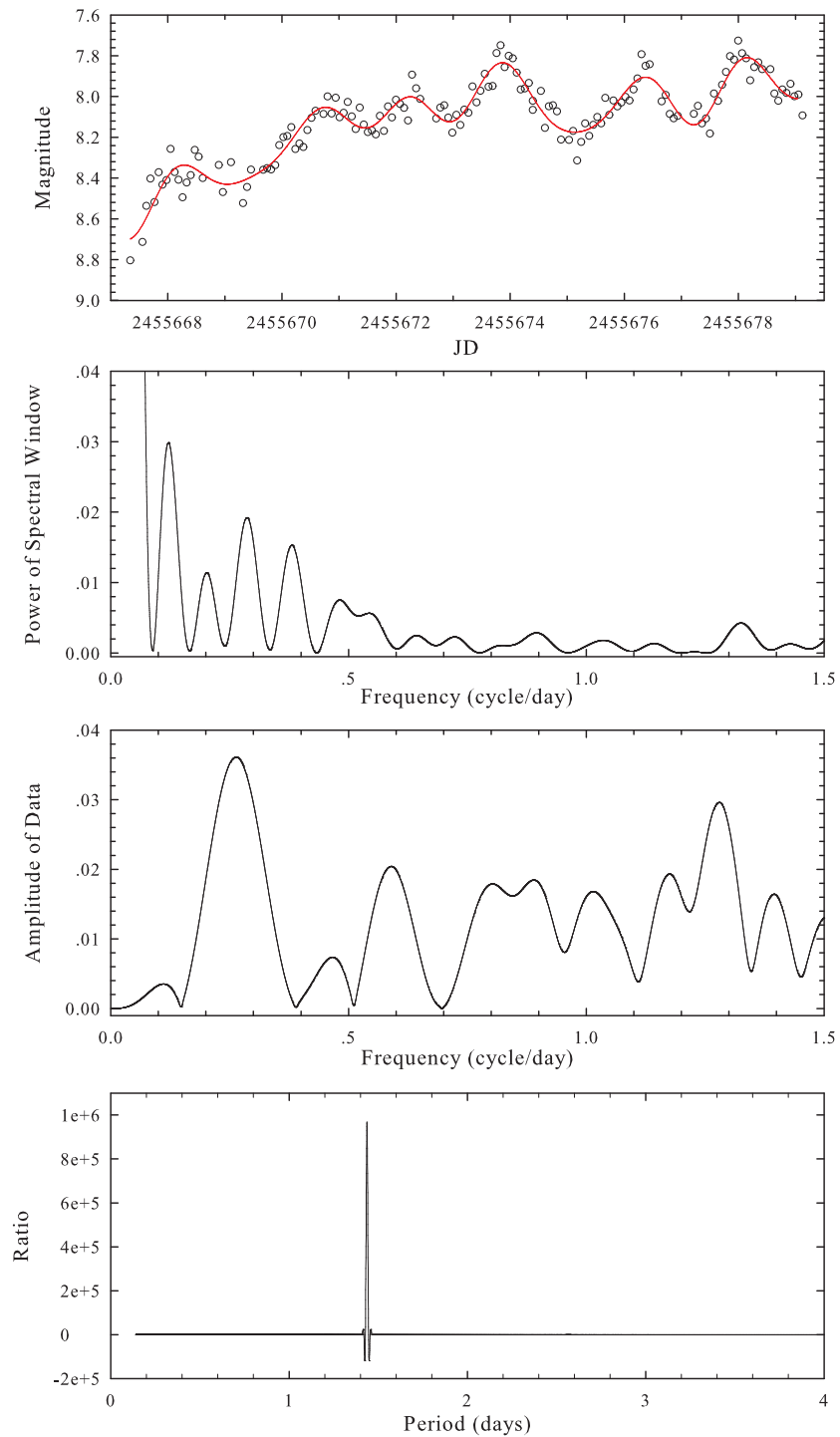


Figure 6.9: As Figure 6.8 but from the beginning of SMEI observations to the end of the pre-maximum halt phase.

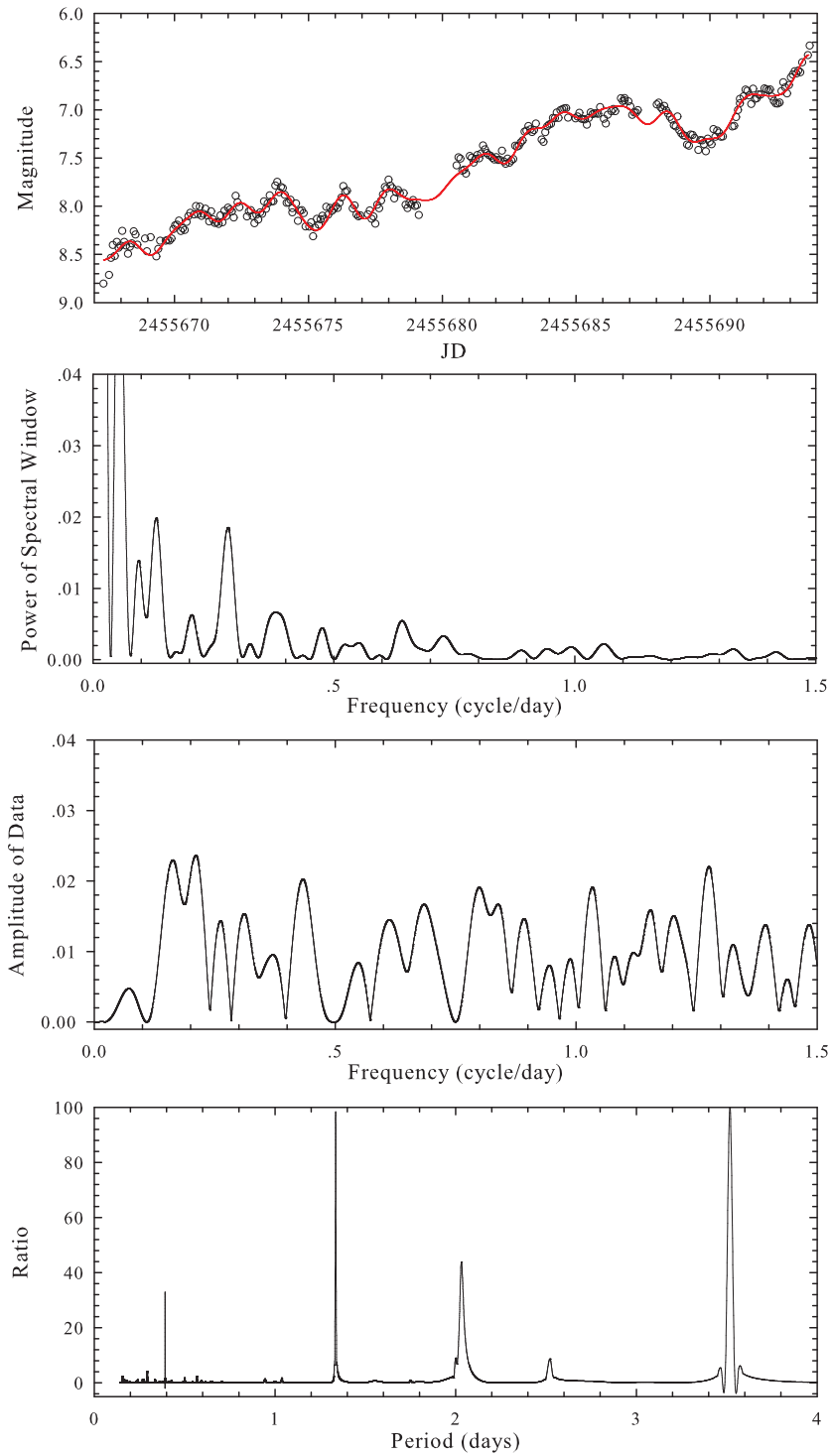


Figure 6.10: As Figure 6.8 but from the beginning of SMEI observations to visual maximum.

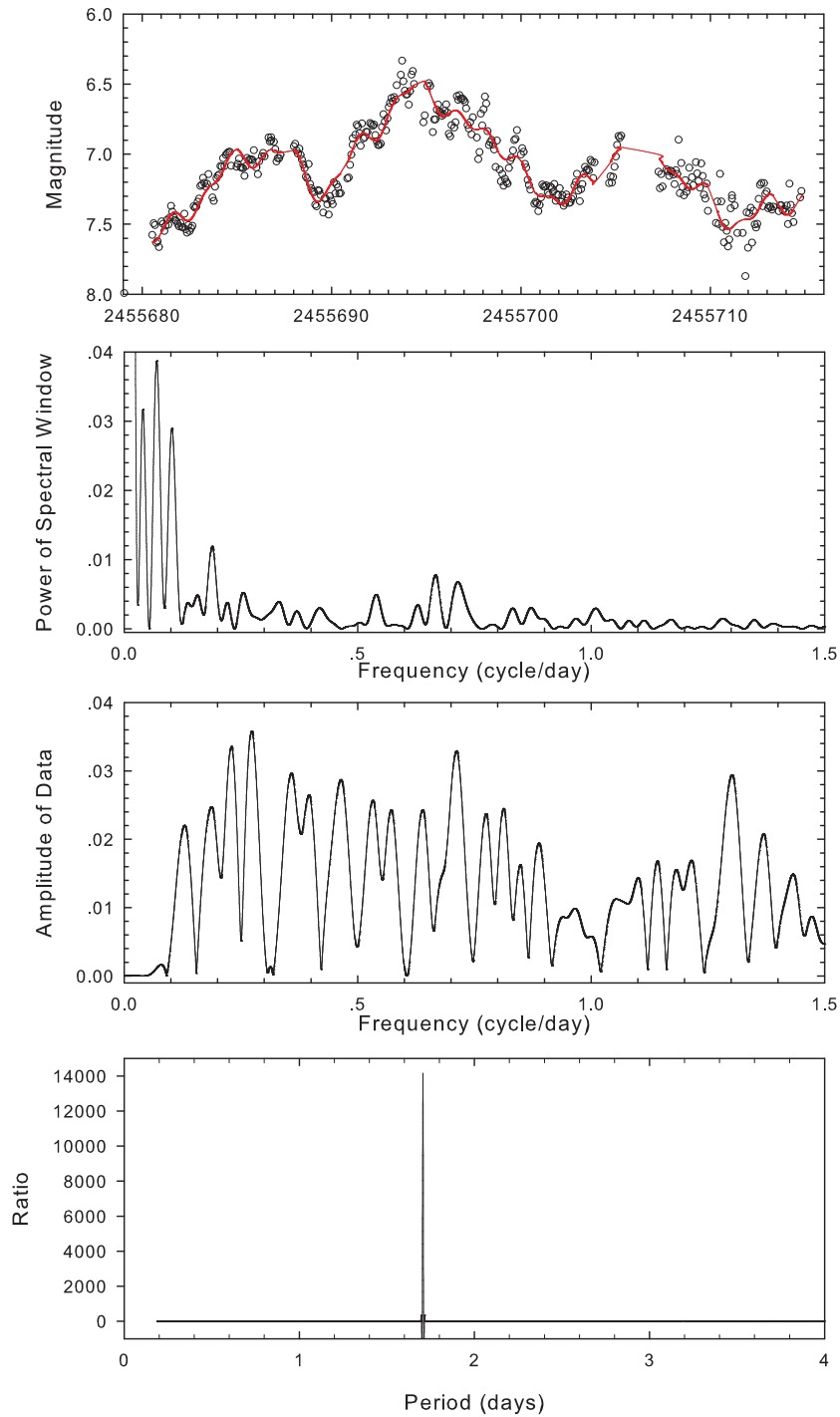


Figure 6.11: As Figure 6.8 but from the end of the pre-maximum halt phase to the last SMEI observation.

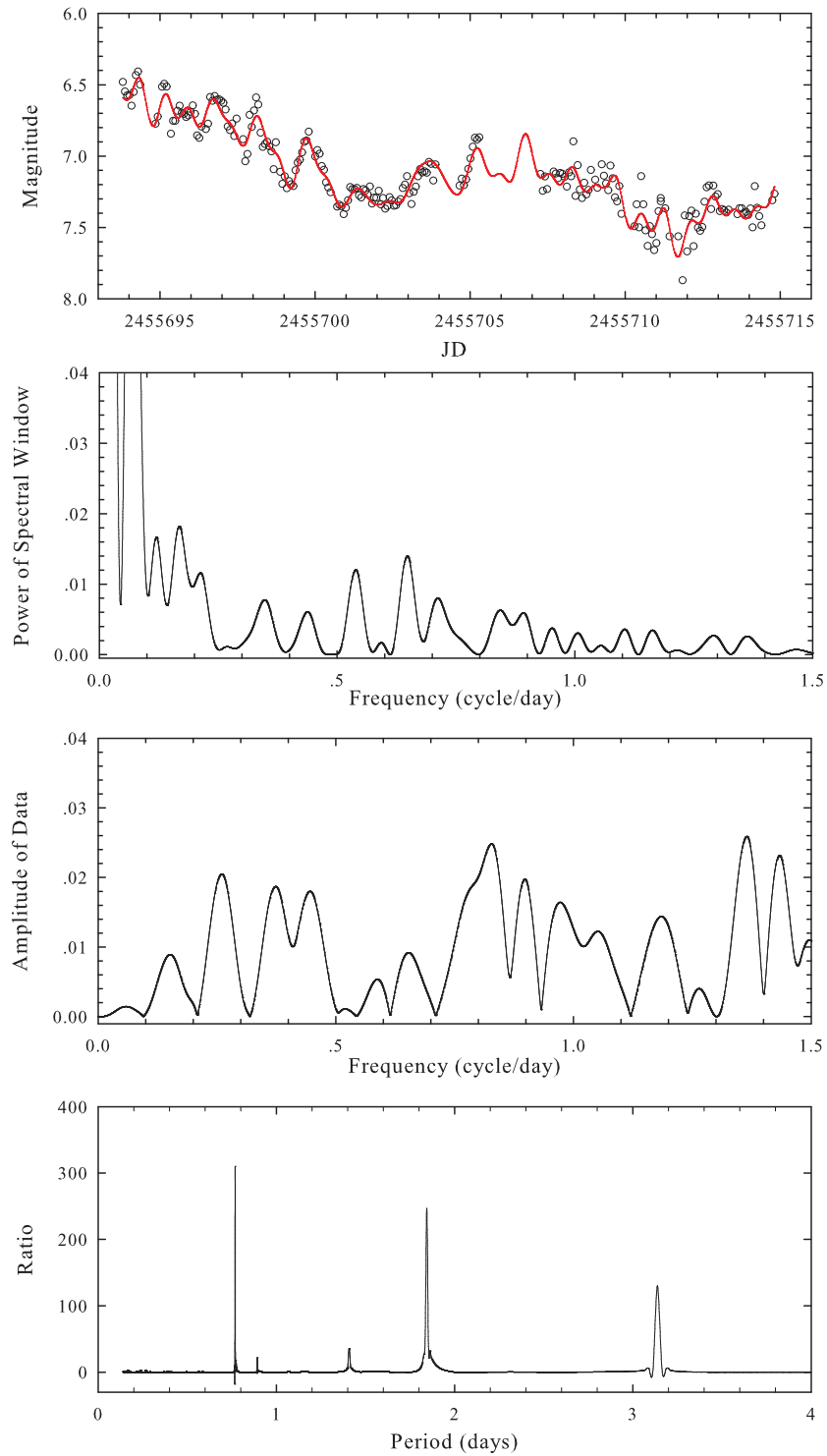


Figure 6.12: As Figure 6.8 but from the visual maximum to the last SMEI observation.

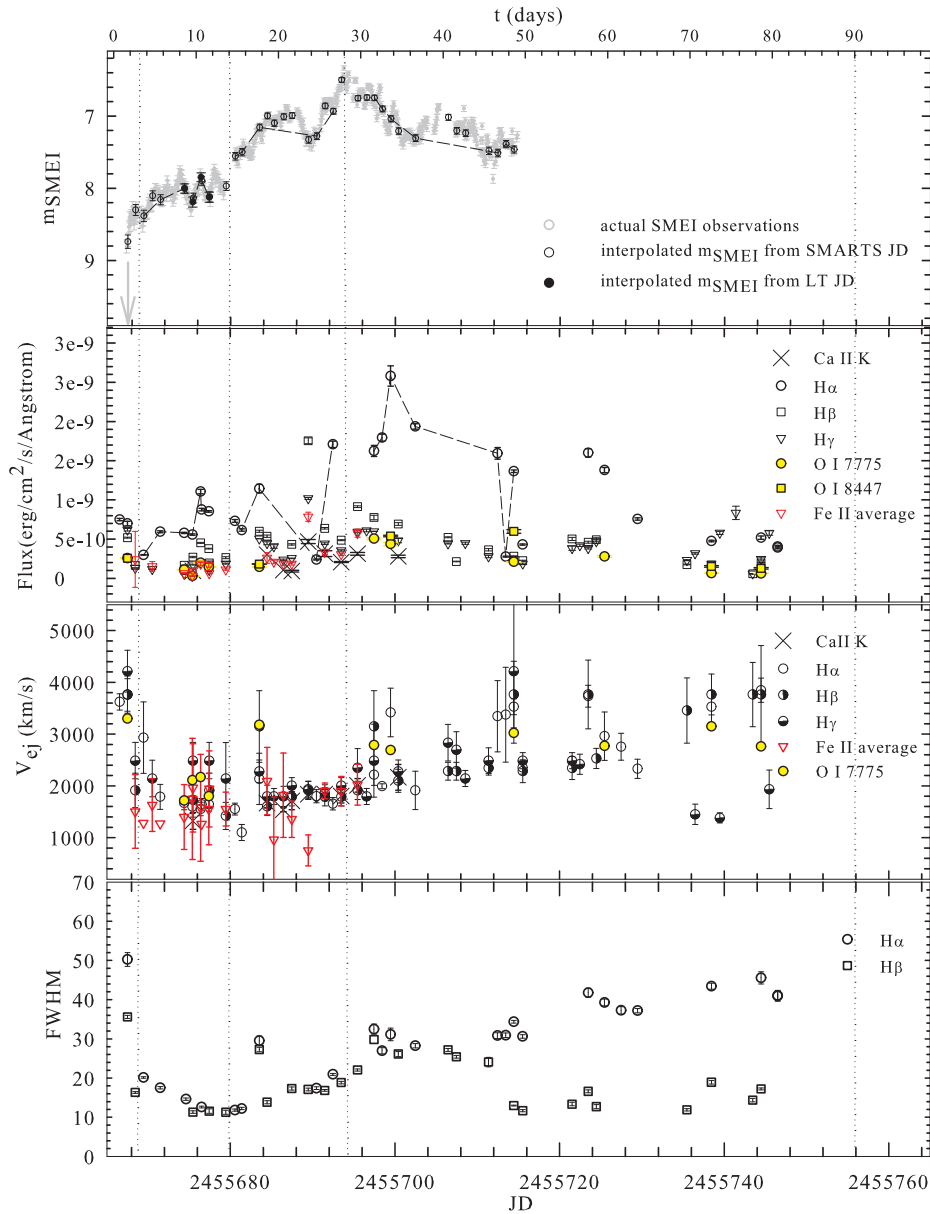


Figure 6.13: SMEI light curve of T Pyx compared to flux and ejection velocity from Balmer, average Fe II (5169, 5018, 4233, 4178, and 4173Å), O I, and Ca II K lines. Dashed lines in the top two panels connect observations of H α flux. The evolution of the FWHM of Balmer lines is also shown (bottom panel). Vertical dotted lines represent phases in the light curve referred to in the text.

Velocities Derived

The ejection velocities (V_{ej}) were measured from the P Cygni profiles. The measured lines include $H\alpha$, $H\beta$, $H\gamma$ which have measurable P Cygni profiles from 2011 Apr 16 - 2011 Jun 1 ($t=2.7$ -48.6 days), Fe II recombination lines at 5169, 5018, 4233, 4178, and 4173Å, O I 7775Å, and the Ca II K line at 3934Å. Figure 6.14 shows the P Cygni profiles of $H\alpha$ lines from the initial rise to the end of the pre-maximum halt phase.

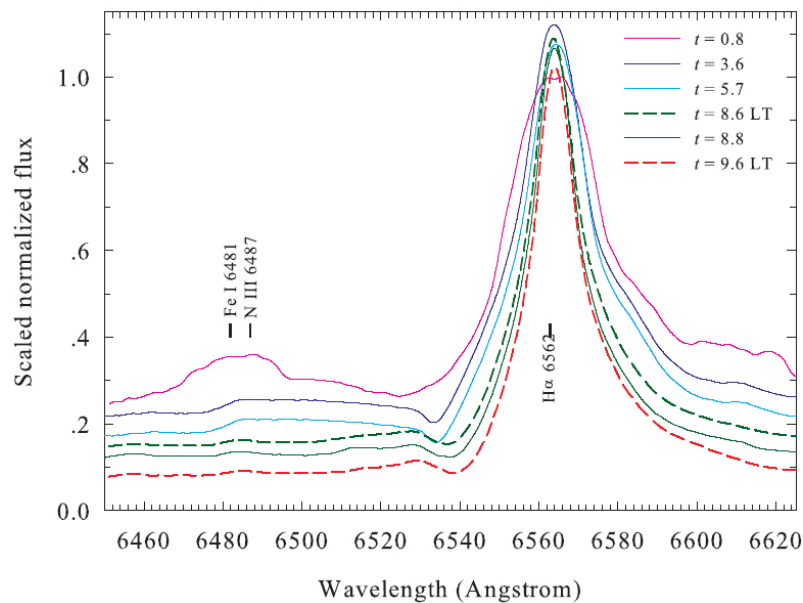


Figure 6.14: P Cygni profiles of $H\alpha$ lines from the initial rise to the end of the pre-maximum halt phase.

Spectral Evolution

Figure 6.15 shows all low-resolution spectra taken from $t=1.7$ -247 days which cover the initial rise phase through to the transition phase of the light curve. In the following, we discuss the spectral evolution based on the idealised nova optical light curve given in Warner (2008) together with a recognition of a common pattern of line development described by McLaughlin (1942, 1944). We also note the physical interpretation of various stages. For example, from the earliest moment, the nuclear explosion on the surface of the WD leads to the ejection of a hot, luminous, and massive shell that expands radially with time. Ney & Hatfield (1978) called this stage the “*pseudo* –

photospheric expansion' for the spectral energy distribution (SED) and spectroscopic features are characteristic of the photosphere of a star with spectral type A to F (Payne-Gaposchkin, 1964). Gehrz (1988) called this stage the “*fireball*” because it has been used to describe the early development of man-made atomic explosions and therefore he used it to describe the expanding pseudo-photosphere of the nova.

The fireball’s envelope is initially small and dense with the radiation peak at X-ray wavelengths. Then the envelope cools adiabatically as it increases in size. As a result, the opacity increases, the ejecta become optically thick after the outburst, and the radiation peak shifts towards longer wavelengths (Shore et al., 1994). Therefore, this cooling of the ejecta envelope together with the rapid expansion of the photosphere (Ennis et al., 1977; Gehrz et al., 1980) provide the rapid initial rise in the optical light curve.

Following optical maximum, the effective temperature (T_{eff}) of a nova, which is radiating at constant bolometric luminosity (as mentioned in Section 1.4), rises as the pseudo-photosphere shrinks back onto the WD and as the mass loss rate from the WD decreases (Bath & Harkness, 1989). As a result, the peak emission now shifts toward shorter wavelengths. The effective temperature of the pseudo-photosphere changes as the visual flux declines according to

$$T_{eff} = T_0 \cdot 10^{\Delta V/2.5} \quad (6.1)$$

where ΔV is the decline in magnitude from visual maximum, and T_0 is the photospheric temperature at optical peak (Bath & Harkness, 1989). We take $T_0=8000\text{K}$ (Evans et al., 2005) and use the equation above to estimate T_{eff} . According to Bath & Harkness (1989), the physical state of the photosphere (i.e. temperature, radius, density, and pressure) is approximately the same at equal magnitudes below the optical maximum in all novae. Consequently, one might anticipate that the spectral appearance of a nova should be the same at the same magnitude below peak in all novae if this simple model is correct. It can then be applied before and after peak if the mass-loss rate from the WD is the governing factor.

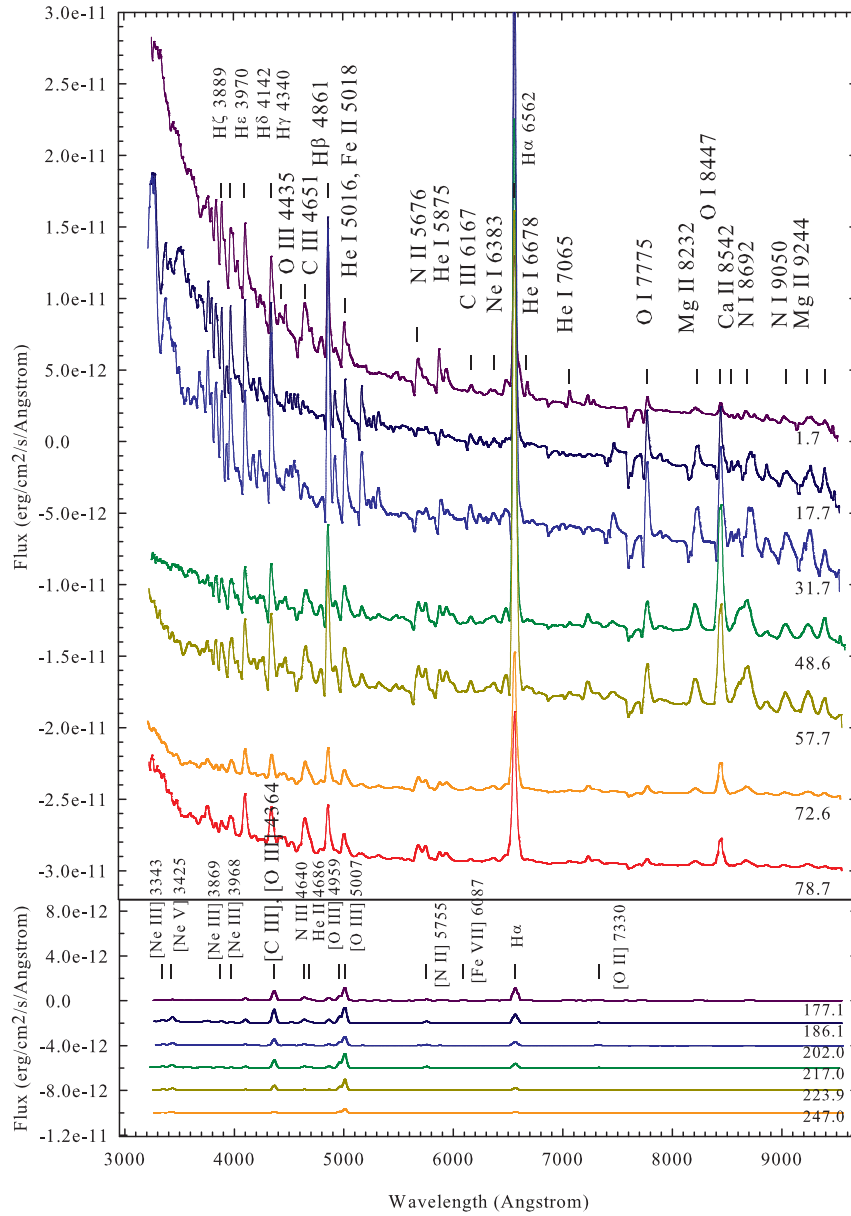


Figure 6.15: Low-resolution spectra of T Pyx taken from $t=1.7$ -247 days. Spectra before the seasonal gap (top) are offset in flux for clarity, as indicated, with the spectrum at 1.7 days representing the observed flux and those from 17.7-78.7 days being offset in steps of 5×10^{-11} $\text{erg cm}^{-2} \text{\AA}^{-1}$. Spectra after the seasonal gap (bottom) are offset in flux with the spectrum at 177.1 days representing the observed flux and those from 186.1-247.0 days being offset in steps of 2×10^{-11} $\text{erg cm}^{-2} \text{\AA}^{-1}$.

1. *The initial rise (2011 Apr 14-16, $t=0.8-3.3$ days):* The first red spectra were obtained on 2011 Apr 15.05 UT (JD 2455666.55056, $t=0.8$ days) about 27 days before the visual maximum. At this time, the AAVSO visual magnitude was $V\sim 8.7$ (about 6.8 mags brighter than quiescence at $V\sim 15.5$ and about 2.4 mags below visual maximum - see Figure 6.2). The top panel of Figure 6.16 reveals that the lines were broad and diffuse. $H\alpha$ and $H\beta$ emissions were strong while the P Cygni profiles were not yet seen clearly when compared to other later spectra, shown in Figure 6.14. Moreover, the spectrum at $t=1.7$ days in Figure 6.15 shows the brightness of the nova comes almost entirely from the continuum at this early stage of the outburst. This is consistent with the characteristics of the *pre – maximum spectrum* stage given by Payne-Gaposchkin (1964) - see Chapter 1. This is expected as the expanding pseudo-photosphere is of similar extent to the maximum radius initially reached by the ejecta.

The *pre – maximum spectrum* is defined as the earliest spectrum at which any given nova has been observed on the rise until at least one or two days after maximum light (McLaughlin, 1942). It usually contains lines which are broad and diffuse with negative velocity displacement (Payne-Gaposchkin, 1964).

Our spectra showed P Cygni profiles in the Balmer, Fe II, and O I lines quite early in the first spectra, during this fireball phase. This aspect is similar to that observed at this time in DQ Her and LMC 91 as mentioned in Schwarz et al. (2001). The absorption components of P Cygni profiles became broader and shallower from $t=0.8$ to 2.7 days.

The initial rise ended just after 2011 Apr 16.95 UT (JD 2455668.44853, $t=2.7$ days) where the first medium-resolution blue spectra were obtained. At $t=0.8$ days, the H I Balmer lines were present in emission and becoming stronger with blue-shifted absorptions and the presence of He I. By $t=2.7$ days, the rise of ionized iron emission lines was evident. There were emissions of high excitation lines (see Table 6.3) i.e. C III, N III, Ne II, O II, N II, He I, and Ne I present during this phase (see Fig 6.16) which disappeared later around 2011 Apr 22-23 ($t=8.6-9.7$ days). These O II and N II lines are also those expected as the ionized

elements that should be found at ~ 1.5 mag below peak (Bath & Harkness, 1989) - see Table 6.4. Other expected emission lines at 2.9 mag below peak are O III at 4435\AA which is also seen at $t=1.7$ -2.7 days.

Table 6.3: High ionization lines and some lower ionization lines present in the spectra of T Pyx 2011 in its initial rise and pre-maximum halt phases.

High excitation lines	Ionization potential (eV)	λ (\AA)	Days since discovery	
			First detected	Last detected
O III	54.90	4435.0	1.7	2.7
C III	47.90	4651.4	1.7	3.6
		6167.5	0.8	3.6
		6727.0	0.8	3.6
N III	47.24	5943.0 [†]	0.8	5.7
		6487.0 ^{††}	0.8	8.6
Ne II	41.00	4713.4	1.7	2.7
		5178.5 ^{†††}	1.7	2.7
O II	35.10	4676.2	2.7	9.7
N II	29.60	5045.0	1.7	2.7
		5686.2	3.6	10.7
		5938.0	3.6	11.6
		4120.8	2.7	8.6
He I	24.60	5875.6	0.8	14.8
		6678.1	0.8	14.8 or 26.7?
		7065.2	1.7	17.7
Ne I	21.60	4663.5	2.7	9.7
		5156.6	2.7	8.6
		5684.6	0.8	3.6
		5934.4	0.8	8.6
		6213.8	0.8	0.8

[†] N III 5943\AA + Ne I 5934\AA could account for N II 5938\AA .

^{††} Could also be N II 6487\AA .

^{†††} Could also be Mg I 5178\AA .

A marked drop in the derived expansion velocity (V_{ej}) during this phase is also noted (see Figure 6.13). We note that Imamura & Tanabe (2012) and Shore et al. (2011) also report a decline in derived expansion velocities at early times. The first observations show a derived expansion velocity of $\sim 4000 \text{ km s}^{-1}$ at $t=0.8$ days which then drops to $\sim 2000 \text{ km s}^{-1}$ at $t=2.7$ days for Balmer lines. This should not be interpreted as a deceleration. This aspect of the pre-maximum spectrum with the dramatic decrease in V_{ej} during the initial rise is also found

Table 6.4: Ionization levels at various decline stages according to Bath & Harkness (1989, Only species with strong optical lines noted).

ΔB	B	Element ionization level	t (days)	T_{eff} (K)
1.45	7.78	O II	2.7, 3.6-13.6, 33.7-61.7	30,000
1.55	7.88	N II	2.7, 3.6-10.7, 36.7-80.8	33,000
2.85	9.18	N III	0.8-2.7, 5.7, 8.6, 73.7, 155.1-221.9	110,000
3.15	9.48	O III	0.8-1.7, [45.6] ¹ -246	145,000
4.85	11.18	N V	73.7 (N V 4603Å)	700,000

¹ Marginally detected at this time.

in the slow nova DQ Her (McLaughlin, 1937) for Balmer lines. Meanwhile the fast nova V603 Aql (Wyse, 1940) also showed the decrease in V_{ej} for Balmer and metal lines from a few observations during the final rise.

If the initial ejection is a Hubble-like flow, then one will see high V_{ej} initially which declines as one sees into deeper layers. We also note, as an aside, a comparison to the high velocity features (HVF) found in all Type Ia SNe and believed to be the result of the interaction of initial highest velocity ejecta with a circumstellar envelope (Benetti et al., 2005). The subsequent change in behaviour of the derived V_{ej} during the pre-maximum halt phase suggests two different stages of mass loss: a short-lived phase first occurring immediately after outburst and then followed by a more steadily evolving and higher mass loss phase.

2. *The pre-maximum halt (2011 Apr 17-27, $t=3.6-13.7$ days):* The SMEI light curve at this phase has $m_{SMEI} \sim 8$ mag (with 0.1-0.3 mag variations) which is about 2 magnitudes below maximum (6.33 mag). This phase lasts for about ten days. As Warner (2008) notes, the pre-maximum phase is generally much longer-lasting in slow novae than in fast novae.

All of the C III lines disappeared by $t=3.6$ days while other lower ionization lines such as N III, Ne II, N II and Ne I lasted a little longer until disappearing approximately around $t=5.7-10.7$ days as shown in Table 6.3 and Figure 6.18, consistent with behaviour reported in Shore et al. (2011). The spectra at $t=3.6-$

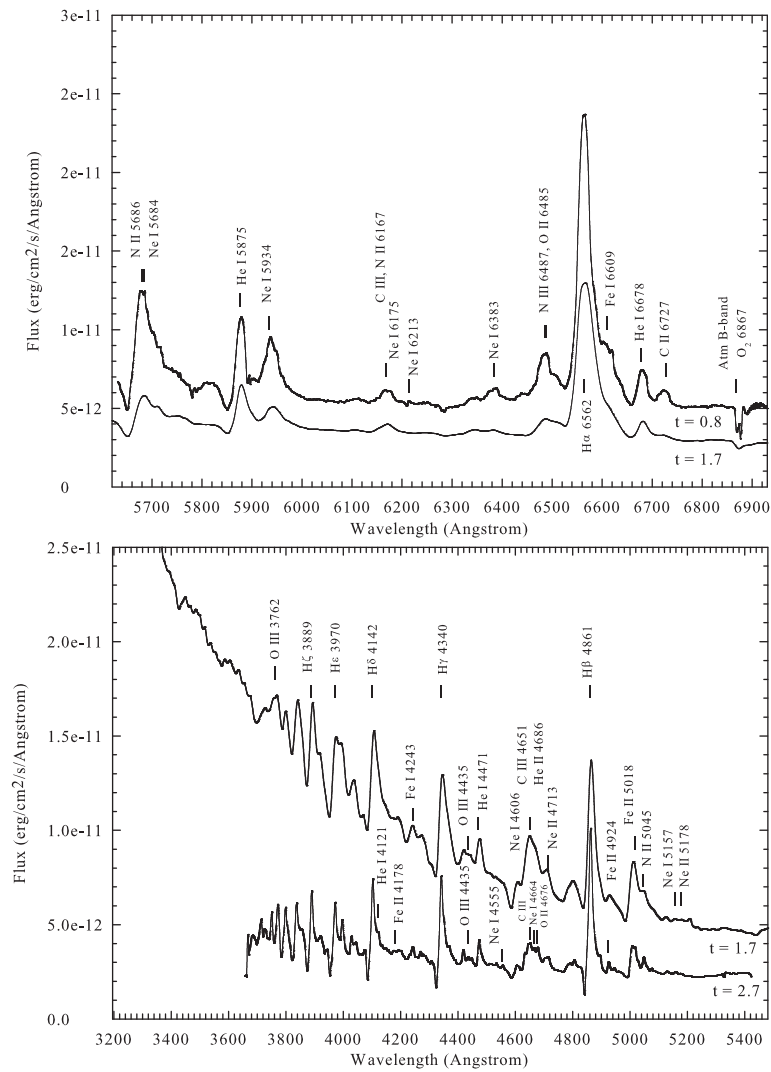


Figure 6.16: Detection of high ionization lines (e.g. O III and N III) present in red spectra (top) and in blue spectra (bottom) during the initial rise ($t=0.8-2.7$ days). Spectra show the observed flux in each case.

5.7 days show broad and strong emission lines present between $\lambda \sim 6480\text{-}6530\text{\AA}$ and then these fade away. Lines which were present all the time during this phase are O I, O II, He I and Fe I which is again consistent with the behaviour proposed by Bath & Harkness (1989) at this magnitude below peak. We note that He I 5875\AA and 6678\AA were present from $t=0.8$ days then became weaker and totally disappear by $t=14.8$ days. They appeared again at $t=80.7$ days.

The end of the *fireball* stage occurs around $t=8.6$ days which is also the beginning of the next optically thick phase called the “*iron curtain*”. The iron curtain (Hauschildt et al., 1992; Schwarz et al., 2001) occurs when the pseudo-photosphere reaches its minimum temperature ($\sim 10^4\text{K}$). The iron-peak elements recombine at this temperature. The overlapping of absorptions of Fe II lines in the near UV region results in line blanketing in the UV which dominates the UV SED and redistributes most of the emitted light into the optical and IR.

At this stage, we found three characteristics of the iron curtain which are mentioned in Schwarz et al. (2001). First, is the increase in the width of the emission lines which is clearly occurring in the final rise (see Figure 6.13); second, is the increase in the derived expansion velocity which Schwarz et al. (2001) suggested could be due to the gradually accelerating optically thick wind that is proposed to begin after the initial outburst (Kovetz, 1998); finally, the increase in the intensity of Fe II multiplets and O I 7775\AA and 8447\AA . Figures 6.17 and 6.19 show that the low excitation lines such as Fe-peak transitions, particularly Fe II recombination lines at $5169, 5018, 4233, 4178, 4173\text{\AA}$, begin to rise from $t=8.6$ days.

There is also a tendency for the absorption components, especially those of the Fe II lines, to become sharper and stronger as maximum is approached. We note that during this phase (for particular ions) the spectrum tends to develop such that the shorter wavelength lines are evident first and then followed by the next lines toward the longer wavelength. For example, Fe I 7443\AA develops first, followed by Fe I 7446\AA . This also happens with Fe I $7469\text{-}7473\text{\AA}$, O II $7895\text{-}7898\text{\AA}$, and Fe I $8468\text{-}8471\text{\AA}$.

The variation of the light curve during the pre-maximum halt phase seems to be consistent with variations in the strength of the H α , H β , H γ , and Fe II lines during this halt as shown in Figure 6.13. There is an obvious sharp variation in the light curve during $t=8.6-11.6$ days where spectra show some Fe I lines were present at $t=9.6-10.6$ days but not before or after that (bottom panel of Figure 6.18). For example, the Fe I 7854Å line was not detected at $t=8.6$ days but was present on days 9.6 and 10.6 before disappearing again at $t=11.6$ days. Meanwhile Fe I 8838Å was present only at $t=10.6$ days.

Imamura & Tanabe (2012) and Ederoclite (2013) suggested that T Pyx evolved from a He/N to an Fe II-type nova (Williams, 1992) by the time it reached visual maximum. Here we can point out the exact time that this process began was during this pre-maximum halt phase and was completed by the final rise. We note, however, that this spectral classification is normally applied to novae from maximum light onwards. The evolution of T Pyx from a He/N nova to an Fe II type nova suggests that there was sufficient mass loss for the optical thickness in the outer layers to increase during the rise to maximum so that we were seeing less deep into the expanding layers. This type of evolution could be typical for many novae in outburst but has not been seen before because of insufficient observations early in the outburst.

The maximum V_{ej} of approximately 2200 km s⁻¹ (Figure 6.13) during this phase derived from the Balmer lines agrees very well with that obtained by Imamura & Tanabe (2012). Although we do not have information from the P Cyg profiles in Fe II lines until $t=3.6$ days to verify the very high V_{ej} at the same initial rise phase as the Balmer lines, the Fe II lines seem to show a similar trend subsequently to that of the Balmer lines in that V_{ej} stabilises at ~ 1500 km s⁻¹ during the pre-maximum halt and tends to increase afterward.

3. *Final rise (2011 Apr 28 - May 11, $t=14.7-27.9$ days):* Here the light curve rises more steeply toward maximum. As noted above, the iron curtain stage is expected to peak around this time. However Figure 6.17 shows the Fe II flux rose to a sharp peak just before $t\sim 23$ days when there is a major dip in the SMEI light

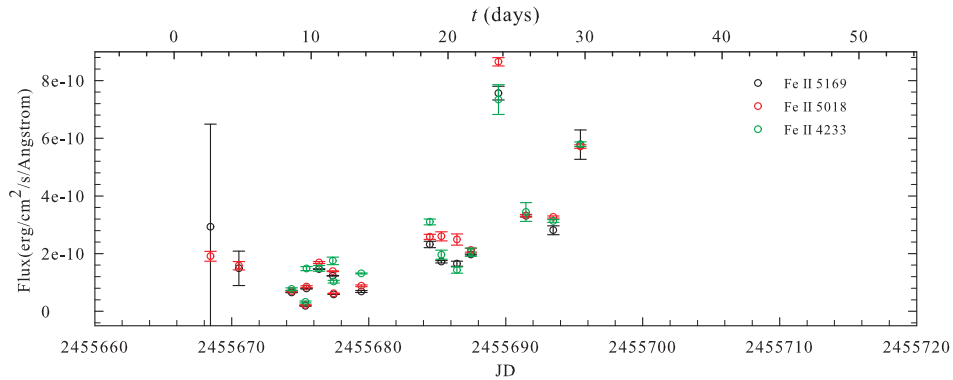


Figure 6.17: Evolution of the flux of Fe II lines at 5169, 5018, and 4233 Å.

curve with a minimum at $t=23.7$ days. The visual maximum then occurred four days later at $t=27.9$ days.

The “*principal spectrum*” which dominates CNe spectra at visual maximum (Payne-Gaposchkin, 1964; Warner, 2008) displays strong lines of O I (i.e. the “O I flash”). In T Pyx these became apparent around $t\sim 17$ days and grew in intensity at about the same rate as the Fe II lines (see Figures 6.20 and 6.21). At the O I flash, the V magnitude was ~ 1.5 mag below peak which agrees with that expected by Bath & Harkness (1989) from the ΔB at this time. Strong bright lines of Fe II and Ca II are always present (see Chapter 1). The emission of [N II] 5755 Å begins to grow stronger at $t=26.7$ days, about ten days after the O I flash, since N lines, i.e. [N II] 5755 Å together with emission lines of N III, N IV and N V in the UV, are expected to be seen in the principal spectrum phase of novae (Jaschek & Jaschek, 2009)⁴.

Again the Balmer lines and other lines show a similar trend of V_{ej} , i.e. gradually increasing (after the initial decrease at early times) as seen in Figure 6.13. This may imply that here the innermost layers of material now move faster than the outer layers (i.e. the relative radius of the pseudo-photosphere to that of the ejecta was shrinking significantly and therefore revealing higher velocity material again). As noted above, this was proposed by Schwarz et al. (2001) in terms

⁴ The section (about emission lines of NII in novae) published in the book is available at <http://ned.ipac.caltech.edu/level5/Glossary/Jaschek/N.html>

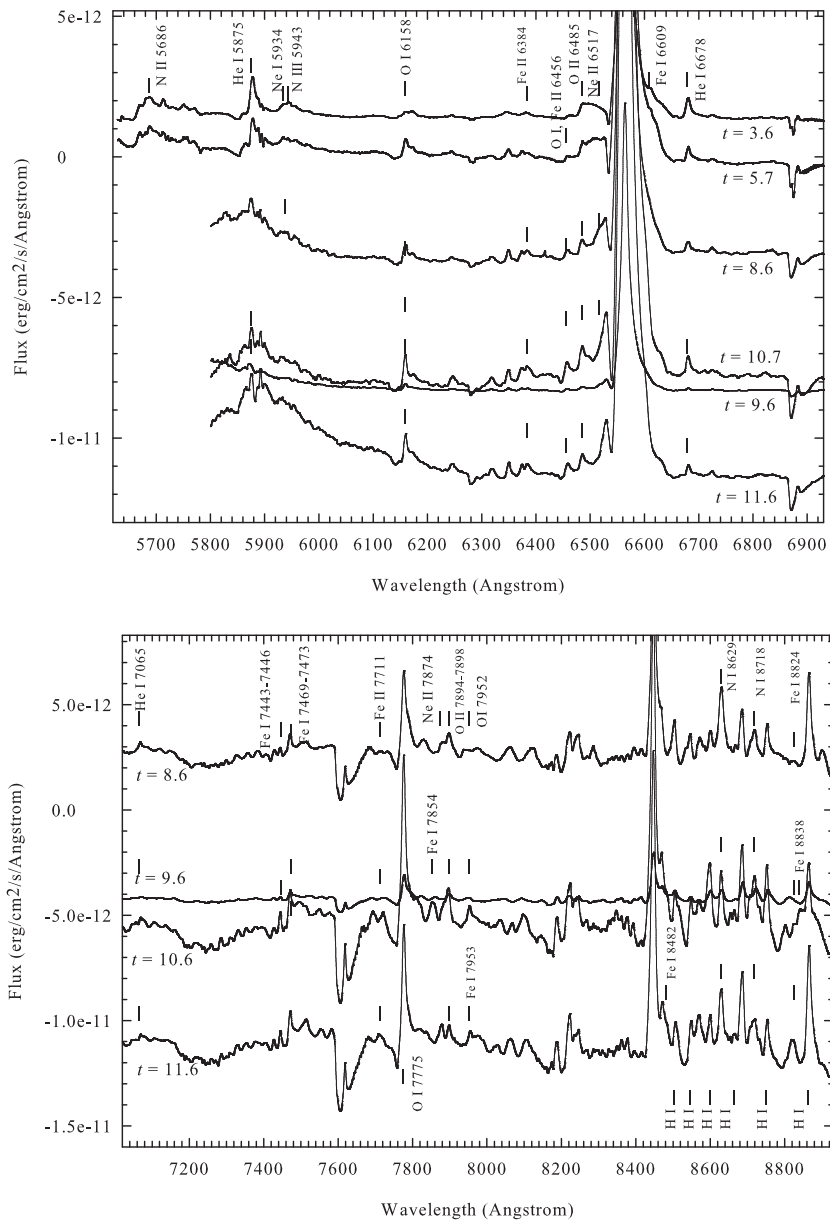


Figure 6.18: The red spectra during the pre-maximum halt phase. Spectra are offset for clarity in flux with the spectrum at 3.6 days (top panel) and 8.6 days (bottom panel) representing the observed flux and the later spectra being offset in steps of 3×10^{-12} and $5 \times 10^{-12} \text{ erg cm}^{-2} \text{ \AA}^{-1}$ in each figure, respectively.

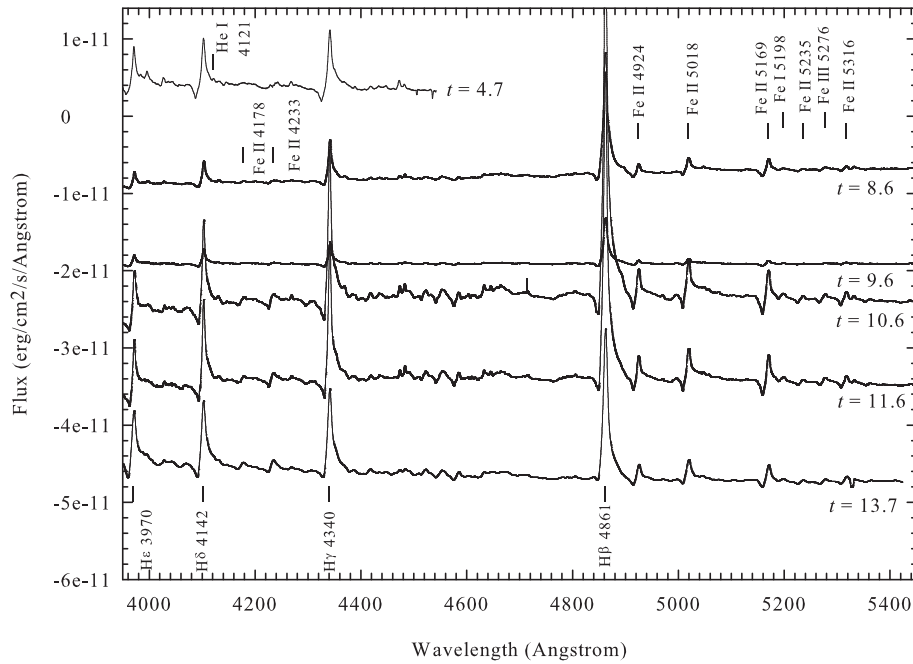


Figure 6.19: The blue spectra during the pre-maximum halt phase. Spectra are offset in flux for clarity with the spectrum at 4.7 days representing the observed flux and the later spectra being offset in steps of $1 \times 10^{-11} \text{ erg cm}^{-2} \text{ \AA}^{-1}$.

of a gradually accelerating wind in nova LMC 1991 and has been used to model early hard X-ray emission in some CNe (e.g. O'Brien et al., 1994). The visual maximum at $t=27.9$ days seems to exhibit the lowest ionization lines, again as predicted in the simple Bath & Harkness (1989) models.

The three characteristics of the iron curtain which are first mentioned in the pre-maximum halt phase persist in this final rise phase. Returning to the major dip in the light curve at $t=23.7$ days, we find that the normalized flux of the blue spectra with respect to the $H\alpha$ line on the day before, at, and after the dip (at $t=21.7$, 23.7, and 25.7 days respectively) all looked exactly the same in shape but only difference in the $H\alpha$ flux that dropped very significantly at the dip. Thus the mechanism that causes the very marked drop in emission line strength of $H\alpha$, and other lines at longer wavelengths, must be responsible for the major dip in the total flux in the final rise. Meanwhile, there are almost no other emission lines apart from $H\alpha$ in the red spectra at $t=24.7$ days.

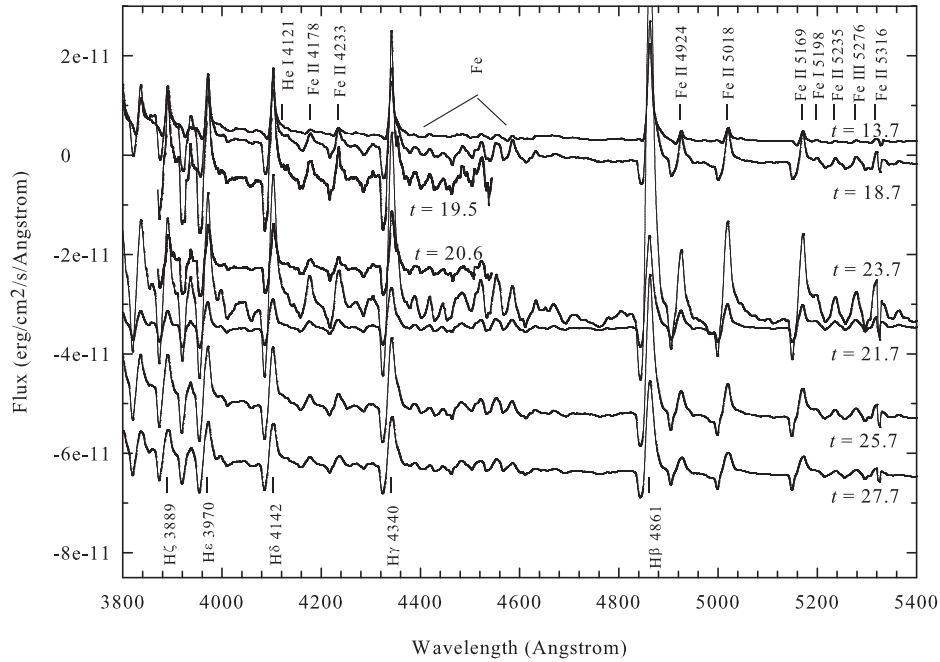


Figure 6.20: The blue spectra during the final rise phase. Spectra are offset in flux for clarity with the spectrum at 13.7 days representing the observed flux and the later spectra being offset in steps of $1 \times 10^{-11} \text{ erg cm}^{-2} \text{ \AA}^{-1}$.

4. Early decline (2011 May 11 - Oct 3, $t=27.9-90$ days):

The early decline phase of the CN light curve is defined as the beginning of the decrease in brightness to ~ 3.5 magnitudes below peak (Warner, 2008). The SMEI light curve declines in brightness from $m_{\text{SMEI}}=6.5$ ($t=27.9$ days) to $m_{\text{SMEI}}=7.26$ at the last SMEI detection ($t=49.7$ days). The multi-colour light curves from AAVSO subsequently show sharp drops in all colours at $t \sim 90$ days, where $\Delta V \sim 2.5-3.5$ magnitudes from maximum.

$H\alpha$ reached its maximum observed flux at $t=31.7$ days, which is after visual maximum was reached at $t=27.9$ days. The strong emission of Fe II and Ca II, which is always present in the conventional principal spectrum (Payne-Gaposchkin, 1964), persist until sometime before $t \sim 48$ days. About five days after optical maximum, the nebular lines of [O I] 6300 and 6363 Å appeared. The O II lines, which are the expected to become apparent at $\Delta B \sim 1.5$ mag below peak (Bath & Harkness, 1989), are always present from $t=33.7-61.7$ days.

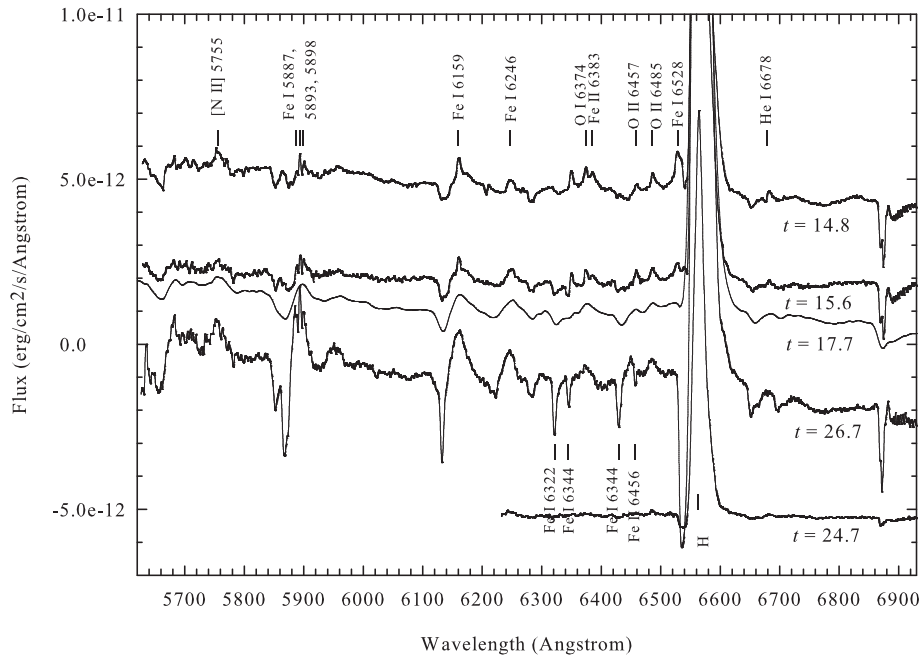


Figure 6.21: The red spectra during the final rise phase. Spectra are offset in flux for clarity with the spectrum at 14.8 days representing the observed flux and the later spectra being offset in steps of $2 \times 10^{-12} \text{ erg cm}^{-2} \text{ \AA}^{-1}$.

The Balmer lines began to show a double-peaked structure from the spectrum taken at $t=42.7$ days. About twenty days after the maximum ($t=45.6$ days), the forbidden line of [O III] 5007 \AA appeared. The flux of Balmer lines began to fade around $t=70$ days. The “4640 emission” (Payne-Gaposchkin, 1964) produced by a blend of N III and N II lines and known as the characteristic of the “*Orion spectrum*” (see Chapter 1) becomes apparent at $t \sim 70$ –80 days as shown in Figure 6.22. The emission line of N V at 4603 \AA , which is expected to appear during the Orion spectrum phase of a typical nova (Jaschek & Jaschek, 2009), also begins to emerge at $t=73.7$ days. The emergence of these lines is designated the ‘nitrogen flaring’ (see Chapter 1). Thus we find that the *Orion spectrum* stage (Payne-Gaposchkin, 1964; Warner, 2008) started around $t=70$ days. We note that the N III and N V lines appeared earlier than would have been expected from the simple Bath & Harkness model.

This evolution is in line with the progression toward the “*nebular spectrum*” stage of Classical Novae (Warner, 2008). Meanwhile the pseudo-photosphere is

continuing to shrink in radius and the effective temperature is increasing.

The He I 5876Å line and the [Fe X] 6375Å coronal line were marginally detected at $t=80.7$ days which was the last spectrum observed before the seasonal gap. When spectroscopic observations started again at $t=155.1$ days the nova displayed the expected nebular spectrum (see Figure 6.23).

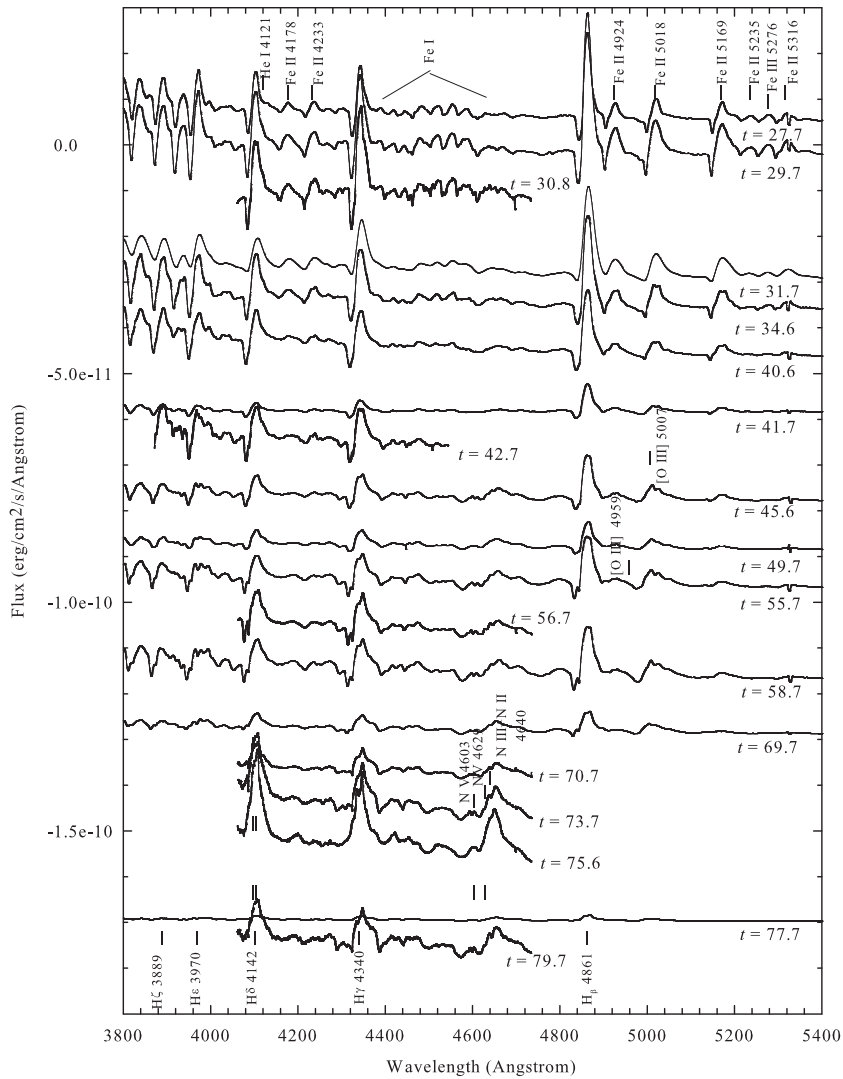


Figure 6.22: The blue spectra during the early decline phase. Spectra are offset in flux for clarity with the spectrum at 27.7 days representing the observed flux and the later spectra being offset in steps of $1 \times 10^{-11} \text{ erg cm}^{-2} \text{ \AA}^{-1}$.

5. *Transition to the nebular phase (2011 Oct 3 - Dec 19, $t=90-250$ days):* After the seasonal gap, T Pyx had declined to about 5 magnitudes below maximum. By

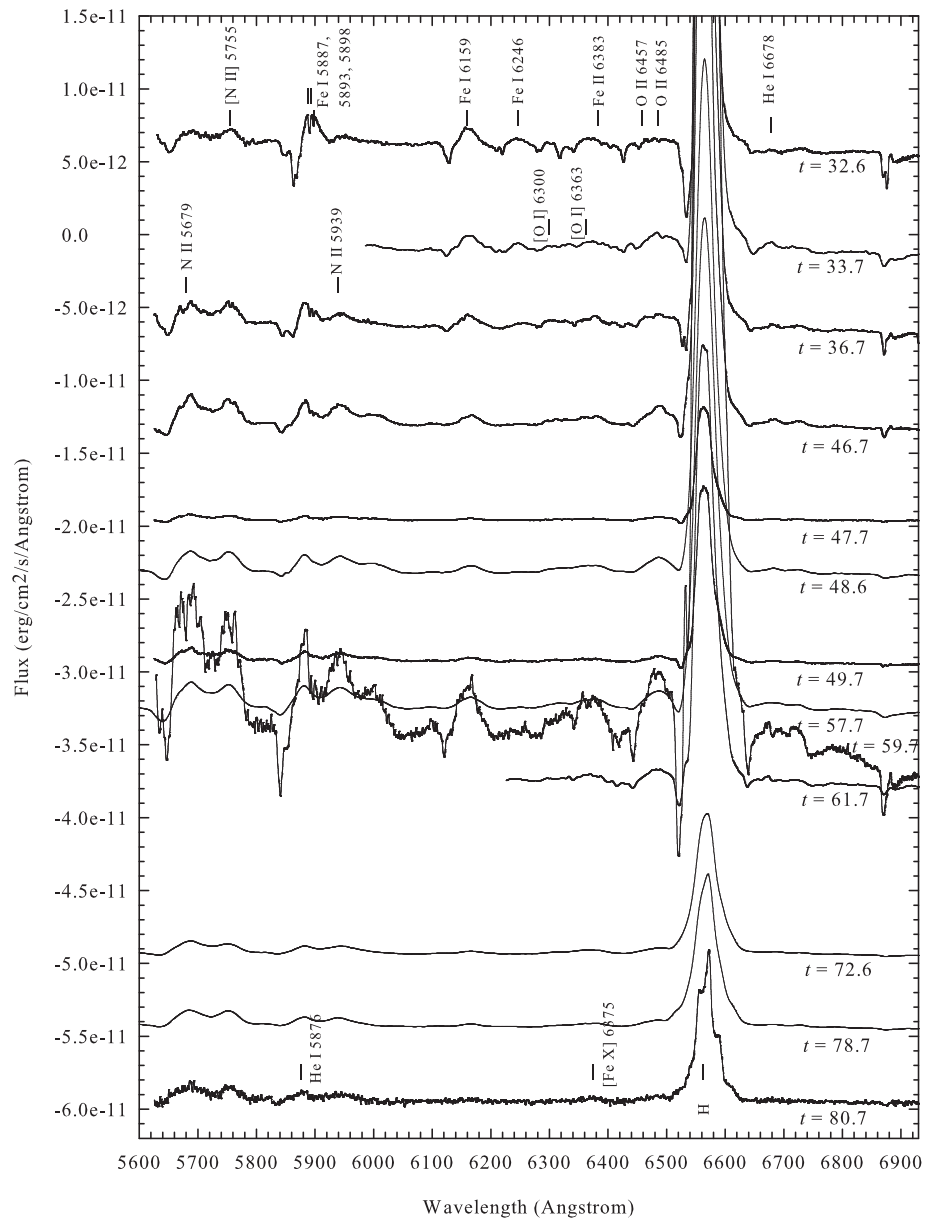


Figure 6.23: The red spectra during the early decline phase. Spectra are offset in flux for clarity with the spectrum at 32.6 days representing the observed flux and the later spectra being offset in steps of $1 \times 10^{-11} \text{ erg cm}^{-2} \text{ \AA}^{-1}$.

this time, as indicated in the previous phase, the [O III] 5007Å nebular and [Fe X] 6375Å coronal lines had clearly developed (see Figures 6.24 and 6.25). It is then of interest to note that the Swift satellite detected the rise in the X-ray light curve at $t=111$ days (see below).

The first blue spectrum ($t=155.1$ days) already showed [Ne III] 3869Å, [C III] 4364Å, N III 4640Å and these were increasing in intensity, especially the [C III] line as shown in Figure 6.24. The appearance of N III at $t\sim 90$ days is consistent with the expectations of Bath & Harkness (1989) for $\Delta B=2.9$ mag. H ϵ , H δ , and H γ have already faded. Moreover, the coronal lines [Fe X] 6375Å and [Fe VII] 6087Å were clearly present in the first red spectrum at $t=161.1$ days as shown in Figure 6.25. The Balmer lines are still stronger than [O III] 5007Å, however, and they present a multi-peak structure. [O III] 5007 was the strongest rival to the Balmer lines at $t=165.1$ days. The emission of [O III] and N III was strongest again at $t=221.9$ days. The last spectroscopic observation was made at $t=249.9$ days where the nova was clearly in the nebular spectrum stage and still exhibited [NII], He I, [Fe VII], and [Fe X] lines.

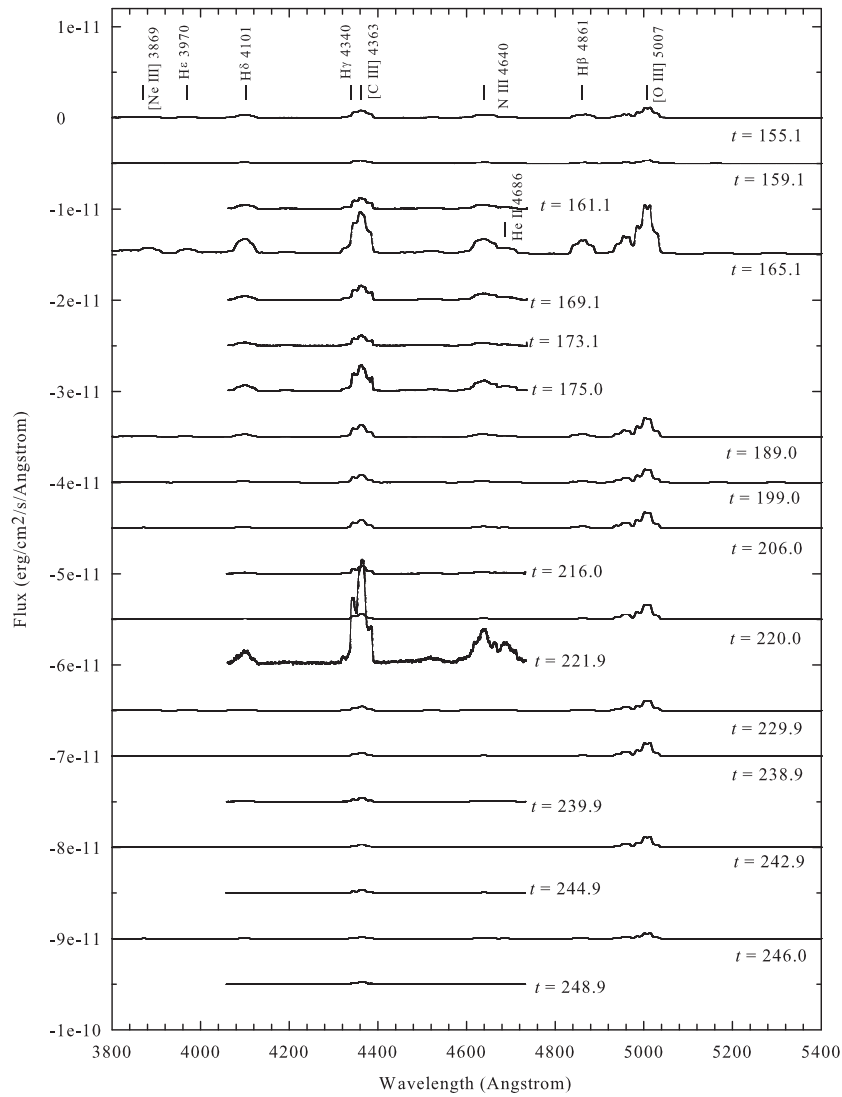


Figure 6.24: The blue spectra during the transition phase. Spectra are offset in flux for clarity with the spectrum at 155.1 days representing the observed flux and the later spectra being offset in steps of $5 \times 10^{-12} \text{ erg cm}^{-2} \text{ \AA}^{-1}$.

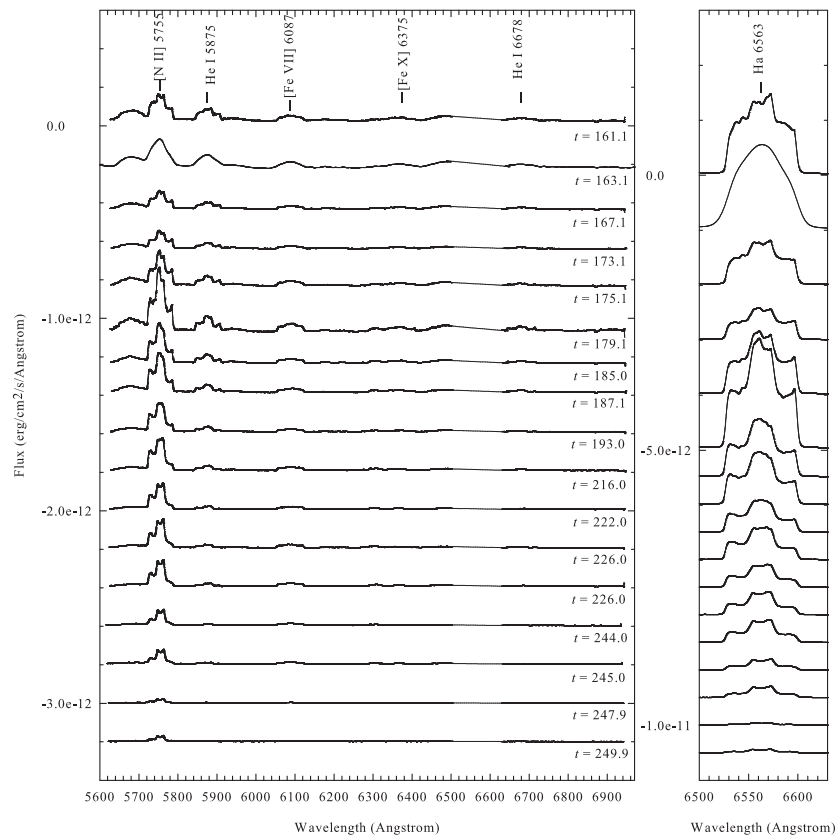


Figure 6.25: The red spectra during the transition phase. Spectra are offset in flux for clarity with the spectrum at 161.1 days representing the observed flux and the later spectra being offset in steps of 2×10^{-13} erg cm⁻²Å⁻¹ for the left panel and steps of 1×10^{-12} erg cm⁻²Å⁻¹ for the right panel.

6.3.3 Comparison to the X-ray and Radio Light Curves

Figure 6.26 shows the optical light curves from AAVSO and SMEI, together with the expected appearance of various spectral lines from Bath & Harkness (1989), the X-ray light curve from SWIFT, and the radio light curves from the VLA as presented in Nelson et al. (2012). During the pre-maximum halt phase in the SMEI light curve, the rise of the high frequency (33 GHz) radio emission was detected at $t=7-15$ days but X-rays were not yet detected. During the final rise through the early decline (until $t\sim 45$ days) radio emission at all frequencies tended to be stable with a small trend of increase during the optical decline. At $t\sim 45$ days, [O III] 5007Å appeared, and while the radio emission subsequently rose steeply, the X-rays were still not detected.

The Swift satellite detected the rise of X-ray emission (0.3-10 keV) at $t=111$ days, at $\Delta V\sim 4$ mag below peak. From Equation 6.1, T_{eff} would be $\sim 320,000$ K. This is typical for a SSS (see Kahabka, 2006). Taking $L_{bol}\sim 2\times 10^{38}$ erg s⁻¹, calculated from $M_{bol}=-7.0$ given by Schaefer (2010), the approximate radius of the pseudo-photosphere at this time would be 5.1×10^9 cm. As expected, this is smaller than the binary separation calculated from the binary parameters given in Uthas et al. (2010) as 6.1×10^{10} cm, but larger than the radius of $\sim 4.9\times 10^8$ cm of a $1M_{\odot}$ WD (Starrfield et al., 2012). We note however that the Chandra grating spectra at this phase showed that emission lines were very strong in the X-ray spectrum (Orio, 2012). The X-ray emission at this time is likely a mix of a SSS and shocked circumstellar gas.

The X-ray emission then rose to a peak at $t\sim 144$ days (Kuulkers et al., 2011). This is consistent with the appearance of lines from highly ionized species such as [Ne III] 3869Å, [C III] 4364Å, and N III 4640Å, that we found in the first blue spectrum ($t=155.1$ days) right after the seasonal gap. The presence of the N III line was expected some time between 85 and 90 days in the seasonal gap according to ΔB (Bath & Harkness, 1989) although N III+ N II 4640Å was detected slightly earlier at 73.7 days. By the time of the rise in X-rays H ϵ , H δ , and H γ had already faded.

The clear presence of the coronal lines [Fe VII] 6087Å and [Fe X] 6375Å at $t=161.1$ days coincides with the middle of the X-ray plateau phase and also the peak of the

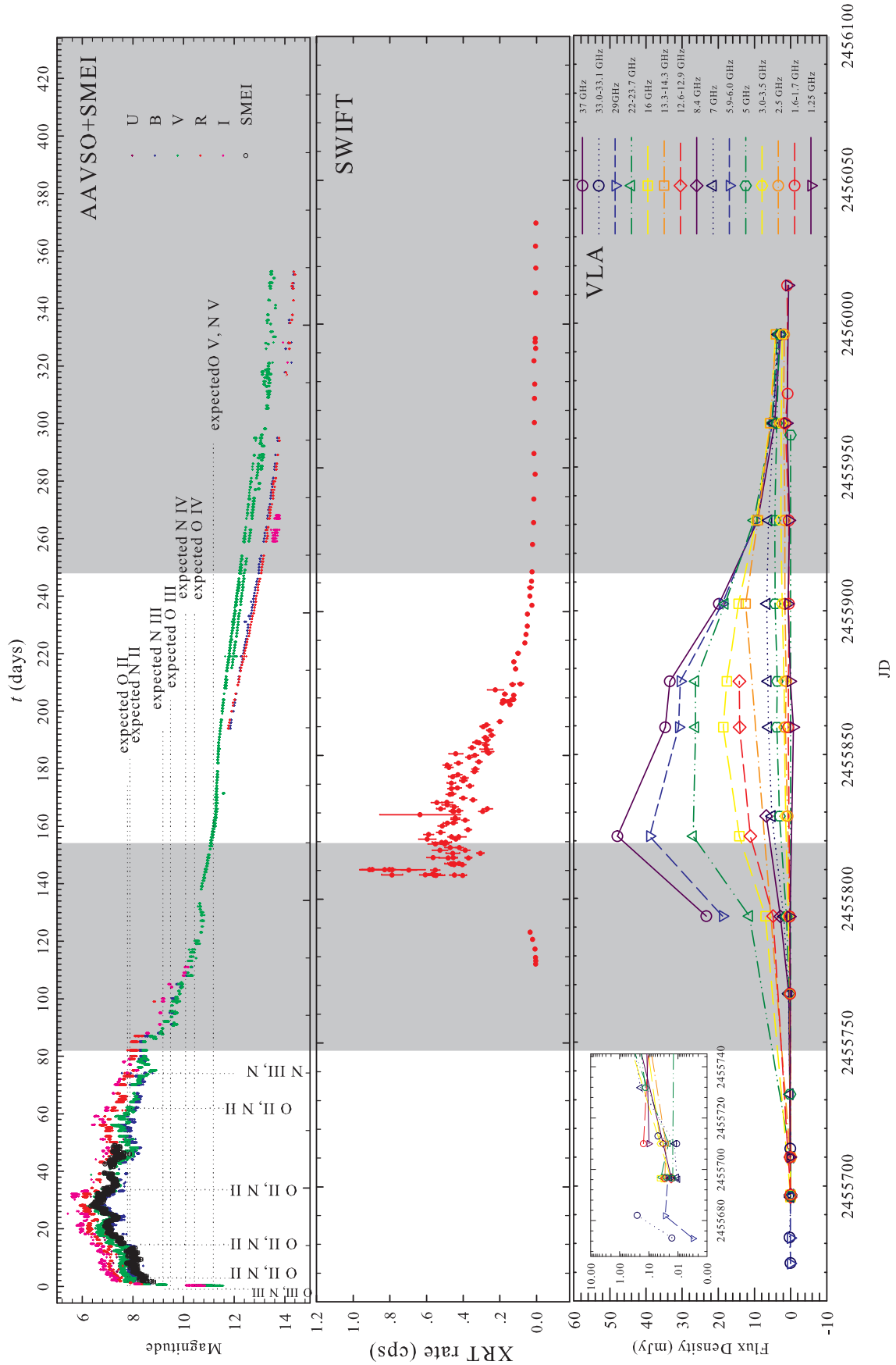


Figure 6.26: Comparison between optical, radio and X-ray light curves with the top panel also indicating the expected appearance of various ionized species from the models of Bath & Harkness (1989). Shaded areas represent the epochs where we do not have spectroscopic coverage. The early evolution of the radio flux is shown in the inset in the bottom panel with a logarithmic flux scale for clarity.

radio emission (see below). The X-ray emission again became undetectable at $t \sim 222$ days. The blue optical spectrum at $t = 221.9$ days shows the strongest emission to be [C III] 4364Å and N III 4640Å.

The radio light curve kept increasing throughout the X-ray rise and peaked at around $t \sim 155$ days for the highest frequency (37 GHz) corresponding to the middle of the plateau in the X-ray light curve. In contrast, the lowest frequency (1.25 GHz) seemed to reach its peak at $t = 290-330$ days. Nelson et al. (2012) suggested that it was the material ejected during the 2011 outburst that gave rise to the radio emission not the ionization of a pre-existing circumbinary medium. They note that although the resolved pre-outburst $H\alpha + [N II]$ emitting nebula surrounding T Pyx could be conceived to cause the rise ($t \sim 62-149$ days) and fade of the radio light curve, the observed $H\alpha$ luminosities during the outburst are much too low to be consistent with this. In addition, they concluded that dense material in the immediate vicinity of the central binary should have similar characteristics to a stellar wind and, therefore, exhibit a partially optically thin radio spectrum while the observed spectrum during the rise appears to be completely optically thick (Nelson et al., 2012).

6.4 Conclusions

In this Chapter, we investigated the optical light curve of T Pyx in its 2011 outburst through compiling a database of SMEI and AAVSO observations. The SMEI light curve, providing unprecedented detail with high cadence data, was divided into four phases based on the idealised nova optical light curve: the initial rise; the pre-maximum halt; the final rise, and the early decline.

A period of 1.44 ± 0.05 days was the most strongly detected and was found in the interval from the first observation to the end of the pre-maximum halt phase, before the visual maximum. We compared this result to oscillations found in CVs and ascribed to accretion disk precession (Hirose & Osaki, 1990). Our observed $P_{orb}/P_{precession}$ is then 5.3% corresponding to $q = 0.125-0.15$ which compares to $q = 0.2 \pm 0.03$ derived by Uthas

et al. (2010). Although the period is in line with that expected from studies of disk precession in CVs, we question however whether the disk would again be present so early in the outburst. Such oscillations are however present in some of the light curves derived by Hillman et al. (2013) from TNR models and may be related to restructuring and rebalancing of the ejected envelope as it expands. We find no spectral variations related to the light curve periodicity however.

The pre-maximum halt and subsequent dip in the SMEI light curve at $t \sim 22-24$ days again resemble features in the light curves produced by Hillman et al., with the latter possibly mirroring the shorter duration feature seen in other novae observed by SMEI (Hounsell et al., 2010). We note that this is coincident with a sharp transitory decline in $H\alpha$ flux and an equally sharp increase in that from Fe II.

The spectra from the LT and SMARTS were investigated through each of the 4 phases of the optical light curve, in order to study the spectral evolution and investigate the physical causes of the variations of the light curve. We conclude, taking each phase in turn:

Initial Rise ($t=0.8-3.3$ days). The spectra show lines of high ionization species consistent with the presence of a high effective temperature pseudo-photosphere. The emission comes almost entirely from the continuum in this the “fireball” stage. The marked drop in the derived expansion velocity (4000 km s^{-1} at $t=0.8$ days to $\sim 2000 \text{ km s}^{-1}$ at $t=2.7$ days) is consistent with the initial ejection in the form of a Hubble-like flow, but also resembles that noted in Type Ia SNe and ascribed to interaction with pre-outburst material.

Pre-Maximum Halt ($t=3.6-13.7$ days). The subsequent change in behaviour of the derived V_{ej} during the pre-maximum halt phase may suggest 2 different stages of mass loss: a short-lived phase occurring immediately after outburst and then followed by a more steadily evolving and higher mass loss phase. The fireball spectrum is maintained until $t=8.6$ days which is also the beginning of the typical iron curtain stage. Overall, the ionization/excitation and effective temperature of the underlying pseudo-photosphere appear to be decreasing through this phase, in line with basic models.

Final Rise ($t=14.7-27.9$ days). The typical principal spectrum of a CN seems to be apparent and displays the O I flash beginning at $t\sim 17$ days with the characteristics of the iron curtain phase still persisting. The gradual increase in V_{ej} , starting to appear in the final rise ($t=14.8$ days) and later, may be related to increasing ejection velocities from the central system, as proposed in other novae. The visual maximum at $t=27.9$ days seems to exhibit the lowest ionization lines, as expected.

Early Decline ($t=27.9-90$ days). The Balmer lines began to have a double-peaked structure from $t=42.7$ days and this is shortly followed by the emergence of forbidden lines. The typical Orion spectrum is suggested to start at $t\sim 70$ days. The emission line of N V at 4603\AA begins to emerge at $t=73.7$ days. The strong enhancement of N lines is associated with ‘nitrogen flaring’ in the typical Orion spectrum stage.

Transition to the Nebular Phase ($t=90-280$ days). By this time, the [O III] 5007\AA nebular and [Fe X] 6375\AA coronal lines have developed, the latter having been marginally detected at $t=80$ days while the rise in the X-ray light curve was detected at $t=111$ days. The last spectroscopic observation reported here at $t=249.9$ days in the nebular stage still exhibited [NII], He I, [Fe VII], and [Fe X] lines.

The overall spectral development of T Pyx is similar to that of CNe whose ejected mass is higher and velocity of ejection is lower than in typical RNe such as U Sco and RS Oph. We also found that in general the detected ionized elements are in line with those expected from the simple pseudo-photosphere models of Bath & Harkness (1989) at the same ΔB as shown in Table 6.4 and Figure 6.26. An exception to this occurred near the end of the early decline phase where for example N III and N V emission lines emerged earlier than would have been predicted.

In terms of the relationship of the optical development described here to that at other wavelengths, we found that the rise of the high frequency (33 GHz) radio emission was detected at $t=7-15$ days during the pre-maximum halt phase in the SMEI light curve, while X-rays were not yet detected.

At $t\sim 45$ days, where the [O III] 5007\AA was first present, the radio emission rose steeply while the X-rays were still undetectable. The rise in the X-ray emission, which then

began at $t=111$ days and rose to peak at $t\sim 144$ days (Kuulkers et al., 2011), is consistent with the appearance of lines from highly ionized species such as [Ne III] 3869Å, [C III] 4364Å, N III 4640Å, found in the first blue spectrum ($t=155.1$ days) right after the seasonal gap.

If the onset of the X-ray phase and the start of the final decline in the optical are related to the cessation of significant mass loss, this occurred at $t\sim 90-110$ days. During the rise in X-rays, the radio flux kept increasing and peaked at around $t\sim 155$ days for the highest frequency (37 GHz) corresponding to the middle of the plateau in the X-ray light curve where we clearly detected the coronal lines [Fe X] 6375Å and [Fe VII] 6087Å in our spectra ($t=161.1$ days).

Although the appearance of the X-ray emission is in line with predictions of the emergence of the SSS from the simple Bath & Harkness (1989) model, we note that X-ray emission may be a mix of SSS and shocked circumstellar gas.

Having discussed the results of our work on T Pyx in this penultimate Chapter, we now summarise the work contained in this thesis and make suggestions for future studies in Chapter 7.

Chapter 7

Summary, Conclusions and Future Work

7.1 Summary and Conclusions

The results of the research conducted within this thesis are discussed below.

7.1.1 Observations of Galactic Novae in Quiescence

The proposal that RNe occupy a region separated from CNe in an outburst amplitude versus speed class diagram was adopted. The low amplitude results from the existence of an evolved secondary and/or high mass transfer rate in the quiescent system. The 93 novae with observed V amplitudes given in the literature and 43 novae with published photographic amplitudes have been combined and plotted on an outburst amplitude versus rate of decline diagram as shown in Figures 2.2 and 2.3. From these, 16 target novae suspected to be RNe candidates were selected for the photometric and spectroscopic observations.

Quiescent photometric magnitudes in u , B , V , r , i and z were obtained for 10 novae at quiescence using RATCam on LT (see Table 3.1). Spectra for twelve of them were

obtained using FRODOSpec on LT and RSS on SALT (see Table 3.2). Of these, only nine spectra could be successfully fully reduced for further analysis (see Table 3.4). Spectra for the other three objects (CN Vel, LZ Mus and V888 Cen) were not fully reduced due to the unclearly matched arc line identifications which causes a shift in wavelength (for CN Vel and V888 Cen) and an underestimate of the exposure times making the spectra indistinguishable from the background (for LZ Mus).

All sixteen initially selected novae were plotted in a NIR CMD to determine the spectral type of the secondaries. Meanwhile ten novae observed by LT were plotted in an optical CMD to compare with results determined by the NIR CMD. Determinations of reddening were adopted from the literature for seven novae with known extinction. Extinction for another five novae was estimated from extinction maps and equivalent widths of Na I D lines.

As discussed in Chapter 4, the dereddened spectra were used to determine luminosity class by using relations including the $EW(\text{CaT})$ versus $\log g$, the Na I 8190 index versus TiO 8465 index, and the identification of specific line indicators.

Determination of spectral types was accomplished by identifying specific lines and calculating indices from TiO bands, VO bands, and the Na atomic line for giants (4 stars) and sub-giants/giants (3 stars). A spectral library template was used instead of the indices in cases of main-sequence stars (2 stars). The summary of findings on the evolutionary status of secondaries in nine novae with observed spectra is shown in Table 4.6.

Comparison of results between the optical and NIR CMDs found that 7 systems show consistent results; 3 RG-Novae (T CrB, V749 Oph, FS Sct), 3 RG/SG-Novae (V3964 Sgr, V2487 Oph, CI Aql), and 1 MS-Novae (V368 Aql).

Comparison of results from NIR CMD (based on the definition of secondaries in nova systems given by Darnley et al., 2013) to those from spectroscopy again shows 7 systems are in good agreement (4 RG-Novae: T CrB, V2487 Oph, V3964 Sgr and EU Sct; and 3 SG-Novae: CI Aql, V794 Oph and V368 Aql). Only 2 systems (AR Cir and V3645 Sgr) show inconsistent results. In the case of AR Cir, this is due to the

erroneous acquisition of the nearby companion star in SALT spectroscopy. The cause for V3645 Sgr is still to be determined.

Our investigation also confirmed the positions of AR Cir, V794 Oph and EU Sct where there had been some ambiguity previously. Ultimately, we suggest here four prime candidates (2 RG-Novae - V3964 Sgr and EU Sct, and 2 SG-Novae - V794 Oph and V368 Aql) which are currently classified as CNe, to look for more than one outburst in archival plates or large sample sky surveys.

7.1.2 Investigation of Novae with the Solar Mass Ejection Imager (SMEI)

We have introduced the high cadence full-sky space-based observational archive of SMEI. Selected targets were added into SMEI's object list, each was inspected in SMEI's sky maps by eye to identify bad orbits. Background light and sidereal zodiacal light were then subtracted from sky maps, and finally the magnitudes of the targets were obtained by fitting the standard PSF.

Using data thus derived from the SMEI archive, we derived light curves of one Mira (O Cet) and two novae with known outbursts during 2003-2011 (V2467 Cyg and V1187 Sco). The SMEI light curves potentially reveal for more details of the progress of an outburst in the optical than those given by ground-based observations. The pre-maximum halt was found in V2467 Cyg as well as oscillations in light curves found earlier than those found in previous studies. The precise date of optical maximum of each nova was determined.

Four bright novae that are potentially RNe candidates, as suggested in Chapters 2 and 3, were searched for second outbursts, but none were found.

Among the nova outbursts detected by SMEI, the unprecedented detail in first class data of the Recurrent Nova T Pyx in its 2011 outburst reveals important results which were used for detailed investigations.

7.1.3 T Pyxidis in Its 2011 Outburst

We investigated the optical light curve of T Pyx in its 2011 outburst through compiling a database of SMEI and AAVSO observations. The SMEI light curve, providing unprecedented detail with high cadence data, was divided into four phases based on the idealised nova optical light curve: the initial rise; the pre-maximum halt; the final rise, and the early decline.

A period of 1.44 ± 0.05 days was the most strongly detected and was found the interval from the first observation to the end of the pre-maximum halt phase, before the visual maximum. Although the period is in line with that expected from studies of disk precession in CVs, we question however whether the disk would again be present so early in the outburst. Such oscillations are however present in some of the light curves derived by Hillman et al. (2013) from TNR models and may be related to restructuring and rebalancing of the ejected envelope as it expands. No spectral variations that mirror the light curve periodicity were found however.

The spectra from the LT and SMARTS were investigated through each of the 4 phases of the optical light curve, in order to study the spectral evolution and investigate the physical causes of the variations of the light curve. We conclude, taking each phase in turn:

Initial Rise ($t=0.8-3.3$ days). The spectra show lines of high ionization species consistent with the presence of a high effective temperature pseudo-photosphere. The emission comes almost entirely from the continuum in this the “fireball” stage. The marked drop in the derived expansion velocity (4000 km s^{-1} at $t=0.8$ days to $\sim 2000 \text{ km s}^{-1}$ at $t=2.7$ days) is consistent with the initial ejection in the form of a Hubble-like flow, but also resembles that noted in Type Ia SNe and ascribed to interaction with pre-outburst material.

Pre-Maximum Halt ($t=3.6-13.7$ days). The subsequent change in behaviour of the derived V_{ej} during the pre-maximum halt phase may suggest 2 different stages of mass loss: a short-lived phase occurring immediately after outburst and then followed by

a more steadily evolving and higher mass loss phase. The fireball spectrum ended and the typical iron curtain stage began at around $t=8.6$ days. Overall, the ionization/excitation and effective temperature of the underlying pseudo-photosphere appear to be decreasing through this phase, in line with basic models.

Final Rise ($t=14.7-27.9$ days). The typical principal spectrum of a CN seems to be apparent and displays the O I flash beginning at $t\sim 17$ days with the characteristics of the iron curtain phase still persisting. The gradual increase in V_{ej} , starting to appear in the final rise and later, may be related to increasing ejection velocities from the central system, as proposed in other novae. The visual maximum at $t=27.9$ days seems to exhibit the lowest ionization lines, as expected.

Early Decline ($t=27.9-90$ days). The Balmer lines began to have a double-peaked structure followed by the emergence of forbidden lines. The typical Orion spectrum is suggested to start at $t\sim 70$ days. The strong enhancement of N lines associated with ‘nitrogen flaring’ emerges in this stage.

Transition to the Nebular Phase ($t=90-280$ days). By this time, the [O III] nebular and [Fe X] coronal lines have developed while the rise in the X-ray light curve was detected at $t=111$ days. The last spectroscopic observation reported here at $t=249.9$ days in the nebular stage still exhibited [NII], He I, [Fe VII], and [Fe X] lines.

The overall spectral development of T Pyx is similar to that of CNe whose ejected mass is higher and velocity of ejection is lower than in typical RNe such as U Sco and RS Oph. We also found that in general the detected ionized elements are in line with those expected from the simple pseudo-photosphere models of Bath & Harkness (1989) at the same ΔB .

If the onset of the X-ray phase and the start of the final decline in the optical are related to the cessation of significant mass loss, this occurred at $t\sim 90-110$ days. During the rise in X-rays, the radio flux kept increasing and peaked at around $t\sim 155$ days for the highest frequency (37 GHz) corresponding to the middle of the plateau in the X-ray light curve where we clearly detected the coronal lines [Fe X] 6375Å and [Fe VII] 6087Å in our spectra ($t=161.1$ days).

Although the appearance of the X-ray emission is in line with predictions of the emergence of the SSS from the simple Bath & Harkness (1989) model, we note that the X-ray emission may be a mix of SSS and shocked circumstellar gas.

7.2 Future Work

Future work proposed to be conducted on areas of research presented within this thesis is discussed below.

7.2.1 Galactic Novae in Quiescence

A further investigation could be made of the nova spectra encountering the shift in wavelength of the calibration arcs and also data on other novae observed by HET (V1330 Cyg) and the Yunnan Observatory (BT Mon) could be fully reduced and analysed. In addition, more novae with low outburst amplitudes could be from an A' versus t_3 diagram and their spectra investigated. While the spectra in the red region can determine the types of the secondaries, further blue spectra could be gathered to investigate the accretion disk contribution and thus perhaps determine the accretion rate.

From this study, we know that the luminosity class determination is the first step to identify the evolutionary status of the secondaries, whether they are class V, IV or III stars, by using relations including the $EW(\text{CaT})$ versus $\log g$ or the Na I 8190 index versus the TiO 8465 index. Therefore one may quickly classify the secondary stars of novae by obtaining spectra in only the red region covering Ca II at 8498Å 8542Å 8662Å, Na I 8190 and TiO 8465. This method could be done at a 2-m class telescope in order to reduce the observation times.

7.2.2 Investigation of Novae with the Solar Mass Ejection Imager (SMEI)

It should be noted that further investigation of bright novae with high priority in Table 5.1 should be carried out. Hounsell (2012) proposed that over 50 novae may be found within the SMEI data archive since the estimated number of novae brighter than 8th magnitude occurring each year is ~ 6 (Shafter, 2002).

When considering light curves of novae throughout the years overall, two features were noticed in general. First, the background sky levels have a wave shape over the year (see Figure 5.13 - 5.16) which might be fitted and subtracted and yield therefore better results. Second, there were some detections which are brighter than the line indicating the previous recorded outburst magnitude (see e.g. Figure 5.15). More intensive investigation should be carried out in the future on this.

Features in the nova light curves from SMEI (first-class data) should be compared in detail with the TNR modelled light curves of typical CNe given by Hillman et al. (2013) which provides detailed nova evolution from pre-nova rise, mass loss phase and post-nova decline phase. Finally we note that the SMEI archive is still a relatively untapped resource for investigating transient and variable astrophysical sources of many types.

Appendix A

Acquisition of SMEI Data

Here we describe the subsequent steps in accessing and reducing the data remotely from LJM U.

A.1 Connecting to the SMEI Computer and Accessing the Database

In order to access the SMEI database running on the UCSD computer from abroad, the remote control software was installed. In this study we used two software packages, working together called ‘PuTTY’¹ and ‘TightVNC’² to run on the Windows machine properly.

Once the PuTTY and TightVNC were installed, we connected PuTTY to the host name `soft@smei.ucsd.edu` via Port 22 and logged in as username:soft. Then we opened TightVNC and connected to server: localhost 3. The SMEI desktop appeared and allowed us to work on its Linux terminal.

¹ PuTTY is an SSH and telnet client, developed originally by Simon Tatham for the Windows platform. PuTTY is free open source software that is downloadable at <http://www.putty.org/>

² TightVNC is a free remote control software package allowing you to see the desktop of a remote machine and control it with your local mouse and keyboard. It can be downloaded at <http://www.tightvnc.com/download.php>

A.2 Adding New Objects to SMEI's Object List

Before fitting the point sources in SMEI maps, the objects must be included in SMEI's object list which requires information including name, magnitude, RA and DEC. Access the list can be achieved by the following steps below:

```
zaphod:~$ ssh cass185.ucsd.edu
cass185:~$ cd smei/ucsd/camera/idl/star
cass185:~/smei/ucsd/camera/idl/star$ vi nova-list.txt
<<< add new objects, save and quit :wq >>>
cass185:~/smei/ucsd/camera/idl/star$ exit
cass185:~/smei/ucsd/camera/idl/star$ ssh smei
cass185:~/smei/ucsd/camera/idl/star$ full_refresh
```

A.3 Object Visual Inspection in SMEI's Sky Maps

Objects and their surrounding region on SMEI's sky map were inspected visually prior to the point source fitting for bad orbits (i.e. orbits that are contaminated by artefacts from the pipeline reduction process) which were then identified and excluded.

To see if the object is visible in SMEI's sky map at a given date and time, the orbit number³ is required. For example, the image of the Recurrent Nova T Pyx at visual maximum (on 2011 May 12.22 UT corresponding to orbit number 43279) can be obtained by the following steps:

SMEI's user interface is written in IDL programmed by the SMEI team at UCSD. The main window is `qsmei_sky` that can call several other associating modules including `qTool` and `qEphem`.

1. Open a terminal.

```
zaphod:~$ idl
```

³ Orbit number, date, time, and operation status of three cameras for each orbit are provided at <http://smei.ucsd.edu/sky/index.html>

```
IDL> qsmei_sky
```

- In a `qsmei_sky` window (Figure A.1 top), input general parameters; the orbit number (1); selected map which can be either non-subtracted or subtracted by either background or zodiacal light (2); selected Camera (3); and size of the monitor (4 and 5). Then call `qTool` (6) and `qEphem` (7) modules. The `qTool` (Figure A.1 middle) allows us to zoom (8), choose the box's colour (9), and adjust the brightness (10) of the monitor. While the `qEphem` (Figure A.1 bottom) targets the input object i.e. T Pyx (11) and presents as a resizable box (12). The `qsmei_sky`'s monitor will activate on pressing the Enter key (Figure A.2).

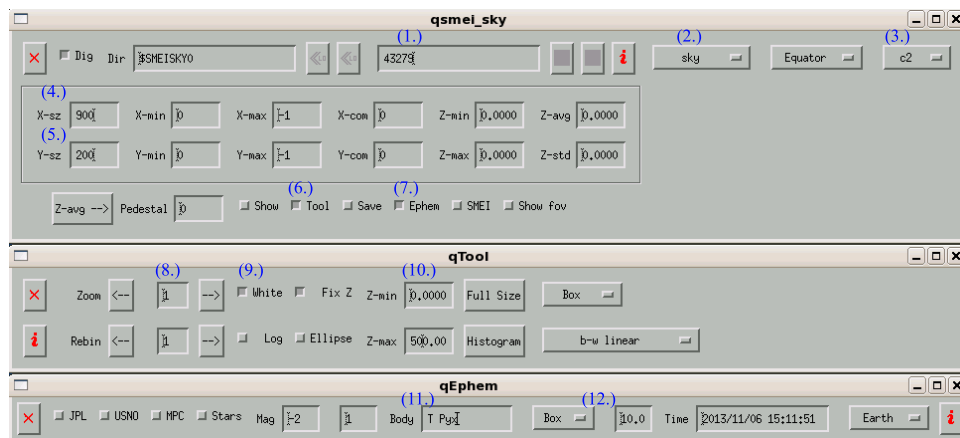


Figure A.1: SMEI user interface showing the modules used for this work. The main `qsmei_sky` window (top) with the associating modules `qTool` (middle) and `qEphem` (bottom). The general input parameters are labelled.

Figure A.3 shows the PSF of T Pyx in different 2 epochs: prior to the outburst (top panels) and around visual maximum (bottom panels), and also shows brightness changes due to the subtraction of the sky map, from without any subtraction (left) to those with background subtraction (middle) and with both background and zodiacal light subtraction (right). Note that the rotation in angle of PSFs depending on position in the sky map (Hick et al., 2007) can also be seen in the Figure.

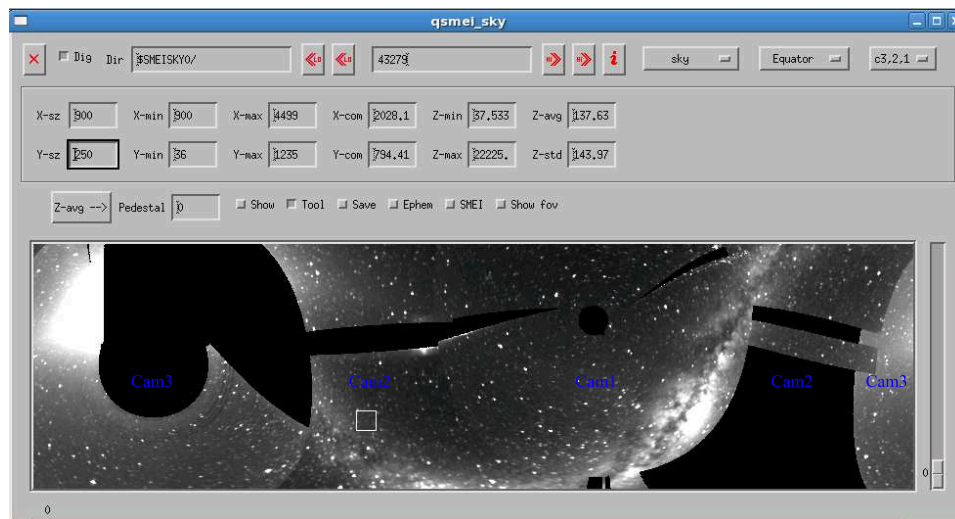


Figure A.2: Object point source displayed on SMEI’s sky map. Different patches of sky covered by three cameras are labelled. The object T Pyx is located in a white square box. This image is taken from orbit number 43279 (2011 May 12 at 05:07:52 UT).

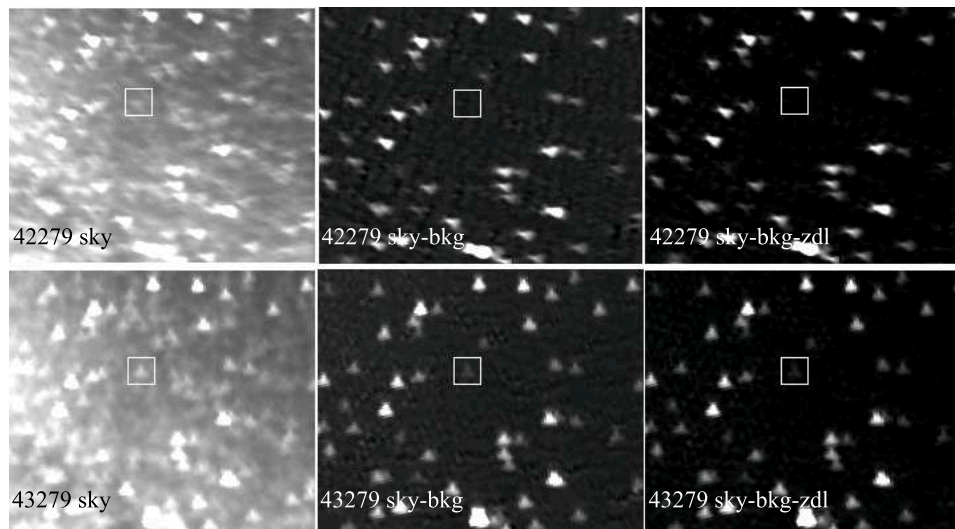


Figure A.3: SMEI sky maps for T Pyx at different epochs; HJD 2455623.1767 or orbit number 42279 (top), and HJD 2455693.7145 or orbit number 43279 (bottom). All images are viewed by Camera 2 with non-subtraction (left), with background subtraction (middle) and with background and zodiacal light subtraction (right).

A.4 Fitting a Point Source

The photometry of a single point source was obtained by fitting the standard PSF mentioned above using a least-squares procedure implemented in IDL (see Hounsell, 2012, for more details). In this study, all investigated objects were fitted by using the same set

of parameters, e.g. automatic adjusting for PSF centroid (`fix_centroid`), automatic calculating of the size of the PSF radius which depends on the object's brightness (`auto_wing`), removal of background (`rmbkgnd`), removal of zodiacal light (`rmzld`), cleaning edge (`cleanedge`) when an object moves from one camera to another .

For example, fitting the data of T Pyx from Camera 2 from an orbit number 011231 which is observed on a Day of Year (DOY) 60 in year 2011 to an orbit number 214758 (DOY 269 in year 2011) can be done by using the routine `smei_star_fitone` as follows:

```
IDL> smei_star_fitone, 'T Pyx',  
[timeset('2011_060_011231'),  
timeset('2011_269_214758')], /fix_centroid,  
/auto_wing, /degrees, /use_weights, /rmzld, /rmbkgnd,  
destination='/home/soft/Momay/', cat='*', mode='sky',  
camera=2, /cleanedge, /fix_fovangle, /fix_psfangle
```

Then once the output file 'T_Pyx____.txt' is automatically saved, it can then be transformed from the intensity in the image to m_{SMEI} by using the routine `startimes` given below. This also can be done by the simple calculation $m_{SMEI}=[-2.5*\log((I/I_{std})/Gain)-a]/b$, where $a=1.65$ and $b=0.99$ (Hounsell, 2012).

```
IDL> startimes, 'Momay/T_Pyx____.txt',  
outfile='Momay/TPyx_magC2.txt'
```

References

- Anupama, G. C. 2008, in *Astronomical Society of the Pacific Conference Series*, Vol. 401, *RS Ophiuchi (2006) and the Recurrent Nova Phenomenon*, ed. A. Evans, M. F. Bode, T. J. O'Brien, & M. J. Darnley, 31
- Anupama, G. C. 2013, in *IAU Symposium*, ed. R. Di Stefano, M. Orio, & M. Moe, Vol. 281, 154
- Anupama, G. C., & Mikołajewska, J. 1999, *A&A*, 344, 177
- Baraffe, I., Chabrier, G., Allard, F., & Hauschildt, P. H. 1998, *A&A*, 337, 403
- Barbon, R., Benetti, S., Rosino, L., Cappellaro, E., & Turatto, M. 1990, *A&A*, 237, 79
- Barnsley, R. M., Smith, R. J., & Steele, I. A. 2012, *Astronomische Nachrichten*, 333, 101
- Bath, G. T., & Harkness, R. P. 1989, in *Classical Novae*, 1st Edition, ed. M. F. Bode & A. Evans, Wiley, New York, 61
- Benetti, S., Cappellaro, E., Mazzali, P. A., Turatto, M., Altavilla, G., Bufano, F., Elias-Rosa, N., Kotak, R., Pignata, G., Salvo, M., & Stanishev, V. 2005, *ApJ*, 623, 1011
- Bianchini, A., della Valle, M., Orio, M., Ogelman, H., & Bianchi, L. 1991, *The Messenger*, 64, 32
- Bode, M. F. 2010, *Astronomische Nachrichten*, 331, 160
- Bode, M. F., Darnley, M. J., Shafter, A. W., Page, K. L., Smirnova, O., Anupama, G. C., & Hilton, T. 2009, *ApJ*, 705, 1056

- Buckley, D. A. H., Swart, G. P., & Meiring, J. G. 2006, in Society of Photo-Optical Instrumentation Engineers (SPIE) Conference Series, Vol. 6267, 32
- Buffington, A., Band, D. L., Jackson, B. V., Hick, P. P., & Smith, A. C. 2006, *ApJ*, 637, 880
- Buffington, A., Bisi, M. M., Clover, J. M., Hick, P. P., & Jackson, B. V. 2007, AGU Fall Meeting Abstracts, A1080
- Catchpole, R. M. 1969, *MNRAS*, 142, 119
- Chesneau, O., et al. 2011, *A&A*, 534, L11
- Contini, M., & Privalnik, D. 1997, *ApJ*, 475, 803
- Crocker, M. M., Davis, R. J., Spencer, R. E., Eyres, S. P. S., Bode, M. F., & Skopal, A. 2002, *MNRAS*, 335, 1100
- Cutri, R. M., et al. 2003, The IRSA 2MASS All-Sky Point Source Catalog, NASA/IPAC Infrared Science Archive.
- Darnley, M. J. 2005, Automated Searches for Extragalactic Novae, PhD Thesis, Liverpool John Moores University
- Darnley, M. J., Ribeiro, V. A. R. M., Bode, M. F., Hounsell, R. A., & Williams, R. P. 2012, *ApJ*, 746, 61
- Darnley, M. J., Ribeiro, V. A. R. M., Bode, M. F., & Munari, U. 2011, *A&A*, 530, A70
- Darnley, M. J., et al. 2006, *MNRAS*, 369, 257
- Darnley, M. J., Bode, M. F., Harman, D. J., Hounsell, R. A., Munari, U., Ribeiro, V. A. R. M., Surina, F., Williams, R. P., & Williams, S. C. 2013, ArXiv e-prints, 1303.2711
- Deeming, T. J. 1960, *MNRAS*, 121, 52
- Di Stefano, R. 2010, *ApJ*, 712, 728

- Diaz, M. P., & Bruch, A. 1994, *Information Bulletin on Variable Stars*, 4079, 1
- Dilday, B., et al. 2012, *Science*, 337, 942
- Dobashi, K., Uehara, H., Kandori, R., Sakurai, T., Kaiden, M., Umemoto, T., & Sato, F. 2005, *PASJ*, 57, 1
- Downes, R. A., Webbink, R. F., Shara, M. M., Ritter, H., Kolb, U., & Duerbeck, H. W. 2001, *PASP*, 113, 764
- . 2005, *Journal of Astronomical Data*, 11, 2
- Duerbeck, H. W. 1981, *PASP*, 93, 165
- . 1988a, *Bulletin d'Information du Centre de Donnees Stellaires*, 34, 127
- . 1988b, *A&A*
- Duerbeck, H. W. 2008, in *Classical Novae*, 2nd Edition, ed. Bode, M. F. & Evans, A., Cambridge University Press, Cambridge, 1
- Duerbeck, H. W., & Grebel, E. K. 1993, *MNRAS*, 265, L9
- Duerbeck, H. W., & Seitter, W. C. 1979, *The Messenger*, 17, 1
- Ederoclite, A. 2013, *ArXiv e-prints*, 1304.1305
- Eggleton, P. P. 1983, *ApJ*, 268, 368
- Ennis, D., Beckwith, S., Gatley, I., Matthews, K., Becklin, E. E., Elias, J., Neugebauer, G., & Willner, S. P. 1977, *ApJ*, 214, 478
- Evans, A., Tyne, V. H., Smith, O., Geballe, T. R., Rawlings, J. M. C., & Eyres, S. P. S. 2005, *MNRAS*, 360, 1483
- Fabas, N., Lèbre, A., & Gillet, D. 2011, *A&A*, 535, A12
- Gallagher, III, J. S., & Code, A. D. 1974, *ApJ*, 189, 303
- Gehrz, R. D. 1988, *ARA&A*, 26, 377

- Gehrz, R. D., Hackwell, J. A., Grasdalen, G. I., Ney, E. P., Neugebauer, G., & Sellgren, K. 1980, *ApJ*, 239, 570
- Goranskij, V., Shugarov, S., Zharova, A., Kroll, P., & Barsukova, E. A. 2010, *Pere-mennye Zvezdy*, 30, 4
- Griffin, R. F., & Redman, R. O. 1960, *MNRAS*, 120, 287
- Hachisu, I., Kato, M., Kato, T., & Matsumoto, K. 2000, *ApJ*, 528, L97
- Hachisu, I., Kato, M., Kato, T., & Matsumoto, K. 2002, in *Astronomical Society of the Pacific Conference Series*, Vol. 261, *The Physics of Cataclysmic Variables and Related Objects*, ed. B. T. Gänsicke, K. Beuermann, & K. Reinsch, 629
- Hachisu, I., Kato, M., Kiyota, S., Kubotera, K., Maehara, H., Nakajima, K., Ishii, Y., Kamada, M., Mizoguchi, S., Nishiyama, S., Sumitomo, N., Tanaka, K., Yamanaka, M., & Sadakane, K. 2008, in *Astronomical Society of the Pacific Conference Series*, Vol. 401, *RS Ophiuchi (2006) and the Recurrent Nova Phenomenon*, ed. A. Evans, M. F. Bode, T. J. O'Brien, & M. J. Darnley, 206
- Han, Z., & Podsiadlowski, P. 2004, *MNRAS*, 350, 1301
- Hanes, D. A. 1985, *MNRAS*, 213, 443
- Harrison, T. E. 1992, *MNRAS*, 259, 17P
- Hauschildt, P. H., Wehrse, R., Starrfield, S., & Shaviv, G. 1992, *ApJ*, 393, 307
- Hellier, C. 2001, *Cataclysmic Variable Stars*, ed. Hellier, C., Springer–Praxis Publishing Ltd, Chichester
- Hick, P., Buffington, A., & Jackson, B. V. 2005, in *Society of Photo-Optical Instrumentation Engineers (SPIE) Conference Series*, Vol. 5901, 340
- Hick, P., Buffington, A., & Jackson, B. V. 2007, in *Society of Photo-Optical Instrumentation Engineers (SPIE) Conference Series*, Vol. 6689, 1

- Hillman, Y., Prialnik, D., Kovetz, A., Shara, M. M., & Neill, J. D. 2013, MNRAS, in press
- Hirose, M., & Osaki, Y. 1990, PASJ, 42, 135
- Hoard, D. W., Wachter, S., Clark, L. L., & Bowers, T. P. 2002, ApJ, 565, 511
- Hounsell, R., Bode, M. F., Hick, P. P., Buffington, A., Jackson, B. V., Clover, J. M., Shafter, A. W., Darnley, M. J., Mawson, N. R., Steele, I. A., Evans, A., Eyres, S. P. S., & O'Brien, T. J. 2010, ApJ, 724, 480
- Hounsell, R., Darnley, M. J., Harman, D. J., Bode, M. F., Clover, J. M., Hick, P. P., Buffington, A., Jackson, B. V., Osborne, J., & Shafter, A. W. 2011, The Astronomer's Telegram, 3373, 1
- Hounsell, R. A. 2012, The Outbursts and Environments of Novae, PhD Thesis, Liverpool John Moores University
- Huth, H. 1976, Information Bulletin on Variable Stars, 1205, 1
- Iben, Jr., I., & Tutukov, A. V. 1984, ApJS, 54, 335
- Imamura, K., & Tanabe, K. 2012, PASJ, 64, L9
- Ireland, M. J., Scholz, M., & Wood, P. R. 2008, MNRAS, 391, 1994
- Jackson, B. V., et al. 2004, Sol Phys, 225, 177
- Jaschek, C., & Jaschek, M. 2009, The Behavior of Chemical Elements in Stars, Cambridge University Press, Cambridge
- Jones, J. E., Alloin, D. M., & Jones, B. J. T. 1984, ApJ, 283, 457
- Kahabka, P. 2006, Advances in Space Research, 38, 2836
- Kahabka, P., Hartmann, H. W., Parmar, A. N., & Negueruela, I. 1999, A&A, 347, L43
- Kato, M. 1990, ApJ, 362, L17
- Kenyon, S. J., & Fernandez-Castro, T. 1987, AJ, 93, 938

- Kenyon, S. J., & Garcia, M. R. 1986, *AJ*, 91, 125
- Knigge, C. 2006, *MNRAS*, 373, 484
- Knigge, C., King, A. R., & Patterson, J. 2000, *A&A*, 364, L75
- Kotak, R. 2008, in *Astronomical Society of the Pacific Conference Series*, Vol. 401, RS Ophiuchi (2006) and the Recurrent Nova Phenomenon, ed. A. Evans, M. F. Bode, T. J. O'Brien, & M. J. Darnley, 150
- Kovetz, A. 1998, *ApJ*, 495, 401
- Kuulkers, E., et al. 2011, *The Astronomer's Telegram*, 3285, 1
- Landolt, A. U. 1970, *PASP*, 82, 86
- Langer, N., Deutschmann, A., Wellstein, S., & Höflich, P. 2000, *A&A*, 362, 1046
- Lenz, P., & Breger, M. 2004, in *IAU Symposium*, Vol. 224, The A-Star Puzzle, ed. J. Zverko, J. Ziznovsky, S. J. Adelman, & W. W. Weiss, 786
- Lenz, P., & Breger, M. 2005, *CoAst*, 146, 53
- Li, W., et al. 2011, *Nature*, 480, 348
- Liu, W.-M., Chen, W.-C., Wang, B., & Han, Z. W. 2010, *A&A*, 523, A3
- Lundmark, K. 1935, *Medd. Lunds Astr. Obs., Ser. II, Band VIII, No. 74*
- Lundstrom, I., & Stenholm, B. 1977, *Information Bulletin on Variable Stars*, 1351, 1
- Lynch, D. K., et al. 2006, *ApJ*, 638, 987
- Mallik, S. V. 1997, *A&A Supp*, 124, 359
- Marin, E., & Shafter, A. W. 2009, *PASP*, 121, 1090
- Marsh, T. R. 2000, *NewAR*, 44, 119
- Mattei, J. A., Menali, H. G., & Waagen, E. O. 2002, *Omicron Ceti light curves (1838-2000)*, Cambridge, MA (USA), American Association of Variable Star Observers

- McLaughlin, D. B. 1937, *PoMic*, 6, 107
- . 1939, *Popular Astronomy*, 47, 410,481,538
- . 1942, *ApJ*, 95, 428
- . 1944, *Popular Astronomy*, 52, 109
- McLaughlin, D. B. 1960, in *Stellar Atmospheres*, ed. Greenstein, J. L. (Chicago: University of Chicago Press)
- Merritt, D., & Petterson, J. A. 1980, *ApJ*, 236, 255
- Mobberley, M. 2009, *Cataclysmic Cosmic Events and How to Observe Them*, ed. M. Mobberle
- Munari, U., Dalla Via, G., Valisa, P., Dallaporta, S., & Castellani, F. 2007, *Central Bureau Electronic Telegrams*, 897, 1
- Munari, U., & Renzini, A. 1992, *ApJ*, 397, L87
- Nakano, S., Tago, A., Nishiyama, K., & Sakamoto, T. 2007, *IAU Circular*, 8821, 1
- Napiwotzki, R., Yungelson, L., Nelemans, G., Marsh, T. R., Leibundgut, B., Renzini, R., Homeier, D., Koester, D., Moehler, S., Christlieb, N., Reimers, D., Drechsel, H., Heber, U., Karl, C., & Pauli, E.-M. 2004, in *Astronomical Society of the Pacific Conference Series*, Vol. 318, *Spectroscopically and Spatially Resolving the Components of the Close Binary Stars*, ed. R. W. Hilditch, H. Hensberge, & K. Pavlovski, 402–410
- Neckel, T., Klare, G., & Sarcander, M. 1980, *A&A Supp*, 42, 251
- Nelson, T., Chomiuk, L., Roy, N., Sokoloski, J. L., Mukai, K., Krauss, M. I., Mioduszewski, A. J., Rupen, M. P., & Weston, J. 2012, *ArXiv e-prints*, 1211.3112
- Ness, J.-U., Schwarz, G., Osborne, J. P., Page, K., Drake, J. J., & Krautter, J. 2008, *The Astronomer's Telegram*, 1747, 1
- Newsham, G., Starrfield, S., & Timmes, F. 2013, *ArXiv e-prints*, 1303.3642

- Ney, E. P., & Hatfield, B. F. 1978, *ApJ*, 219, L111
- Nomoto, K. 1982, *ApJ*, 253, 798
- O'Brien, T. J., Lloyd, H. M., & Bode, M. F. 1994, *MNRAS*, 271, 155
- O'Connell, R. W. 1973, *AJ*, 78, 1074
- Orio, M. 2012, *Bulletin of the Astronomical Society of India*, 40, 333
- Paczynski, B., & Schwarzenberg-Czerny, A. 1980, *Acta Astronom*, 30, 127
- Parthasarathy, M., Branch, D., Jeffery, D. J., & Baron, E. 2007, *NewAR*, 51, 524
- Patterson, J., Oksanen, A., & Monard, B. 2013, *The Astronomer's Telegram*, 4743, 1
- Patterson, J., Thorstensen, J. R., & Kemp, J. 2005, *PASP*, 117, 427
- Patterson, J., Kemp, J., Shambrook, A., Thorstensen, J. R., Skillman, D. R., Gunn, J., Jensen, L., Vanmunster, T., Shugarov, S., Mattei, J. A., Shahbaz, T., & Novak, R. 1998, *PASP*, 110, 380
- Payne-Gaposchkin, C. 1964, *The galactic novae*, Dover Publication, New York
- Peat, D. W. 1964, *MNRAS*, 128, 475
- Perryman, M. A. C., & ESA, eds. 1997, *ESA Special Publication*, Vol. 1200, *The HIPPARCOS and TYCHO catalogues. Astrometric and photometric star catalogues derived from the ESA HIPPARCOS Space Astrometry Mission*
- Pietsch, W. 2010, *Astronomische Nachrichten*, 331, 187
- Poggiani, R. 2009, *Astronomische Nachrichten*, 330, 77
- Poznanski, D., Prochaska, J. X., & Bloom, J. S. 2012, *MNRAS*, 426, 1465
- Reid, M. J., & Goldston, J. E. 2002, *ApJ*, 568, 931
- Ribeiro, V. A. R. M. 2011, *Investigation of the Nebular Remnants of Novae*, PhD Thesis, Liverpool John Moores University

- Ribeiro, V. A. R. M., Darnley, M. J., Bode, M. F., Munari, U., Harman, D. J., Steele, I. A., & Meaburn, J. 2011, *MNRAS*
- Richmond, M. W., Treffers, R. R., Filippenko, A. V., Paik, Y., Leibundgut, B., Schulman, E., & Cox, C. V. 1994, *AJ*, 107, 1022
- Ringwald, F. A., Naylor, T., & Mukai, K. 1996, *MNRAS*, 281, 192
- Rowles, J., & Froebrich, D. 2009, *MNRAS*, 395, 1640
- Sahman, D. I., Dhillon, V. S., Marsh, T. R., Moll, S., Thoroughgood, T. D., Watson, C. A., & Littlefair, S. P. 2013, *MNRAS*, 433, 1588
- Schaefer, B. E. 1990, *ApJ*, 355, L39
- . 2005, *ApJ*, 621, L53
- . 2010, *ApJS*, 187, 275
- Schaefer, B. E., Landolt, A. U., Vogt, N., Buckley, D., Warner, B., Walker, A. R., & Bond, H. E. 1992, *ApJS*, 81, 321
- Schaefer, B. E., & Pagnotta, A. 2012, *Nature*, 481, 164
- Schaefer, B. E., Pagnotta, A., & Shara, M. M. 2010a, *ApJ*, 708, 381
- Schaefer, B. E., Pagnotta, A., Xiao, L., Darnley, M. J., Bode, M. F., Harris, B. G., Dvorak, S., Menke, J., Linnolt, M., Templeton, M., Henden, A. A., Pojmański, G., Pilecki, B., Szczygieł, D. M., & Watanabe, Y. 2010b, *AJ*, 140, 925
- Schaefer, B. E., Landolt, A. U., Linnolt, M., Stubbings, R., Pojmanski, G., Plummer, A., Kerr, S., Nelson, P., Carstens, R., Streamer, M., Richards, T., Myers, G., & Dillon, W. G. 2013, *ApJ*, 773, 55
- Schlegel, D. J., Finkbeiner, D. P., & Davis, M. 1998, *ApJ*, 500, 525
- Schwarz, G. J., Shore, S. N., Starrfield, S., Hauschildt, P. H., Della Valle, M., & Baron, E. 2001, *MNRAS*, 320, 103

- Selvelli, P., González-Riestra, R., Gilmozzi, R., & Cassatella, A. 2010, *MmSAI*, 81, 388
- Shafter, A. W. 2002, in *American Institute of Physics Conference Series*, Vol. 637, *Classical Nova Explosions*, ed. M. Hernanz & J. José, 462
- Shafter, A. W., Bode, M. F., Darnley, M. J., Misselt, K. A., Rubin, M., & Hornoch, K. 2011a, *ApJ*, 727, 50
- Shafter, A. W., Rau, A., Quimby, R. M., Kasliwal, M. M., Bode, M. F., Darnley, M. J., & Misselt, K. A. 2009, *ApJ*, 690, 1148
- Shafter, A. W., Darnley, M. J., Hornoch, K., Filippenko, A. V., Bode, M. F., Ciardullo, R., Misselt, K. A., Hounsell, R. A., Chornock, R., & Matheson, T. 2011b, *ApJ*, 734, 12
- Shahbaz, T., Livio, M., Southwell, K. A., & Charles, P. A. 1997, *ApJ*, 484, L59
- Shara, M. M., Zurek, D. R., Williams, R. E., Prialnik, D., Gilmozzi, R., & Moffat, A. F. J. 1997, *AJ*, 114, 258
- Sharpless, S. 1956, *ApJ*, 124, 342
- Shore, S. N., Schwarz, G. J., De Gennaro Aquino, I., Augusteijn, T., Walter, F. M., Starrfield, S., & Sion, E. M. 2013, *A&A*, 549, A140
- Shore, S. N., Sonneborn, G., Starrfield, S., Gonzalez-Riestra, R., & Polidan, R. S. 1994, *ApJ*, 421, 344
- Shore, S. N., Wahlgren, G. M., Augusteijn, T., Liimets, T., Page, K. L., Osborne, J. P., Beardmore, A. P., Koubsky, P., Šlechta, M., & Votruba, V. 2011, *A&A*, 527, A98
- Shugarov, S., Chochol, D., Volkov, I., & Pribulla, T. 2010, in *Astronomical Society of the Pacific Conference Series*, Vol. 435, *Binaries - Key to Comprehension of the Universe*, ed. A. Prša & M. Zejda, 315
- Slesnick, C. L., Hillenbrand, L. A., & Carpenter, J. M. 2008, *ApJ*, 688, 377

- Starrfield, S. 2008a, in RS Ophiuchi (2006) and the Recurrent Nova Phenomenon
- Starrfield, S. 2008b, in *Classical Novae*, 2nd Edition, ed. Bode, M. F. & Evans, A., Cambridge University Press, Cambridge, 44
- Starrfield, S., Timmes, F. X., Iliadis, C., Hix, W. R., Arnett, W. D., Meakin, C., & Sparks, W. M. 2012, *Baltic Astronomy*, 21, 76
- Steele, I. A., et al. 2004, in *Society of Photo-Optical Instrumentation Engineers (SPIE) Conference Series*, Vol. 5489, 679
- Strope, R. J., Schaefer, B. E., & Henden, A. A. 2010, *AJ*, 140, 34
- Surina, F., Bode, M. F., & Darnley, M. J. 2013a, *The 11th Asian-Pacific Regional IAU Meeting 2011, NARIT Conference Series*, Vol. 1, p161-164
- Surina, F., Hounsell, R. A., Bode, M. F., Darnley, M. J., Harman, D. J., & Walter, F. M. 2013b, *ArXiv e-prints*, 1303.6592
- . 2014, *AJ*, in press
- Swierczynski, E., Mikolajewski, M., Tomov, T., Ragan, E., Galan, C., Karska, A., Wychudzki, P., Wiecek, M., Cikala, M., & Lewandowski, M. 2010, in *Astronomical Society of the Pacific Conference Series*, Vol. 435, *Binaries - Key to Comprehension of the Universe*, ed. A. Prša & M. Zejda, 297
- Tomov, T., et al. 2007, *Information Bulletin on Variable Stars*, 5779, 1
- Turatto, M., Benetti, S., & Cappellaro, E. 2003, in *From Twilight to Highlight: The Physics of Supernovae*, ed. W. Hillebrandt & B. Leibundgut, 200
- Turnshek, D. E. 1985, *An Atlas of digital spectra of cool stars (Tucson, Arizona: Western Research Co.)*, 85
- Uthas, H., Knigge, C., & Steeghs, D. 2010, *MNRAS*, 409, 237
- van den Heuvel, E. P. J., Bhattacharya, D., Nomoto, K., & Rappaport, S. A. 1992, *A&A*, 262, 97

- van Dokkum, P. G. 2001, *PASP*, 113, 1420
- Verbunt, F. 1982, *Space Science Reviews*, 32, 379
- Walder, R., Folini, D., & Shore, S. N. 2008, *A&A*, 484, L9
- Walter, F. M., Battisti, A., Towers, S. E., Bond, H. E., & Stringfellow, G. S. 2012, *PASP*, 124, 1057
- Warner, B. 1986, *MNRAS*, 222, 11
- . 1987, *MNRAS*, 227, 23
- . 1995, *Cataclysmic Variable Stars*, ed. Warner, B. (Cambridge: Cambridge University Press)
- Warner, B. 2002, in *American Institute of Physics Conference Series*, Vol. 637, *Classical Nova Explosions*, ed. M. Hernanz & J. José, 3
- Warner, B. 2008, in *Classical Nova*, 2nd Edition, ed. Bode, M. F. & Evans, A., Cambridge University Press, Cambridge, 16
- Webbink, R. F., Livio, M., Truran, J. W., & Orio, M. 1987, *ApJ*, 314, 653
- Weight, A., Evans, A., Naylor, T., Wood, J. H., & Bode, M. F. 1994, *MNRAS*, 266, 761
- Whelan, J., & Iben, Jr., I. 1973, *ApJ*, 186, 1007
- Williams, R. E. 1982, *ApJ*, 261, 170
- . 1992, *AJ*, 104, 725
- Woudt, P. A., & Warner, B. 2003, *MNRAS*, 343, 313
- Wyse, A. B. 1940, *Publications of Lick Observatory*, 14, 93
- Yamaoka, H. 2004, *IAU Circular*, 8380, 1
- Yoon, S.-C., & Langer, N. 2003, *A&A*, 412, L53
- Yungelson, L., & Livio, M. 1998, *ApJ*, 497, 168